CRANFIELD UNIVERSITY

Domenico di Cugno

Tightly-Wound Vortex and Self-Generated Intake Distortion Effects on Turbomachinery Performance

School of Engineering

Ph.D. Thesis

SCHOOL OF ENGINEERING
DEPARTMENT OF POWER AND PROPULSION

Full Time Ph.D.

Academic Year 2010 – 2013

Domenico di Cugno

Tightly-Wound Vortex and Self-Generated Intake Distortion Effects on Turbomachinery Performance

Supervisors: Dr V. Pachidis, Dr D.G. MacManus

July 2013

This report is submitted in partial fulfilment of the requirements for the degree of Doctorate of Philosophy

Abstract

Current developments of civil and military applications may require the installation of aero-engines embedded into the aircraft structure. Consequently, complex diffusing S-ducts are necessary to convey air from the intake to the compressor. In addition, civil applications require the reduction of specific fuel consumption and noise levels. These targets can be met by increasing the engine mass flow and reducing the specific thrust by increasing the bypass ratio. In underwing installations there is an increased tendency of ground vortex creation. Generally, the application of complex S-shaped intakes as well as the ingestion of vortices can lead to inlet flow distortion in terms of total pressure and swirl. Consequently, blade vibrations and changes in turbomachinery performance are likely to occur. The aim of this research is to provide qualitative and quantitative information regarding the effect on a fan rotor performance caused by the self-generated distortion of an S-duct and its combination with that attributed to a tightly-wound vortex.

A purely numerical coupled system S-shaped intake/fan rotor configuration was defined in this research to analyze the effect of total pressure combined with swirl distortion on the fan rotor performance. Steady-state CFD simulations were carried out on this system by considering clean conditions and, for the first time, the vortex ingestion at the intake inlet and with the rotor operating at two different rotational speeds. Under clean inlet conditions, the self-generated distortion of the S-duct causes a degradation of rotor performance. Moreover, the rotor operability range reduces significantly due to a localized blade overloading. On the other hand, as a vortex is ingested in the system, this interacts with the self-generated distortion in different manners depending on the location and polarity of the vortex itself. Consequently, the level of flow distortion at the AIP changes accordingly. The sign of the change in rotor corrected mass flow is essentially established by the polarity of the vortex ingested. Therefore, the effect of the swirl is predominant compared to that of the total pressure distortion. In particular, the vortices ingested at the centre of the intake inlet plane cause the largest change in rotor corrected mass flow. Regarding the loss of stability pressure ratio, this is established by the swirl distortion even though the effect of total pressure distortion is also notable. Amongst the case studies characterized by low total pressure distortion, a swirl distortion correlation is defined between the loss of stability pressure ratio and the mass flow average of the

relative rotor incidence change calculated at the aerodynamic interface plane. A scatter between the CFD results and the established correlation can be attributed to the variations in total pressure distortion.

In addition, a CFD based methodology was assessed to determine the location of the aerodynamic interface plane for swirl distortion. This was applied on the datum NASA Rotor 67 configuration working with a vortex ingested at different span locations and for two relevant operating conditions. The outcome of this analysis confirms that, in the worst scenario, the location of the aerodynamic interface plane is located in a position that is an order of magnitude closer to the rotor face compared to what established by previous research for total pressure distortion. This finding would allow the application during the experiments of shorter upstream ducts than that required for total pressure distortion. However, the assessment of a methodology providing a more precise information on location of the aerodynamic interface plane for total pressure distortion would be necessary.

Acknowledgements

I would like to acknowledge a large number of people who have contributed to this research in many ways and have been very close to me.

Firstly, the Head of the Department of Power and Propulsion and the Director of the Cranfield Rolls-Royce UTC, Prof. Pericles Pilidis and Prof. Riti Singh. They gave me the opportunity to conduct this research and to gain experience of business development around the United Kingdom and Europe.

My academic supervisors at Cranfield University, Dr. Vassilios Pachidis and Dr. David G. MacManus. Since the beginning of my research, they provided effective guidance and constant help. They have always believed in my work and their support has been invaluable!

My industrial supervisors from Rolls-Royce UK, Barry Moore, Richard Tunstall and Gordon Warnes. I thank them for providing financial support necessary to complete this project. Many thanks also to Paul Hield, Steve Moore, Kevin Menzies, Arthur Rowe, Stephen Brown and Christopher Sheaf of Rolls-Royce UK.

My PhD research team colleagues, Ahad Medhi and Grant McLelland. The success of this research has been in part due to the help I received from them. Their suggestions and point of view have been essential. In addition, they have been very good friends with whom I shared good times outside of the academic environment.

During this research I have had the opportunity to work with a number of very talented MSc students: Javier Castaneda, Darshan Metha, Jesus Lopez Ruiz, Timothy Tramontin, Francisco Fernandez and Emile Raya. I would also like to thank the MSc students Roberto Jemerez and Taieb Ben Sghaier who worked with my colleague Ahad Medhi. All of them contributed with new ideas to my research.

Dr. Robert Sawko. He spent a lot of time helping me to resolve many programming issues. Thanks to the knowledge he has imparted I have developed a passion for the Linux operating system, which I believe will be fundamental to my future career.

The Department of Power and Propulsion was full of interesting people with whom I interacted to share knowledge and receive advices. Particularly, I would like to mention

Dr. Joao Teixeira, Dr. Vishal Sethi, Dr. Uye Igie, Dr. P. Zachos and Mr. John Witton.

The IT department staff. A special thanks to Dr. Les Oswald, Mr. Andy Gittings and Mr. Chris Cooper who have provided me a lot of support for High Performance Computing and Linux issues. I learned many interesting things throughout these years.

The UTC and departmental administrators Maria Negus, Gillian Hargreaves and Nicola Datt. They provided essential administrative support.

My very close PhD colleagues: Alice C. Stitt, Panagiotis Giannakakis, Tom Elson, Eduardo Anselmi, Adbullahi Abu, Devaiah Nalianda Karumbaiah, Rukshan Navaratne and Isaiah Allison. They helped for several technical problems as well as they supported me morally during very difficult periods which I encountered during the doctoral research period.

However, I would like to say a special thanks to Serena Zoppellari, Nick Greek and his wife Claire who have given help in solving problems both within the academic environment and life in general.

My housemates in Milton Keynes: Emile Thomas, Antonio Rivas, Pavel Litos, Valerie Maupuvire, Rafik Boullelou and his wife Amina. They supported me during very difficult periods encountered throughout this research.

Giuseppina di Lorenzo. She has been like a sister supporting me morally in very difficult situations encountered during this doctoral program.

Professor Pietro De Palma at Politecnico di Bari. He raised in me a passion for turbomachinery and CFD.

Finally, this would not have been possible without the love of my family. Much appreciation goes to my Dad, Mum, my brother Francesco, my sister Rosanna and my brother in law, Leonardo. They have and will never give up on helping me in very difficult situations!

Domenico di Cugno
Cranfield, July 2013

Contents

List of Figures

List of Tables

Nomenclature

English symbols

a	Shock waves length measured along the axial direction, m
A	Wake axial momentum constant, m^2s^{-1} / Area, m^2
c_0	Speed of sound, m^2s^{-1}
D	Diameter, m
fd	Flow direction component
h	Vertical distance from lowest point of the highlight plane to ground, m
k	Specific turbulent kinetic energy, m^2s^{-2} / Constant for vortex circulation calculation
KE	Kinetic energy, W
L	S-duct length, m
M	Mach number
n	Vatistas model constant
N_d	Design rotational speed of the NASA Rotor 67
N_O	Number of intervals on mesh edges of the rotor defined for the O-grid around the blade
N_θ	Number of intervals on mesh edges of the rotor defined along the tangential direction
N_r	Number of intervals on mesh edges of the rotor defined along the spanwise direction
$N_{r,i}$	Number of intervals on mesh edges of the intake defined along the radial direction with $i = 1,\ldots 4$
N_{tot}	Total number of mesh elements for intake or rotor CFD domain

N_x	Number of intervals on mesh edge defined for the central *O*-grid of the intake along the horizontal direction (x)
N_y	Number of intervals on mesh edge defined for the central *O*-grid of the intake along the vertical direction (y)
$N_{z,i}$	Number of intervals on mesh edges of the intake defined along the streamwise direction with $i = 1, \ldots 10$
$N_{z,in}$	Number of intervals on mesh edges defined along the streamwise direction and at the inlet region of the rotor CFD domain
$N_{z,out}$	Number of intervals on mesh edges defined along the streamwise direction and at the outlet region of the rotor CFD domain
$NDMF_2$	Rotor outlet non-dimensional mass flow (Eq. 4.2), $kgs^{-1}K^{0.5}Pa^{-1}$
O_f	S-duct Offset, *m*
p	Static pressure, *Pa*
P	Generic point
P_C	Vortex prescription point aligned to the centre of the intake inlet plane of the coupled system configuration (see § 5)
P_S	Vortex prescription point aligned to the starboard edge of the intake of the coupled system configuration (see § 5)
P_B	Vortex prescription point aligned to the bottom edge of the intake of the coupled system configuration (see § 5)
P_0	Total pressure, *Pa*
P_P	Vortex prescription point aligned to the port edge of the intake of the coupled system configuration (see § 5)
P_T	Vortex prescription point aligned to the top edge of the intake of the coupled system configuration (see § 5)
PR	Rotor pressure ratio
PRS	Rotor stability pressure ratio
r	Radial distance (or radius), *m*
r_c	Vortex core radius, *m*
R	Radius of curvature of an S-shaped intake, *m*
s	Blade span, *m*
SD	Swirl directivity (Eq. A.5)

SF	Scaling factor
SI	Swirl intensity (Eq. A.4)
SP	Swirl pairs (Eq. A.6)
SS	Sector swirl (Eq. A.3 and A.2), $deg(^o)$
S	Generic stability limit operating point
t	Time, s
T_0	Total temperature, K
V	Velocity, ms^{-1} / Vortex centre
$\mathbf{V}$	Velocity vector, ms^{-1}
W	Mass flow, kgs^{-1}
W_{cor}	Rotor corrected mass flow (Eq. 4.1), kgs^{-1}
W_{NC}	Rotor mass flow at near choking, kgs^{-1}
W_{NS}	Rotor mass flow at near stall, kgs^{-1}
z	Axial position, m

Greek symbols

α	Swirl angle (Eq. 2.1), $deg(^o)$
α_s	Swirl angle attributed to the vortex, $deg(^o)$
β	Flow angle relative to the rotor, $deg(^o)$
γ	Specific heat ratio / Vortex location at a generic time-step, $deg(^o)$
γ_0	Vortex location at a time-step of reference, $deg(^o)$
Γ	Vortex circulation, m^2s^{-1}
δ	Tolerance to determine the location of the AIP for swirl distortion
$\overline{\lvert\Delta\beta\rvert}$	Mass flow average of the magnitude of the relative flow angle change (Eq. 3.3), $deg(^o)$
$\Delta\gamma_p$	Angular extent relative to a single blade passage, $deg(^o)$
∂	Differential operator
ε	Turbulent kinetic energy dissipation rate, m^2s^{-3}

η_{is}	Rotor isentropic efficiency
θ	Circumferential location, $deg(^o)$ / Swirl extent, $deg(^o)$
θ_{max}	Total intake subtended angle, $deg(^o)$
λ	Shock wave length (Eq. 6.9), m
Π	Shock wave strength
Π_0	Initial shock wave strength
ρ	Density, kgm^{-3}
τ	Blade pitch, m / Shear stress, Nm^{-2}
ϕ	Shock wave angle, $deg(^o)$ / Circumferential position relative to the intake, $deg(^o)$
ψ	Yaw angle, $deg(^o)$
ω	Vorticity, s^{-1} / Turbulent frequency, s^{-1}

Non-dimensional parameters

C_f	Skin friction coefficient (Eq. 3.9)
C_p	Static pressure coefficient (Eq. 2.2)
C_{P_0}	Total pressure coefficient (Eq. 2.3)
DC_{60}	Distortion coefficient based on the lowest average 60^o sector pressure (Eq. A.1)
DC_{120}	Distortion coefficient based on the lowest average 120^o sector pressure (Eq. A.1)
h/D_l	Ground clearance
M^*	Normalized Mach number component defined for Wellborn S-duct (Eq. 2.4)
$(p')^*$	Non-dimensional standard deviation of static pressure (Eq. 3.4)
P_0^*	Non-dimensional total pressure
U^*	Velocity ratio
U^*_{max}	Velocity ratio at which Γ^* is maximum
$U_R^\star$	Critical to maximum velocity ratio (Eq. B.8)
$U^\sim$	Normalised velocity ratio (Eq. B.10)
$\left(V'_\theta\right)^*$	Non-dimensional standard deviation of tangential velocity component (Eq. 3.6)
W^*	Rotor normalized mass flow (Eq. 3.8)

y^+	Non-dimensional wall distance
γ	Non-dimensional S-duct diffusing profile (Eq. 3.2)
Γ^*	Non-dimensional circulation (Eq. B.7)
$\Delta NDMF_2$	Relative change of rotor outlet non-dimensional mass flow (Eq. C.1)
ΔPRS	Loss of stability pressure ratio (Eq. 3.13)
$\Delta V_z\%$	Relative axial velocity change (Eq. 3.26)
$\Delta V^*_{z,ex}$	Axial velocity excess ratio (Eq. 3.26)
$\Delta\alpha$	Swirl angle change
$\Delta\beta$	Relative flow angle change
$\Delta\gamma^*$	Non-dimensional vortex angular location relative to that of the blade passage (Eq. 6.11)
ζ	Non dimensional S-duct centreline offset (Eq. 3.1)
η	Pressure recovery (Eq. 3.12) / Normalised non-dimensional circulation (Eq. B.15)
$\rho^\star$	Density ratio

Subscripts

$1,2$	Aero-stations defined for the NASA Rotor 67 / Inlet and outlet stations of the Wellborn S-duct
60	Minimum 60^o sector
$A80$	Operating point of the datum NASA Rotor 67 configuration working at 80% N_d under clean inlet conditions such that $\Delta NDMF_{2,A80} = \Delta NDMF_{2,S80}$ (§ 4.3.4)
$A100$	Operating point of the datum NASA Rotor 67 configuration working at 100% N_d under clean inlet conditions such that $\Delta NDMF_{2,A100} = \Delta NDMF_{2,S100}$ (§ 4.2.4)
AIP	Aerodynamic Interface Plane
cl	Clean inlet conditions
dist	Distorted inlet conditions
h	Rotor hub
i	Generic ring defined at the AIP
in	CFD inlet plane / Intake inlet centerline of Wellborn S-duct

j	Generic cross flow plane
k	Number of swirl pairs per revolution
l	Intake highlight plane
max	Maximum value
$mean$	Arithmetic averaged value
min	Minimum value
out	CFD rotor outlet plane / S-duct outlet plane
p	Primary flow relative to an S-shaped intake
$peak$	Peak value
P	Generic point
r	Radial direction
ref	Standard atmospheric conditions
rel	Relative frame of reference
s	Spinner / Secondary flow relative to an S-shaped intake
$S80$	Near stall operating point of the NASA Rotor 67 mounted on the coupled system and working at 80% N_d under clean intake inlet conditions (§ 4.3.4)
$S100$	Near stall operating point of the NASA Rotor 67 mounted on the coupled system and working at 100% N_d under clean intake inlet conditions (§ 4.2.4)
t	Rotor tip
V	Vortex centre
w	S-duct wall
z	Axial direction (or streamwise direction at the S-duct outlet)
θ	Circumferential direction
∞	Free-stream conditions

Superscripts

G	Global coordinate system
L	Coordinate system local to the vortex centre
$\sim$	Area averaged value
$^-$	Mass flow averaged value
$\star$	Non-dimensional or normalized quantities
$+$	Positive value
$-$	Negative Value
$'$	Standard deviation

Abbreviations

AGARD	Advisory Group for Aerospace Research and Development
AIP	Aerodynamic Interface Plane
AIR	Aerospace Information Report
ARA	Aircraft Research Association
ARP	Aerospace Recommended Practice
ASME	American Society of Mechanical Engineering
CFD	Computational Fluid Dynamics
DES	Detached Eddy Simulation
HMF	High Mass Flow
IGV	Inlet Guide Vane
LMF	Low Mass Flow
NACA	National Advisory Committee for Aeronautics
NACRE	New Aircraft Concepts Research
NASA	National Aeronautics and Space Administration
PIV	Particle Image Velocimetry
RAE	Royal Aircraft Establishment
RANS	Reynolds Averaged Navier-Stokes

RMS	Root Mean Square
RNS	Reduced Navier-Stokes
SAE	Society of Automotive Engineers
SFC	Specific Fuel Consumption
SST	Shear Stress Transport
URANS	Unsteady Reynolds Averaged Navier-Stokes
UTC	University Technology Centre
VGs	Vortex Generators

Chapter 1

Introduction

Future propulsive concepts for civil applications may require the installation of aero-engines to be more closely coupled to, or even embedded into the aircraft structure. Clearly, the recent trend of military applications has been for fully embedded engines. Typical examples are the General Dynamics F-16 and McDonnel-Douglas F/A-18 [1,2] (Fig. 1.1).

Figure 1.1: McDonnel-Douglas F/A-18 ©Bumbu Pas (November 2012)

Their propulsion systems use complex diffusing S-ducts to convey air from the intake to the compressor. To match appropriate engine performance, the S-duct must provide minimum total pressure loss up to the rotor face while ensuring that the flow enters

the compressor with uniform pressure and velocity. Unfortunately, the curvature associated with S-duct geometry produces secondary flows to which total pressure and swirl distortion are attributed. Consequently, the engine surge and stall limits reduce. Moreover, the need to reduce the velocity at the engine face is obtained with an increase of cross-sectional area along the S-duct by making flow separation likely to manifest within the duct[3]. Hence, the total pressure recovery and, consequently, the propulsion efficiency reduce. For these reasons, the reduction of flow distortion as well as the improvement of total pressure recovery of the intake are the key concerns for the industry[4].

For civil turbofan engines, one of the solutions applied to reduce the specific fuel consumption (SFC) and noise level is to increase the engine mass flow and reduce the specific thrust through an increase in bypass ratio. This is one of the solutions proposed by the New Aircraft Concepts Research (NACRE) group[5] which causes an increase in propulsive efficiency. Nevertheless, for underwing installations, this increases the risk of ground vortex ingestion. On the other hand, when the bypass ratio becomes too large underwing installations have to be replaced by rear installations. In this case, however, fuselage or junction vortices can arise and be ingested into the aero-engine. Major consequences include loss of stability pressure ratio, blade vibration and mechanical damage of the turbo-engine components due to, in the case of ground vortex, the ingestion of foreign objects[6,7].

1.1 The inlet flow distortion background

The inlet flow distortion is one of the most troublesome and least understood problems for intake designers. In real operating conditions a fan or compressor of an aircraft engine works with a non-uniform inlet flow field. Hence, the introduction of non-axisymmetric flow at the compressor inlet face can severely alter the compressor operation in terms of performance, engine stability, and structural integrity. Consequently, compressor stall and surge as well as combustion flame out or overheating of the engine may occur[8]. In general, three main types of inlet flow distortion can be identified. These are the total temperature, total pressure and swirl distortion[9].

Total temperature distortion This type of flow distortion is mainly caused by external disturbances[9] such as hot gas ingestion during weapons' firing, vertical take off and landing and steam ingestion during carrier operations[8]. Compressor stability issues related to this type of distortion determined the establishment of correlations by the early 1990s[10]. Within the frame of the current research, this type of distortion is not considered.

Total pressure distortion This is the most common type of inlet flow distortion, which is generally caused by flow separation and wakes[9]. The early focus of engine/inlet compatibility investigations was on large gas turbine engines mounted on wings or fuselages that used straight Pitot-style inlet systems. Hence, the emphasis was addressed on understanding performance and stability issues related to engines installed with straight inlet systems. Consequently, the Aerospace Recommended Practice (ARP) 1420[11] and the Aerospace Information Report (AIR) 1419[12] addressed the inlet/engine compatibility by considering only the inlet total pressure distortion. Intake lip and wall separation occurring within intake bodies produce flow conditions around the lip or wall which depend on intake mass flow. For civil aircraft there is a low risk of total pressure distortion except for take-off and landing operations when high angles of attack may be reached.

Swirl distortion This type of flow distortion has been recognised as the third type of distortion after that attributed to total pressure and total temperature[13,14]. Although there has been a substantial amount of research in the general field of inlet flow distortion, the existing methodologies are not directly applicable to this type of distortion since they have been mainly developed to address total pressure[12] and bulk swirl distortions applied separately. Since the current research involves S-shaped intake flow fields and tightly wound vortex ingestion the swirl distortion is analyzed with the total pressure distortion.

The need to consider swirl distortion arose from previous experiences, for example that of the Tornado jet fighter[15]. This aircraft presents a pair of side-mounted air intakes with horizontal-turning S-shaped diffuser ducts, disposed on each side of the forward fuselage, as shown in Fig. 1.2. Limited full scale tests of the engine/inlet combination were performed. Then, as prototypes flight testing of the aircraft began, engine surge was occurring at the port (left) engine for subsonic flight speed and high angle of attack. A similar phenomena occurred at the starboard (right) engine and at supersonic flight speed near zero angle of attack. In general, it was noticed that the presence of the swirl distortion at the Aerodynamic Interface Plane (AIP) could combine with total pressure distortion and generate a more severe compressor stability problem than with either distortion acting alone. As a result, for counter-rotating swirl distortion, an overloading of the fan was observed, which caused engine instabilities, even though the total pressure distortion was within allowable limits established for total pressure distortion acting alone. At subsonic conditions, a difference in the fan rotational speed between port and starboard engines, increasing with the angle of attack, was observed. In particular, the port and starboard engine speed decreased and increased, respectively, with a consequent increase loading on the port engine. As the angle of attack increased above a critical value, the flow on the lower lip separated. Consequently, the low energy located in the separated zone interacted with the pressure gradient existing in the horizontal S-bend by generating a bulk swirl which was superimposed to the twin swirl pattern characterizing an S-duct (Fig. 1.2). Since both engines were rotating in the same direction, the port and starboard

engine were exposed to a counter- and a co-rotating bulk swirl, respectively. In particular, the port engine in the Tornado experiences the counter-rotating bulk swirl by surging consistently at high angle of attack and subsonic flight Mach number.

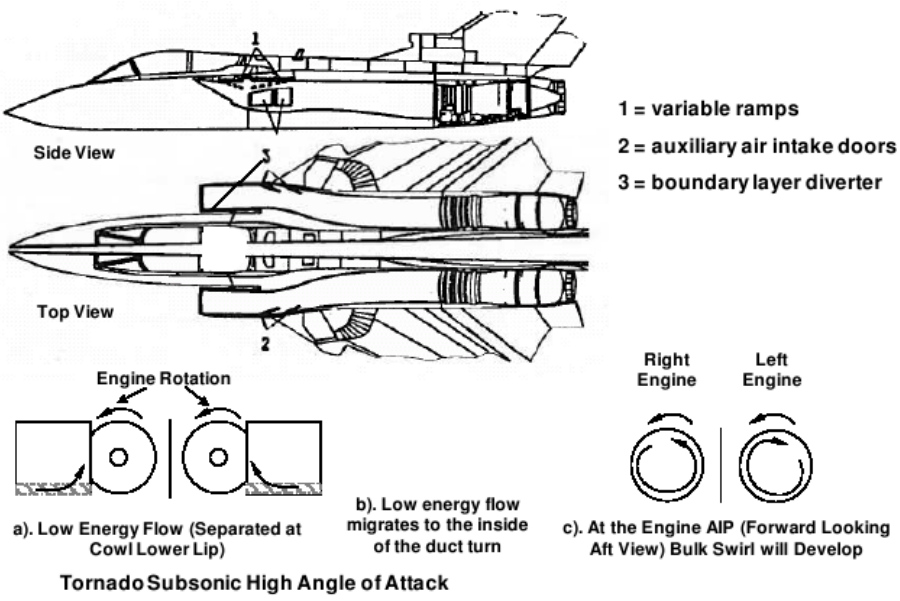

Figure 1.2: Example of Tornado side inlet generating opposite bulk swirl pattern due to a lower lip separation [15]

Figure 1.3 shows the flow angle resulting from the combination of the bulk and twin swirl pattern and the total pressure isobars measured at the AIP of the port engine. As a result, total pressure and swirl distortion are correlated since the largest flow angles measured at the AIP occurs where the lowest total pressure region takes place.

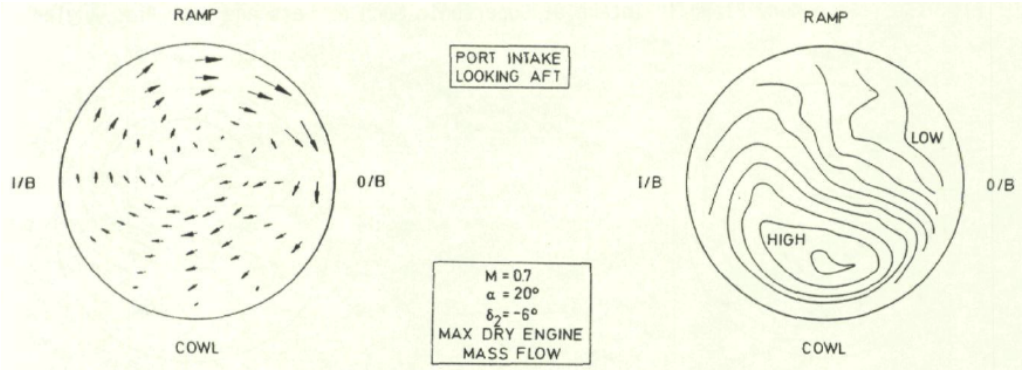

Figure 1.3: Absolute flow angle (left) and total-pressure isobars (right) measured at AIP of the Tornado aircraft [15]

1.1.1 Effect of inlet flow distortion on turbomachinery performance

Generally, the types of inlet flow distortion introduced in § 1.1 may occur simultaneously. Consequently, it is challenging to quantify the change of turbomachinery performance attributed to each type of inlet flow distortion separately. For this reason, previous research[16,12,11] has introduced numerical models to account for the effect of each type of flow distortion separately. In this section, the main findings regarding the effect of total pressure and swirl distortion on turbomachinery performance are presented. They represent the type of flow distortion normally involved in an S-duct or attributed to a tightly-wound vortex which were considered in this research.

1.1.1.1 Total pressure distortion

The main consequence of the total pressure distortion on turbomachinery performance is the reduction of stability pressure ratio. The amount of reduction depends on the circumferential extent of the total pressure distortion pattern (Fig. 1.4).

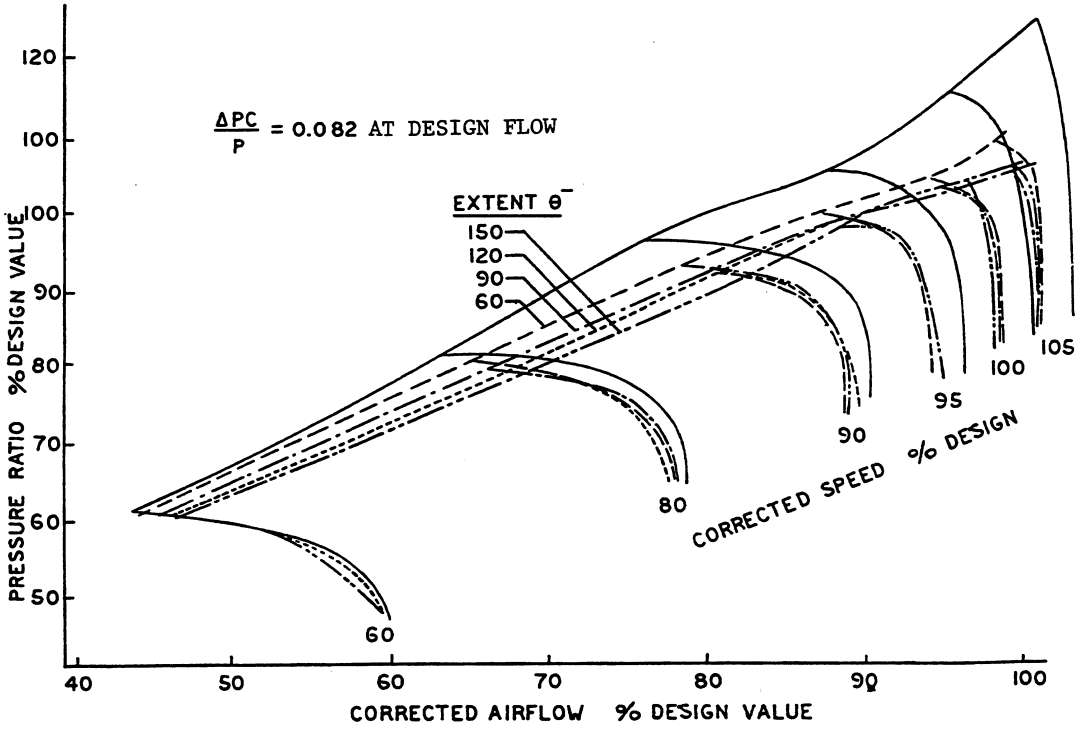

Figure 1.4: Change of compressor performance for different extents of one-per-revolution square wave circumferential total pressure distortion[12]

As the blades encounter a low total pressure region, their loading increases and, consequently, the rotor surge margin reduces[17]. Meanwhile, the blades are subjected to unbalanced load cycles which cause a reduction in fatigue life. The total pressure distortion is then converted by the compressor into total temperature distortion at the inlet of the combustor[18]. This can cause a circumferential non-uniform temperature profile distribution at the turbine inlet with a corresponding detrimental effect on the turbine life.

In some cases total pressure distortion induces swirl distortion. This is due to the static pressure defect generated upstream of the engine face when total pressure distortion and uniform static pressure are imposed[19,20]. The compressor attempts to handle the distortion and the deficit in static pressure over the spoilt sector by causing a cross flow from the clean to the spoilt sector. In turn, this cross flow generates a counter- and a co-rotating swirl that contributes to the reduction of the compressor performance (Fig. 1.5).

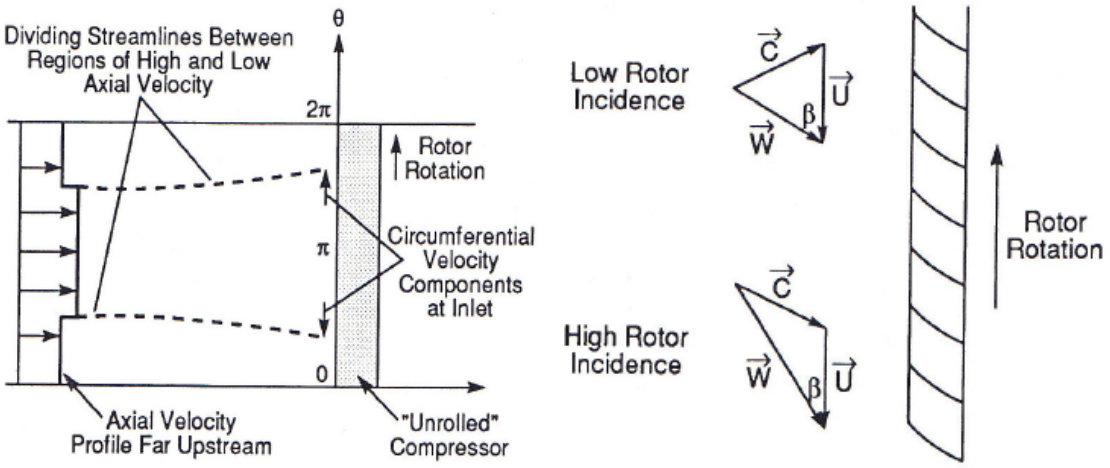

(a) Induced cross flow related to the static pressure redistribution

(b) Induced swirl ahead of the compressor face

Figure 1.5: Swirl distortion at compressor inlet induced by the upstream flow redistribution[20]

1.1.1.2 Swirl distortion

The swirl distortion was extensively studied by the Society of Automotive Engineers (SAE) S-16 Committee[16]. They classified this type of distortion in four categories: bulk swirl, paired swirl, cross flow swirl and tightly-wound vortices. These were observed at the Aerodynamic Interface Plane (AIP) and described in detail in § 2.1. It was noticed that the magnitude of the change in compressor performance due to the swirl distortion depended on the aforementioned categories.

Regarding the pure bulk swirl, its effect on compressor performance was extensively identified in previous research[21,16,22] and can be easily described. The SAE S-16 Committee revealed that the bulk swirl increases or decreases the flow incidence angle over the blades depending on its polarity. Hence, the reduction of incidence obtained with a co-rotating bulk swirl entails an increase in surge margin as shown in Fig. 1.6. Consequently, the compressor speedlines are displaced to the left and downwards, reducing the pressure ratio and corrected mass flow. The opposite situation manifests by considering a counter-rotating bulk swirl.

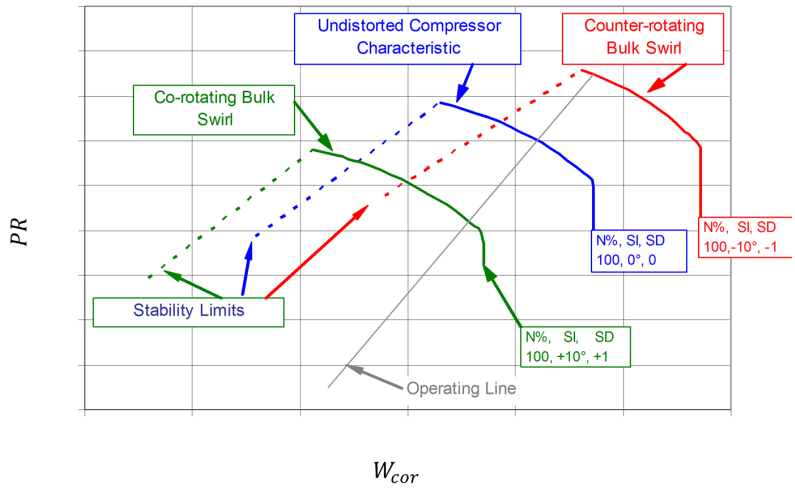

Figure 1.6: Effect of pure bulk swirl on compressor performance[16]

In addition, Sheoran et al.[22] carried out RANS CFD simulations relative to the first stage of the Low Pressure Compressor (LPC) of the Honeywell ASE120 industrial gas-turbine operating at its design rotational speed. The compressor performance was analyzed by considering the prescription of different swirl distortion patterns at the inlet of the CFD domain. They included the swirl, twin and the positive and negative offset swirl patterns. For each swirl distortion pattern, the compressor performance were analyzed within its range of operability as indicated in Fig. 1.7.

As a counter-rotating and co-rotating bulk swirl was prescribed at the inlet, an increase and decrease of corrected mass flow and pressure ratio were observed. However, for a fixed intensity of the bulk swirl, measured by means of swirl intensity (see § A), the magnitude of the change in performance is higher for a co- than for a counter-rotating bulk swirl. This is related to the fact that the efficiency drop is higher when counter-rotating swirl occurs (Fig. 1.7(b)). Although negative swirl increases the stability pressure ratio, the adiabatic efficiency is lower than both clean (baseline) and positive bulk swirl inlet conditions as shown in Fig. 1.7(a). Therefore, regardless of the conditions of the swirl distortion level, the adiabatic efficiency of the compressor for any case taken into consid-

eration. In general total pressure distortion however causes a more severe effect than swirl distortion and is therefore more problematic as far as uniformity of total temperature is concerned.

For twin swirl, it was observed that both the co-rotating and counter-rotating swirl regions contributed to reduce the rotor efficiency (Fig. 1.7(b)). However, following the analysis of the bulk swirl, the counter-rotating swirl region reduces the efficiency much more than the co-rotating swirl region. For this reason, reduces in minor measure than a purely co-rotating bulk swirl.

Regarding the case of offset swirls, the negative offset swirl speed line is almost coincident with the baseline speedline. This is a function of the swirl directivity (see § A) for the swirl pattern generated. As discussed in § A, the swirl directivity can be considered as spectrum of values which change from twin to bulk swirl. Therefore, it is expected that the speedlines on the compressor map will also migrate correspondingly up or down from the twin swirl towards the bulk swirl speedlines, indicated in Fig. 1.7.

Regarding the effects that more complex swirl patterns, i.e that attributed to complex intake geometries (paired swirl), tightly wound-vortices and/or their combination, determine on the compressor performance are still under investigation.

1.1.1.3 Combined effect of total pressure and swirl distortion

To quantify the effect that the total pressure combined with swirl distortion determines on turbomachinery performance, a decoupling of these two types of flow distortion is required. However, this is not a simple procedure since the two types of distortion interact each other. Moreover, the number of possible combinations of vorticity pattern, pressure distortion extent and severity is infinite. Hence, a lot of research in this field is nowadays considered.

The SAE S-16 Committee carried out numerical investigations considering two particular combinations of total pressure and swirl distortion. They included a paired twin swirl with a spot of total pressure superimposed on the co- and counter-rotating swirl part as shown in Fig. 1.8(a) and 1.8(b). As a result, the swirl alleviates the effect of the total pressure distortion in the case of co-rotating swirl (Fig. 1.8(a)). On the other hand, the counter-rotating swirl reduces the stability margin below the expected operating value with the total pressure distortion alone (Fig. 1.8(b)).

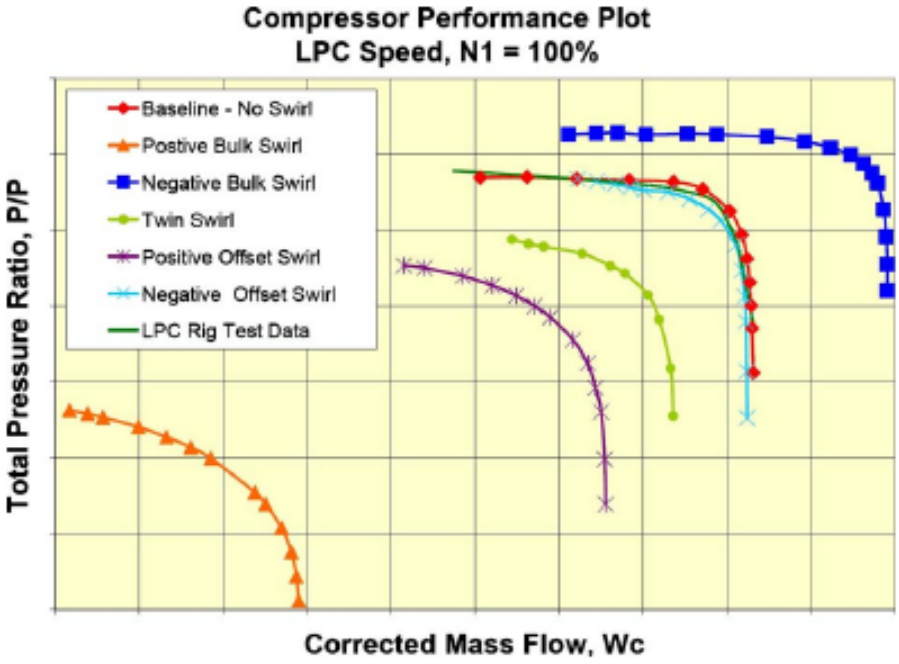

(a) Compressor pressure ratio versus corrected mass flow

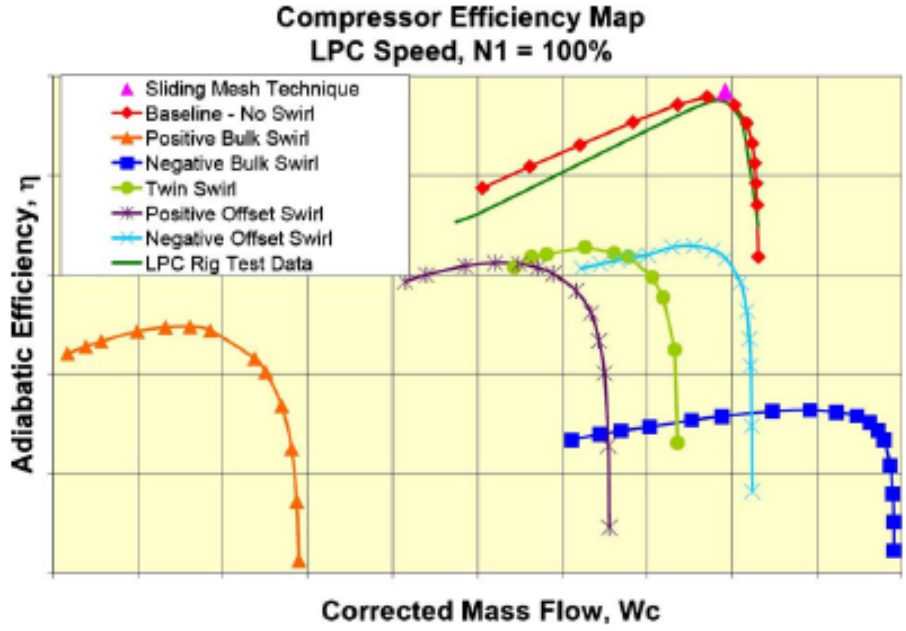

(b) Compressor adiabatic efficiency versus corrected mass flow

Figure 1.7: Effect of bulk and paired swirls of the Low Pressure Compressor (LPC) of the Honeywell ASE120 industrial gas-turbine operating at design rotational speed[22]

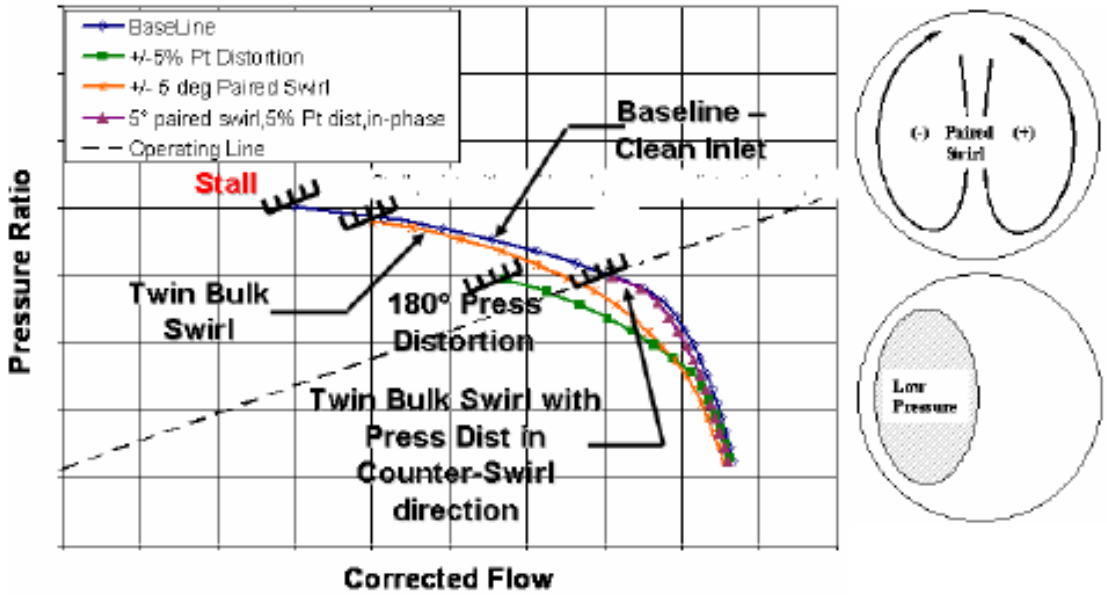

(a) Total pressure combined with counter-rotating swirl distortion

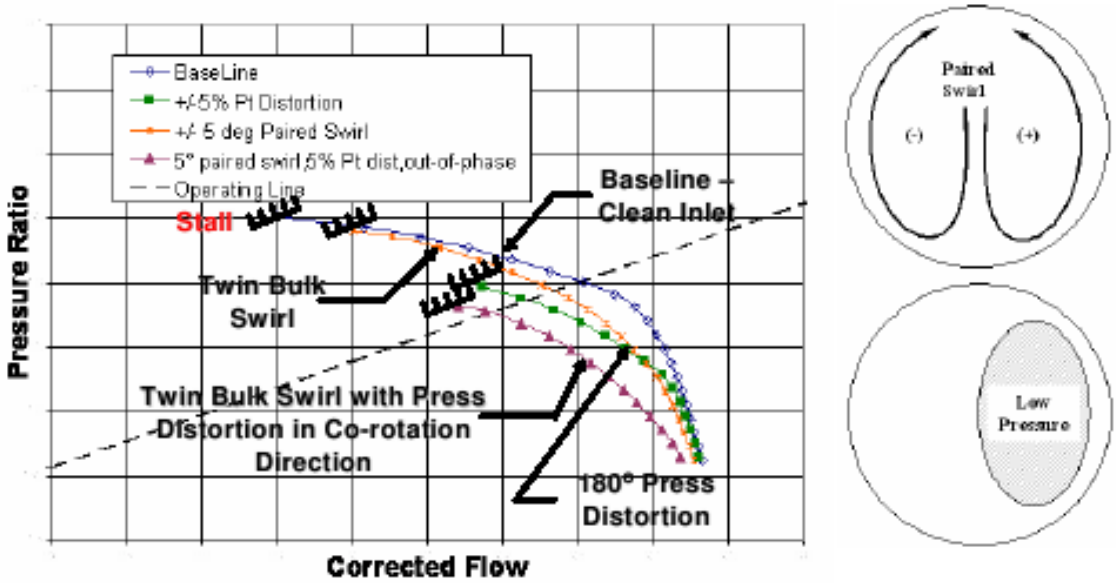

(b) Total pressure combined with co-rotating swirl distortion

Figure 1.8: Effect of total pressure combined with swirl distortion on the compressor performance [16]

1.2 Project aims and objectives

The aim of this research is to provide qualitative and quantitative information regarding the effect on a fan rotor performance relative to the self-generated distortion typical of an S-duct and its combination with that attributed to a tightly-wound vortex. Moreover, the assessment of a methodology to determine the location of the AIP for swirl distortion was carried out. To achieve these aims, a number of key objectives was established.

1. Validation of the CFD models defined in this research for two public geometries, one for an S-shaped intake and one for a fan rotor. These were the RAE S-shaped intake 2129 and the NASA Rotor 67.

2. Definition a purely numerical coupled system S-shaped intake/fan rotor configuration based on the aforementioned CFD models.

3. Investigation of the effect of the inlet flow distortion on the rotor part of the coupled system operating under clean inlet conditions.

4. Assessment of distorted boundary conditions representative of a tightly-wound vortex in terms of flow direction and total pressure distribution at the inlet plane of the computational domain.

5. Investigation of the effect of the flow distortion on the rotor part of the coupled system operating with a vortex ingested at the intake inlet plane and by analyzing the effects of both vortex characteristics and throttle setting.

6. Establishment of numerical correlations between the change of rotor performance and the inlet swirl distortion.

7. Assessment of a methodology to determine the location of the AIP for swirl distortion. This was applied on the NASA Rotor 67 coupled with a straight annular duct where a tightly-wound vortex was prescribed at the CFD inlet plane.

1.3 Thesis structure

An overview of the contents relative to each Thesis chapter is presented below.

In the current Chapter, the rationale and the scope of the work are presented. Then, the inlet flow distortion background as well as the main findings regarding its effect on turbomachinery performance are discussed.

Chapter 2 presents an overview of the published work up to date concerning different swirl distortion patterns. More attention is addressed to provide information regarding the type of distortion attributed to the S-shaped intake operating under clean and with a tightly-wound vortex ingested at the inlet of the intake itself.

Chapter 3 is divided into three sections. The first section presents the conditions imposed to define the computational method valid for any CFD models created in this work. In the second section, the geometries of an intake and a fan rotor selected from the public domain, the relative CFD models and their validation against experimental data are reported. Moreover, a purely numerical coupled system configuration, proposed in this research to analyze the inlet flow distortion, is defined. The third section introduces the key parameters used to analyse the CFD results obtained throughout this research. Finally, in the fourth section, the boundary conditions defined to prescribe a tightly-wound vortex at the inlet of the CFD domain are presented.

Chapter 4 discusses the numerical results obtained on the coupled system operating under clean inlet conditions. Firstly, a Reynods number effect analysis, carried out to ascertain the validity of the CFD results of the intake for the coupled system is reported. Then, numerical investigations are presented for two rotational speeds, defined with the typical rotor operability. These include the aerodynamics of the intake,the description of the flow field at the AIP and the effect of the S-duct on rotor performance. Finally, a comparison of the results obtained for the two rotational speeds investigated is discussed.

Chapter 5 discusses the numerical results obtained on the coupled system operating with a tightly-wound vortex ingested at the inlet of the intake and for the same rotational speeds already investigated under clean inlet conditions. In particular, the effect of vortex characteristics and throttle settings were analyzed, each at a different rotational speed.

Chapter 6 presents a methodology assessed to determine the location of the AIP for swirl distortion.

Chapter 7 lists the conclusions of the current research and the recommendations for future work.

Chapter 2

Literature review

In this chapter, a concise review of the published work regarding the swirl distortion is presented. The first part of the review introduces the types of flow distortion identified in previous research. The second part provides details of the type of inlet swirl distortion attributed to an S-shaped intake since it represents the main interest of this work. Finally, the third part reports examples of experimental and numerical research regarding different S-shaped intake geometries operating under clean and with an ingested vortex at the inlet.

2.1 Swirl distortion

The SAE S-16 Committee[16] conducted experimental and numerical research regarding the swirl distortion. They proposed a methodology to quantify the swirl distortion. For this purpose, the identification of an AIP for swirl distortion was necessary. This is the crossflow section upstream of the engine face after which the swirl distortion no longer changes before reaching the engine face itself. So far, AIR 1419[12] carried out a detailed analysis of the AIP relative to total pressure distortion only. Hence, it was concluded that for conventional aircraft inlets, this AIP should be placed at 1.5 fan diameters upstream of the engine face. On the other hand, the location of the AIP for the swirl distortion is still undefined and, therefore, is usually considered as close as possible to the engine face. Hence, the swirl distortion in an inlet duct is identified by the angle defined between the local flow velocity vector $\mathbf{V}=(V_r, V_\theta, V_z)$ and the normal direction to the AIP. Generally, the local velocity vector is function of both radial and tangential flow velocity components (V_r and V_θ). However, for engines without IGVs, the radial velocity component (V_r) can be neglected with respect to the circumferential velocity component (V_θ). The latter, therefore, affects directly the incidence angle on the rotor blade and then the rotor performance. Hence, the methodology is based on the swirl angle (α) (Eq. 2.1) defined

between the tangential and axial velocity components (V_θ and V_z), both expressed with respect to a coordinate system having the origin coincident to the centre of the AIP (Fig. 2.1).

$$\alpha = \arctan \frac{V_\theta}{V_z} \tag{2.1}$$

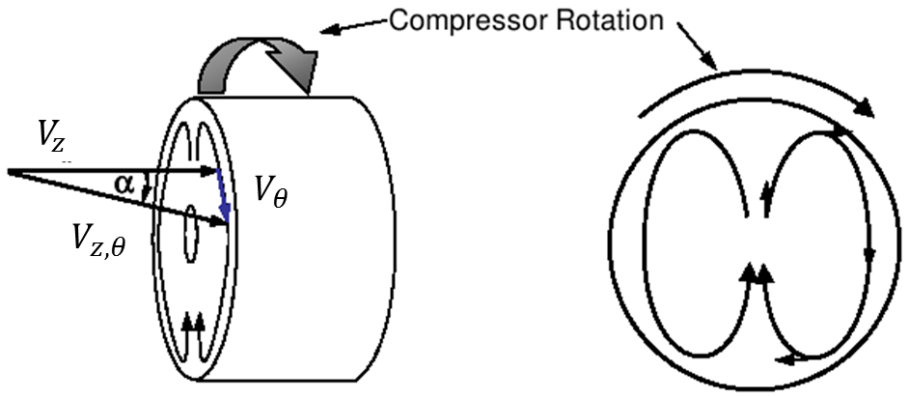

Figure 2.1: Definition of swirl angle (α)[16]

Moreover, the SAE S-16 Committee[16] categorized swirl distortion into four types. They are identified by the swirl topology observed at the AIP which entails a specific effect on the turbomachinery. These are bulk swirl, paired swirl, cross flow swirl, and tightly-wound vortices. Their details are presented in the following sections, since for this work swirl distortion pattern have been assessed.

2.1.1 Bulk swirl

The whole flow approaching a compressor face can be rotational in only one direction. Hence, according to the rotational direction of the flow against that of the compressor, a co- and a counter-rotating bulk swirl is defined. This is characterized by a swirl angle (α) relatively constant along the circumferential position of a generic i^{th} ring of the AIP as shown in Fig. 2.2.

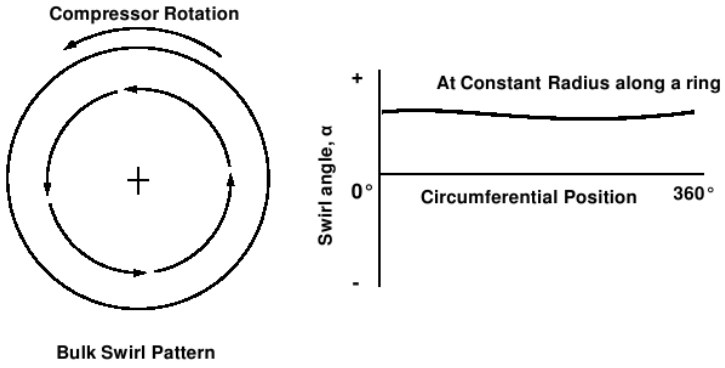

Figure 2.2: Swirl angle pattern of the bulk swirl for a generic i^{th} ring[16]

2.1.2 Paired swirl

The formation and development of the paired swirl is attributed to the presence of an S-shaped turned intake ahead of the a compressor rotor. The paired swirl would be one- or two-per-revolution whether the flow crosses a single or double turn (see Fig. 2.3). This type of swirl distortion is characterized by a swirl angle (α) which oscillates between positive and negative values along the circumferential position of a generic i^{th} ring of the AIP. The number of oscillations depends on the number of the flow turnings. In particular, the double turn represents the case of an S-shaped intake (or duct). Moreover, according to the symmetry conditions at the inlet, two paired swirl configurations are identified: twin and offset paired swirl. These occur when the flow field entering the duct is uniform or not, respectively. Consequently, the distorted outlet flow pattern is symmetric or not, as shown in Fig. 2.4(a) and 2.4(b), respectively. Since this type of swirl distortion was investigated in this research, more details are presented in § 2.2.

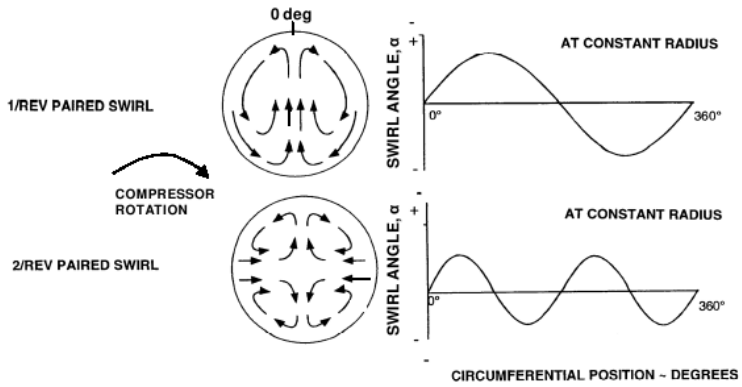

Figure 2.3: Swirl angle (α) versus the circumferential location for one (top) and two (bottom) paired swirl per revolution

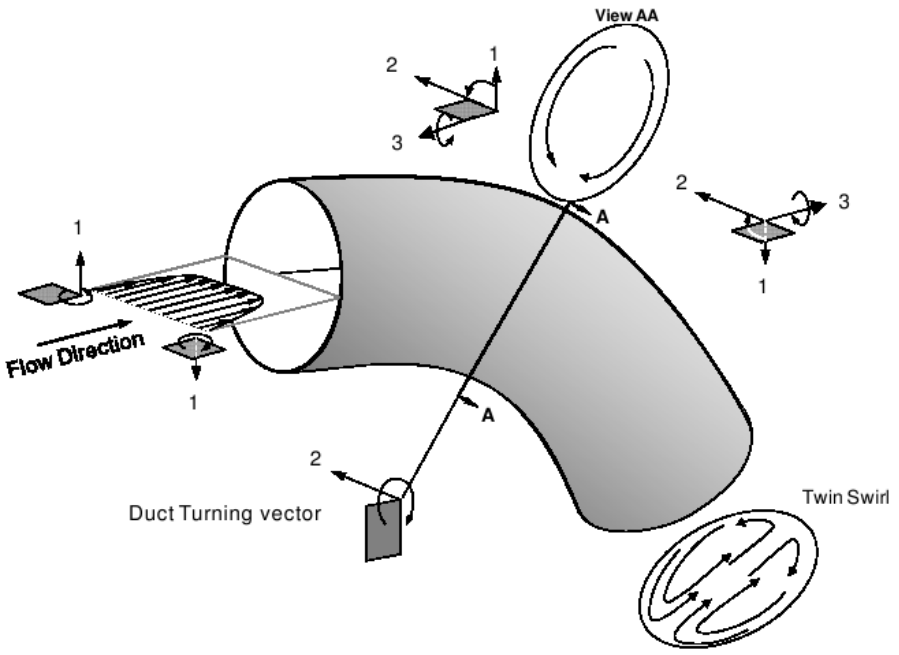

(a) Twin paired swirl

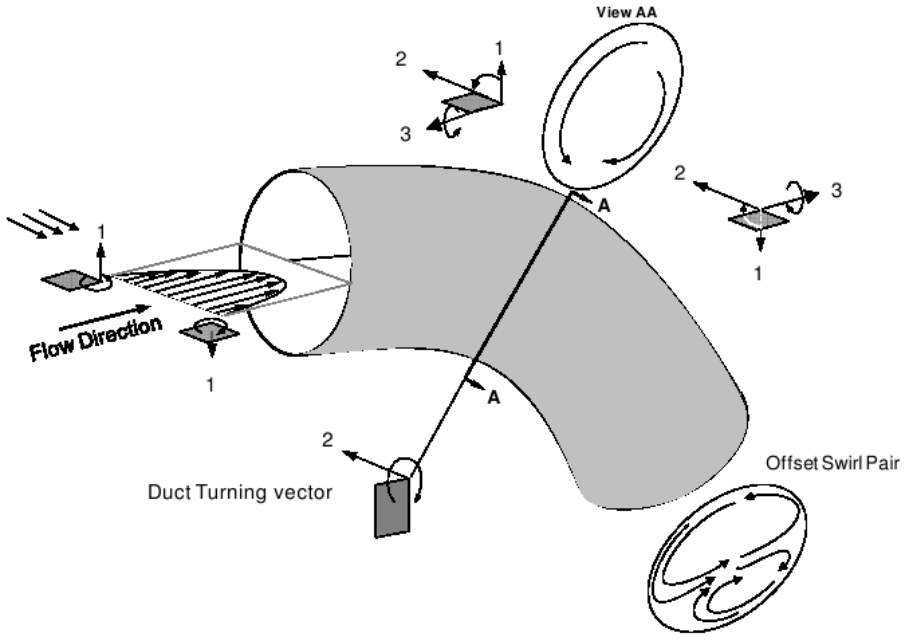

(b) Offset paired swirl

Figure 2.4: Visualization of the possible paired swirl cases according to the inlet flow conditions[16]

2.1.3 Cross flow swirl

In some cases, such as lift fans with very short and straight inlet ducts exposed to cross-flow in forward flight, cross-flow swirl may be experienced. Consequently, the flow turns by up to 90^o to reach the compressor face. Hence, swirl distortion in the cross flow direction is generated. This type of swirl distortion differentiates from that of the paired swirl presented in §2.1.2, since the trend of the swirl angle (α) along the circumferential location remains unchanged regardless of the i^{th} ring considered[16] as shown in Fig. 2.5.

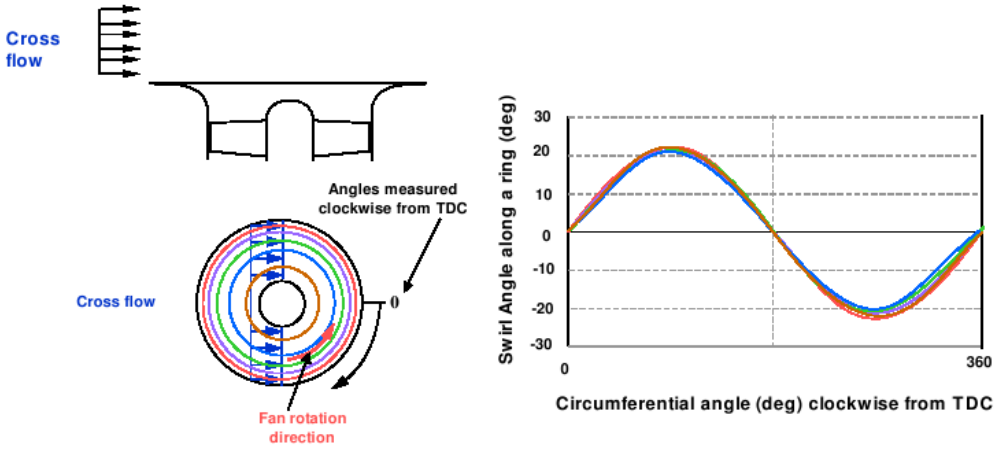

Figure 2.5: Swirl angle pattern measured along a ring in clockwise direction from Top Dead Center (TDC) and for cross-flow swirl[16]

2.1.4 Tightly-wound vortices

Tightly-wound vortices are flow perturbations concentrated in a relatively small portion (about 10%) of the inlet flow area of the intake. They are highly dynamic in location, and extremely difficult to measure. In this category the wing-tip and streamwise vortex (or vortices) are included. The wing-tip vortex (vortices) arise from upstream strakes, whereas the streamwise vortex (or vortices) arise from surfaces which can be part of the aircraft fuselage (Fig. 2.6(a)) or, during static or near-static operations, from the ground. The latter is the case of the ground vortex (or vortices) which represents the most dangerous type of tightly-wound vortex (or vortices) since foreign objects can be ingested into the engine with consequent mechanical damage (Fig. 2.6(b)). Murphy[23] investigated the aerodynamics of this type of vortex at Cranfield University. In particular, according to the wind conditions three mechanisms of formation were considered: quiescent, headwind, and crosswind condition. Also, the main parameters which defined analytically this vortex were identified. They include the ground clearance (h/D_l), velocity ratio ($U^\star$) and yaw angle (ψ). Further details concerning this type of vortex are presented in § B. The

current research is based on this type of vortex by taking the advantages of this research.

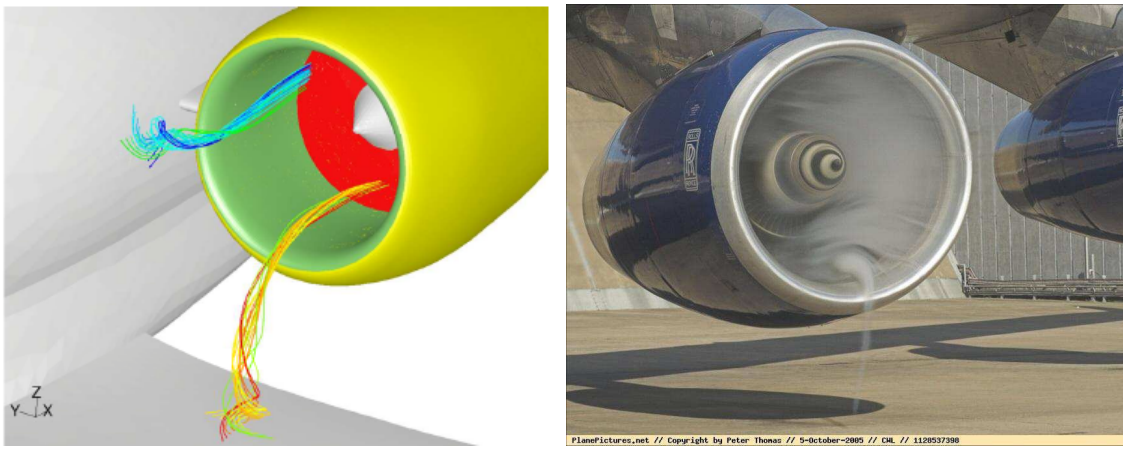

(a) CFD visualisation of streamwise vortex [16]

(b) Ground vortex ingestion on a Rolls Royce RB211-524G ©Peter Thomas 2005

Figure 2.6: Cases of possible tightly-wound vortices

2.2 S-shaped intakes and ducts aerodynamics

Aircraft propulsion systems often use diffusing S-ducts to guide the airflow towards the compressor face[24]. For S-shaped intakes, the flow pattern measured at this location manifests by means of a paired swirl introduced in § 2.1.2. In this section, a description of the S-shaped intake geometry is provided. Then, the flow physics occurring in the S-duct is discussed in details. Finally, the most relevant previous research for the current work and relative to different S-ducts operating under clean inlet conditions as well as with a prescribed vortex ingested at the inlet, is reported.

2.2.1 Geometry description

Referring to Fig. 2.7, S-shaped intakes are designed by considering the limits related to four main geometric parameters. These are length to inlet diameter ratio (L/D_{in}), diffusion ratio (D_{out}/D_{in}), cross section shape and offset to length ratio (O_f/L).

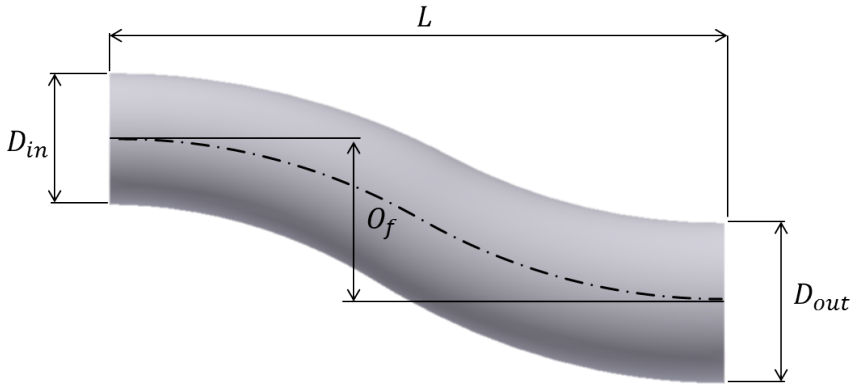

Figure 2.7: Visualization of a generic S-duct geometry

Length to inlet diameter ratio (L/D_{in}) This parameter identifies the flow regime inside of an intake. Hence, it is a compromise between the need to reduce weight[25] and pressure loss, due to an increase of the wall surfaces, and to minimize flow separation due to the increase of the area change along the axial direction[26].

Diffusion ratio (D_{out}/D_{in}) This parameter defines the degree of the diffusion of the flow before entering into the intake. For subsonic flows this is higher than the unity in order to decelerate the flow up to the compressor face. However, the higher the diffusion ratio the higher the level of adverse pressure. This induces in turn flow separation with consequent increase of total pressure loss and swirl distortion[1].

Cross section shape Especially for military applications, this evolves from the inlet to the outlet of the intake where it has to be circular due to the presence of the fan rotor. Ibrahim et al.[27] analyzed numerically the effect of cross section shape on the subsonic diffuser of the F-5 fighter duct. To do so, two geometries were investigated: the actual F-5 duct and a circular cross-sectional duct with similar centerline configuration of the F-5. The baseline intake resulted in a 0.5% increase in pressure recovery and 15% decrease in distortion compared to the circular cross-sectional duct, introduced to isolate the change in cross-section shape. As a result, the change in cross-section was considered as a solution to improve the intake performance in terms of distortion produced at the AIP.

Offset to length ratio (O_f/L) This parameter is correlated with the curvature of the S-shaped intake. Hence, the higher the curvature the higher the flow separation[1].

2.2.2 Internal flow field in S-ducts

Turning flows are subjected to changes in pressure and velocity distributions. Consequently, the flow field is subject to adverse pressure gradients and secondary flows. Their presence can be explained by considering initially a uniform energy flow entering into an S-bend as shown in Fig. 2.8. In this condition, the static pressure measured along the S-duct increases with the radius in order to balance the centrifugal force. Meanwhile, according to Bernoulli, the velocity decreases.

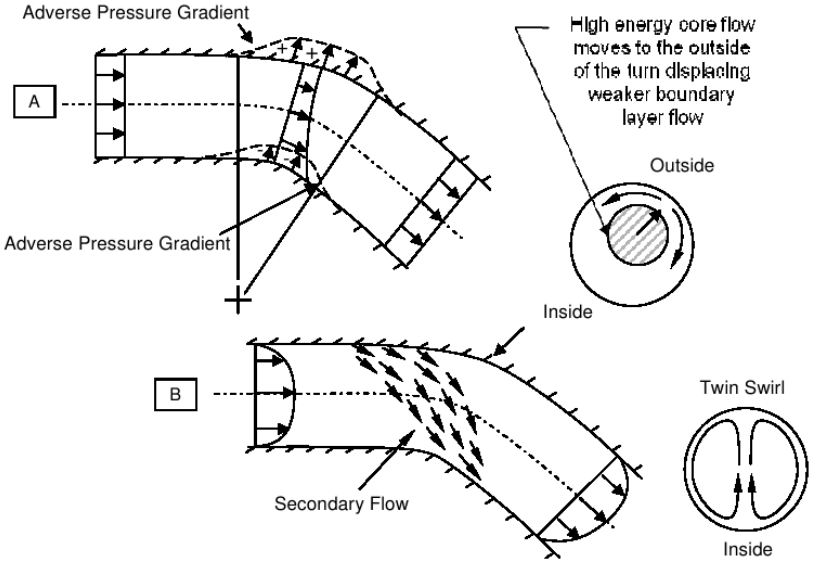

Figure 2.8: Formation of a paired swirl in a duct bend for uniform energy distribution (A) and presence of the boundary layer at the inlet (B)[28]

On the other hand, real flows are characterized by a non-uniform energy distribution due to the presence of the boundary layer. Hence, the velocity is zero at the wall and reaches a maximum value at the core. In this case, the combination of centrifugal and pressure forces on the more quickly moving core flow cause a deflection of the core itself towards the outside of the bend. Fluid approaching the outside of the bend amend the adverse pressure gradient as shown in Fig. 2.8. Energy deficient near-wall flow approaching the outer cannot pass through the adverse pressure gradient. Therefore, it moves around the walls towards the low static pressure region on the inside of the bend. The movement of the low energy fluid towards the inside part of the bend combined with the deflection of high velocity core region towards the outside of the bend sets up two cells of secondary flow taking place all of the cross section (Fig. 2.8). They manifest with a paired swirl which is associated with a separation bubble occurring in the S-duct. A description of the separated flow occurring within the S-duct is presented below.

Referring to Fig. 2.9, the surface of a generic S-duct diffuser is cut along the symmetry plane opposite to the separation zone and, then, unwrapped onto a horizontal plane. The streaklines pattern is also shown. This identifies two halves of the duct surface where four features can be observed. These are the spiral nodes of separation, saddle points, and positive and negative bifurcation lines. Their definitions are provided below.

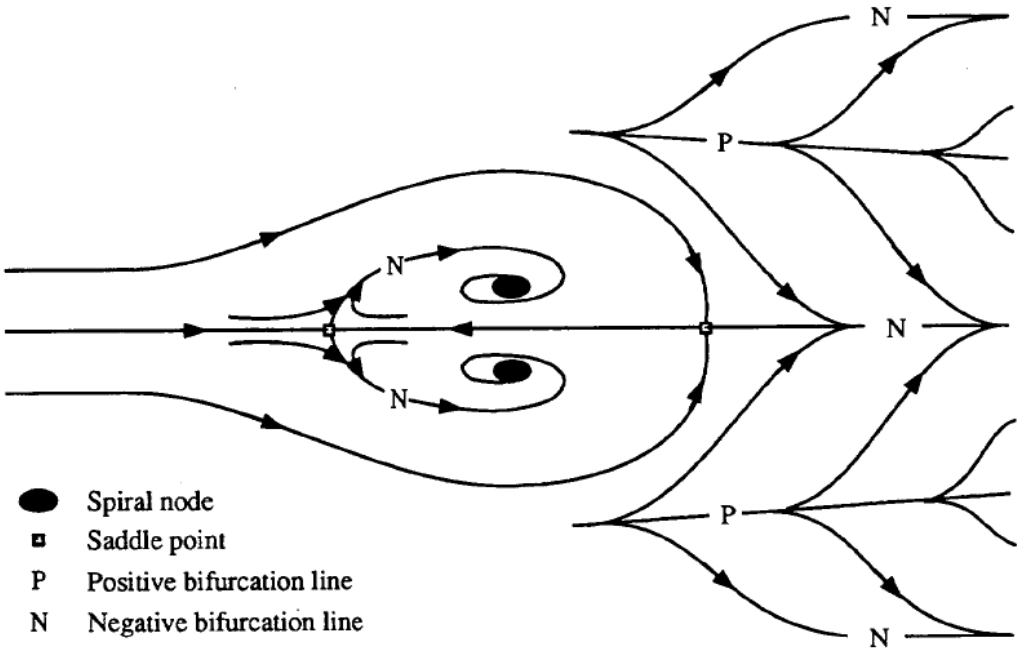

Figure 2.9: Visualization of the skeleton of the skin friction lines on the surface of unwrapped S-duct diffuser[3]

Spiral node of separation This is a point of singularity where an infinite number of streaklines spiral around and towards a certain point of the surface[29] as shown in Fig. 2.9.

Saddle point This is a point of singularity where only two distinct skin friction lines pass through the point itself[29] as shown in Fig. 2.9.

Bifurcation lines These are streamlines defined by considering notions of streamsurface bifurcation theory. Generally, steady 3D flows can be defined by streamsurfaces. Flow fields are usually characterized by special streamsurfaces which appear to bifurcate. A streamsurface can bifurcate in positive or negative manner[30] as shown in Fig. 2.10(a) and 2.10(b), respectively. Positive bifurcation refers to a stagnation streamsurface which divides along a stagnation line. Hence, a single streamline within the stagnation streamsurface appears to bifurcate into two different streamlines (Fig. 2.10(a)). Usually, positive bifurcations are associated with downwashing counter-rotating vortices. On the other hand, negative bifurcation refers to a streamsurface which emerges from a negative bifurcation line. Hence, two different streamlines near a flow boundary combine to form a single streamline within the streamsurface (Fig. 2.10(b)). Usually, negative bifurcations are connected to uplifting counter-rotating vortices.

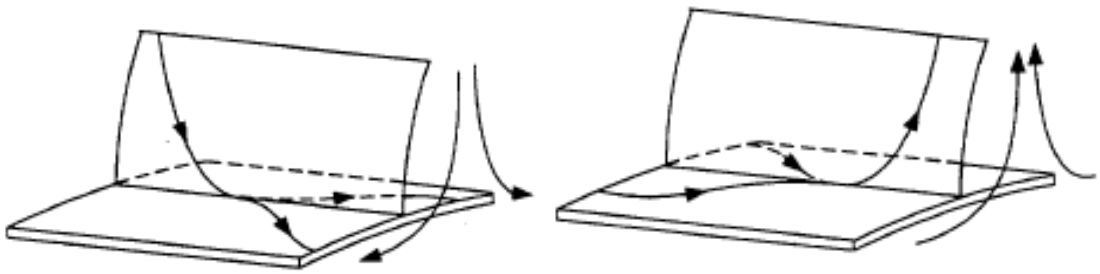

(a) Positive (b) Negative

Figure 2.10: Streamsurface bifurcations on a solid wall[3]

Referring to Fig. 2.9, the streaklines pattern indicate that two negative bifurcation lines emanate from the saddle point located upstream of the recirculation. These bifurcation lines are addressed towards opposite directions in the cross-flow plane and appear symmetric with respect to the centerline. Both of these lines converge towards two spiral nodes of separation symmetrically disposed on the S-duct wall. Also, two other bifurcation lines exist: one arises from the saddle point located downstream of the separation zone and another is located where the duct was cut to be unwrapped. Finally, a pair

of positive and symmetric bifurcation lines arise between the negative bifurcation lines mentioned above.

In theory, the flow topology described above is perfectly symmetric. In reality, however, the flow unsteadiness cause the separation pattern to never be symmetric and to oscillate between the configuration shown in Fig. 2.11 and its mirror configuration[30]. Therefore, no streaklines pass simultaneously between two saddle points.

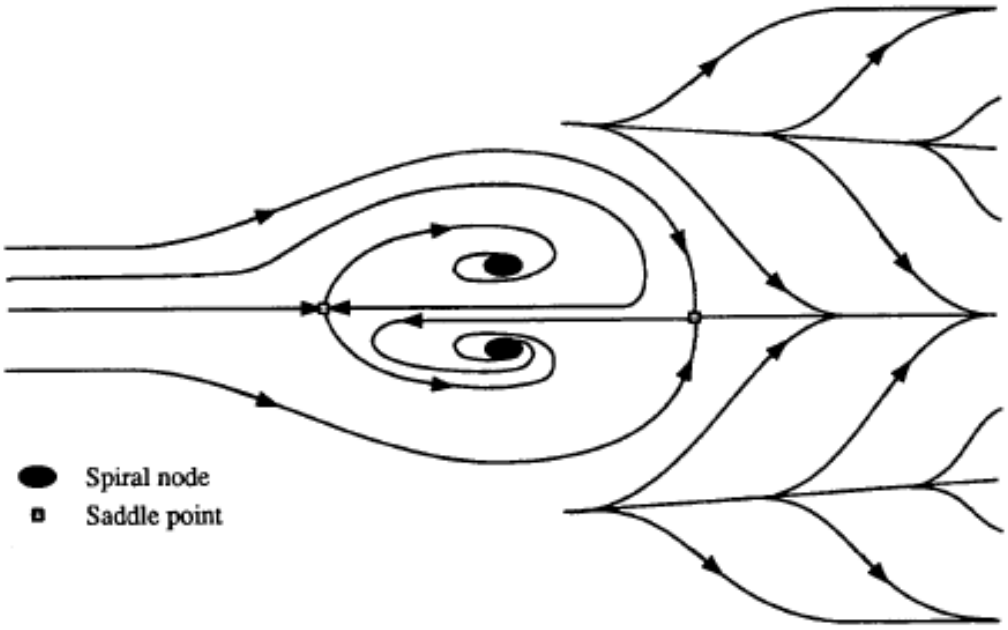

Figure 2.11: Visualization of the skeleton of the skin friction lines on the surface of unwrapped S-duct diffuser for a real asymmetric case[3]

2.2.3 Clean inlet conditions

A lot of experimental and numerical research has been addressed to analyse the flow field of S-ducts operating under clean inlet conditions. Here, the main finding regarding a representative S-duct configuration and that used for the current research are discussed. They are the Wellborn and the Royal Aeronautic Establishment (RAE) model 2129 S-shaped intakes.

2.2.3.1 The Wellborn intake

Wellborn et al.[1] conducted experimental research on a representative diffusing S-duct (see Fig. 2.12(a)) at the Internal Fluid Mechanics Facility of the NASA Lewis Research Cen-

ter[31]. The duct centerline is contained within the plane xz and defined by two circular arcs having the same radius of curvature (R) of 102.1 cm, and the subtended angle ($\theta_{max}/2$) of 30^o. The shape of the generic cross section perpendicular to the centerline is circular throughout the whole S-duct. The axial position within the duct is measured by means of the length along the centerline normalised by the inlet duct diameter (s/D_1). Meanwhile, the position within the polar plane is specified by the combination of the polar angle (ϕ), measured from the vertical in a positive clockwise direction, and the radial distance from the centerline (r). The S-duct inlet and outlet radius (r_1 and r_2) are equal 10.21 and 12.57 cm, respectively, at which correspond an area ratio (A_2/A_1) of 1.52.

Investigation of the flow field relative to the S-duct was accomplished by adopting different experimental techniques. The visualization of the flow field as well as the static pressure were extracted on the S-duct wall. In particular, the wall flow field was visualized with fluorescent oil applied on the duct wall itself. Meanwhile, the wall static pressure was measured with taps located along the axial direction at constant polar angles $\phi = 0^o, 90^o$ and 170^o. On the other hand, the internal flow field was measured with calibrated three- and five- hole probes at five different planes perpendicular to the duct centerline indicated in Fig. 2.12(b). The static and total pressure coefficients (C_p and C_{P_0}) were used to express the static and total pressure (p and P_0) with respect to the intake inlet centerline conditions representing the reference states (Eq. 2.2 and Eq. 2.3). Moreover, the local velocity vectors were converted in Mach number vectors and normalised against that measured at the intake inlet centerline (M_{in}) (Eq. 2.4).

$$C_p = \frac{p - p_{ref}}{P_{0,ref} - p_{ref}} \tag{2.2}$$

$$C_{P_0} = \frac{P_0 - p_{ref}}{P_{0,ref} - p_{ref}} \tag{2.3}$$

$$M^* = \frac{M}{M_{ref}} \tag{2.4}$$

The experimental tests relative to this intake were conducted at constant values of intake inlet centerline Mach number (M_{in}) of 0.6 and Reynolds number of $2.6 \cdot 10^6$ based on the intake inlet diameter (D_1) and centerline velocity.

As a result, the wall flow visualization showed that the points of onset separation and reattachment were located at $s/D_1 = 2.02$ and 4.13, respectively. Overall, the flow was essentially symmetric and the separated region was characterized by two saddle points and two spiral nodes on each symmetric duct half as expected for an isolated intake (see § 2.2.2). Also, the boundary layer presented a cross flow component identified by the direction of the streamlines at the wall.

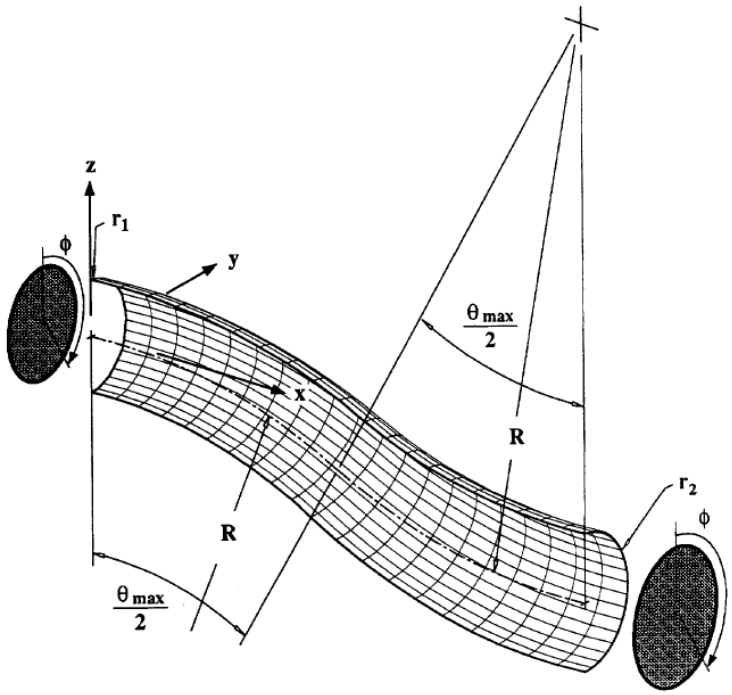

(a) S-duct geometry

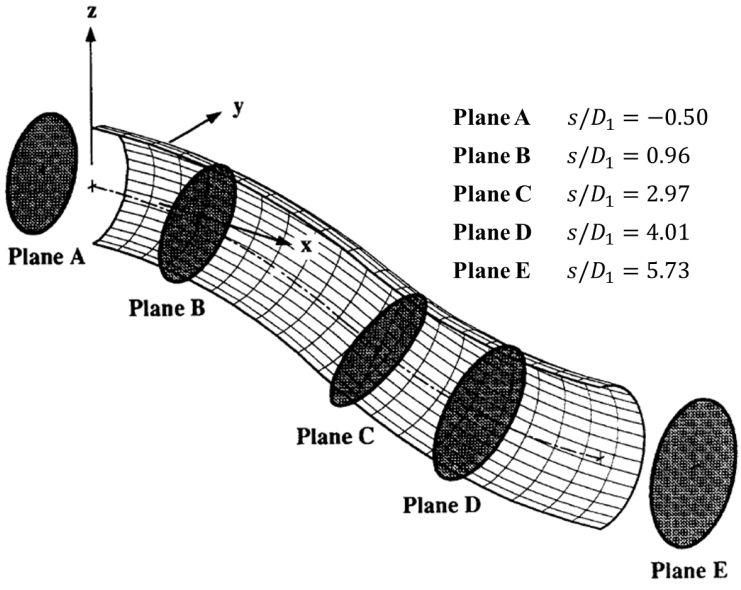

(b) Experimental crossflow planes

Figure 2.12: Visualization of the geometry (a) and experimental measurement crossflow planes (b) of the Wellborn S-duct [1]

Figure 2.13 shows the trend of static pressure coefficient (C_p) along the axial position of the S-duct and for $\phi = 10^o, 90^o$, and 170^o. Moreover, the axial range of the separated flow region, obtained experimentally from the flow visualization at the duct wall, is also indicated. Through the first bend of the S-duct, the effect of streamline curvature is evident by the difference of static pressure between the extreme circumferential locations ($\phi = 10^o$ and $\phi = 170^o$), while the effect of diffusion is evident by the overall pressure rise towards the S-duct outlet. The presence of the separation is visible at $\phi = 90^o$ and $\phi = 170^o$ within the axial range where the static pressure remains essentially constant. This means that there is almost no change in flow speed in the lower half of the duct. Moreover, due to the flow blockage generated by the separated region, a favourable pressure gradient manifests in the higher half of the duct ($\phi = 10^o$). After reattachment the pressure distributions converge towards a common value regardless of the circumferential position.

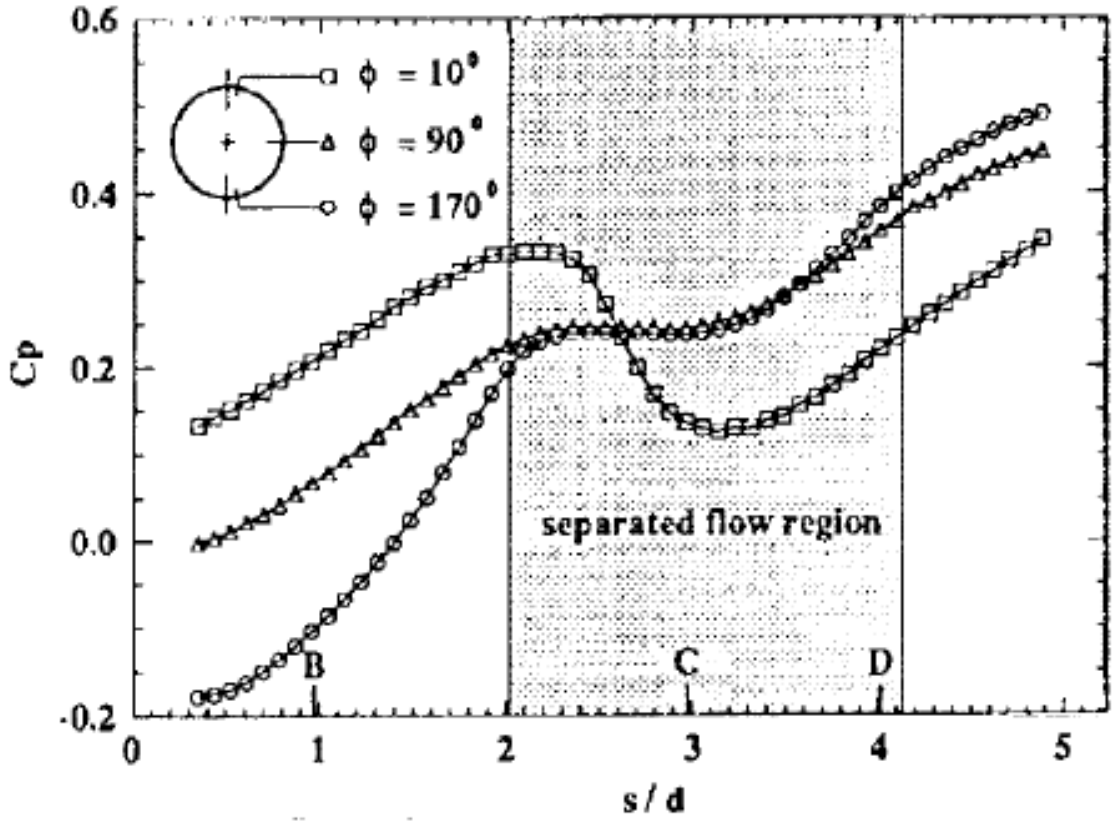

Figure 2.13: Static pressure coefficient (C_p) along the S-duct for $\phi = 10$, 90, and 170^o and with indications of the cross flow planes B, C, and D[1]

Referring to the cross flow planes indicated in Fig. 2.12(b), an analysis of the internal duct aerodynamics was carried out. The contours of total pressure coefficient (C_{P_0}) and normal component of the normalised Mach number (M^*) are shown in Fig. 2.14(a) and 2.14(b), respectively. At plane B, located at the first bend, the boundary layer is thickest at the top ($\phi = 0^o$) and the lowest at bottom edge of the duct ($\phi = 180^o$). This phenomena is a consequence of the streamwise pressure gradients that accelerate the flow near the bottom ($\phi = 180^o$) and decelerate the flow near the top edge ($\phi = 0^o$) of the duct[1]. This difference is visible in Fig. 2.14(b), where the local inlet Mach number is greater than that at the inlet (M_{in}) near the bottom of the duct. A total pressure deficit region is notable in the last three planes (C,D and E shown in Fig. 2.12(b)) located towards the S-duct outlet where the flow separation region, indicated in Fig. 2.13, is well developed. At the plane E, the axial flow direction returned back to that relative to the inlet and cross stream static pressure gradients were eliminated. However, before reaching this plane, static pressure gradients were sufficiently strong to reverse the direction of the boundary layer flow on the upper surface of the duct. Hence, a large pair of counter-rotating vortices located in the lower half of the plane E evolved. These vortices continually convected the low momentum fluid of the boundary layer towards the centre of the duct. As a consequence, the magnitude and uniformity were degraded.

The transverse Mach number components were also investigated for the last four planes (B, C, D and E shown in Fig. 2.12(b)) as shown in Fig. 2.15. At plane B, the transverse Mach number components occur only near the duct surface, essentially due to the lower momentum fluid which moves from the top ($\phi = 0^o$) to the bottom edge of the duct ($\phi = 180^o$). Also, the boundary layer thickness at this plane changes slightly with the circumferential position.

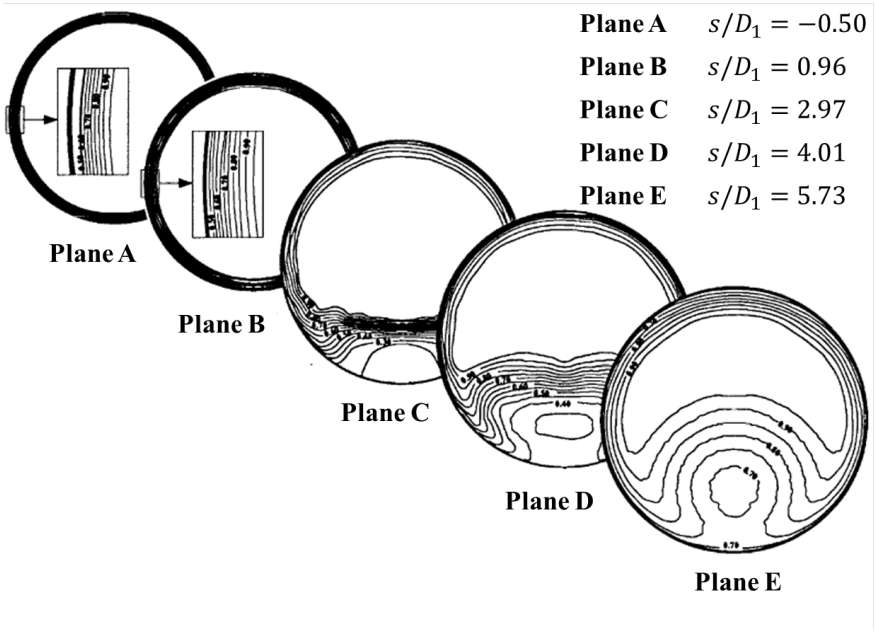

(a) Total pressure coefficient (C_{P_0})

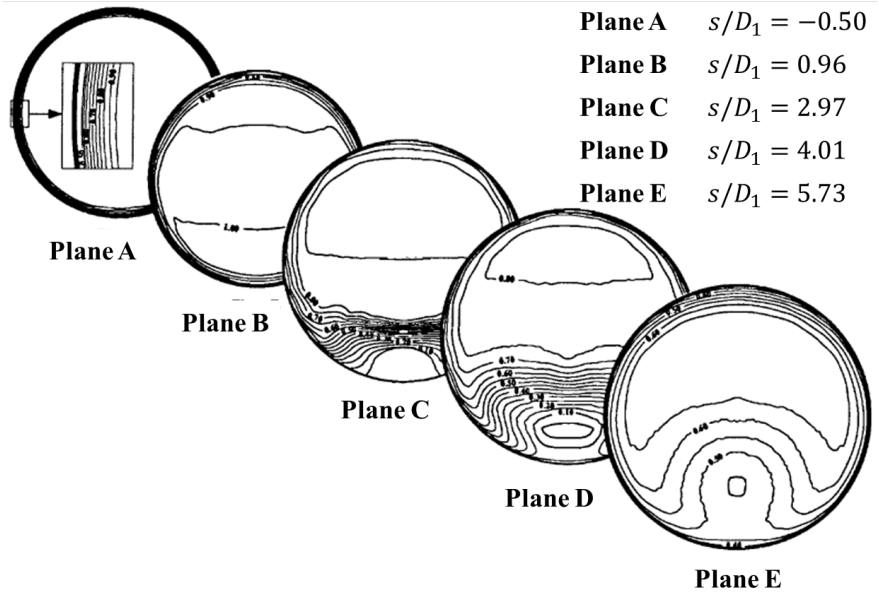

(b) Normal component of normalised Mach number (M^*)

Figure 2.14: Contours of (a) total pressure coefficient (C_{P_0}) and (b) normal Mach number component (M^*) on experimental crossflow planes [1]

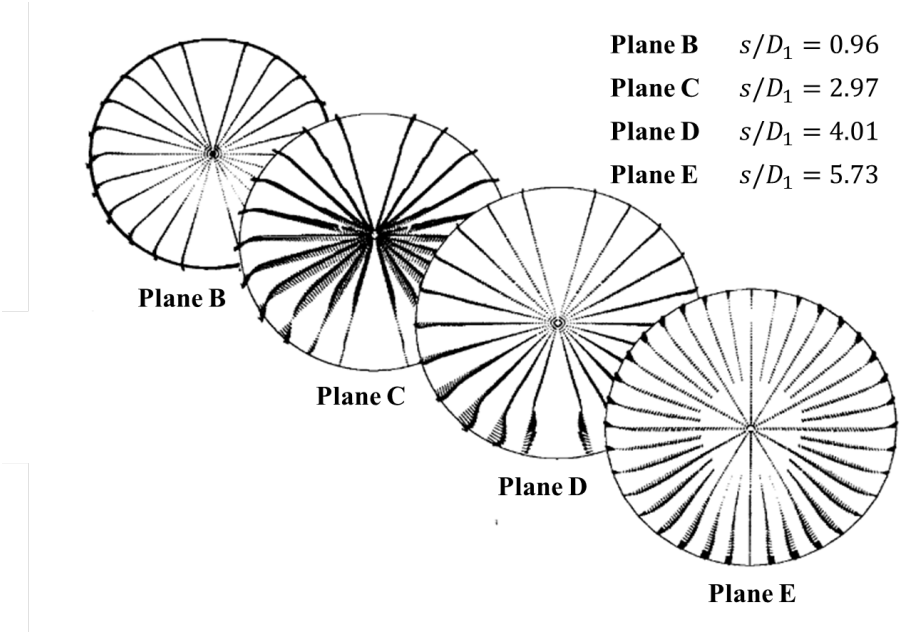

Figure 2.15: Transverse component of the Mach vector (M^*) on experimental crossflow planes [1]

2.2.3.2 The RAE S-shaped intake 2129

Another complex intake widely investigated in the public domain is the RAE S-shaped intake model 2129 [32]. Since this intake represents that selected to conduct numerical analyses relative to the current research, its details as well as the validation process carried out on a CFD domain are presented in § 3.2.1.

2.2.4 Vortex ingestion

Most of the computational and experimental investigations carried out till date on complex intake geometries considered clean inlet conditions [24]. However, current research is also addressed to consider intake flow field characterized by the ingestion of tightly-wound vortices (see § 2.1.4), ingested at the inlet of the intake. In this section, the most interesting experimental and numerical analyses carried out to date and considered for this research are reported below.

2.2.4.1 Previous experimental research

Wendt et al.[33] analyzed experimentally the effects on the flow field within a diffusing S-duct of an ingested trailing vortex. This represents, for example, that coming from a forward component of the airframe during a high angle of attack manoeuvre.

Two S-duct configurations were selected for this analysis. The first was the baseline Wellborn S-duct, already defined in § 2.2.3 (Fig. 2.12). The second was the same S-duct with the addition of an array of vortex generators (VGs), introduced by Reichert et al.[4], and placed on the S-duct wall upstream of the saddle point of separation (Fig. 2.16).

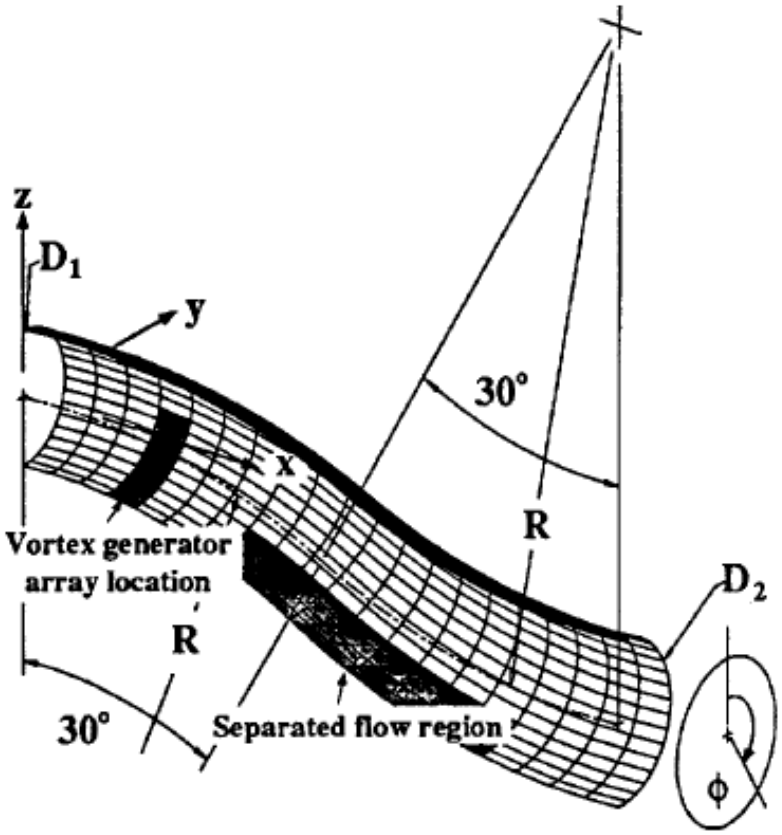

Figure 2.16: Geometry of the Wellborn S-duct with VGs array[4]

In absence of VGs and upstream of the axial location of flow separation, the flow converges towards the saddle point of separation as normally expected in an S-duct (see § 2.2.2). On the other hand, VGs mounted to counter or redirect the secondary flow converging near the duct surface determined the reduction of the duct distortion accompanied with an increase of total pressure recovery. Generally, the inclusion of VGs increases the

level of total pressure at the engine face resulting in a higher value of pressure recovery. The configuration of vortex generator array that mostly improved the total pressure recovery and reduced the flow distortion was used in the analysis of Wendt et al.[33]. In particular, an increase in total pressure recovery of 0.5% and a reduction in the total pressure distortion parameter (DC_{60}) by more than 50% were observed.

The ingested vortex was generated by means of a stationary eight bladed pinwheel mounted upstream of the diffusing duct (Fig. 2.17). The ingested vortex was rotating in counter-clockwise direction when observed upstream into the inlet duct.

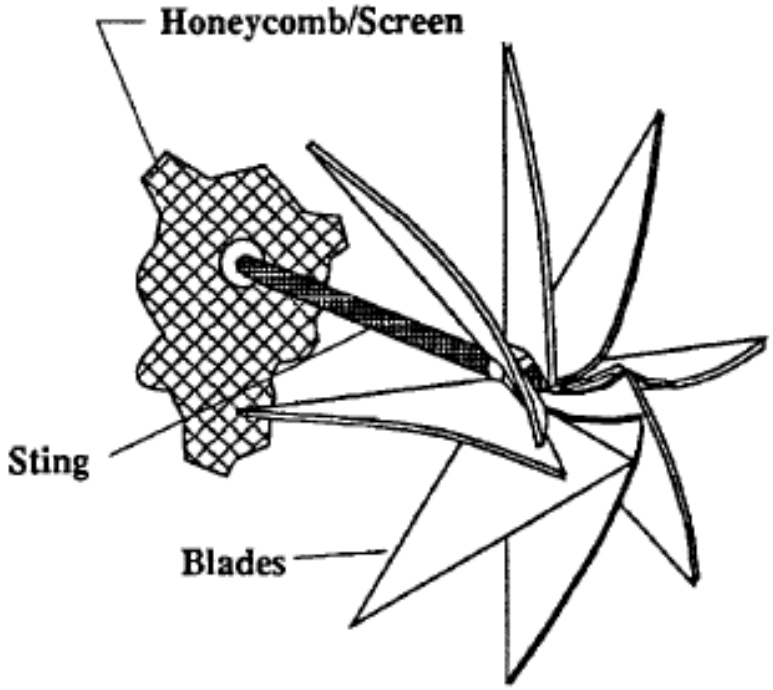

Figure 2.17: Stationary eight bladed pinwheel for vortex generator[33]

Hence, a parametric analysis based on the variation of the vortex ingested position within the inlet crossflow plane was accomplished. Referring to the baseline Wellborn S-duct (see § 2.2.3), three vortex positions were considered in experimental tests. The first position corresponded to the centerline of the inlet crossflow plane. The second position coincided with the edge of the crossflow plane for a circumferential location where strong secondary flow of the intake occurs ($\phi = 180^o$). The third position was simply circumferentially opposite to the second position ($\phi = 0^o$). The test cases are summarised in Table 2.1.

S-duct configuration	**Inlet boundary conditions**			
	Clean	**Vort. ing. at centerline**	**Vort. ing. near duct wall at $\phi = 180^o$**	**Vort. ing. near duct wall at $\phi = 0^o$**
Baseline S-duct	1	3	5	7
S-duct with VGs array	2	4	6	8

Table 2.1: List of numbers relative to experiments conducted by Wendt et al. on the Wellborn S-duct without and with VGs array[33]

Visualizations of the flow field at the wall of the S-ducts investigated were obtained by pressing absorbent paper over oil flow pattern on the duct surface (Fig. 2.18). The symmetric separation region discussed in § 2.2.2 was evident for the baseline Wellborn duct operating under clean inlet conditions as shown in Fig. 2.18(a). Then, by considering the ingestion of a vortex,the largest change in the aerodynamics of the baseline Wellborn duct occurred when this was ingested at the angular position aligned with the separation ($\phi = 180^o$). For this case the flow separation is still notable between $s/D1 = 2$ and 4 although was no longer symmetric as shown in Fig. 2.18(e). Downstream of this region, the surface streaklines converge and trail off towards higher values of the angular position (ϕ) generating an asymmetric pattern. This condition was related to the crossflow of the ingested vortex in proximity to the wall. On the other hand, the lowest influence on the flow separation occurred because of the vortex ingested on the duct centerline or near the duct wall at $\phi = 0^o$ than the case presented above, as shown in Fig. 2.18(c) and 2.18(g).

On the other hand, the application of the VGs array to the baseline Wellborn intake operating under clean conditions caused the disappearance of the S-duct separation region, while the flow remained symmetric as shown in Fig. 2.18(b). Then, the ingestion of a vortex caused the surface flow within the S-duct to be qualitatively similar to that occurring under clean inlet conditions as shown in Fig. 2.18(b). Hence, the flow separation presented the divergence of two concentrated patterns of converging streaklines. This is related to the effect of VGs which counter the crossflow naturally occurring in the baseline Wellborn S-duct.

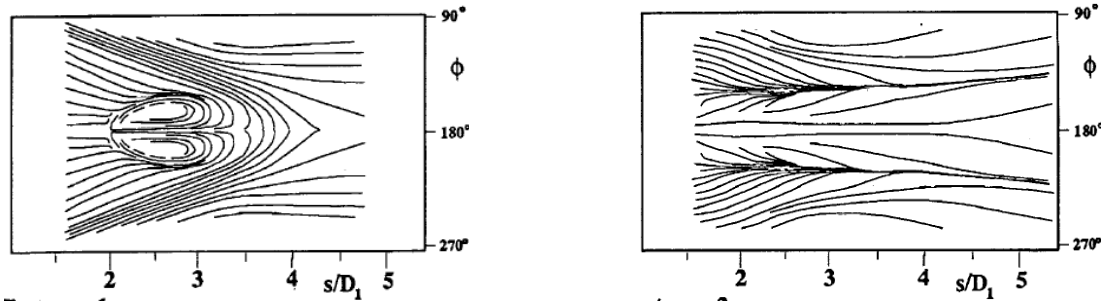

(a) Test case 1

(b) Test case 2

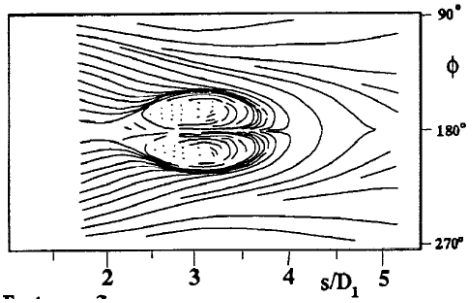

(c) Test case 3

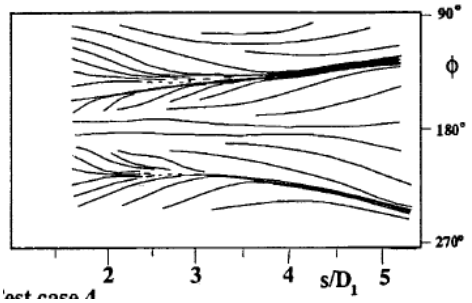

(d) Test case 4

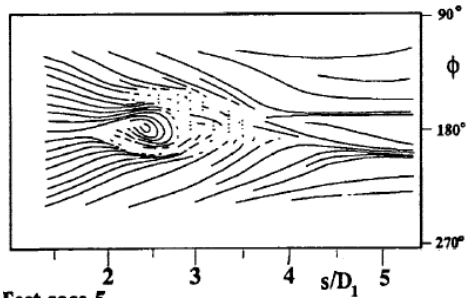

(e) Test case 5

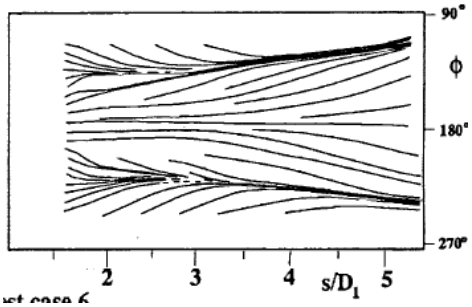

(f) Test case 6

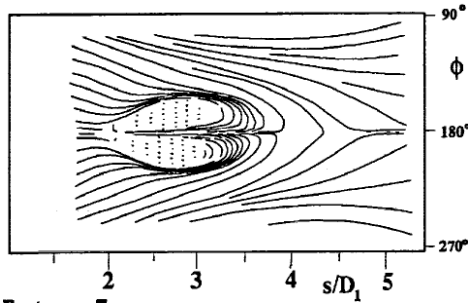

(g) Test case 7

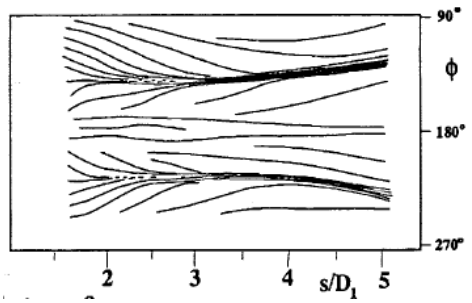

(h) Test case 8

Figure 2.18: Surface flow visualization on the separated region of the Wellborn S-duct[33]

The flow field was also investigate at the exit plane (plane E) of the ducts considered, indicated in Fig. 2.12(b). The baseline Wellborn S-duct operating under clean inlet conditions (Test case 1) presented the natural paired swirl characteristic of the S-duct and the flow field possesses mirror image symmetry (Fig. 2.19(a)).

As the vortex is ingested at the centerline of the baseline Wellborn duct (test case 3), its perturbation on the velocity vectors is notable, while its effect on total pressure field is minimal (see Fig. 2.19(c)). Referring to Fig. 2.19(e), as the vortex is ingested near the duct wall at the angular position aligned with the separation ($\phi = 180^o$), no vortex structure is identifiable. Nevertheless, the vortex determines a convective influence on the S-duct flow separation. Therefore, the vortices normally occurring in the S-duct shift towards the right. This shift is also evident in terms of total pressure contours. On the other hand, as the vortex is ingested near the duct wall at the angular position opposite to the separation ($\phi = 0^o$), the solution at the exit plane is less influenced compared to that relative to the test case 5 (see Fig. 2.19(g) and Fig. 2.19(e)). In terms of total pressure, a distortion is observed in the boundary layer on the wall opposite to the self-generated distortion.

The investigation of the exit plane on the Wellborn S-duct with an array of vortex generators operating under clean inlet conditions (Test case 2) presented the presence of four vortices (Fig. 2.19(b)). The exterior vortices are that relative to the natural S-duct flow separation. Meanwhile, the internal vortices are that created by the array of vortex generators. For this intake, as the vortex is ingested at the centerline (test case 4), its perturbation on the velocity vectors is notable as shown in Fig. 2.19(d), while its effect on total pressure field is minimal. On the other hand, as the vortex is ingested near the duct wall at the angular position aligned with the separation ($\phi = 180^o$), the effect of the vortex generators on the flow field increases (see Fig. 2.19(f)). This is evident by comparing the vortices attributed to the presence of vortex generators shown in Fig. 2.19(b) and 2.19(f). Finally, as the vortex is ingested at $\phi = 0^o$, the flow pattern is similar to that obtained under clean inlet conditions except the fact that a small distortion in the boundary layer occurs in a location opposite to that of the S-duct flow separation.

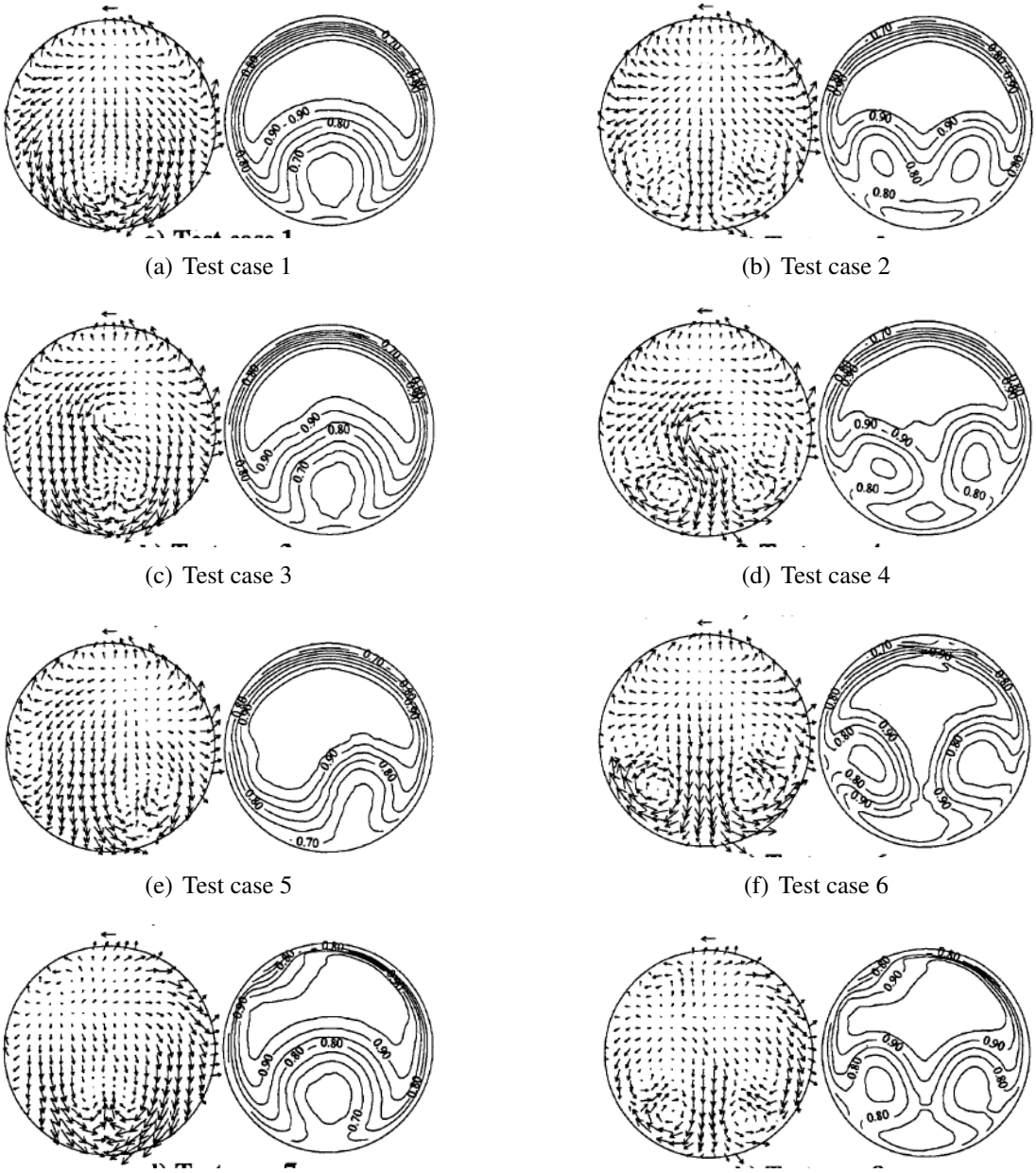

(a) Test case 1 (b) Test case 2

(c) Test case 3 (d) Test case 4

(e) Test case 5 (f) Test case 6

(g) Test case 7 (h) Test case 8

Figure 2.19: Transverse velocity vectors and total pressure distribution at the plane E defined for the Wellborn S-duct[33]

2.2.4.2 Previous numerical research

Anderson[2] conducted numerical investigations regarding the effect of an ingested vortex on the flow field of the S-duct of the F/A-18 (Fig. 2.20).

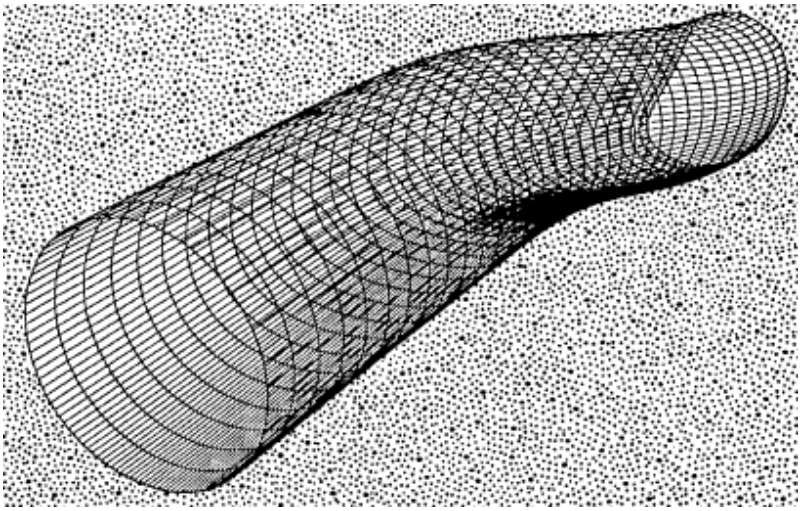

Figure 2.20: Visualization of the F/A-18 inlet duct[2]

The analysis was accomplished using a 3D Reduced Navier-Stokes (RNS) code. A preliminary validation of this duct was carried out on an equivalent circular diffusing S-duct. This had a centerline following that of the F/A-18 and the diameter distribution based on the hydraulic diameter of the original model.

Then, numerical calculations were carried out with a Mach number (M_{in}) of 0.6 and a Reynolds number of $8 \cdot 10^5$, both measured at intake inlet. The latter was based on the hydraulic inlet diameter. In these conditions, three groups of vortices were ingested. For the first and second group, the vortex location at the inlet was held constant while the swirl angle attributed to the vortex (α_s) increased up to 45^o in counter and co-rotating clockwise direction, respectively. For the third group, the swirl angle associated to the vortex (α_s) was held constant while the radial location towards the wall was increased.

The results showed that from the intake inlet plane (Fig. 2.21(a) and 2.21(b)) to the engine face (Fig. 2.21(c) and 2.21(d)), the ingested vortex had the tendency to spiral out around the inside surface of the duct in a direction corresponding to the sense of the ingested vortex itself. Therefore, for the Reynolds number considered, the overall qualitative nature of the vortex ingested was essentially 'inviscid like'. Hence, the dominant aerodynamic characteristics have their origin in inviscid flow theory. On the other hand, viscous effects are important, but their influence is felt by increasing the boundary layer blockage. This phenomena cause to the vortex to move radially inward.

The effect of the ingested vortex was quantified by means of the kinetic energies of the primary, secondary and swirl flow relative to the direction of the duct centreline (KE_p, KE_s and KE_θ), calculated along the S-duct as given in Eqs. 2.6, 2.7 and 2.5, respectively.

$$KE_p = \int_A \rho V_p \frac{V_p^2}{2} dA \tag{2.5}$$

$$KE_s = \int_A \rho V_p \left[\frac{V_{r,s}^2 + V_{\theta,s}^2}{2} \right] dA \tag{2.6}$$

$$KE_\theta = \int_A \rho V_p \frac{V_\theta^2}{2} dA \tag{2.7}$$

These parameters enabled the definition of two non-dimensional metrics: the secondary and swirl kinetic energy ratios (k_s and k_θ), expressed in Eqs. 2.8 and 2.9.

$$k_s = \frac{KE_s}{KE_p} \tag{2.8}$$

$$k_\theta = \frac{KE_\theta}{KE_p} \tag{2.9}$$

Figures 2.22(a) and 2.22(b) show the trend of secondary and swirl kinetic energy ratio (k_s and k_θ) along the axial direction with and without an ingested vortex at the inlet. The ingested vortex under consideration is characterized by a swirl angle $\alpha_s = 10^o$. It is assumed that the swirl kinetic energy component (k_θ) is the portion of secondary flow kinetic ratio that would be eliminated with the application of IGVs. Hence, these parameters can track and quantify the passage of each and every vortex disturbance entering the inlet duct. These trends provide a quantitative methodology where the aerodynamic flow quantities characterizing the vortex ingestion can be directly related to the main geometric quantities relative to the inlet duct.

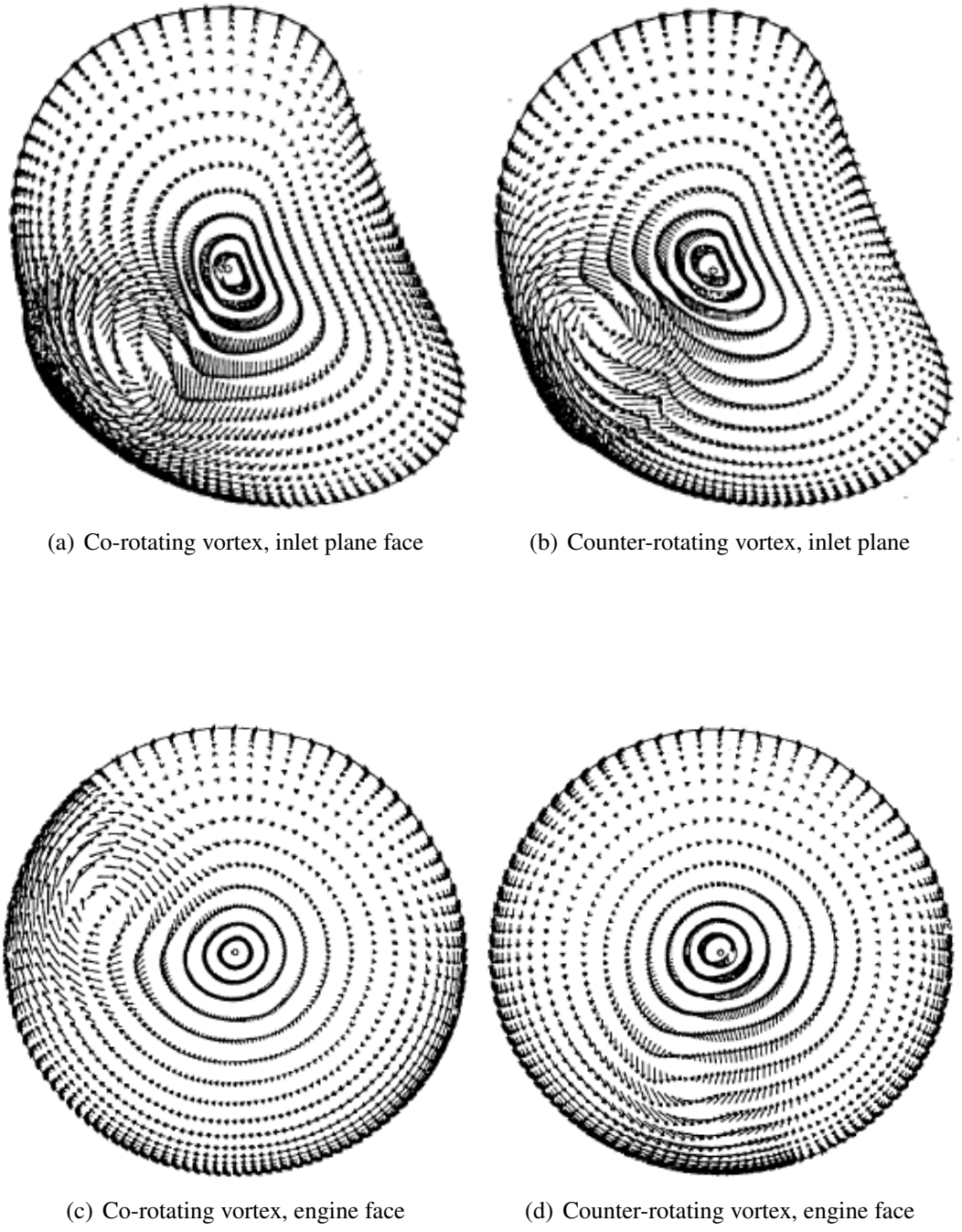

(a) Co-rotating vortex, inlet plane face

(b) Counter-rotating vortex, inlet plane

(c) Co-rotating vortex, engine face

(d) Counter-rotating vortex, engine face

Figure 2.21: Velocity vectors at the inlet plane and engine face of the F/A-18 duct for a vortex swirl angle (α_s) of $10^{o\,2}$

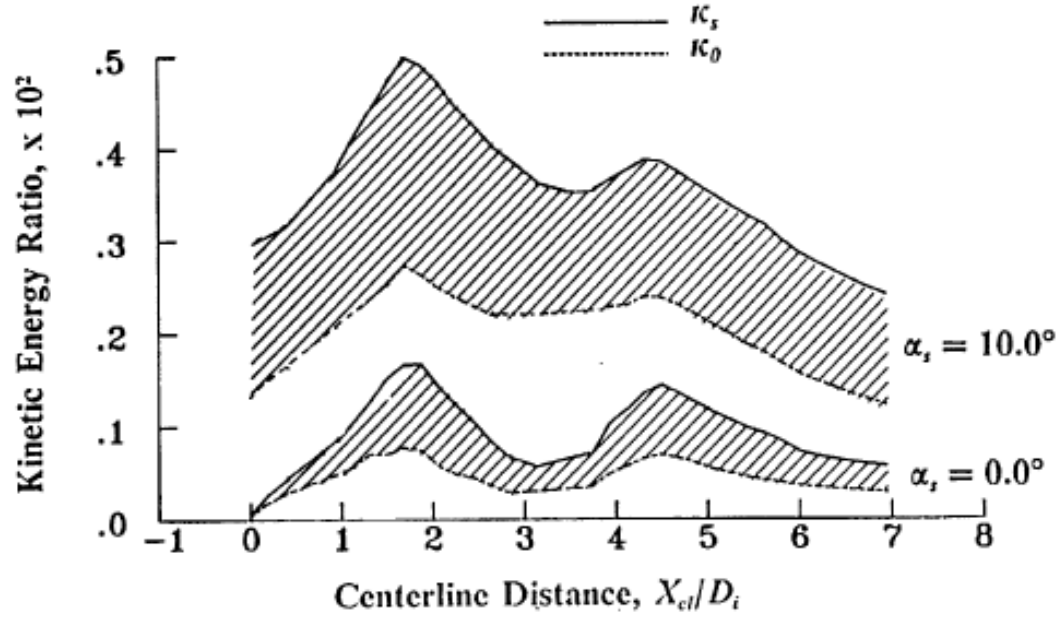

(a) Co-rotating vortex

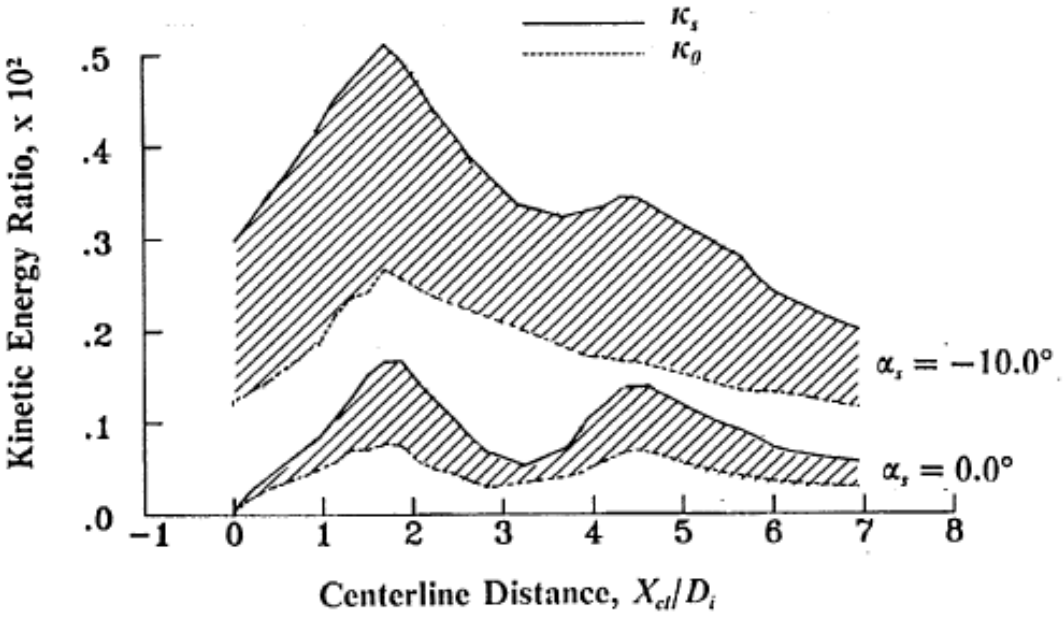

(b) Counter-rotating vortex

Figure 2.22: Secondary and swirl kinetic energy ratio (k_s and k_θ) along the axial position of the duct for (a) co- and (b) counter-rotating vortex ingested at the inlet as compared with the clean inlet conditions[2]

2.3 Conclusive remarks

The most relevant literature review concerning the effects of the inlet flow distortion on turbomachinery performance, the inlet flow distortion characterization, and flow field analyses into S-shaped intakes operating under clean and with a prescribed vortex ingested at the inlet have been reviewed. The main findings within the previous research are listed below. Then, a summary relative to the key aspects that this research is addressed to analyse is also provided.

2.3.1 Main findings and contributions

1. Murphy[23] conducted experimental research to predict the characteristics of the ground vortex related to the wind and engine conditions.
2. The S-duct internal aerodynamics by considering clean inlet conditions has been extensively analyzed experimentally and numerically.
3. Anderson[2] investigated numerically the aerodynamic characteristic of an ingested vortex into a closed duct. He confirmed that the inviscid vortex theory could be applied to the vortex itself.
4. Wendt et al[33] carried out parametric analysis relative to the effect of an ingested vortex location on the S-duct aerodynamics. He confirmed that the largest influence was determined by a vortex ingested to a location at the intake inlet aligned with the S-duct flow separation.
5. The effects of both bulk and paired swirl on turbomachinery performance have been extensively investigated either experimentally and numerically.
6. The S-16 Committee[16] estimated the location of the AIP for total pressure distortion valid for conventional aircraft inlets..

2.3.2 Deficiencies in current understanding

1. Effect of the rotor blades on the S-duct flow field.
2. Effect of the S-duct flow separation on the turbomachinery performance.
3. Effect of the S-duct self-generated distortion combined with that attributed to a vortex ingested at the intake inlet on the performance of a fan rotor.
4. Estimation of the location of the AIP for swirl distortion.

Chapter 3

Computational models and methodology

To quantify the effect that different inlet flow distortion patterns determine on the turbomachinery performance the realization of a large number of experiments involving different rotor geometries, operating conditions and swirl distortion patterns are required. Alternatively, the assessment of CFD calculations can allow an easier variation of aforementioned parameters. Meanwhile, the time and expenses can be reduced according to the complexity of the CFD models used. For this reason, CFD was the approach adopted for the current research.

In this chapter, the CFD tools developed as well as the methods applied to carry out numerical investigations of the CFD results and to prescribe vortical flows at the inlet of the CFD domains are discussed. Firstly, the conditions defining the computational method applied to the CFD solver adopted in this work are specified. Secondly, the geometries selected from the public domain to carry out the current research, the relative CFD models created and their validation against experimental data are reported. In particular, these geometries were the RAE S-shaped intake 2129 and the NASA Rotor 67. Then, a purely numerical coupled system S-shaped intake/fan rotor configuration based on the aforementioned geometries, defined in this research to analyze the inlet flow distortion, is presented. Thirdly, the descriptors used to quantify both the total pressure and swirl distortion as well as the non-dimensional groups introduced to analyse the flow field and the performance of the aero-engine components considered in this research are presented. Finally, the procedure followed to implement a tightly-wound vortex into the CFD code as inlet boundary condition and the characteristics of a datum vortex are defined.

3.1 Computational method

The CFD solutions of this research were obtained by using ANSYS CFX v14.0 CFD code. This is an implicit pressure based and vertex centered CFD solver[34]. In this section, the conditions defining the computational method, applied to the CFD solver, are presented.

3.1.1 Type of simulations

Most of the CFD simulations carried out in this research adopted the Reynolds Averaged Navier-Stokes (RANS) approach. Therefore, the numerical results obtained were time averaged, by implying an approximation of the real flow behaviour. However, this is the most used approach in engineering field since it provides results sufficiently accurate within a reasonable computational time. On the other hand, to determine of the AIP for swirl distortion, which will be presented in § 6.3, the CFD simulations were performed by using the Unsteady Reynolds Averaged Navier-Stokes (URANS) approach. This complication was introduced because of the limitation of the CFD code to solve the flow field involving a single CFD rotating domain having a distorted flow prescribed at the inlet plane. The details relative to the assessment of these simulations are discussed in § 6.3.

Moreover, according to the flow velocities reached for the case studies of this research, transonic zones existed throughout the computational domains. Therefore, it was necessary to account for the compressibility effects with the activation of the energy equation in the CFD solver.

3.1.2 Convergence criteria

To confirm the convergence of a CFD solution, two conditions had to be verified. Firstly, the convergence was reached when the values of the root mean square (RMS) of the residuals relative to mass conservation, Navier-Stokes, energy and turbulence model equations were below $5 \cdot 10^{-5}$. Secondly, the mass flow imbalance had to stabilize to zero with the numerical iterations.

3.1.3 Advection scheme

The discretization of the advection terms of Navier-Stokes equation system followed a numerical scheme already implemented into CFX solver v14.0 called 'High Resolution'[34]. Normally, this is a first order which switches gradually to a second order advection scheme by applying a blending factor as the gradient of the CFD solution overcome an established limit.

3.1.4 Turbulence modelling

As discussed in § 2.2.2, the flow field in S-shaped intakes is characterized by complex secondary flows and adverse pressure gradients. These conditions put high demands in terms of turbulence modelling. Amongst the turbulence models considered in the literature for this kind of applications there are Spalart Allmaras[35], $k-\varepsilon$[36], $k-\omega$[36], and $k-\omega$ shear stress transport (SST).

The one-equation turbulence model Spalart Allmaras was mainly developed for aerodynamic flows. This model consists in a transport equation for the eddy viscosity.

The two-equations turbulence model $k-\varepsilon$ requires the specification of two transported variables, the specific turbulent kinetic energy (k) and the turbulent kinetic energy dissipation rate (ε). As an advantage, this model provides an accurate CFD solution in the outer region and outside of the boundary layer. Also, the CFD solution is not significantly affected by the values of k and ε imposed at the free stream boundaries. However, this model is unable to calculate the numerical solution up to the wall and, therefore, uses a wall function. Hence, it is recommended that the non-dimensional wall distance $(y^+)^*$ of the mesh adopted has to be between 11 and 100. Moreover, this model does not predict accurately large adverse pressure gradients, due to the overprediction of the turbulent kinetic viscosity.

The two-equations turbulence model $k-\omega$ requires the specification of the turbulent kinetic energy (k) and the turbulent frequency (ω). As compared with $k-\varepsilon$, the numerical solution is calculated up to the wall without specifying a wall function. Consequently, the non-dimensional wall distance (y^+) has to be below 1. However, this model strongly depends on the values of k and ω imposed at the free stream boundaries and, as for the $k-\varepsilon$ model, overpredict the turbulent viscosity.

The two-equations turbulence model $k-\omega$ SST was introduced by Menter[37]. Essentially, it is a combination of the $k-\omega$ model in the inner boundary layer, and $k-\varepsilon$ model in the outer region of and outside of the boundary layer. This is analytically realized by using a blending factor function of the physical distance from the wall. Moreover, to avoid the overprediction of the shear stress (and then the separation) when adverse pressure gradients occur, the turbulent viscosity is artificially reduced by adopting the methodology assessed by Johnson at al.[38]. As compared to $k-\varepsilon$ and $k-\omega$, this $k-\omega$ SST turbulence model is the most accurate in predicting flow separation. Also, according to previous research this model is accurate to simulate transonic compressors flows[39] as well as predicts their shock wave system upstream of the rotor face[40]. As for the $k-\omega$, the application of the $k-\omega$ SST turbulence model, the CFD code solves the flow up to the wall, without requiring the specification of the non-dimensional wall distance. Hence,

*The non-dimensional wall distance (y^+) provides an indication of the distance between the wall and the first cell node in accordance with the operating conditions.

by imposing a priory a value of non-dimensional wall function (y^+), Reynolds number and length of reference, the corresponding spacing normal to a solid surface relative to the first cell of the mesh was estimated by adopting a toolbox available on internet[41].

3.2 Geometries, CFD models and validations

In this section, the geometries selected from the public domain and applied for this research, the relative CFD domains and their validation against experimental data are described in detail. These geometries are the RAE S-shaped intake 2129 and the NASA Rotor 67. Moreover, a full scale CFD model defined for a coupled system S-shaped intake/fan rotor based on the aforementioned geometries and introduced in the this research to carry out analysis of the inlet flow distortion is presented.

3.2.1 RAE S-shaped intake 2129

In this research, a sensitivity analysis of the flow distortion was conducted on a coupled system S-shaped intake/fan rotor where the intake part was based on the geometry of the RAE S-shaped intake 2129. In this section, the description of the geometry and the experimental and numerical previous research relative to this intake are presented. Moreover, the details of the CFD model created for this intake and the relative validation process are reported.

3.2.1.1 Geometry description

The RAE S-shaped intake 2129 is a side mounted intake with a circular cross section and an horizontal symmetry plane. The position of the intake with respect to the aircraft is identified with the starboard, bottom, port and top edges indicated in Fig. 3.1. The details regarding the geometry of this intake was extensively provided in previous research[42,43,44,45]. In particular, the S-duct inlet corresponds to the throat station, while the engine face, or AIP, is located at 1.0655 ft, where the duct straightens out again. Moreover, the main intake dimensions are shown in Fig. 3.2 and their numerical values are listed in Table 3.1.

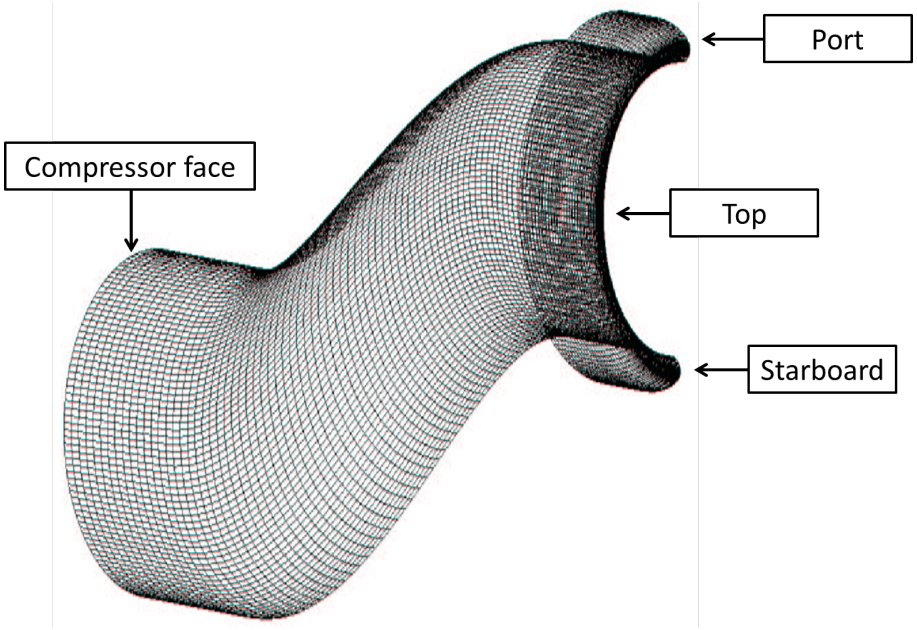

Figure 3.1: Rotated 3D view of the RAE S-shaped Intake 2129[46]

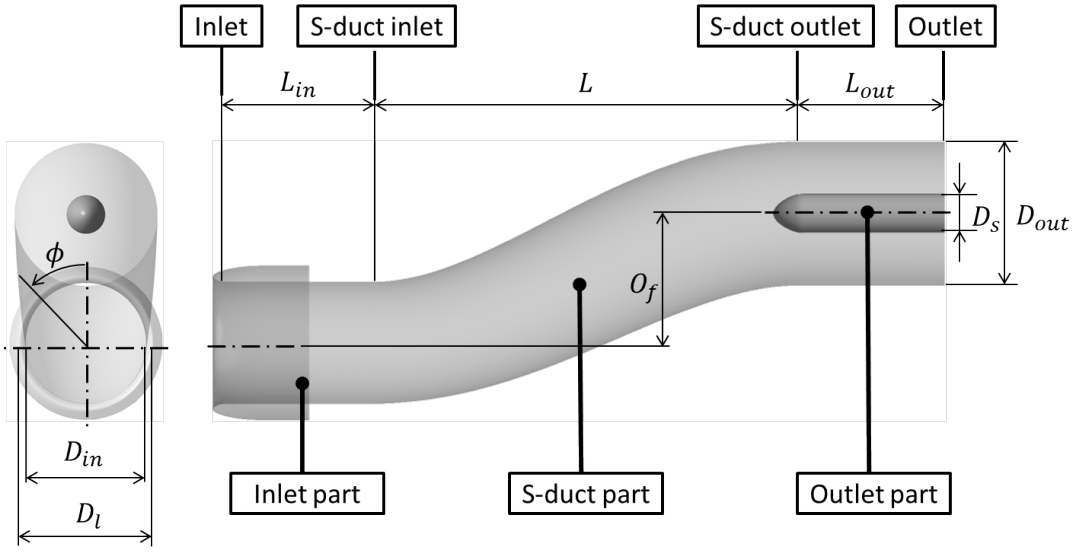

Figure 3.2: Visualization of the dimensions of the RAE S-shaped intake 2129 from the front (left) and top side (right)

Dimension	Value
D_{in} $[mm]$	128.7
L_{in} $[mm]$	152.4
D_l/D_{in}	1.102
D_{out} $[mm]$	152.4
L_{out} $[mm]$	152.4
D_s $[mm]$	41.1
L/D_{in} $[mm]$	3.552
O_f/L	0.3

Table 3.1: Values of main dimensions of RAE S-shaped intake 2129[44]

Along the axial direction, the intake can be split into three parts: a constant cross section inlet part, an S-duct diffuser and a constant cross section outlet part (Fig. 3.2). Both, the inlet and outlet parts extend for one outlet diameter (D_{out}). The intake cowl is internally defined by an ellipse and externally by the airfoil NACA $1-854-351$[47]. The S-duct diffuser part is analytically defined by means of the non-dimensional centerline offset (ζ) and the non-dimensional diffusing profile (γ), both as functions of the axial position (z), Eqs. 3.1 and 3.2.

$$\zeta = \frac{y}{L} = \frac{1}{2}\frac{O_f}{L}\left[1-\cos\left(\frac{\pi\cdot z}{L}\right)\right] \tag{3.1}$$

$$\gamma = \frac{D-D_{in}}{D_{out}-D_{in}} = 3\left(1-\frac{z}{L}\right)^4 - 4\left(1-\frac{z}{L}\right)^3 + 1 \tag{3.2}$$

3.2.1.2 Previous research

The flow field of the RAE S-shaped intake 2129 was widely analyzed both experimentally[48,32] and numerically[42,46,43,49,44,45], for different operating conditions and working fluids. The most relevant previous research for the current work is presented below.

The Advisory Group for Aerospace Research and Development (AGARD) carried out experiments on this intake[32]. In particular, two test cases, namely the High Mass Flow (HMF) and Low Mass Flow (LMF), were conducted. The experiments were conducted by ensuring a uniform total pressure and total temperature ($P_{0,in}$ and $T_{0,in}$) and free-stream Mach number (M_∞) at the intake inlet. Meanwhile the Mach number at the AIP (M_{AIP}) identified the test case. The values relative to these quantities are listed in Table 3.2.

Parameter	**HMF**	**LMF**
$P_{0,in}$ $[Pa]$	101215.8	101134.5
$T_{0,in}$ $[K]$	293	
M_∞	0.21	
M_{AIP}	0.536	0.304

Table 3.2: Specifications of AGARD test cases[32]

Referring to these experiments, AGARD also reported sensitivity of the flow to numerical procedures and concluded that more detailed experimental data could have been beneficial[32]. Hence, the aforementioned experiments were repeated by the Aircraft Research Association (ARA)[48]. As a result, differences were notable especially for the AGARD HMF test case as shown in Fig. 3.3. Menziez[43] concluded that this difference could be attributed to an improvement of the measurement techniques which were achieved with the ARA measurements. Hence, the experimental data relative to ARA measurements of the AGARD test cases were used as a reference for the current work to validate the CFD model defined for this intake.

On the other hand, Menzies et al.[46,43] carried out RANS CFD calculations to validate the flow field within the RAE S-shaped intake 2129 against ARA experiments mentioned above. He considered the Spalart Allmaras, $k-\varepsilon$ and $k-\omega$ SST as turbulence models. He found the $k-\omega$ SST was found to provide the best flow prediction. As already discussed in § 3.1.4, this turbulence model is the most suitable for flows characterized by adverse pressure gradients which normally occurs in S-shaped intakes. The numerical results of this research were used as the CFD reference of the current work.

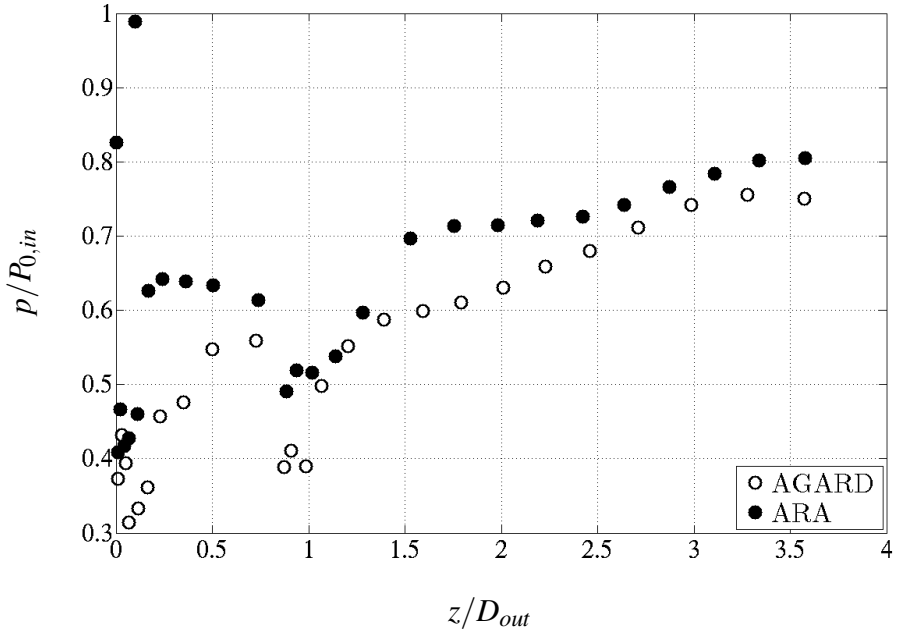

(a) Starboard edge ($\phi = 0^o$)

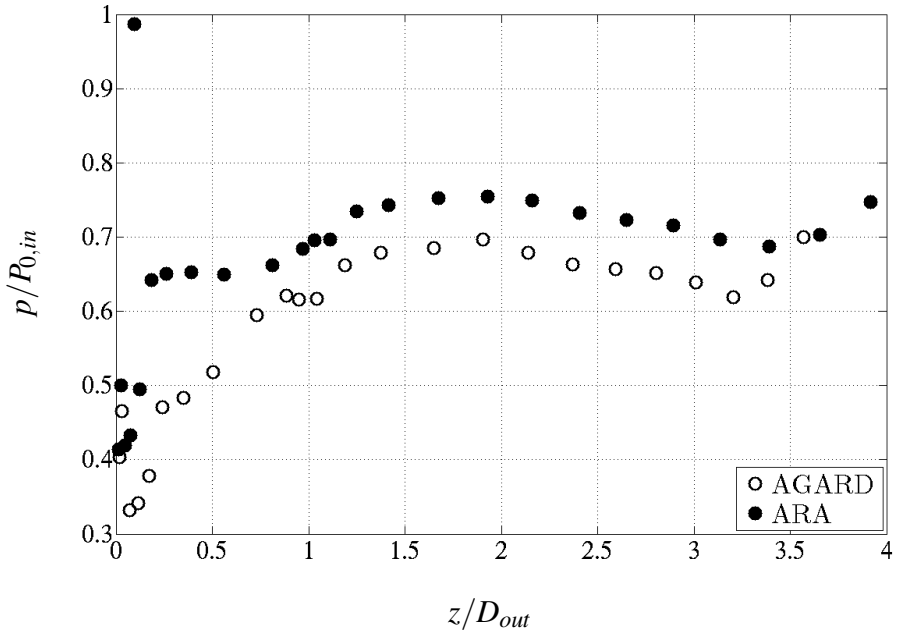

(b) Port edge ($\phi = 180^o$)

Figure 3.3: Static to inlet total pressure ($p/P_{0,in}$) versus axial position (z/D_{out}) for AGARD HMF test case compared between AGARD[32] and ARA[48] experiments

In addition, Mohler[49] conducted numerical research on the RAE S-shaped intake 2129 by using the CFD code Wind-US, developed by NPARC Alliance, and by adopting structured and unstructured meshes. Uniform total pressure and temperature of 14.667 *psi* and 517 ^{o}R were imposed at the inflow plane. Meanwhile, at the outflow plane a uniform static pressure was imposed to match a throat Mach number between 0.4 and 0.8. Due to limitations of the CFD solver used, the Spalart-Allmaras was used as turbulence model. As a result, the application of a structured mesh determined slightly more precise results as compared with that relative to an unstructured mesh (Fig. 3.4). This can be attributed to a better accuracy generally achieved with structured meshes in resolving the boundary layer, since it plays an important role on the internal flow structure. However, the generation of a structured mesh for a complex geometry such as an S-shaped intake is a very arduous process, while unstructured meshes generation is a more automated process but can be advantageous in some applications[49].

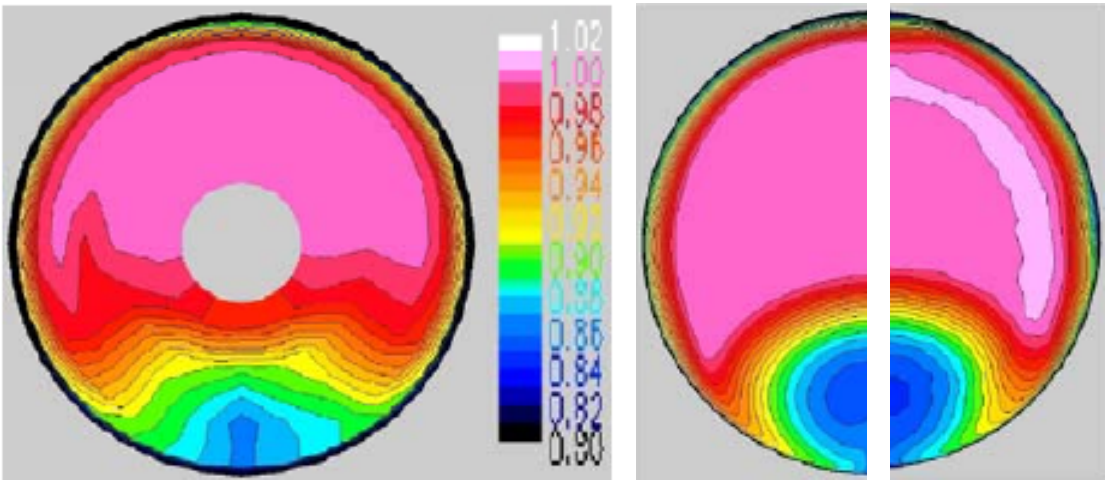

(a) Experimental (b) Structured mesh (c) Unstructured mesh

Figure 3.4: Comparison of contours of total pressure recovery at the engine face of the RAE S-shaped intake 2129[49] for different meshes for a throat Mach number of 0.8

Finally, Chevalier et al.[45] investigated the flow passing through the RAE 2129 intake by using both RANS and Detached Eddy simulation (DES) numerical approaches for a free stream Mach number (M_∞) of 0.207 and a mass flow (W) of 2.87 kgs^{-1}. A common computational domain of about 6.13 million elements was adopted. As compared with the RANS solution, the DES model indicated an earlier separation onset occurring in the S-duct with respect to the experiments and, therefore, a more extended separation bubble. As a consequence, the reattachment location moved futher downstream. Therefore, according to the mesh used, RANS performed better than DES approach.

3.2.1.3 Description of the CFD model

Figure 3.5 shows the CFD domain for the RAE S-shaped intake 2129. Tramontin[50] defined this intake using ICEMCFD mesh generator.

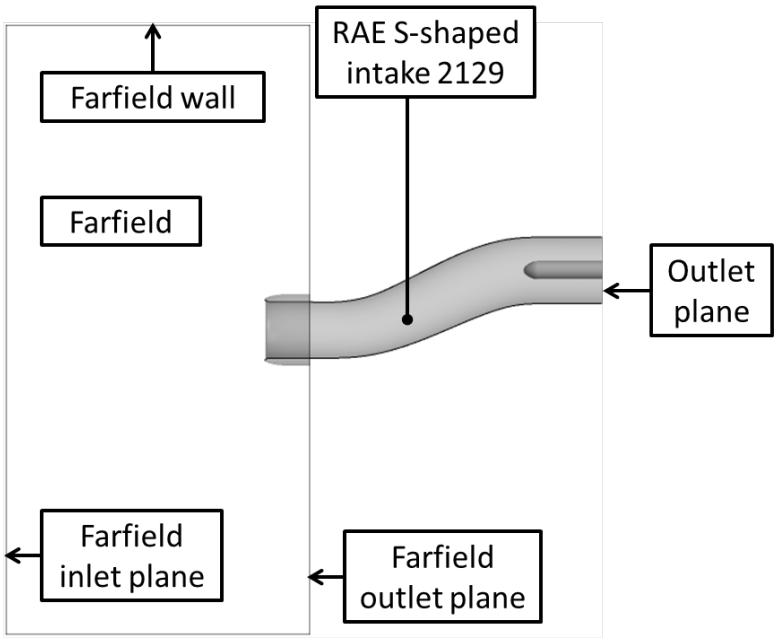

Figure 3.5: Top view of the CFD domain and boundary conditions of the RAE S-shaped intake 2129

A farfield zone was defined upstream of the intake and sufficiently extended to replicate the natural deviation of the flow entering the intake within the capture streamtube as obtained during ARA experiments[48] and to avoid the influence due to the presence of the artificial farfield wall. Hence, according to CFD experience matured during the doctoral research the farfield extended of $4.38 \cdot D_{in}$ along the axial direction (z) and $10.27 \cdot D_{in}$ along the two main directions perpendicular to the axial direction (x, y). The S-duct wall was built upon 16 circumferences representing the traces of equidistant planes perpendicular to the axial direction and defined along the S-duct itself. The intake cowl was generated from the revolution of a curve around the axis of the intake at the inlet. The relative coordinates were calculated using a methodology proposed by Williams[51]. Finally, the coordinates of the spinner were extracted from a drawing of the intake reported in the public domain[48].

After the definition of the geometry, several blocks were strategically placed throughout the CFD domain (Fig. 3.6 and 3.7) to ascertain a high quality of the fully structured mesh which was then created. The blocking strategy applied around the intake cowl con-

sisted of the creation of *O*-grid blocks along the intake and the external region of the inlet cowl as shown in Fig. 3.6(b). In this manner, the resolution relative to the mesh was highest within the *O*-grid placed at the centre of the intake and, then, gradually decreased moving away from the intake itself (Fig. 3.8(c)), where high mesh resolution was no longer required. Due to the intake offset, five *O*-grid blocks were defined and interconnected along the S-duct as shown in Fig. 3.7(a). Finally, close to the spinner body a block was extruded from the central *O*-grid of the S-shaped intake towards the leading edge of the spinner itself as shown in Fig. 3.7(b). As recommended by Menzies[43], the aforementioned blocks were filled by fully structured submeshes. To guarantee an acceptable mesh quality, quantified by skewness and aspect ratio of the mesh elements, CFD simulations were conducted iteratively with modifications on the mesh to satisfy the convergence criteria introduced in § 3.1.2. These modifications involved mainly the mesh blocking defined around the cowl and spinner shown in Fig. 3.8(a) and 3.8(b).

Finally, the mesh resolution was established by the number of elements defined along the main edges of the blocks indicated in Fig. 3.6 and 3.7. Also, to carry out a grid dependency study, three meshes with different resolution were defined. The number of elements defined along the main edges as well as the total number of mesh elements are listed in Table 3.3.

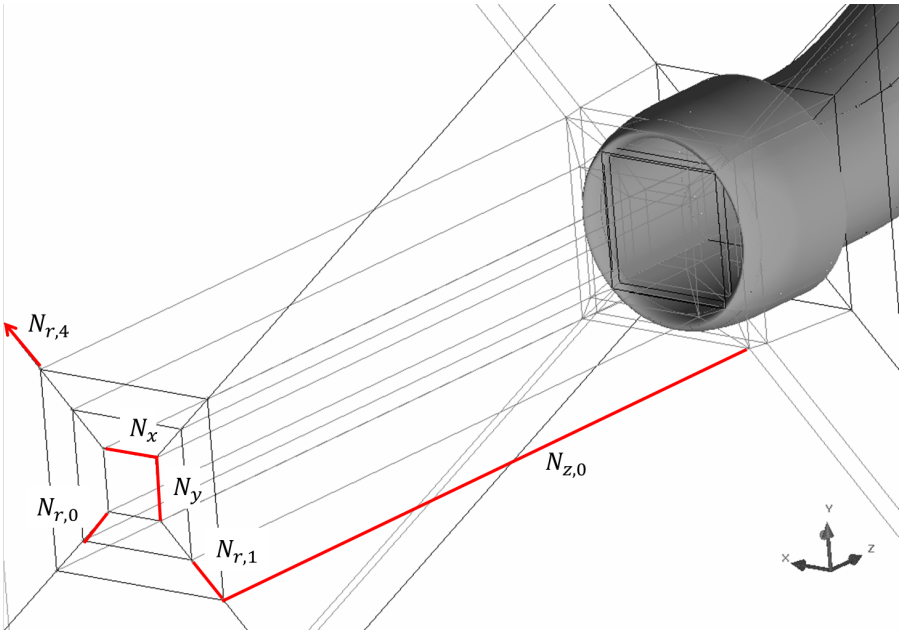

(a) Farfield zone

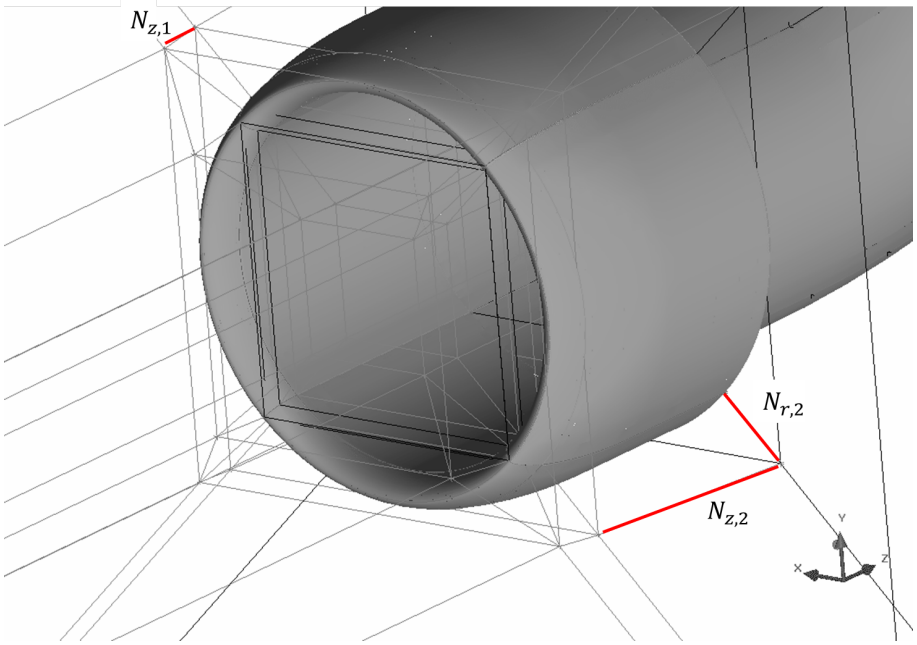

(b) Cowl zone

Figure 3.6: Visualization of the main block edges (a) around the farfield and (b) cowl zone of RAE S-shaped intake 2129

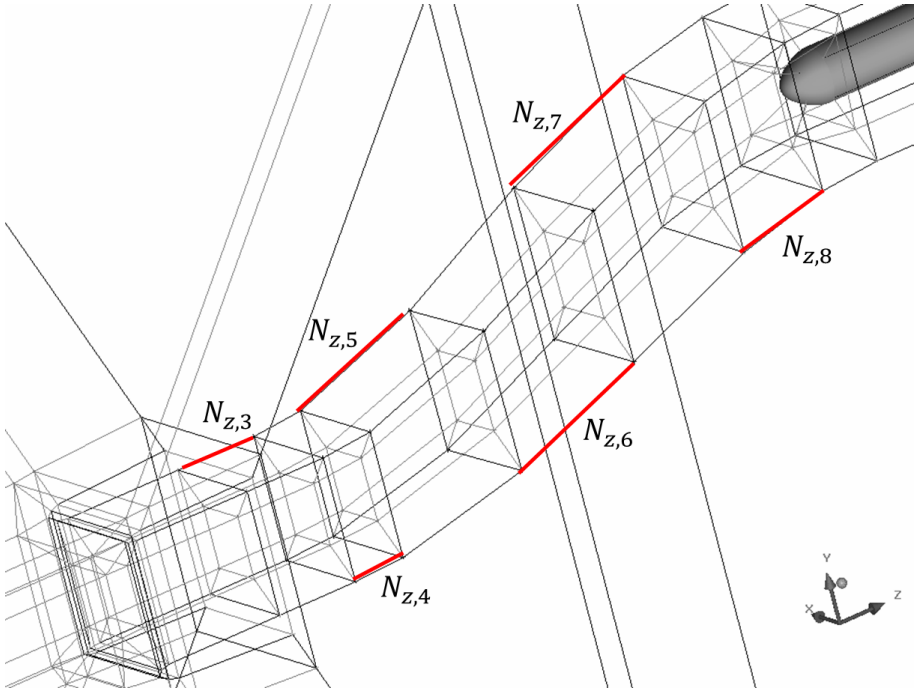

(a) S-duct zone

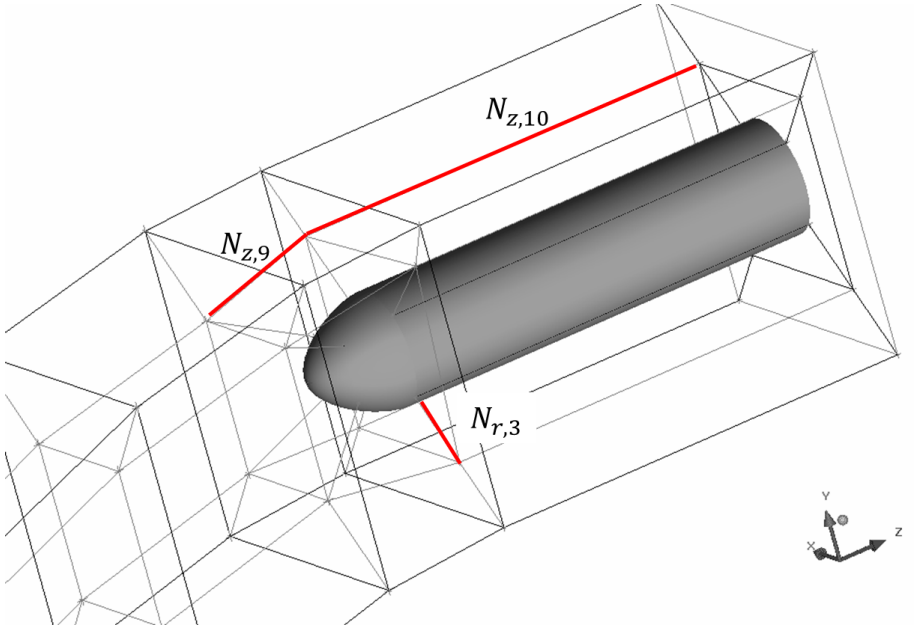

(b) Spinner zone

Figure 3.7: Visualization of the main block edges (a) along the S-duct and (b) around the spinner of RAE S-shaped intake 2129

Edge	Mesh		
	Coarse	Medium	Fine
N_x	30	34	58
N_y	30	34	58
$N_{r,0}$	23	27	44
$N_{r,1}$	23	28	45
$N_{r,2}$	26	29	46
$N_{r,4}$	55	55	55
$N_{z,0}$	100	100	100
$N_{z,1}$	11	12	20
$N_{z,2}$	34	35	40
$N_{z,3}$	16	21	34
$N_{z,4}$	12	14	22
$N_{z,5}$	30	35	58
$N_{z,6}$	31	37	61
$N_{z,7}$	30	36	59
$N_{z,8}$	20	24	39
$N_{z,9}$	15	17	27
$N_{z,10}$	41	49	81
$N_{tot}(\times 10^6)$	3.825	6.361	12.647

Table 3.3: Details of meshes defined for RAE S-shaped intake 2129

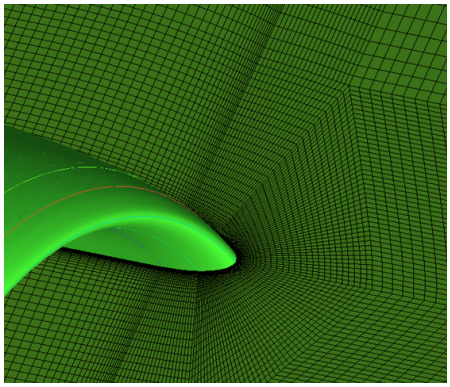

(a) Mesh cut-plane (y,z) at $x = 0\ m$ around the cowl

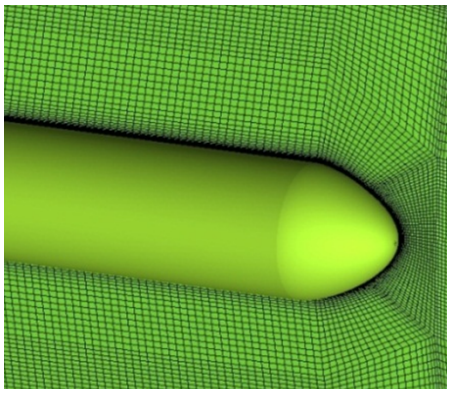

(b) Mesh cut-plane (y,z) at $x = 0\ m$ around the spinner

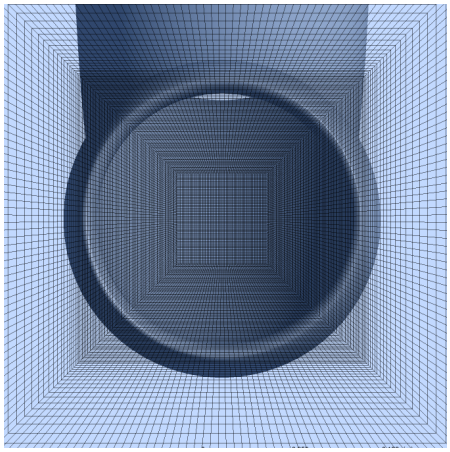

(c) Mesh at the farfield inlet plane ($z = -1.37\ m$)

Figure 3.8: Main mesh features of RAE S-shaped intake 2129 (fine mesh)

3.2.1.4 Grid dependency study

A grid dependency study was carried out by evaluating the total pressure distortion parameter (DC_{60}) and the pressure recovery (η) at the AIP and the static to inlet total pressure distribution ($p/P_{0,in}$) along the port and starboard and port edge of the intake for the three meshes defined in the previous section. The evaluation was relative to both AGARD LMF and HMF test cases (Fig. 3.9(a), 3.9(b), 3.10, and 3.11). As a result, the CFD solution was essentially independent of the mesh considered. Nevertheless, the finest mesh was selected to define the CFD domain of the coupled system in order to reduce as much as possible the level of numerical dissipation attributed to a vortex further ingested into the system itself (§ 5).

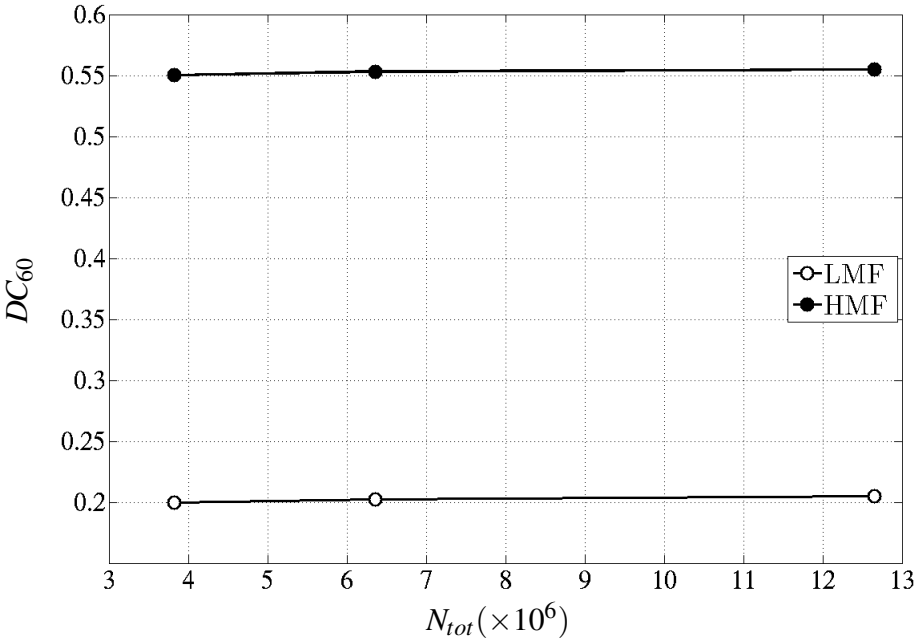

(a) Total pressure distortion parameter (DC_{60})

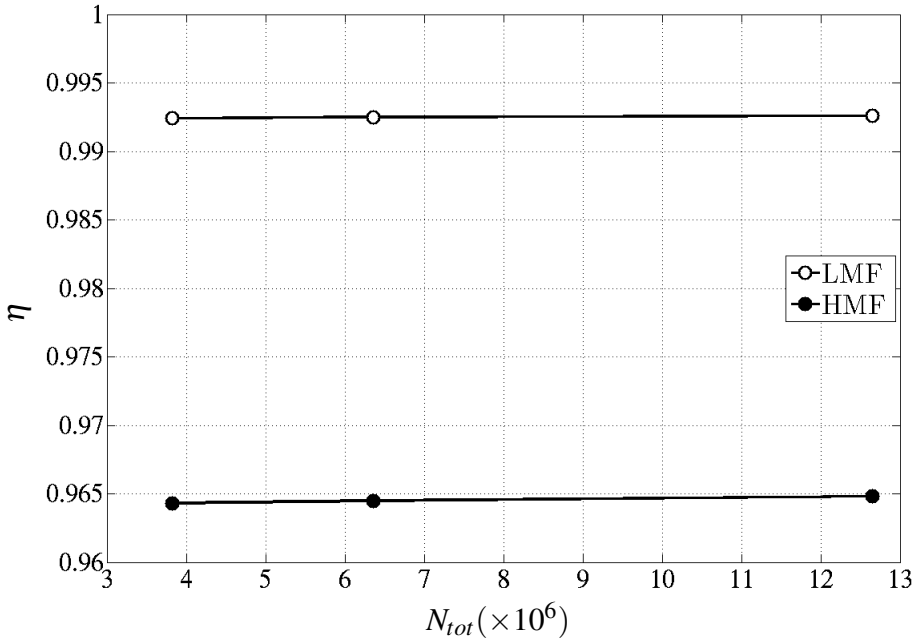

(b) Pressure recovery (η)

Figure 3.9: Total pressure distortion parameter (DC_{60}) and pressure recovery (η) at the AIP relative to AGARD HMF and LMF test cases and for the three meshes defined

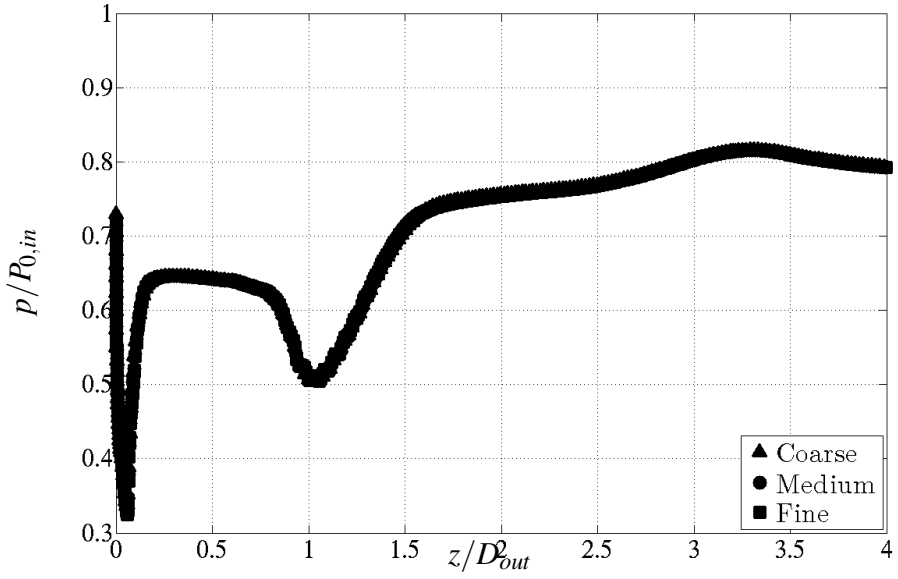

(a) Starboard edge ($\phi = 0^o$)

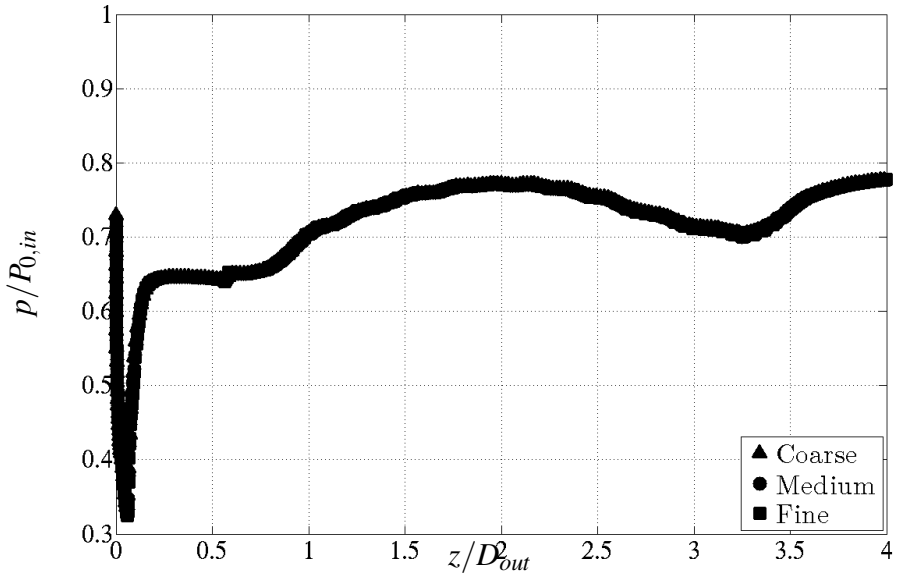

(b) Port edge ($\phi = 180^o$)

Figure 3.10: Static to inlet total pressure ($p/P_{0,in}$) versus axial position (z/D_{out}) for the AGARD HMF test case and for the three meshes defined

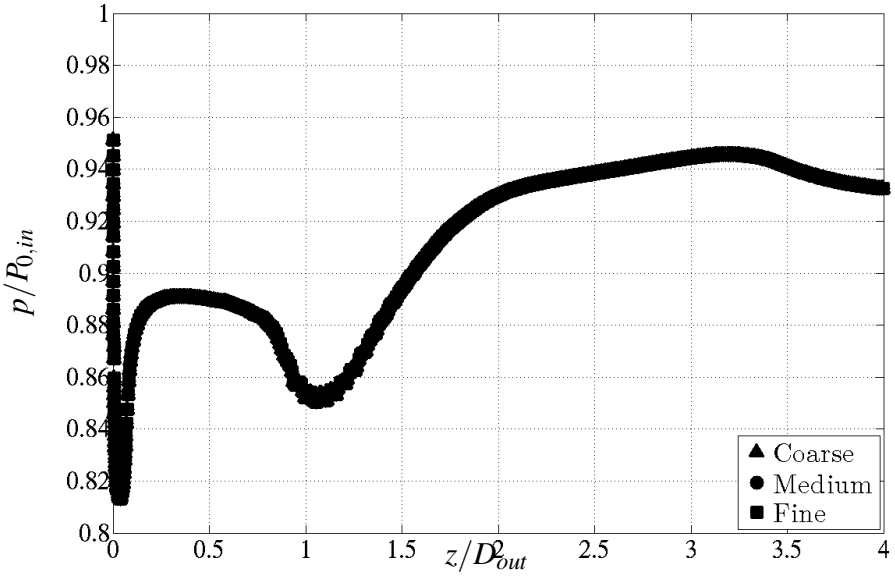

(a) Starboard edge ($\phi = 0^o$)

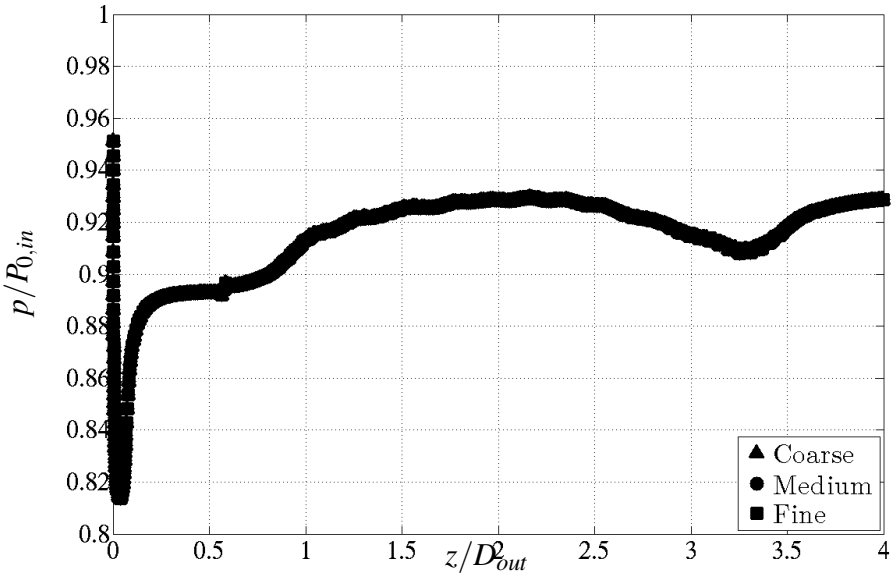

(b) Port edge ($\phi = 180^o$)

Figure 3.11: Static to inlet total pressure ($p/P_{0,in}$) versus axial position (z/D_{out}) for the AGARD LMF test case and for the three meshes defined

3.2.1.5 CFD validation

The CFD model of the RAE S-Shaped intake 2129 described in the previous section was validated against ARA experiments[48], in turn relative to the AGARD HMF and LMF test cases already introduced in § 3.2.1. The validation process consisted to analyse the static pressure distribution along port and starboard edges of the intake, the Mach number at the symmetry plane and flow quantities evaluated at the AIP. Referring to Fig. 3.5 and Table 3.2, the boundary conditions imposed on this CFD domain are specified below.

A uniform total pressure and total temperature corresponding to that imposed in the AGARD test cases at the intake inlet ($P_{0,in}$ and $T_{0,in}$) were imposed at the farfield inlet plane. Meanwhile, a uniform static pressure field was imposed at the farfield outlet and intake outlet planes to match the free-stream Mach number and that at the AIP (M_∞ and M_{AIP}), respectively. Finally, the type of boundary condition 'free-slip wall' was applied at the farfield wall in order to avoid the generation of boundary layers and their influence on the intake flow field.

The AGARD HMF test case Figures 3.12(a) and 3.12(b) show the distribution of static to inlet total pressure ratio ($p/P_{0,in}$) along the axial direction at the starboard ($\phi = 0^o$) and port ($\phi = 180^o$) edges, respectively and for the AGARD HMF test case. The data refer to the ARA experiments[48] and that relative to the CFD solutions obtained by Menzies[43] and in the current work. The trend starts from the highlight plane ($z/D_{out} = 0$). The S-duct inlet and S-duct outlet plane are placed at $z/D_{out} = 1$ and $z/D_{out} = 3$, respectively.

Referring to Fig. 3.12(a), the static pressure at the starboard edge increases gradually along the S-duct part because of the diffusion effect. Then, it decreases slightly towards the S-duct outlet due to the presence of the spinner which reduces the cross section. Therefore, the flow is accelerated. At the S-duct inlet, the values of static pressure at the port edge (Fig. 3.12(b)) were higher than that at the starboard edge (Fig. 3.12(a)). Vice-versa occurs at the S-duct outlet plane. This was due to the centrifugal force that normally manifest in the flow passing through a curved duct (see § 2.2.2). According to this, it would be advantageous to consider the longitudinal and lateral pressure gradients separately. The former is associated with duct diffusion and incidence and plays an important role in determining the severity of flow separation within the duct. The latter is associated with centrifugal effect and has a decisive role in establishing the swirl pattern. As expected, the flow separates within the S-duct part generating a secondary flow. This separation is detected at the starboard edge between $z/D_{out} = 2$ and 3. Overall, the CFD results are in good agreement with the experimental data, although a higher discrepancy occurs at the starboard edge where the recirculation takes place with respect to the rest of the duct. Nevertheless, the CFD model defined in the current work performs better than others proposed in previous research[43].

Moreover, according to the mass flow rate, transonic flow regions are located at the first bend and cowl, while the separation region characteristic of the S-duct is notable at the starboard edge as shown in Fig. 3.13. Also, it was noticed that reattachment of the flow occurs downstream of the separation zone.

The intake performance and the total pressure distortion at the AIP were quantified in terms of pressure recovery (η) and total pressure distortion parameter (DC_{60}), respectively, presented in § A.1 and 3.3.8. These metrics are listed in Table 3.4 for the ARA experiments[48], the CFD results of Menzies[43] and that relative to the model introduced in this work. By considering the numerical analyses carried out either by Menzies[43] and the author, the total pressure distortion parameter (DC_{60}) was generally over predicted against that provided by ARA experiments. As already suggested by Menzies[43], this discrepancy may be related to the reduced number of probes applied during the experiments.

The AGARD LMF test case As for the AGARD HMF test case, similar results were also extracted for the AGARD LMF test case. The AGARD LMF test case delivers a mass flow 0.67 lower than that relative to the AGARD HMF test case. Consequently, the flow field is characterized by lower velocities and higher static pressures throughout the intake, and lower acceleration values at the cowl region. These conditions lead to less discrepancy between numerical results and experimental data than in the AGARD HMF test case. However, according to previous research[32,48], the prediction of the secondary flow taking place at the starboard edge ($\phi = 0^o$) remains more challenging than the AGARD HMF test case. Therefore, a discrepancy between the CFD results, obtained by Menzies[43] and in the current work, the ARA experiments occurs between $z/D_{out} = 1.5$ and 3 (Fig. 3.14(a)). Nevertheless, a better agreement with the ARA experiments was achieved with the current CFD results rather than that obtained by Menzies[43].

Figure 3.15 shows the Mach number contours at the symmetry plane of the intake. This is essentially providing the flow feature. On the outer and inner part of the cowl lip, the stagnation point and the high velocity regions are visible.

Table 3.5 lists the values of pressure recovery (η) and total pressure distortion coefficient (DC_{60}) for the CFD results carried out by Menzies and in the current work and ARA experiments and relative to LMF AGARD test case. Note that regardless of the case study, the values of pressure recovery (η) are very similar and very close to the unity since the level of flow separation reduces consistently with respect to that of AGARD HMF test case presented above. On the other hand, the total pressure distortion coefficient (DC_{60}) obtained from the CFD results were significantly higher with respect to that obtained by the experiments. Again, the reason of that could be attributed to the poor probe resolution adopted during the experiments.

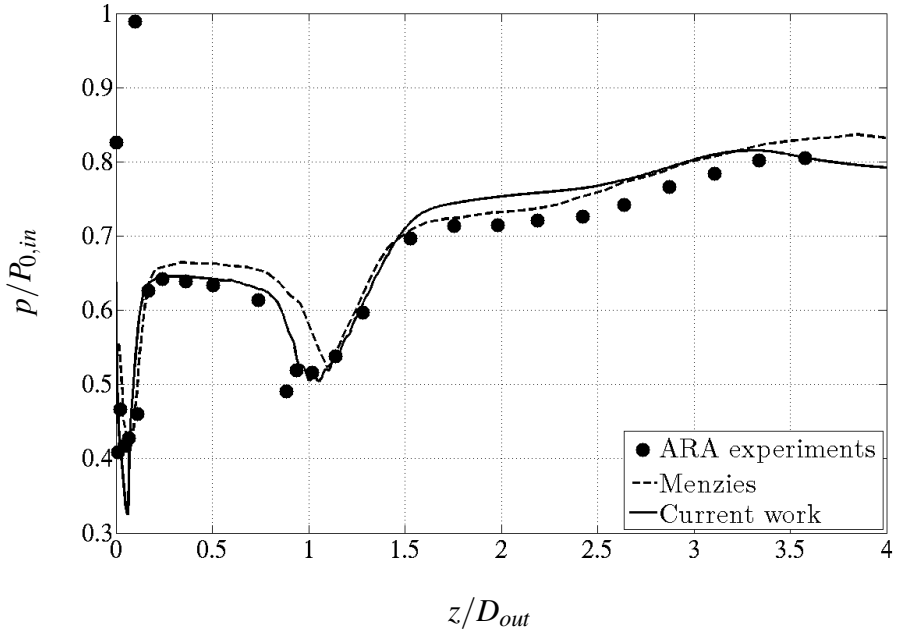

(a) Starboard edge ($\phi = 0^o$)

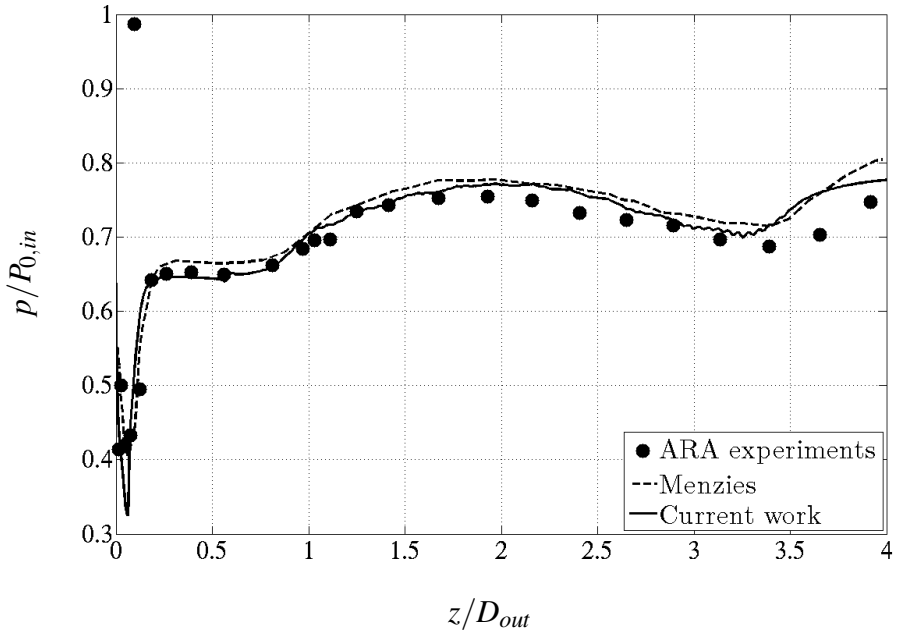

(b) Port edge ($\phi = 180^o$)

Figure 3.12: Static to inlet total pressure ($p/P_{0,in}$) versus axial position (z/D_{out}) for AGARD HMF test case compared between ARA experiments[48] and Menzies CFD results[43]

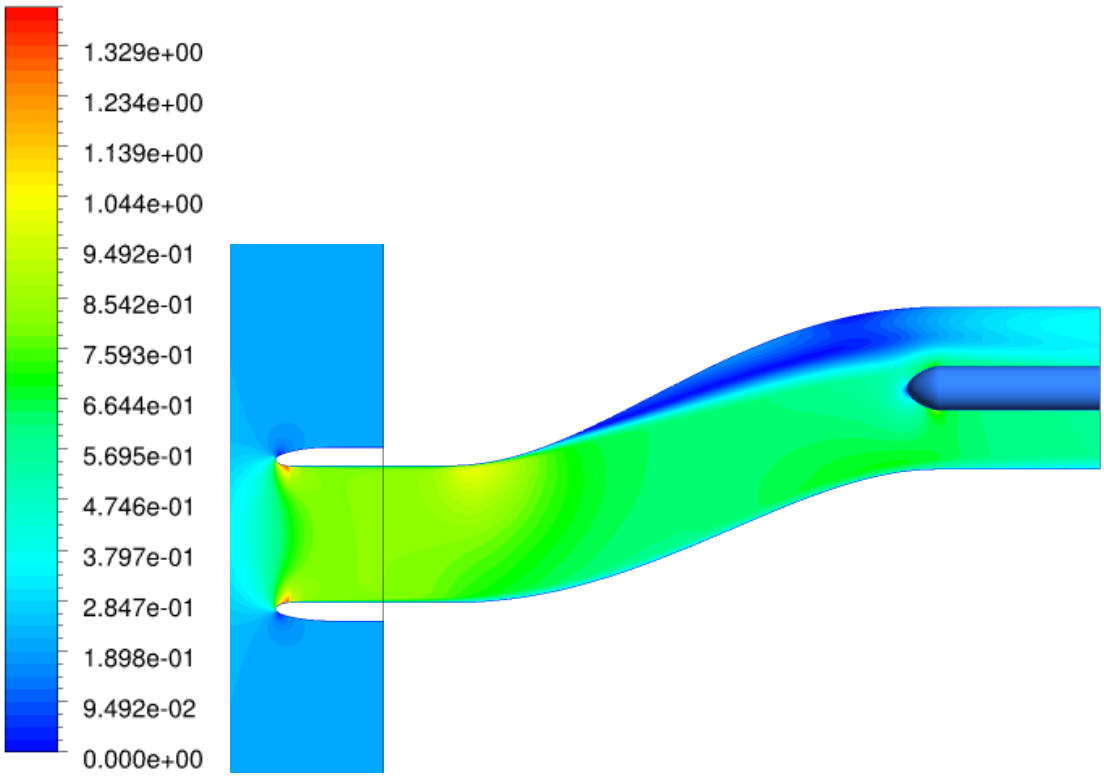

Figure 3.13: Contour of Mach number at symmetry plane ($x = 0$) for AGARD HMF test case

Case	η	DC_{60}
ARA experiments	0.928	0.398
Menzies	0.941	0.688
Current work	0.947	0.595

Table 3.4: Pressure recovery (η) and total pressure distortion parameter (DC_{60}) at the AIP for AGARD HMF test case

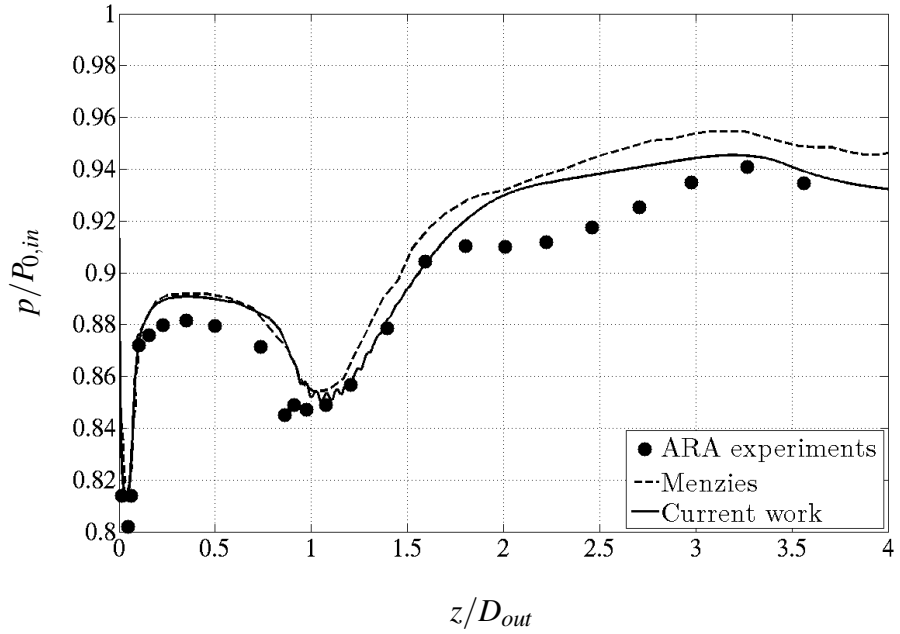

(a) Starboard edge ($\phi = 0^o$)

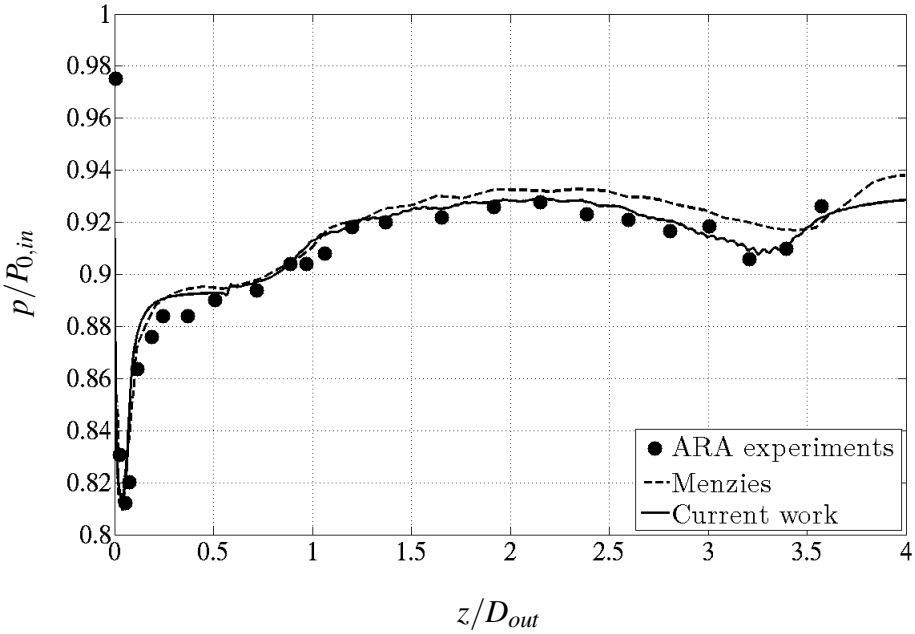

(b) Port edge ($\phi = 180^o$)

Figure 3.14: Static to inlet total pressure ($p/P_{0,in}$) versus axial position (z/D_{out}) for AGARD LMF test case compared between ARA experiments[48] and Menzies CFD results[43]

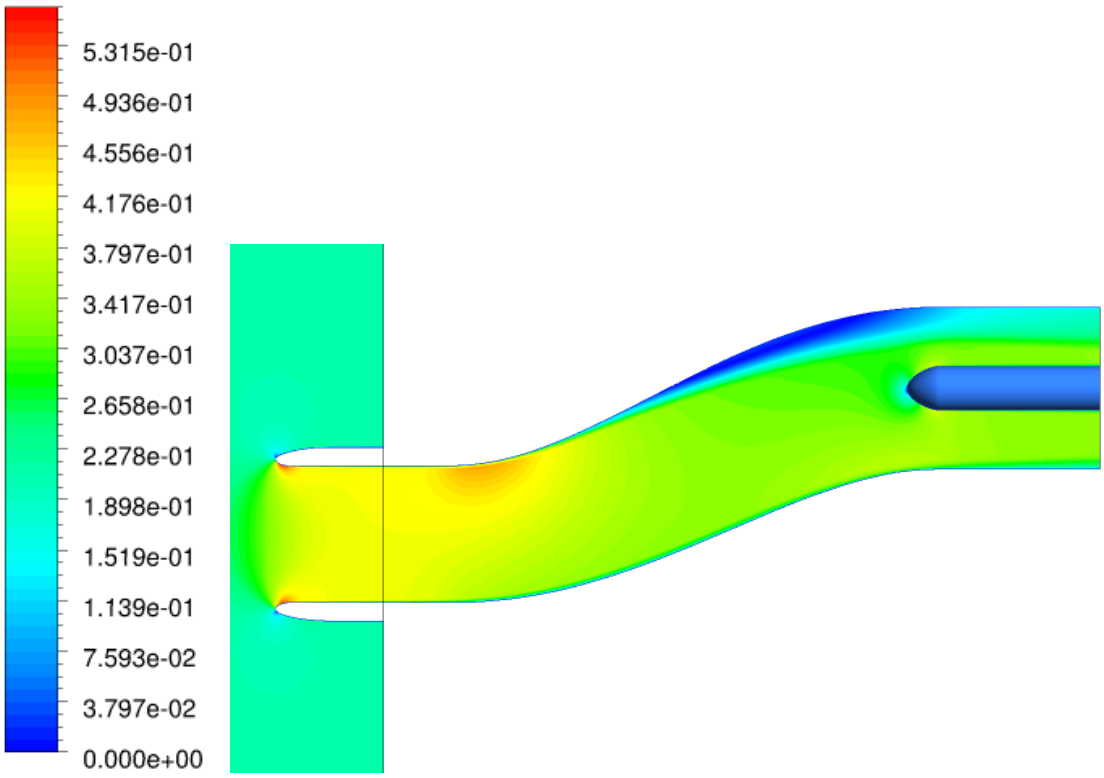

Figure 3.15: Contour of Mach number at symmetry plane ($x = 0$) for AGARD LMF test case

Case	η	DC_{60}
ARA experiments	0.98974	0.226
Menzies	0.99994	0.34
Current work	0.9908	0.205

Table 3.5: Pressure recovery (η) and total pressure distortion parameter (DC_{60}) at the AIP for AGARD LMF test case

3.2.2 NASA Rotor 67

In this research, a sensitivity analysis of the flow distortion was conducted on a coupled system S-shaped intake/fan rotor where the rotor part corresponded to the NASA Rotor 67. In this section, the geometry and the main experimental and numerical previous research regarding this rotor are presented. Also, the details of the CFD model created for this rotor and the relative validation procedure are reported.

3.2.2.1 Geometry description

The NASA Rotor 67 is a low-aspect ratio transonic axial fan rotor[52] and represents the first of a two-stages transonic compressor (Fig. 3.16). This rotor has 22 blades and an aspect ratio of 1.56. The rotor solidity varies from hub to tip between 3.11 and 1.29. The inlet and exit tip diameters are 0.514 and 0.485 *m*, respectively. The inlet and exit hub to tip radius ratio are 0.375 and 0.478, respectively. The rotating part of the hub is defined between 1.374 and 0.335 *cm* upstream and downstream of the hub rotor leading and trailing edge, respectively. The tip clearance is uniform and equal to 0.1016 *cm*.

Figure 3.16: Front view of the NASA Rotor 67[53]

3.2.2.2 Previous research

The NASA Rotor 67 was designed and tested at Lewis Research Center. The measurements were taken by means of aerodynamic probes and laser anemometer distributed along different span locations as shown in Fig. 3.17. In particular, the aero-stations 1 and 2 were introduced to estimate the total conditions necessary to calculate the rotor global performance. They are located at 2.47 and 11.1 *cm*, upstream and downstream of the hub rotor leading edge, respectively.

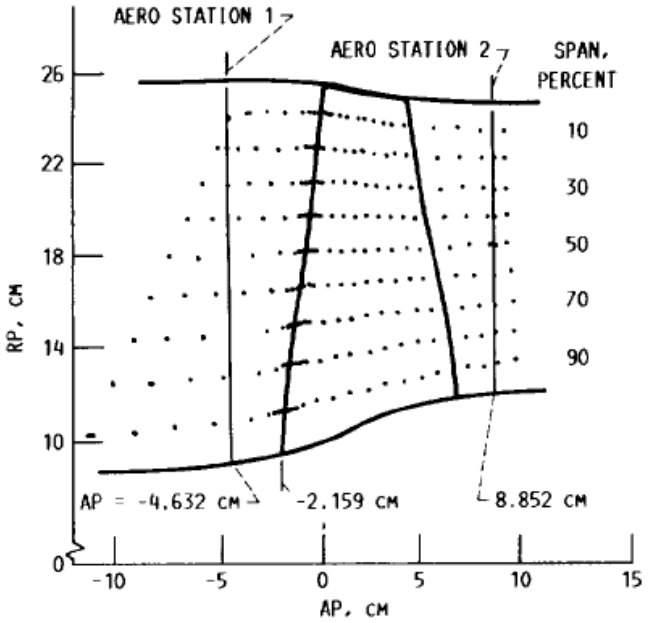

Figure 3.17: Meridional view of NASA Rotor 67 with aerodynamic survey locations[52]

The experiments were conducted at the rotor design rotational speed (N_d) equal to 16043 *RPM* at which the blade speed and inlet relative Mach number at the tip reach values of 429 ms^{-1} and 1.38, respectively. Figures 3.18(a) and 3.18(b) show the rotor pressure ratio (PR) and isentropic efficiency (η_{is})[†] versus the mass flow (W) along the design speedline. Here, two characteristic operating points, called near stall and near peak efficiency, were defined. The pressure ratio, isentropic efficiency and mass flow of the near stall point are equal to 1.722, 0.901 and 32.31 kgs^{-1}, respectively. Meanwhile, the same quantities for the near peak efficiency operating point are equal to 1.6, 0.932 and 33.25 kgs^{-1}, respectively.

[†]Since turbomachinery are essentially adiabatic, the ideal process is isentropic and, therefore, the efficiency is called isentropic efficiency[54]

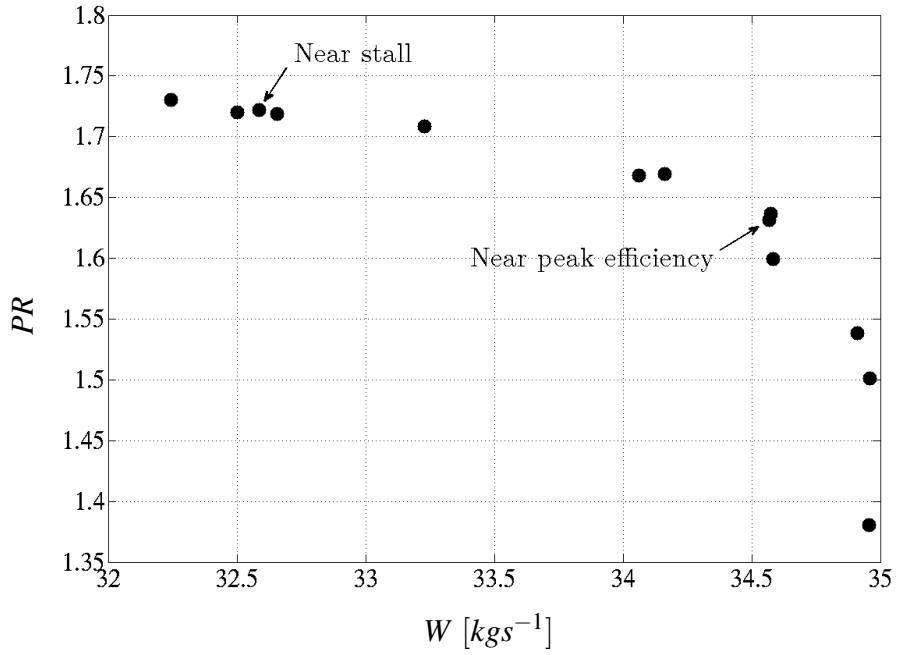

(a) Pressure ratio (PR)

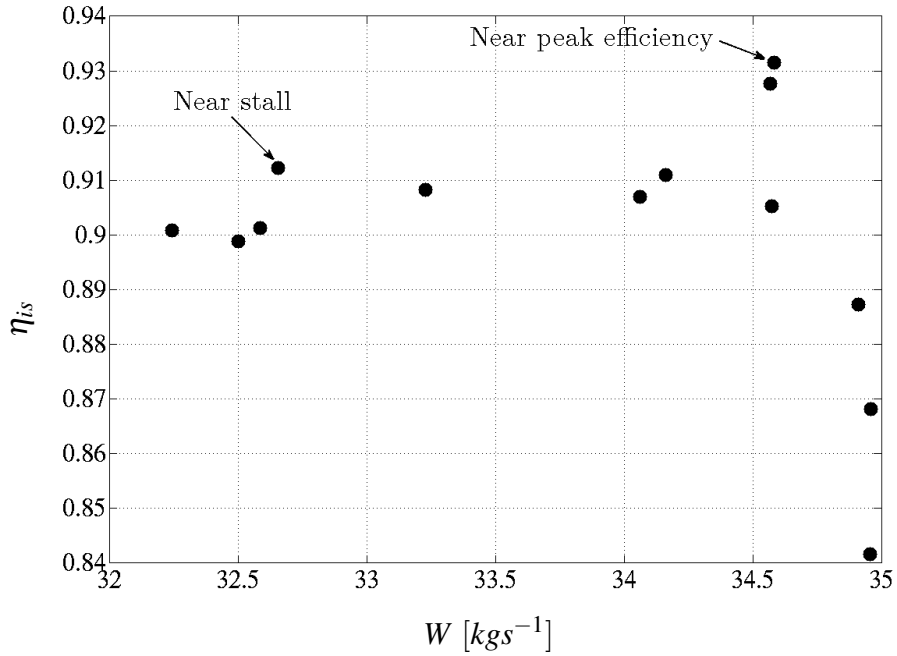

(b) Isentropic efficiency (η_{is})

Figure 3.18: Global performance versus mass flow (W) of the NASA Rotor 67 running at design rotational speed (N_d) with indication of near peak efficiency and near stall operating points of NASA experiments[52]

Due to the low aspect ratio, the flow field relative to the rotor changes from subsonic to transonic regime, moving from hub to tip. Therefore, a shock wave system occurs upstream of the rotor face for blade span locations where the transonic regime occurs. Its characteristics strongly depend on the throttle settings. From experiments, the progression from a near normal shock followed by a small passage shock at near peak efficiency to a single normal shock ahead of the rotor blade leading edge at near stall operating point was observed[55]. These characteristics are shown in Fig. 3.19(a) and 3.19(b) with the contours of relative Mach number (M_{rel}) at 90% of blade span for near stall and near peak efficiency operating poins, respectively, relative to NASA experiments[55].

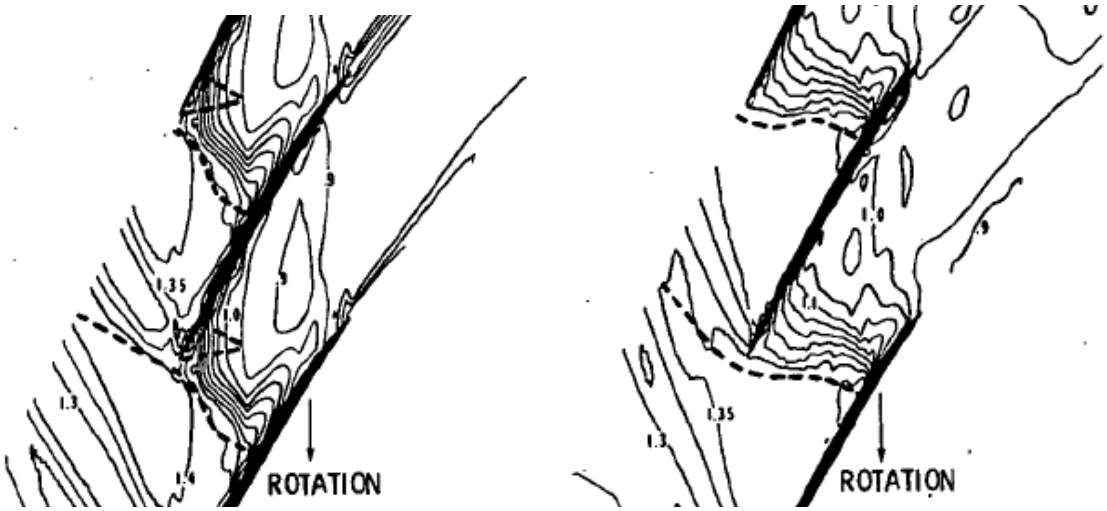

(a) Near stall (b) Near peak efficiency

Figure 3.19: Contours of relative Mach number (M_{rel}) obtained from NASA experiments at 90% of blade span[55]

Other relevant flow features of this rotor for the current work are the vortical flow generated by the tip clearance and the hub corner stall. The relative description and previous research are summarized below.

Tip clearance For a high-speed fan rotor operating near stall, the leakage vortex associated with the tip clearance interacts with the passage shock described above. As this vortex passes through the passage shock, its area increases creating a source of blockage associated with stall. Therefore, the point of stall inception moves to a higher flow rate with a reduction of the rotor flow range[56] (Fig. 3.20). On the other hand, away from stall the shock waves system consists of a series of oblique shock waves propagating within the blade passage without a notable distortion. Consequently, the tip vortex influence reduces.

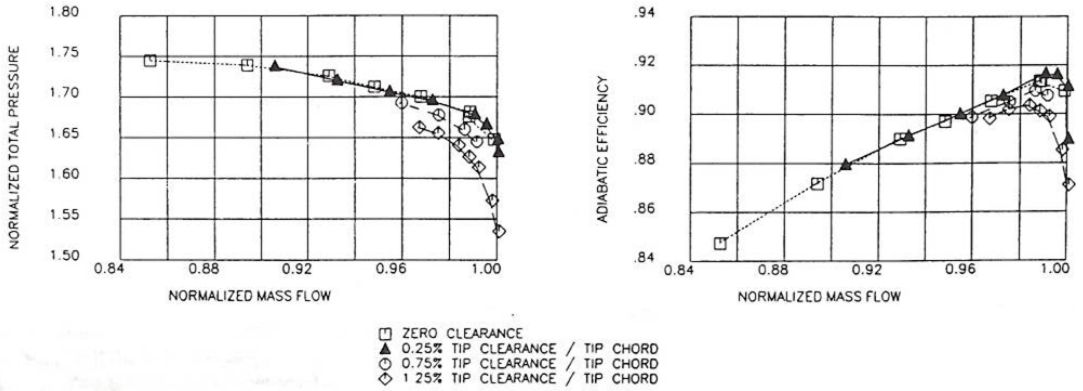

Figure 3.20: Rotor pressure ratio (left) and adiabatic efficiency (right) at design speed of NASA Rotor 67 for different tip clearances[56]

Hub corner stall Regardless of the throttle settings, Chima[57] observed a separation bubble located at the trailing edge and near the hub of the rotor blade suction surface. This separation was attributed to the high flow incidence occurring at the leading edge near the hub of the blade.Therefore, the blade results to be highly loaded. Nonetheless, the measurements at the hub were quite difficult and the presence of such phenomenon has only been captured by some researchers.

3.2.2.3 Description of the CFD model

The geometry data of the NASA Rotor 67 were already available in the public domain[52]. Thirty-five point coordinates were given for 14 blade span surfaces. These points were imported into ANSYS TURBOGRID mesh generator, where a single blade passage CFD domain was defined[‡] (Fig. 3.21). This represented the datum configuration of the NASA Rotor 67 used as a reference to investigate the effect of the S-duct on rotor performance in § 4. The whole CFD domain was divided by the mesh generator into three regions: inlet, outlet, and passage. Each region was in turn divided into several blocks strategically disposed to maximize the quality of a fully structured mesh created upon this. To obtain accurate CFD solutions, the inlet and outlet planes of the CFD domain were placed sufficiently distant with respect to the blades, where the work exchange occurs[58]. According to practical experience, these locations were defined at 35% and 95% of the tip diameter upstream and downstream of the hub rotor leading and trailing edge, respectively. Moreover, according to the geometry of the rotor (see § 3.2.2), the hub was split into three parts along the axial direction: two stationary, defined upstream and downstream of the rotor blades, and one rotating including the rotor blades themselves.

[‡]According to point coordinates provided for the blade, this could operate if rotating in anti-clockwise direction

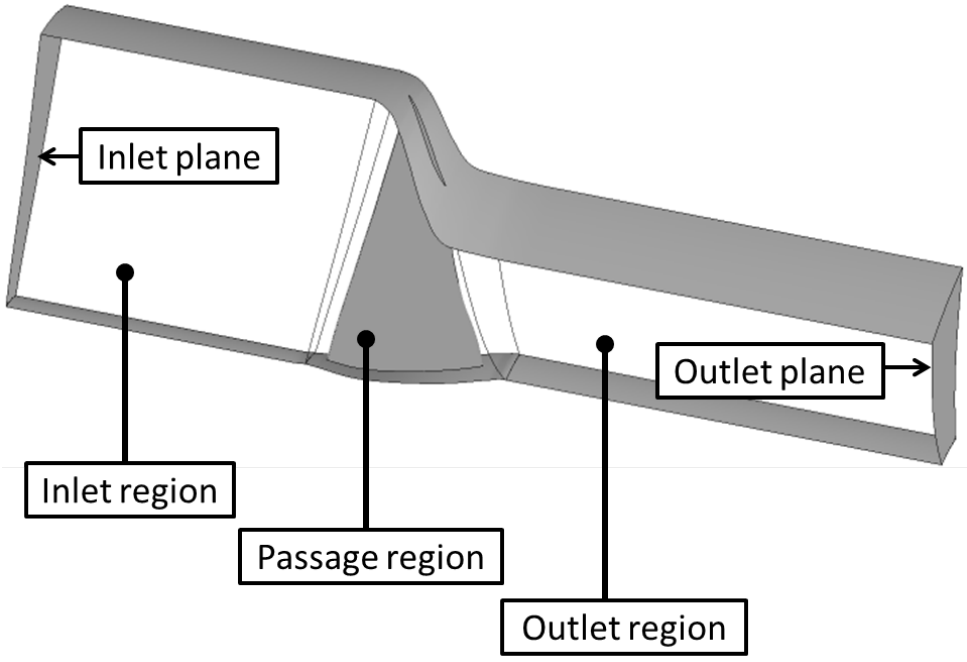

Figure 3.21: Visualization of CFD domain for single blade passage of NASA Rotor 67

This rotor represents also that relative to the coupled system configuration, presented in § 3.2.3, and defined to analyse the inlet flow distortion. However, due to its high complexity, the tip clearance of the rotor component was not modelled. Consequently, the near stall operating point obtained from the CFD calculations was an approximation, as discussed in § 3.2.2.2[56].

To guarantee a high mesh quality, a blocking strategy was adopted across the CFD domain. Referring to Fig. 3.22(a) and 3.22(b), a H-grid topology was defined for both inlet and outlet regions. An O-grid topology was defined around the blade. Finally, a J and a H-grid topology were defined around the leading and trailing edge, respectively. The mesh quality was improved by means of CFD simulations conducted iteratively with modifications on the mesh to satisfy the convergence criteria introduced in § 3.1.2 as well as to match the values of y^+ requested by the turbulence model chosen.

Then, to carry out a grid dependency study three fully structured meshes were created upon these grid topologies. Their resolution was defined by the number of elements specified along the main edges of the blocks indicated in Fig. 3.22(a) and 3.22(b). The number of elements defined along the main block edges as well as the total number of elements for each mesh are listed in Table 3.6.

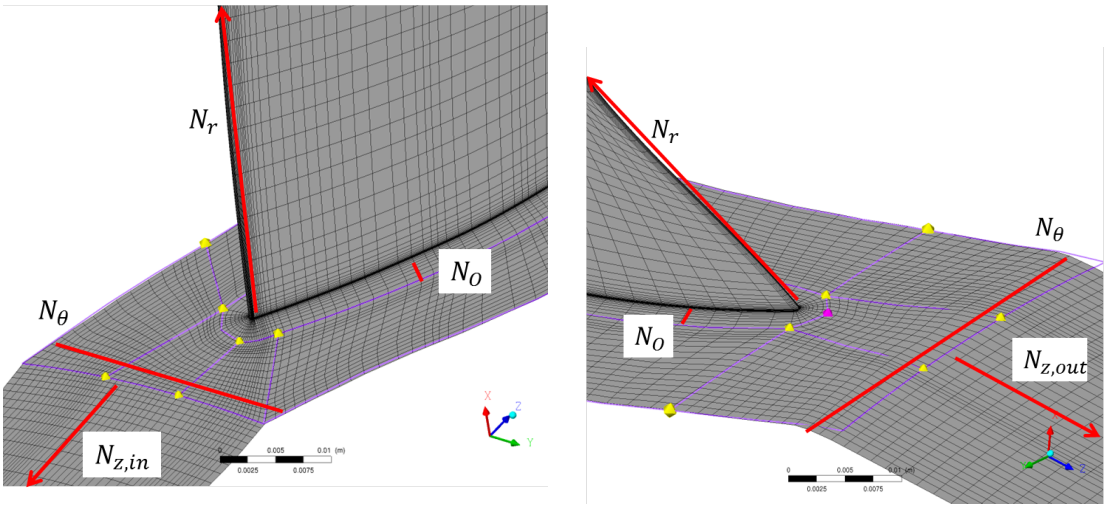

(a) Leading edge (b) Trailing edge

Figure 3.22: Main mesh features on the medium mesh of NASA Rotor 67

	Mesh		
Elements	Coarse	Medium	Fine
N_r	80	120	140
N_θ	41	47	54
N_0	12	17	18
$N_{z,in}$	25	30	30
$N_{z,out}$	37	1.053	1.515
$N_{tot}(\times 10^6)$	.708	1.053	1.515

Table 3.6: Details of meshes defined for the NASA Rotor 67

3.2.2.4 Grid dependency study

A grid dependency study was conducted on the CFD domain of NASA Rotor 67. Hence, the values of pressure ratio (PR) and isentropic efficiency (η_{is}) were extrapolated for the three meshes defined in the previous section at near stall and near peak efficiency operating points of the NASA Rotor 67. These values were based on the mass flow average of total pressure and total temperature calculated at the aero-stations 1 and 2 of the NASA Rotor 67, defined in § 3.2.2. Figures 3.24(a) and 3.24(b) show the trend of pressure ratio (PR) and isentropic efficiency (η_{is}) with the number of mesh elements defined in the previous section. As a result, the global performance changed within 0.5% and tended asymptotically towards constant values with a doubling of mesh resolution as shown in Fig. 3.25. Moreover, the grid dependency study was confirmed by the trend of the total temperature relative to the ambient conditions (T/T_{ref}) along the blade span location and at the aero-station 2 of the NASA Rotor 67 and for both near stall and near peak efficiency conditions, as shown in Fig. 3.23. Overall, as the mesh resolution increase to the medium mesh, the CFD solution could be retained independent. Hence, as a compromise between the computational time and accuracy of the CFD solution required, the medium mesh, made up of 1.053×10^6 elements, was selected to define the coupled system configuration (see § 3.2.3). Note also that, the mesh selected satisfied the grid resolution required upstream of the rotor face to capture accurately the shock wave system, which will be discussed in § 6.1.4.

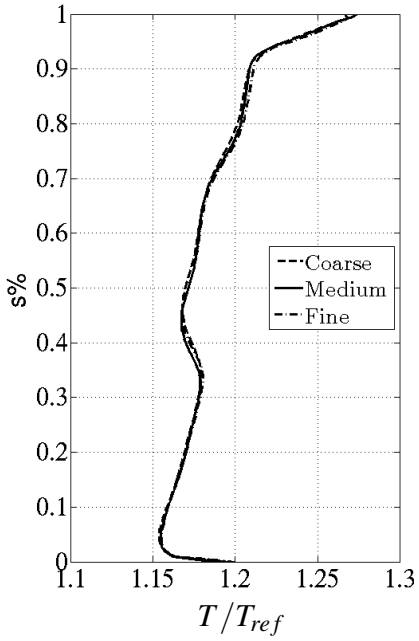

(a) Near stall

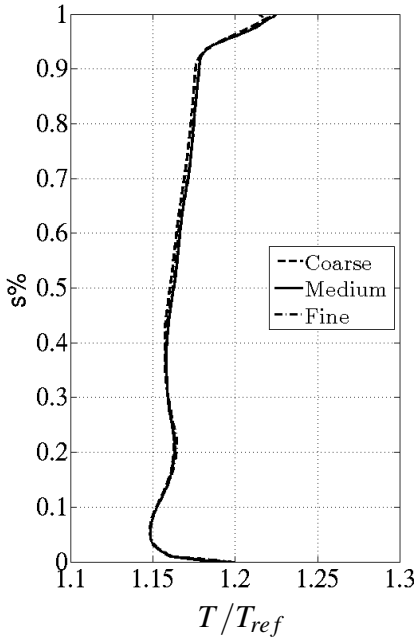

(b) Near peak efficiency

Figure 3.23: Normalized total temperature (T/T_{ref}) along the blade span (s) at the aerostation 2 and relative to the three meshes defined for the NASA Rotor 67

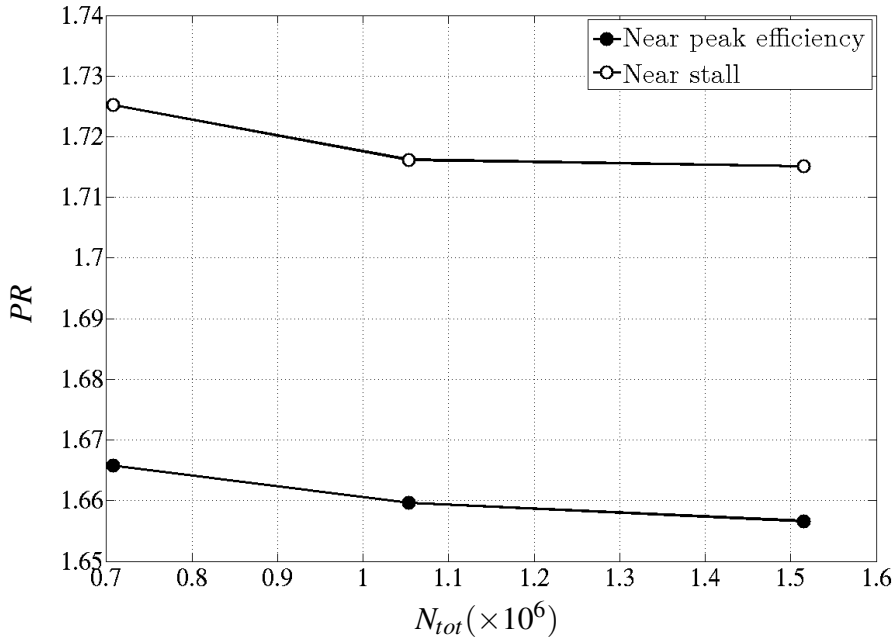

(a) Pressure ratio (*PR*)

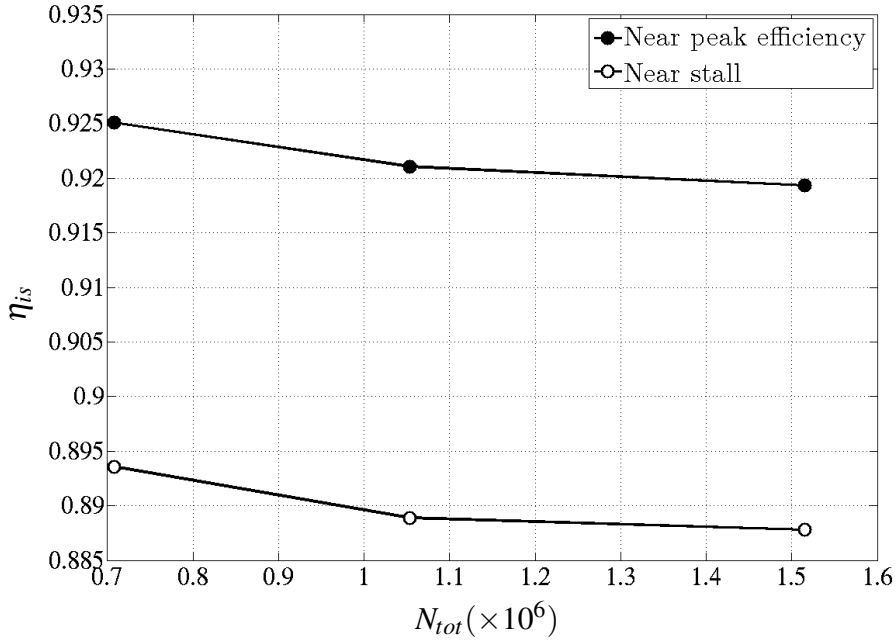

(b) Isentropic efficiency (η_{is})

Figure 3.24: Change of pressure ratio (*PR*) and isentropic efficiency (η_{is}) with the total number of elements (N_{tot}) of the meshes defined for the NASA Rotor 67

3.2.2.5 CFD validation

The validation of the CFD model defined for the NASA Rotor 67 was accomplished by considering the global performance relative to the design rotational speed (N_d). Referring to Fig. 3.21, the standard atmospheric values total pressure and total temperature (i.e. 101325 Pa and 288.15 K), were imposed uniformly at the CFD inlet plane. Meanwhile, a uniform static pressure was imposed at the CFD outlet plane. This was varied within the stability limits of the CFD solution to obtain the whole rotor speedline between near stall and near choking conditions. Hence, the rotor outlet static to inlet total pressure ($p_{out}/P_{0,in}$) varied between 1.25 and 0.967, respectively. Note, however, that the near stall operating point obtained is an approximation due to the limitations of CFD model used. More details regarding the flow field are provided near stall and near peak efficiency operating points, already presented in § 3.2.2.

Global performance Figure 3.25 shows the global performance of the rotor in terms of pressure ratio (PR) and isentropic efficiency (η_{is}) versus mass flow (W)[§] along the rotor design speedline relative to the current work, NASA experiments and previous CFD researchers carried out by Arima et al.[59], Adamczyk et al.[56] and Niazi[60] (Fig. 3.25). Overall, the values of pressure ratio (PR) calculated along the whole speedline are in agreement with the experimental data as well as with previous CFD results. In particular, at near stall and near peak efficiency this value change of 0.35 and -3.74% with respect to that of the experiments. On the other hand, the mass flow (W) reduces more and more with respect to that provided from the experiments as the operating point of the rotor moves towards choking conditions. As a result, the numerical mass flow is 0.98% lower than the experimental mass flow. This reduction confirms that a mass flow blockage occurs towards choking conditions. Essentially, this means that the CFD model calculate a boundary layer thickness higher than that obtained during the experiments. This difference can be associated to the total pressure loss attributed to the shock waves occurring upstream of the rotor leading edge. Also, the mass flow reached at near stall operating point is lower than that predicted by the experiments. As observed in previous research[56], this discrepancy is associated with the absence of the tip clearance in the current CFD model. Finally, regarding the isentropic efficiency (η_{is}) this was in agreement with respect to that of the experiments along the whole rotor speedline as shown in Fig. 3.25(b). Nevertheless, the value at the near peak efficiency operating point was not captured, although a smoother trend was obtained around that operating point. This discrepancy was also observed in previous research. So far, only Niazi[60] predicted most accurately the near peak efficiency operating point. This achievement, however, was obtained with a more accurate CFD model since unsteady calculations were performed.

[§]More correctly it was to consider as handle parameter the inlet corrected mass flow $W_{cor} = W \cdot \sqrt{T_{0,1}/T_{ref}}/(P_{0,1}/P_{ref})$. However, it was assumed that $W_{cor} = W$

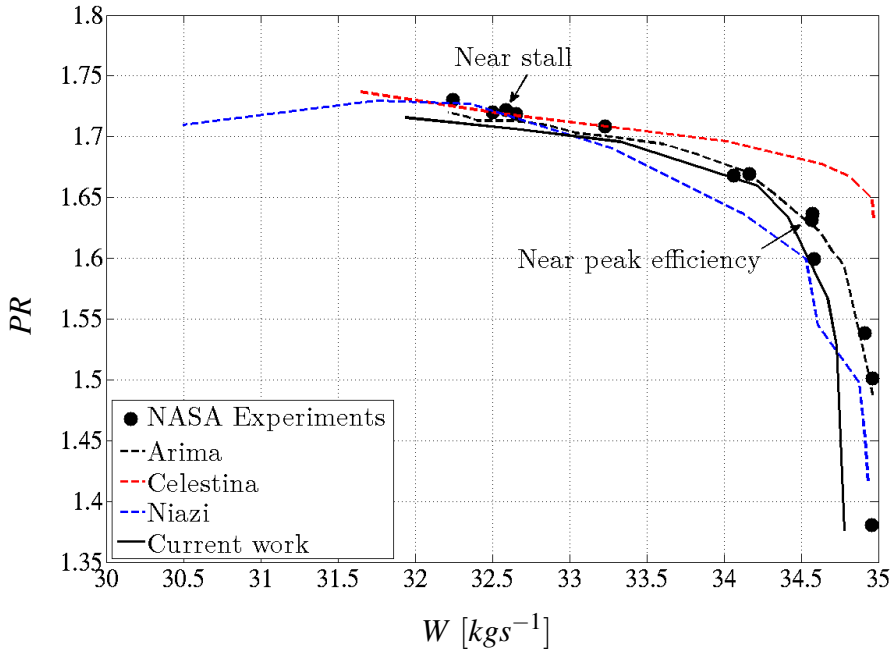

(a) Pressure ratio (PR)

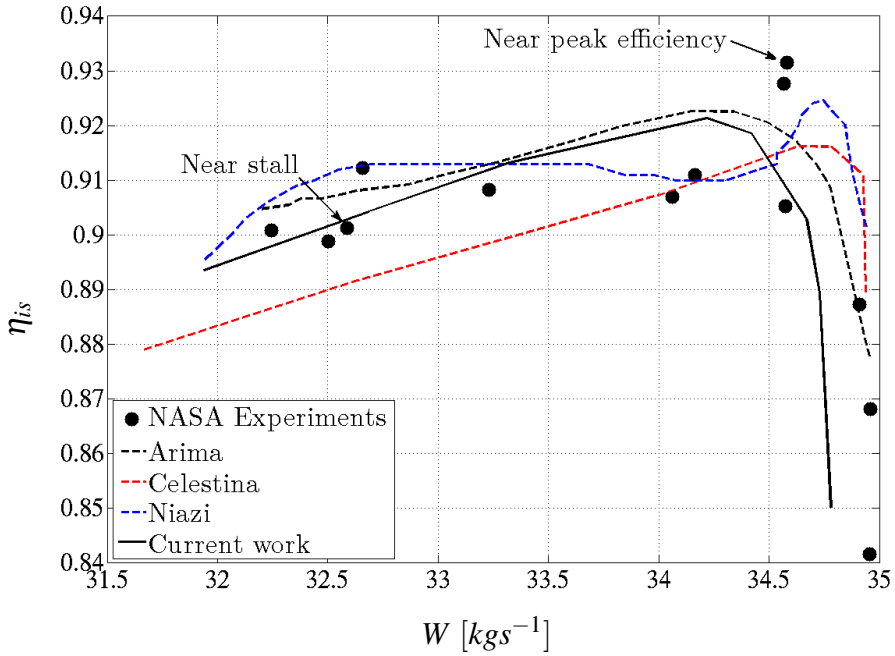

(b) Isentropic efficiency (η_{is})

Figure 3.25: Global performance versus mass flow (W) of the NASA Rotor 67 with indication of near peak efficiency and near stall operating points of NASA experiments[52] and previous and current CFD results of Arima et al.[59], Adamczyk et al.[56] and Niazi[60]

Blade-to-blade distributions The shock wave system occurring upstream of the rotor face was observed at near stall and near peak efficiency operating points and at 90% of blade span where the flow is in transonic regime (Fig. 3.26(a) and 3.26(b)). As a result, the shock wave structure is similar to that observed in experiments, presented in § 3.2.2.2. In particular, bow and passage shocks appear in a form of a lambda structure at near peak efficiency. On the other hand, a bow shock is attached to the leading edge of the blade at near stall operating point while the passage shock disappear.

(a) Near Stall (b) Near peak efficiency

Figure 3.26: Contours of relative Mach number (M_{rel}) at 90% of blade span

For both of the operating points the shock occurring at the leading edge takes place in the second half of the blade span and induces a separation on the suction surface as shown in Fig. 3.27(a) and 3.27(b). Note also that the hub corner stall was well predicted in the CFD results.

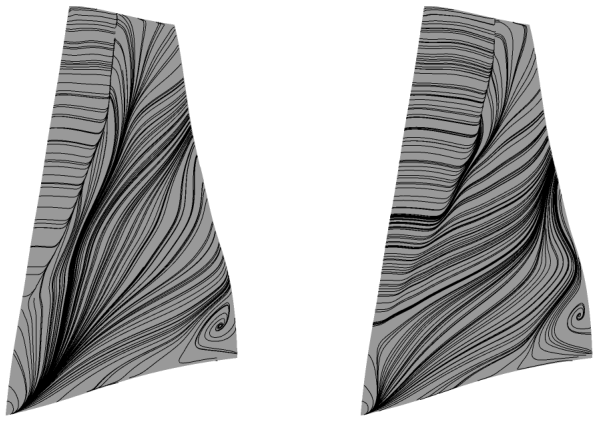

(a) Near stall (b) Near peak efficiency

Figure 3.27: Streaklines on the blade suction side for near stall and near peak efficiency of the NASA Rotor 67

3.2.3 Coupled system

The investigation of the effect that the flow distortion causes on a fan rotor performance was accomplished on a CFD model represented by a coupled system S-shaped intake/fan rotor shown in Fig. 3.28. This model was originally derived from the fine and medium meshes defined for the CFD models of RAE S-shaped intake 2129 and NASA Rotor 67, respectively (see § 3.2.1.3 and 3.2.2.3). Then, these CFD domains were subjected to several modifications[50] which are summarised below.

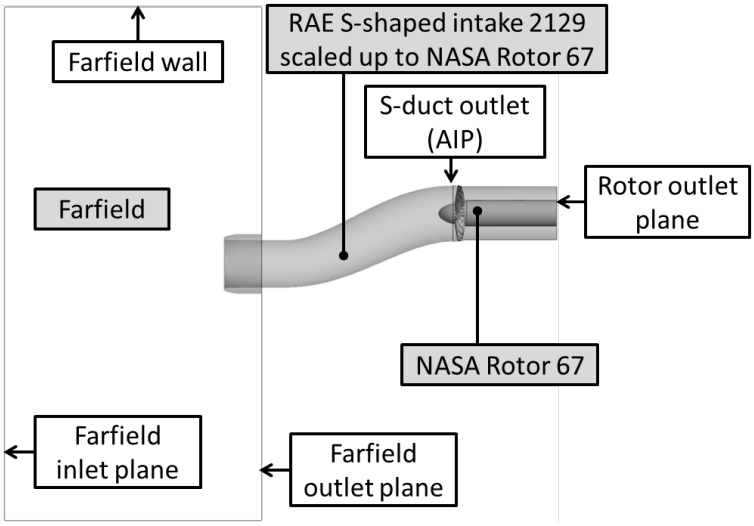

Figure 3.28: Top view of the CFD domain of the coupled system

Referring to Fig. 3.2 and 3.21, the outlet part of the intake was removed, while the inlet part of rotor was shortened up to $z/s = 0.107$ upstream of the hub rotor leading edge. Hence, the S-duct outlet plane was almost coincident with the rotor face where the AIP was located. As suggested by Menzies[43], the AIP was located as close as possible to the rotor face in order to have a very similar flow to that entering into the rotor itself. Also, the outlet part of the rotor was extended up to three tip diameters downstream of the rotor trailing edge. Since a certain level of distortion is expected out of the rotor of the coupled system, this modification allows the flow redistribution downstream of the rotor trailing edge, when a distorted pattern exists at the rotor face. Previous research indicated that the length scale of the inlet flow distortion is as large as the mean radius of the compressor system[61]. Finally, a scaling factor was applied to the intake wall ($SF_w = 3.37$) to match the intake outlet with the rotor tip inlet diameter. Meanwhile, another scaling factor was applied to the spinner ($SF_s = 4.54$) to match the rotor hub inlet diameter. Hence, the resulting CFD domain of the coupled system encompassed about 31 million elements.

Moreover, to allow the propagation of the CFD solution a type of numerical in-

terface between the two CFD subdomains had to be specified. For this model, it was expected that the numerical solutions at the interface were characterized by distorted flow localised within a radial and circumferential range where the flow separation occurs. For this purpose, amongst the different types of numerical interfaces provided by the CFD solver, that named as 'Frozen Rotor' was the most indicated for the current work[34].

Finally, to carry out numerical investigations on the internal S-duct aerodynamics of the coupled system, five cross flow planes were defined within a range of axial locations of the S-duct where the self-generated distortion was found to be strongly developed (Fig. 3.29).

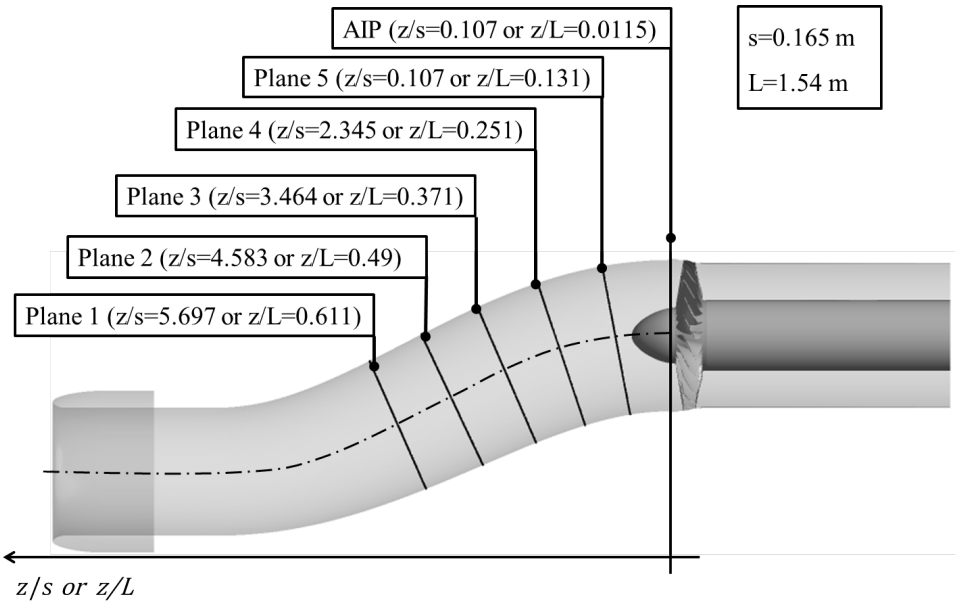

Figure 3.29: Visualization of cross flow planes defined along the S-shaped intake of the coupled system configuration

3.3 Flow analysis parameters for CFD models

In this section, the inlet flow descriptors as well as the non-dimensional groups used to analyse the flow field and the performance relative to the CFD solutions carried out throughout this research are presented. The flow descriptors encompass those relative to the total pressure and swirl distortion. On the other hand, the non-dimensional groups include expressions used to investigate the flow field as well as the performance relative to the coupled system and NASA Rotor 67, defined in § 3.2.3 and 3.2.2, respectively. These parameters were calculated from the CFD solutions obtained in this research and visualized with numerical tools created by means of Unix bash, CFX-post and Matlab.

3.3.1 Flow descriptors

To quantify both the total pressure and swirl distortion occurring at the AIP, several flow descriptors were considered in this work. For the total pressure distortion, the so called total pressure distortion parameter (DC_{60}) was selected as the descriptor [¶]. On the other hand, the swirl distortion was described by means of a unique parameter proposed in this research. This was named as the mass flow average of the magnitude of the relative flow angle (or relative rotor incidence) change ($\overline{|\Delta\beta|}$), expressed in Eq. 3.3. Therefore, it was defined as the absolute difference between the rotor incidences measured under clean and distorted conditions (β_{cl} and β_{dist}).

$$\overline{|\Delta\beta|} = \overline{|\beta_{cl} - \beta_{dist}|} \tag{3.3}$$

Note that the fact of considering the magnitude implied that the changes in rotor performance were supposed independent of the descriptor sign. This parameter is an indication of the change in rotor relative incidence angle at the AIP occurring between the clean and distorted inlet conditions. Note that even with an annular duct upstream configuration and rotor operating under clean inlet conditions, the swirl distortion at the AIP could not be neglected. This was due to the rotor disturbances occurring at the rotational speed investigated, which will be discussed in § 6.2. The inlet swirl distortion was also analyzed and quantified in terms of non-dimensional streamwise vorticity ($\omega_z^\star$), defined in § 3.3.5.

[¶]The CFD results relative to the coupled system, presented in § 4 and 5, considered the total pressure distortion parameter (DC_{60}) as the maximum amongst that computed by considering an angular resolution of 10^o

3.3.2 Non-dimensional standard deviations

Spatial standard deviations were initially introduced in this research to assess a methodology to determine the AIP for swirl distortion (see § 6). The same metrics were also used to investigate the internal S-duct aerodynamics relative to the coupled system operating with vortex ingestion (see § 5). Essentially, these metrics quantify the level of root mean square (RMS) on a j^{th} cross flow plane placed upstream of the rotor face. They were non-dimensionalized against a representative flow quantity evaluated at a position dependent of the CFD configuration analyzed. Conventionally, this location corresponded to the CFD and and intake inlet plane defined for the datum NASA Rotor 67 (see § 3.2.2) and the coupled system configuration (see § 3.2.3), respectively.

Non-dimensional standard deviation of static pressure This parameter represents, by means of a unique number, the spatial fluctuations of static pressure with respect to its area-averaged value ($\widetilde{p}$) evaluated on a j^{th} crossflow plane, of the area A_j, (p'). This is non-dimensionalized against the total pressure imposed at the CFD inlet plane ($P_{0,in}$) as given in Eq. 3.4.

$$\left(p'_j\right)^* = \frac{p'_j}{P_{0,in}} \tag{3.4}$$

where

$$p'_j = \sqrt{\frac{\int_{A_j}(p-\widetilde{p}_j)^2 dA_j}{A_j}} \tag{3.5}$$

Non-dimensional standard deviation of tangential velocity component This parameter represents, by means of a unique number, the spatial fluctuation of the tangential velocity with respect to its mass flow averaged value ($\overline{V}_\theta$) evaluated on a crossflow plane (V'_θ). This is non-dimensionalized against the mass flow averaged axial velocity calculated at the CFD inlet plane ($\overline{V}_{z,in}$) as given in Eq. 3.6.

$$\left(V'_{\theta,j}\right)^* = \frac{V'_{\theta,j}}{\overline{V}_{z,in}} \tag{3.6}$$

where

$$V'_{\theta,j} = \sqrt{\frac{\int_{W_j}(V_\theta - \overline{V}_{\theta,j})^2 dW_j}{W_j}} \tag{3.7}$$

3.3.3 Rotor normalized mass flow

The rotor normalized mass flow (W^*) is defined at constant rotational speed as the mass flow change between a generic operating point (W) and that relative to near stall conditions (W_{NS}), with respect to the mass flow range at the rotational speed considered ($W_{NC} - W_{NS}$) as given in Eq. 3.8.

$$W^* = \frac{W - W_{NS}}{W_{NC} - W_{NS}} \tag{3.8}$$

This parameter was introduced to analyse the effect of throttle setting on the flow distortion. This value ranges between zero and the unit at which correspond the near stall (NS) and near choking (NC) operating conditions, respectively.

3.3.4 Skin friction coefficient

The skin friction coefficient (C_f) is defined as the shear stress (τ) relative to the mass flow average of the dynamic head calculated at the intake inlet plane of the coupled system (Eq. 3.9).

$$C_f = \frac{\tau}{\frac{1}{2}\overline{\rho}\overline{V}_{in}^2} \tag{3.9}$$

This parameter was introduced to visualize the flow separation normally occurring in the S-shaped intake of the coupled system (see § 3.2.3).

3.3.5 Non-dimensional streamwise vorticity

This streamwise vorticity (ω_z) was introduced to describe the flow field at the AIP location of the coupled system as part of swirl distortion analysis. Moreover, to allow comparisons between results obtained at different operating conditions this parameter was non-dimensionalized (ω_z) by considering the rotor inlet tip diameter (D_t) and the mass flow average of the streamwise velocity at the AIP[‖] ($\overline{V}_{z,AIP}$) as given in Eq. 3.10.

$$\omega_z^* = \frac{\omega_z \cdot D_t}{\overline{V}_{z,AIP}} \tag{3.10}$$

[‖]Note that, at the AIP the streamwise corresponds to the axial direction (z)

3.3.6 Relative axial velocity change

The relative axial velocity change ($\Delta V_z\%$) was defined as the axial velocity change between clean and distorted conditions at the AIP relatively to the axial velocity calculated under clean inlet conditions as given in Eq. 3.11.

$$\Delta V_z\% = \frac{V_{z,dist} - V_{z,cl}}{V_{z,cl}} \tag{3.11}$$

This parameter was introduced to investigate the effect that the S-duct determines on the rotor performance for the coupled system configuration operating under clean inlet conditions (see § 4.2.4 and 4.3.4).

3.3.7 Non-dimensional total pressure

The non-dimensional total pressure (P_0^*) was defined as the total pressure at the AIP relatively to that imposed at the inlet of the farfield inlet plane of the coupled system configuration ($P_{0,in}$). This parameter was introduced to identify the extent and location of the total pressure deficit at the AIP of the coupled system (see § 4 and 5).

3.3.8 Pressure recovery

The pressure recovery (η) is expressed as the ratio between the mass flow average of the total pressure calculated at the AIP ($\overline{P}_{0,AIP}$) and that at upstream infinity ($\overline{P}_{0,\infty}$).

$$\eta = \frac{\overline{P}_{0,AIP}}{\overline{P}_{0,\infty}} \tag{3.12}$$

This is a measure of the efficiency of the intake and represents a significant design parameter since the total pressure loss into an intake can be related to the loss in engine thrust. Clearly, a value of pressure recovery as close to unity as possible is desirable and would indicate an efficient intake with a low distortion across the compressor face and, hence, low susceptibility to engine surge[62].

3.3.9 Change of rotor performance

In this research, the changes of rotor performance were quantified by considering the rotor pressure ratio (PR) speedlines as well as the loss of stability pressure ratio (ΔPRS). The latter was that proposed by the ARP 1420[11] defined at constant rotational speed. In this condition, this was defined as the the difference between the stability pressure ratios defined with the rotor operating under clean and distorted inlet conditions, (PRS_{cl} and PRS_{dist}), relatively to that calculated under clean conditions as given in Eq. 3.13.

$$\Delta PRS = \frac{PRS_{cl} - PRS_{dist}}{PRS_{cl}} \tag{3.13}$$

Figure 3.30 shows a sketch of the rotor pressure ratio (PR) versus corrected mass flow (W_{cor}). Here, the rotor speedlines as well as the near stall operating points relative to clean and distorted inlet conditions are indicated.

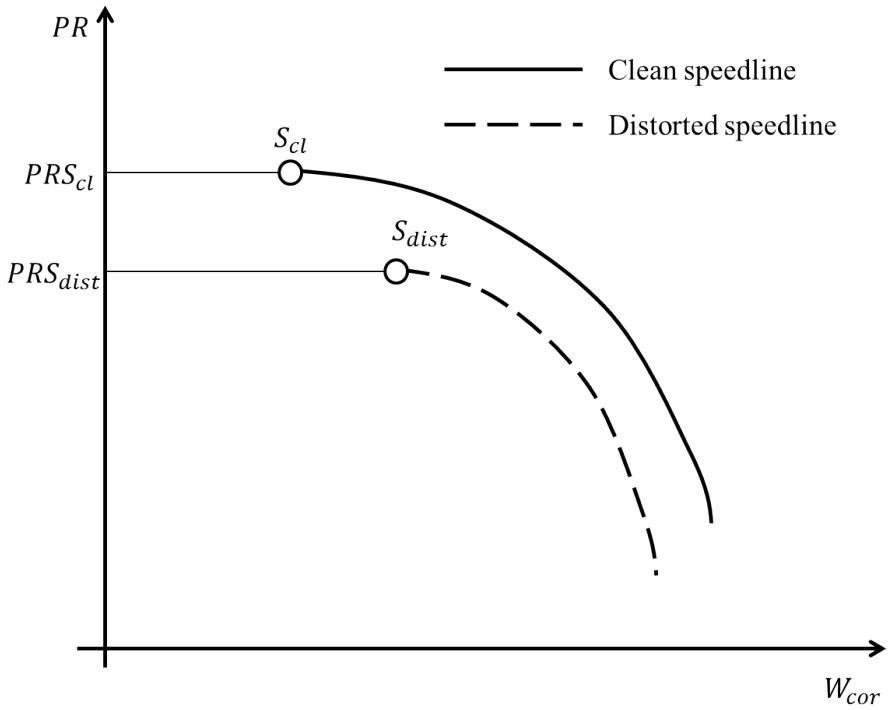

Figure 3.30: Visualization of the parameters necessary to define the loss of stability pressure ratio (ΔPRS) following the constant rotational speed approach introduced by ARP 1420[11]

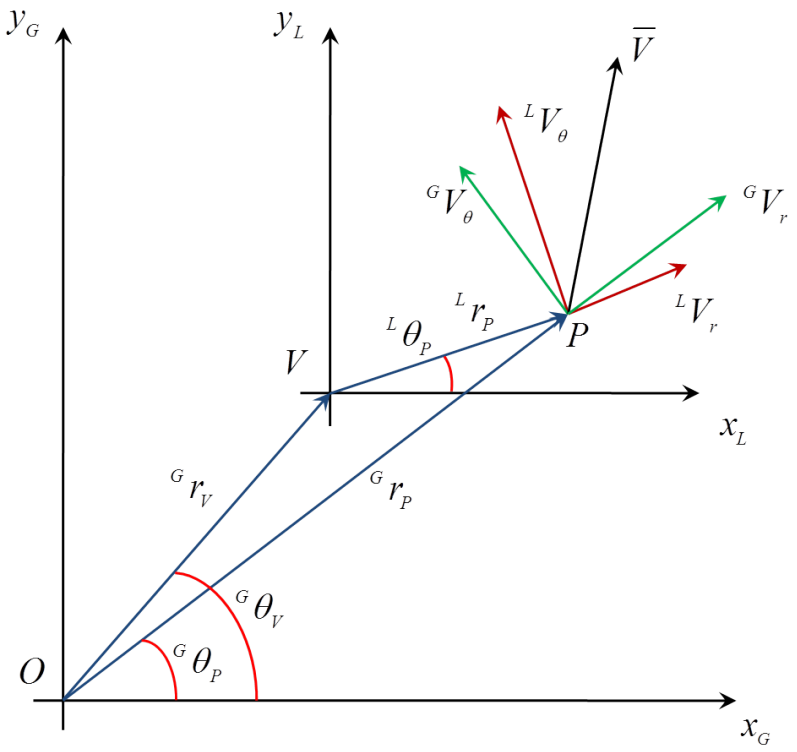

Figure 3.31: Velocity vectors on the local and global coordinates system

3.4 Boundary conditions for a tightly-wound vortex

In this section, the procedure followed to prescribe a tightly-wound vortex at the inlet of the CFD domain is described in detail. Also, the characteristics of a datum vortex used as reference for this research are calculated.

3.4.1 Implementation into generalised coordinates

The vortex perturbation field relative to the Vatistas vortex model was defined with respect to a local cylindrical coordinates system $\{L\} = \{x_L, y_L\}$ placed at the vortex centre (Fig. 3.31) as explained in §B.1. However, to facilitate the vortex prescription as boundary conditions at different locations of the CFD inlet plane, the velocities were expressed with respect to a global coordinate system $\{G\} = \{x_G, y_G\}$. This was accomplished by mapping out the local velocity components onto the global coordinate system. In cylindrical coordinates, and with respect to the global reference system, the position of the generic point (P) and the vortex centre (V) are identified by the ternes $({}^{G}r_P, {}^{G}\theta_P)$ and $({}^{G}r_v, {}^{G}\theta_v)$, respectively (Fig. 3.31).

The coordinate of the generic point P with respect to the local reference system $\{L\}$ ($^{L}r_P$,$^{L}\theta_P$) can be expressed as a function of the coordinates relative to the same point and the vortex centre (V) in the global coordinate system as given in Eqns. 3.14 and 3.15.

$$^{L}r_P = \sqrt{^{G}(r_P)^2 + ^{G}(r_P)^2 - 2\,^{G}r_P\,^{G}r_V \cos(^{G}\theta_P - ^{G}\theta_P)} \tag{3.14}$$

$$^{L}\theta_P = \arctan\left(\frac{^{G}r_P \sin ^{G}\theta_P - ^{G}r_V \sin ^{G}\theta_V}{^{G}r_P \cos ^{G}\theta_P - ^{G}r_V \cos ^{G}\theta_V}\right) \tag{3.15}$$

The tangential and radial velocity components in the global reference system, ($^{G}V_\theta$ and $^{G}V_r$), can be defined as given in Eqns. 3.16 and 3.17.

$$^{G}V_\theta = ^{L}V_\theta \cos(^{G}\theta_P - ^{L}\theta_P) - ^{L}V_r \sin(^{G}\theta_P - ^{L}\theta_P) \tag{3.16}$$

$$^{G}V_r = ^{L}V_\theta \sin(^{G}\theta_P - ^{L}\theta_P) + ^{L}V_r \cos(^{G}\theta_P - ^{L}\theta_P) \tag{3.17}$$

Where the local tangential and radial velocities ($^{L}V_\theta$ and $^{L}V_r$) are computed by replacing r with $^{L}r_P$ in Eqs. B.1 and B.2, respectively. Using basic trigonometry, the previous expressions can be re-written as given in Eqs. 3.18 and 3.19.

$$\begin{aligned} ^{G}V_\theta = {} & ^{L}V_\theta(\sin ^{G}\theta_P \cdot \sin ^{L}\theta_P + \cos ^{G}\theta_P \cdot \cos ^{L}\theta_P) \\ & -^{L}V_r(\sin ^{G}\theta_P \cdot \sin ^{L}\theta_P + \cos ^{G}\theta_P \cdot \cos ^{L}\theta_P) \end{aligned} \tag{3.18}$$

$$\begin{aligned} ^{G}V_r = {} & ^{L}V_\theta(\sin ^{G}\theta_P \cdot \cos ^{L}\theta_P - \cos ^{G}\theta_P \cdot \sin ^{L}\theta_P) \\ & -^{L}V_r(\sin ^{G}\theta_P \cdot \sin ^{L}\theta_P + \cos ^{G}\theta_P \cdot \cos ^{L}\theta_P) \end{aligned} \tag{3.19}$$

In particular, the local radial velocity component ($^{L}V_r$) was neglected. This assumption was also considered by Bhagwat et al.[63] for tip vortices, similar to that applied for the current research.

Since the local and global coordinate systems presented above are both defined in a common plane, the axial velocity component written in the global coordinate system ($^{G}V_z$) does not require any transformation and, therefore, is implemented into the CFD code as given in Eq. 3.20.

$$^{G}V_z = V_\infty - \frac{A}{z}\left[1 - \frac{(^{L}r_P)^2}{(r_c^{2n} + (^{L}r_P)^{2n})^{\frac{1}{n}}}\right] \tag{3.20}$$

The velocity components calculated in Eqs. 3.18, 3.19 and 3.20 enabled the definition of the flow direction components given in Eqs. 3.21, 3.22 and 3.23.

$$fd({}^{G}V_{\theta}) = {}^{G}V_{\theta}/\sqrt{{}^{G}V_{\theta}^2 + {}^{G}V_{r}^2 + {}^{G}V_{z}^2} \tag{3.21}$$

$$fd({}^{G}V_{r}) = {}^{G}V_{r}/\sqrt{{}^{G}V_{\theta}^2 + {}^{G}V_{r}^2 + {}^{G}V_{z}^2} \tag{3.22}$$

$$fd({}^{G}V_{z}) = {}^{G}V_{z}/\sqrt{{}^{G}V_{\theta}^2 + {}^{G}V_{r}^2 + {}^{G}V_{z}^2} \tag{3.23}$$

As already discussed for the axial velocity, the static pressure distribution (p) does also not require any transformation. For the ground vortex case ($n = 1$), this is given in Eq. 3.24.

$$p = p_{\infty} - \frac{\rho}{2}\left[\frac{\Gamma}{2\pi r_c}\right]^2\left[\frac{r_c^2}{r_c^2 + ({}^{L}r_P)^2}\right] \tag{3.24}$$

According to Bernoulli, the distribution of total pressure (P_0) was then calculated as given in Eq. 3.25.

$$P_0 = p + \frac{1}{2}\rho\left({}^{G}V_{\theta}^2 + {}^{G}V_{r}^2 + {}^{G}V_{z}^2\right) \tag{3.25}$$

Finally, the distributions of total pressure and velocity direction (Eqs. 3.21, 3.22, 3.23, and 3.25) were necessary to be specified into the CFD code, in order to obtain a converged solution.

3.4.2 Prediction of vortex characteristics

In this section, the characteristics necessary to define analytically the datum vortex considered in this research are calculated. They are the core radius (r_c), circulation (Γ) and axial velocity distribution relative to the vortex itself. Generally, their numerical values depend on the intake geometrical parameters, operating conditions of the engine and external ambient conditions.

3.4.2.1 Vortex core radius

Murphy[23] conducted experimental research on ground vortex aerodynamics. He observed that the vortex core radius (r_c) at the intake inlet plane was about 6% of the intake inlet diameter (D_{in}). This value was assumed for the datum vortex considered for this work.

3.4.2.2 Vortex circulation

As discussed in § B.2.2, the circulation (Γ) relative to a ground vortex occurring in headwind conditions for a fixed ground clearance (h/D_l), is a function of the velocity ratio (U^*) and reaches a maximum (Γ_{max}) at U^*_{max}. In the current work, the ground clearance was fixed at $h/D_l = 0.25$, while the velocity ratio corresponded to U^*_{max}. According to Eq. B.8, this is function of the critical velocity ratio ($U^\star_{crit}$). In turn, this terms requires the specification of the mass flow (W). This was assumed constant at 28 kgs^{-1}, which is representative of the coupled system operability. Also, since the crosswind condition ($\psi = 90^o$) was considered, the vortex circulation (Γ) calculated for headwind conditions (Eq. B.11 and B.7) and then the correction factor to account for the effect of the yaw angle (Eq. B.15) was applied. In these conditions, the maximum value of vortex circulation was $\Gamma^*_{max} = 25.8\ m^2s^{-1}$ to which corresponds a velocity ratio of about $U^*_{max} = 5.5$ (Fig. 3.32).

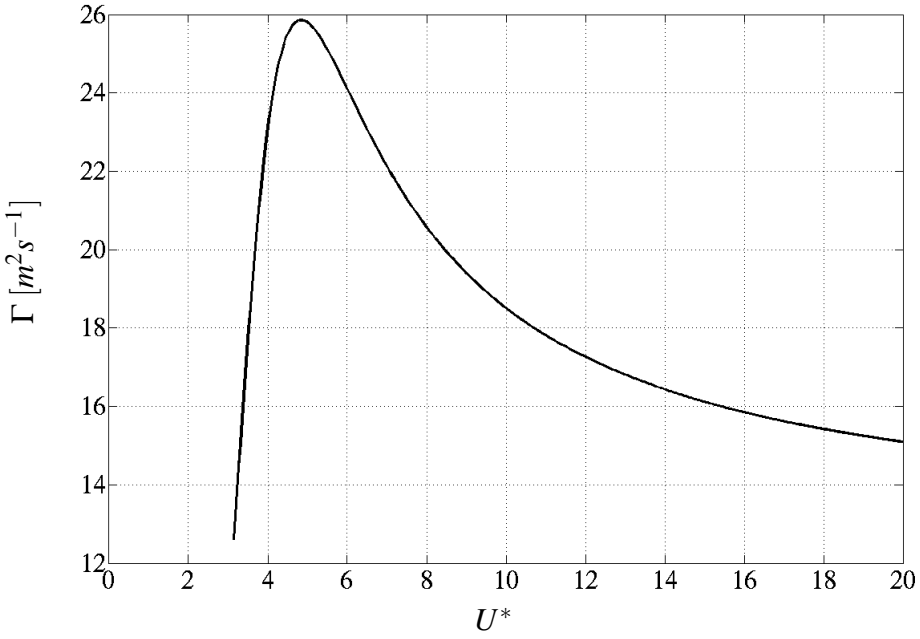

Figure 3.32: Vortex circulation (Γ) versus velocity ratio (U^*) for $h/D_l = 0.25$, $W = 28$ kgs^{-1} and $\psi = 90^o$

3.4.2.3 Axial velocity distribution

According to Eq. 3.20, the definition of the axial velocity distribution in the global coordinate system (${}^GV_z$) requires the knowledge of the constant A and the axial position z. However, these parameters are not separately known for the ground vortex case. Instead,

the present research makes use of the ratio A/z, which represents the maximum axial velocity excess measured at the vortex centre. By assuming valid flow similarity at different scales, this ratio was obtained by introducing a new parameter named as axial velocity excess ratio ($\Delta V^{*}_{z,ex}$). This is function of the maximum axial velocity measured at the vortex centre ($V_{z,max}$) and the mass flow averaged axial velocity ($\overline{V}_z$) as given in Eq. 3.26.

$$\Delta V^{\star}_{z,ex} = \frac{V_{z,max} - \overline{V}_z}{\overline{V}_z} = \frac{A/z}{\overline{V}_z} \tag{3.26}$$

This parameter was determined from previous ground vortex CFD results[64] for three velocity ratio U^*, $h/D_l = 0.25$ and in pure crosswind conditions ($\psi = 90^o$). Then, a polynomial curve fitting those points was calculated as shown in Fig. 3.33. Following the prediction of vortex circulation presented in the previous paragraph, the velocity ratio attributed with the maximum vortex circulation was $U^*_{max} = 5.5$. Therefore, following the fitting curve in Fig. 3.33, the axial velocity excess ratio was $\Delta V^{*}_{z,ex} = 0.5$.

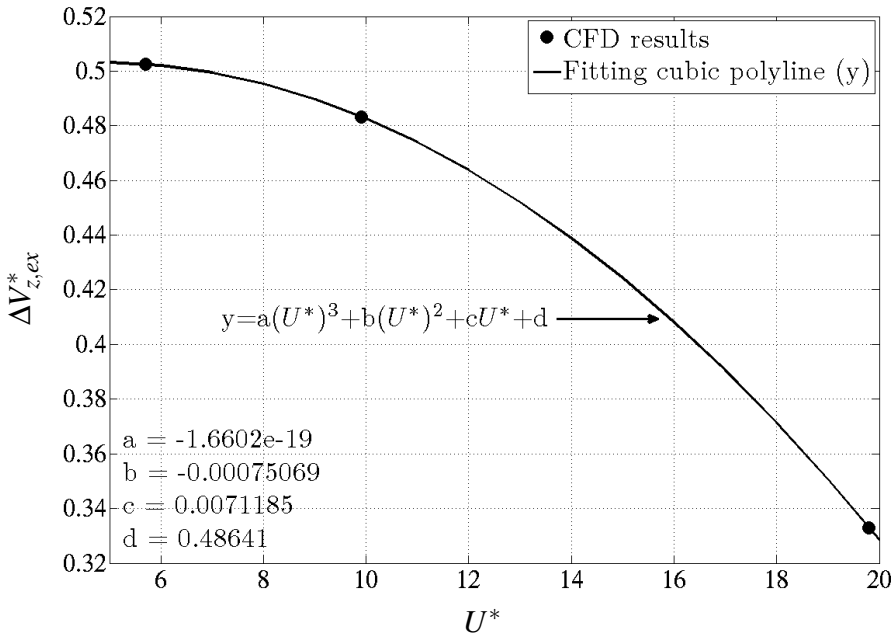

Figure 3.33: Axial velocity excess ratio ($\Delta V^{*}_{z,ex}$) versus velocity ratio (U^*) based on previous CFD results[64] for $h/D_l = 0.25$ and $\psi = 90^0$

Finally, the vortex characteristics relative to the datum vortex are summarised in Table 3.7.

Vortex feature	value
Γ	$25.8\ m^2 s^{-1}$
r_c	$6\% \cdot D_{in}$
n	1
$\Delta V^*_{z,ex}$	0.5

Table 3.7: Characteristics of the datum vortex

3.4.3 Visualization of the vortex boundary conditions

The CFD simulations conducted with a vortex prescribed at the CFD inlet plane required the definition of a global coordinate system introduced in § 3.4.1. Conventionally, this was centered on the rotor axis, having the positive direction towards the rotor outlet. Figures 3.34(a) - 3.34(d) show the distributions of tangential, radial and axial velocity components ($^GV_\theta$, ^GV_r and ^GV_z), and total pressure (P_0), respectively, with respect to the global coordinate system, relative to a co-rotating datum vortex to the centre of the intake inlet plane and imposed at the farfield inlet plane of the coupled system (see § 3.2.3). The imposition of such boundary conditions generated a vortical flow propagating through the fan rotor as shown in Fig. 3.35. In addition, a sensitivity analysis regarding the effect of the aforementioned vortex boundary conditions components on the compressor performance was carried out within the frame of this research[65].

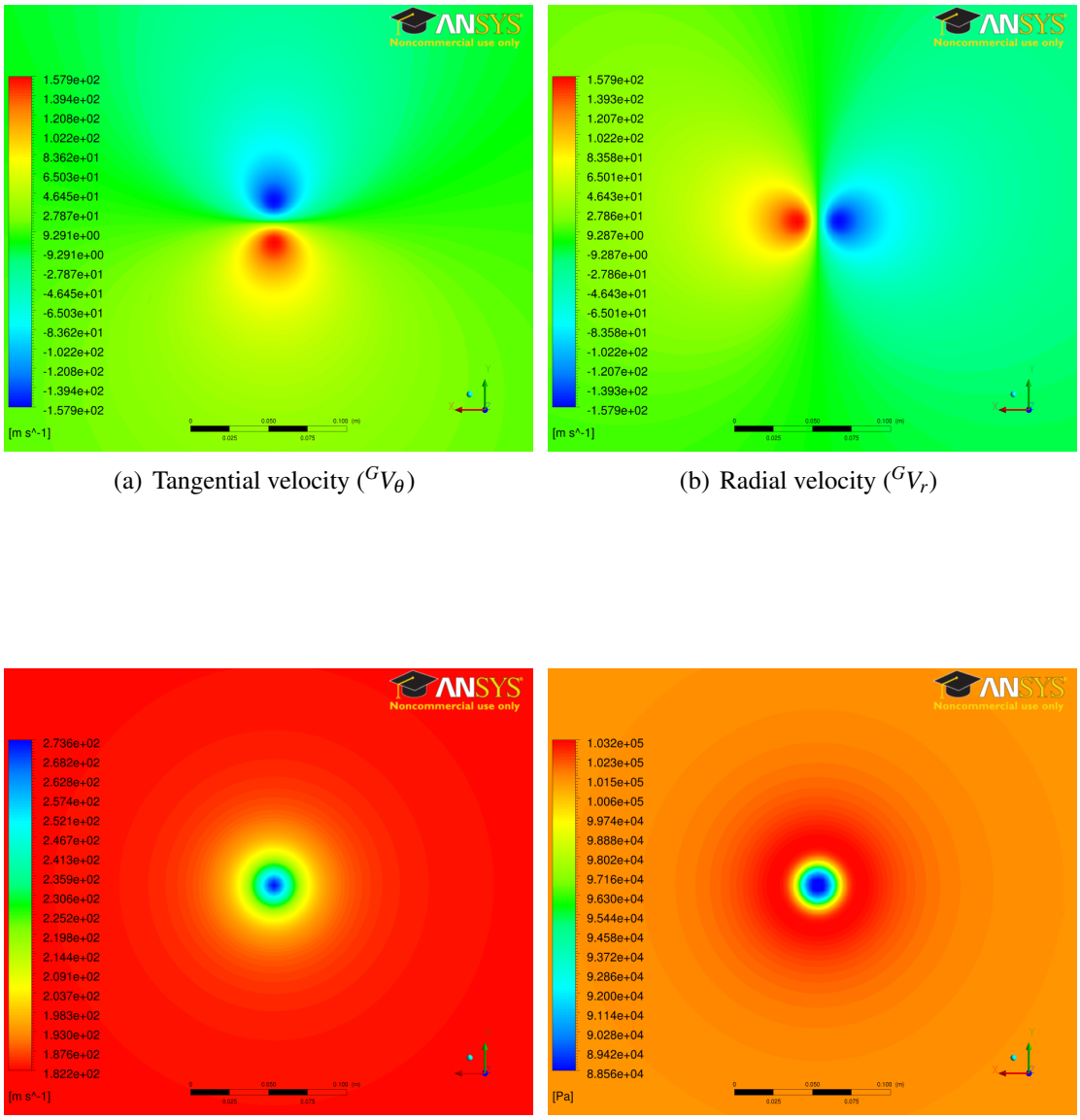

(a) Tangential velocity (${}^{G}V_{\theta}$)

(b) Radial velocity (${}^{G}V_{r}$)

(c) Axial velocity (${}^{G}V_{z}$)

(d) Total pressure (P_0)

Figure 3.34: Contours of boundary conditions components expressed with respect to the global coordinate system and relative to the co-rotating datum vortex prescribed at the farfield inlet plane of the coupled system and aligned with the centre of the intake inlet plane

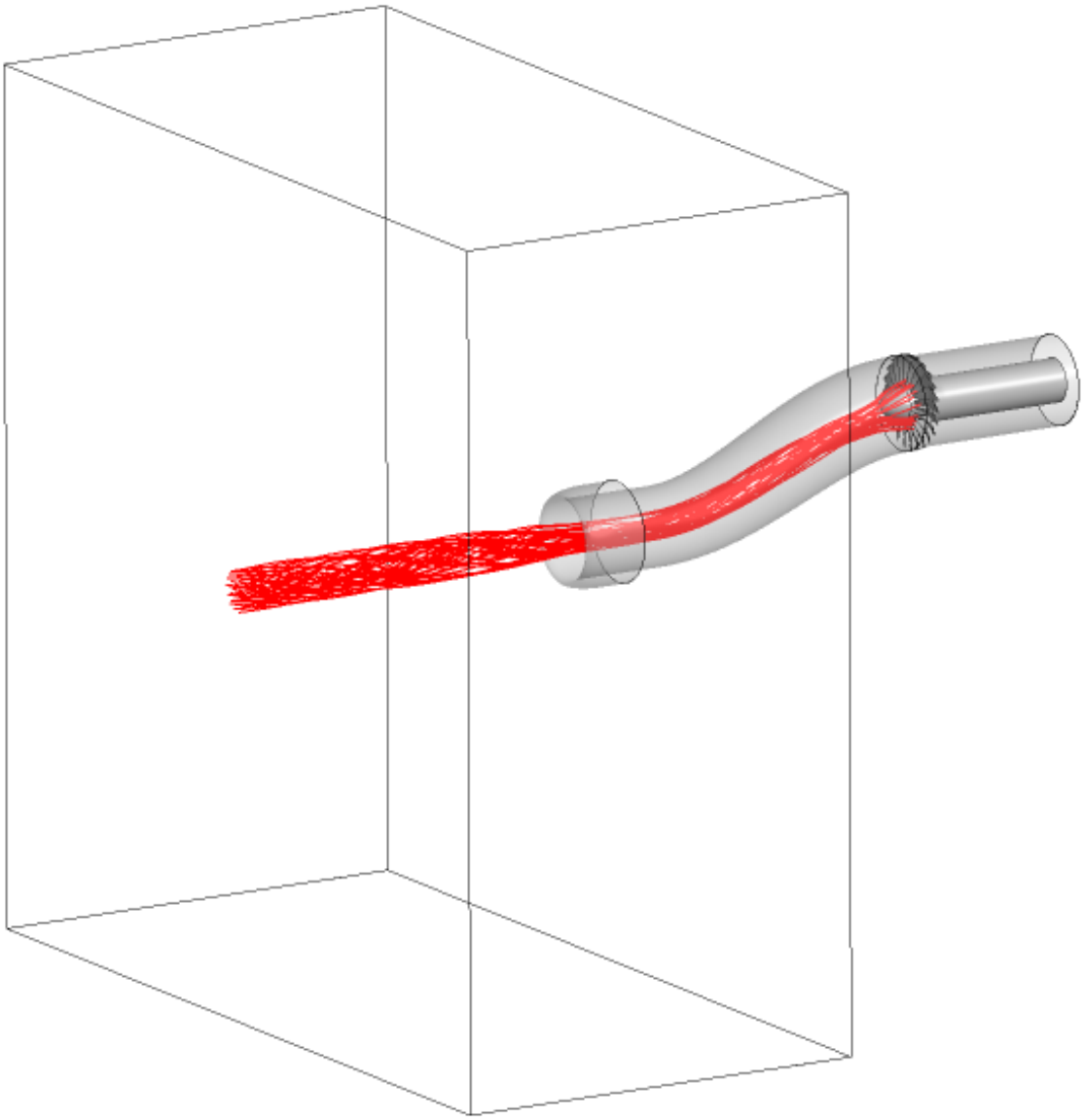

Figure 3.35: Visualization of a co-rotating datum vortex ingested on the coupled system and aligned to the centre of the intake inlet plane

3.5 Summary

In this chapter, the computational models, the parameters used to post-process the results and the boundary conditions implemented into the CFD code to replicate a tightly-wound vortex have been presented. The key messages relative to this chapter are summarized below.

- The computational methods applied to the CFD code, i.e. type of simulation, convergence criteria, advection scheme, turbulence modelling have been specified and described in detail. In particular, the $k-\omega$ SST was selected as turbulence model. Nowadays, this is the most indicated for S-duct flows characterized by adverse pressure gradients.
- The geometries selected from the public domain, including the RAE S-shaped intake 2129 and the NASA Rotor 67, and the previous research relative to these geometries most relevant for the current work have been reported. CFD models relative to these geometries have been defined and validated against experimental data. The validation of the CFD domain relative to the RAE S-shaped intake 2129 was successfull. In particular, the CFD results of the current work predicted the S-duct flow separation better than previous numerical research carried out by Menzies[43]. On the other hand, the validation of the NASA Rotor 67 was in good agreement with the experimental data and previous numerical results.
- A purely numerical coupled system S-shaped intake/fan rotor configuration, based on the two aforementioned geometries, was defined and proposed in this research to accomplish a sensitivity analysis relative to the effect of inlet flow distortion on rotor performance (see § 4 and 5)
- The parameters necessary to conduct the numerical investigation of the flow field of the coupled system as well as to describe the flow distortion at the AIP of it have been introduced. In particular, new descriptors relative to the swirl distortion were proposed in this research.
- Finally, the boundary conditions for a tightly wound vortex procedure to implement as well as the prediction of characteristics relative to a datum vortex considered in this research have been specified.

Chapter 4

Coupled system analysis: clean inlet conditions

Several aircraft for both military and commercial purposes adopt complex shaped ducts to deliver the far-field flow to the compressor face. The S-shaped intakes are an example. As discussed in § 2.2.3, under clean inlet conditions they self-generate total pressure combined with swirl distortion on the flow field because of the curvature and the diffusion of the duct itself. As a result, the engine performance changes accordingly. The purpose of this chapter is to investigate the combined effect of the inlet total pressure and swirl distortion attributed to an S-duct on the rotor performance. This was accomplished by analyzing CFD solutions obtained on a purely numerical coupled system S-shaped intake/fan rotor configuration defined in this research (see § 3.2.3). In total, fourteen CFD solutions were carried out, each requiring about three days of calculations by using the Cranfield University cluster called ASTRAL[66].

This chapter is divided in four sections. Firstly, an analysis of the Reynolds number effect on the RAE S-shaped intake 2129 scaled up to the size of NASA Rotor 67 is presented. This was a step necessary to ascertain the validity of the CFD model relative to the coupled system. The second section presents investigations of CFD solutions relative to the whole coupled system operating under clean inlet conditions and with the rotor running at its original design rotational speed (N_d). These investigations encompass the analysis of the S-duct aerodynamics, the description of the flow field at the AIP and the effect of the S-duct upstream configuration on rotor performance. Similar analyses are reported in the third section with the rotor operating at 80% N_d. Finally, the fourth section reports a comparison between the results of the coupled system relative to the two rotational speed investigated.

4.1 The effect of Reynolds number

As discussed in § 3.2.3, the CFD model of the coupled system introduced in this work was originated from that defined for the RAE S-shaped intake 2129 and the NASA Rotor 67 (see § 3.2.1 and 3.2.2). Both of these models were validated against experimental data available in the literature. On the other hand, the coupled system was a purely numerical model. This required the physical matching of the S-duct intake outlet diameter of the RAE S-shaped intake 2129 (D_{out}) with the rotor tip inlet diameter of the NASA Rotor 67 (D_t). Therefore, it was necessary to scale the intake part up to a scaling factor (SF_w) of 3.37* (see § 3.2.3). Following this geometrical modification, the flow field of the S-duct could not be validated against any experimental data. Hence, the validity of this CFD model was ascertained by investigating the numerical solution of several CFD intake models. These were obtained by applying on the original intake different scaling factors up to that required for the coupling, mentioned above. The boundary conditions were similar to that defined for AGARD HMF test case (see § 3.2.1.1). As a consequence of the scaling, the Reynolds number calculated at the intake inlet plane increased from 1.6 to 5.4×10^6, while the mass flow increased from 2.95 to 33.7 kgs^{-1}, which was relatively close to the mass flow range obtained in this work for the coupled system configuration.

Clearly, the non-dimensional wall distance (y^+) increased with the scale of the intake. For the full scale intake, this value was close to unit on the whole intake wall as shown in Fig. 4.1. This result satisfied the wall treatment condition required by the turbulence model $k-\omega$ SST. Also, note that the highest values of y^+ were achieved around the lip and first bend of the S-duct where the flow acceleration was the highest.

The most important outcome of this analysis was concerning the investigation of the intake performance as well as the flow distortion calculated at the S-duct outlet plane. As discussed in § 3.2.3, this location corresponded to the AIP of the coupled system configuration, where the swirl distortion will be calculated. Referring to Fig. 4.2, the normalised values of pressure recovery (η^*), area average of the swirl intensity ($\overline{SI}^*$) (see § A) and total pressure distortion parameter (DC^*_{60}) were calculated at the AIP. The normalization was carried out by considering the same parameter calculated at the original scale of the intake ($SF_w = 1$). As the Reynolds number increased, the thickness of the boundary layer relative to the scale of the system decreased. Consequently, the flow distortion at the AIP decreased since it was related to this parameter. Therefore, a slight improvement of the intake performance was obtained, where the pressure recovery (η^*) increased from 0.964 to 0.966. Meanwhile, the total pressure and swirl distortion parameters decreased by 4% as indicated in Fig. 4.2. Note also that the trends of these reductions were consistent with that expected for the boundary layer thickness relative to the size of the system.

*Note that to simplify the analysis the spinner of the original intake was scaled up consistently with the intake wall

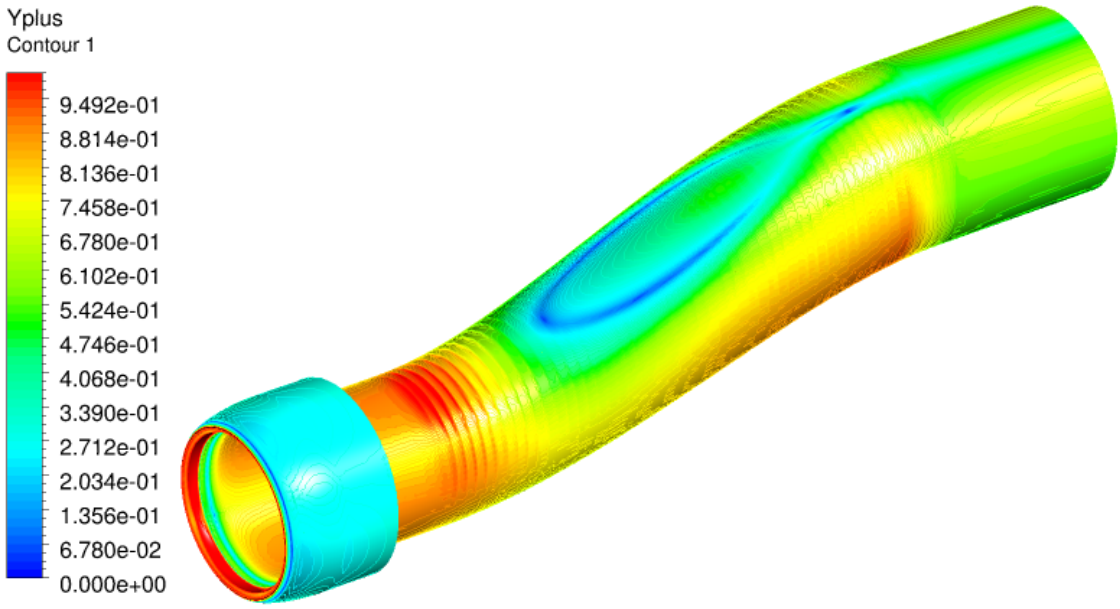

Figure 4.1: Contours of non-dimensional wall distance (y^+) on the RAE S-shaped intake 2129 scaled up to the tip inlet diameter of NASA Rotor 67 ($SF_w = 3.367$)

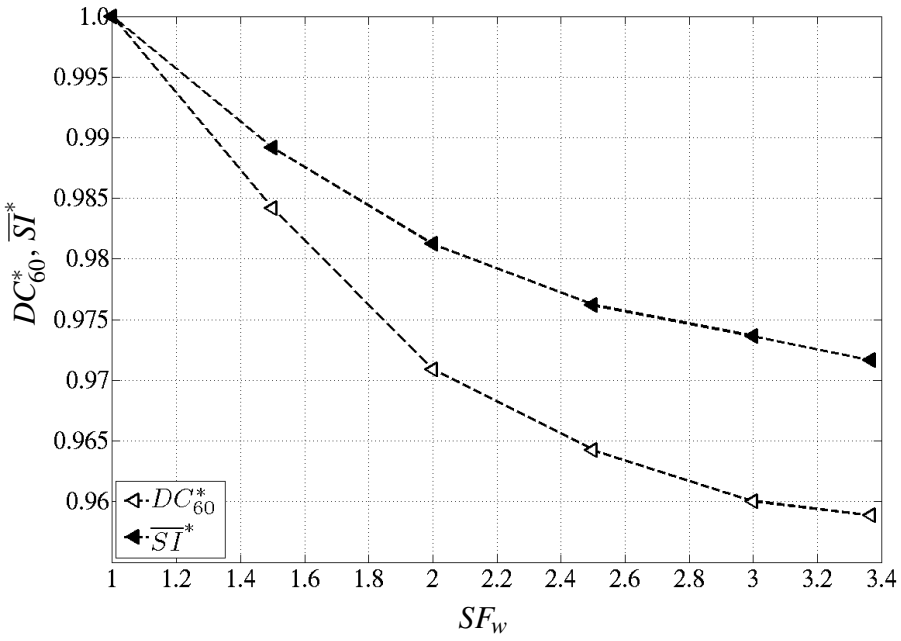

Figure 4.2: Normalised flow distortion descriptors versus the scaling factor of the S-duct wall (SF_w)

4.2 Design rotational speed analysis

In this section, the numerical investigations carried out on the coupled system operating under clean inlet conditions and with the rotor running at its original design rotational speed (N_d) are discussed. Firstly, the boundary conditions specified around the CFD domain of the coupled system are presented. Then, numerical investigations carried out on this system are discussed in detail. These include the analysis of S-duct aerodynamics, the description of the flow field at the AIP, in terms of both total pressure and swirl distortion, and the effect that the S-duct causes on the rotor performance.

4.2.1 Definition of the CFD boundary conditions

Referring to Fig. 3.28, the following boundary conditions were applied on the CFD domain of the coupled system.

The total pressure and total temperature imposed at the CFD inlet plane to validate the datum NASA Rotor 67 configuration (see § 3.2.2.5), were also specified uniformly at the farfield inlet plane. These correspond to that of the standard atmospheric conditions ($P_{0,in} = 101325\ Pa$ and $T_{0,in} = 288.15\ K$). In this manner, the effect on the rotor performance attributed the S-duct configuration placed upstream of the rotor itself was quantifiable.

A uniform static pressure field was imposed at the computational rotor outlet plane. This parameter was gradually changed to obtain the whole rotor speedline between near stall and near choking operating conditions. These two points corresponded to the conditions where any further increase or decrease of static pressure caused instabilities in the solution, resulting in a divergence of the CFD solution. Hence, the rotor outlet static to inlet total pressure ($p_{out}/P_{0,in}$) ranged between 1.017 and 0.957 from near stall to near choking, respectively. Note, however, that the near stall operating point obtained from the calculations of this research was an approximation since steady-state calculations were performed for this analysis. This approximation was also adopted for all the case studies investigated in this research.

A uniform static pressure field was imposed at the farfield outlet plane to match a free stream Mach number (M_∞) of 0.21 already considered in AGARD test cases of the RAE S-shaped intake 2129 (see § 3.2.1.5). For all the case studies relative to the coupled system, this value was kept the same. In this manner, the flow regime in the farfield was similar occurring for the ingestion of a ground vortex. This is the type of vortex considered in the current research, which is normally ingested at low free stream (or flight) Mach number, when the aircraft is landing or taking-off[23].

4.2.2 S-shaped intake aerodynamics

In this section, the results relative to the intake performance, the S-duct flow separation and the internal S-duct aerodynamics of the coupled system with the rotor operating at design rotational speed (N_d) between near stall and near choking conditions, are presented.

4.2.2.1 Intake performance

The intake performance was quantified by means of the pressure recovery (η), defined in § 3.3.8. As the throttle settings changed from near stall to near choking this value increased from 0.979 to 0.976. As discussed for the validation study of the original intake (see § 3.2.1.5), this change was attributed to the change in mass flow, which will be analyzed in § 4.2.4.

4.2.2.2 Description of the S-duct flow separation

The S-duct flow separation relative to the self-generated distortion was investigated by means of the skin friction coefficient (C_f) with the streaklines on the starboard side of the intake wall with the rotor operating near stall and near choking conditions and 100% N_d as shown in Fig. 4.3(a) and 4.3(b), respectively. Regardless of the operating conditions, the skin friction coefficient (C_f) reached the highest values at the first bend of the duct due to the high flow acceleration occurring in that zone, already observed for the validation of the intake at original scale (see § 3.2.1.5). Then, the S-duct flow separation occurs for a relatively width axial range. This remained essentially symmetric within the rotor operability range as expected for an isolated intake (see § 2.2.2). Consequently, the characteristics of the duct separation along the axial direction could be estimated by considering the trend of the skin friction coefficient (C_f) along the starboard edge ($\phi = 0^o$) as shown in Fig. 4.3(c) for near stall and near choking conditions. By moving towards the AIP, the skin friction coefficient (C_f) exhibited two minimum values. The first and second value corresponded to the onset of separation and point of reattachment, located at 0.7 and $0.2 \cdot z/L$ upstream of the rotor face, respectively. Clearly, their relative distance corresponds to the axial extent of separation. As a result, no significant change of the duct separation characteristics were registered within the rotor operability range. This result is also in agreement with that of the pressure recovery (η) which remained essentially unchanged (see § 4.2.2.1).

4.2.2.3 Internal duct aerodynamics

The S-duct aerodynamics were investigated by considering the flow topology on crossflow planes distributed throughout the S-duct itself indicated in Fig. 3.29. These planes were

located where the S-duct flow separation was well developed. In this manner, the whole separation could be also monitored in the transversal direction. As discussed in § 4.2.2.1 and 4.2.2.2, the S-duct flow field remained unchanged with the rotor operability range. Therefore, the internal S-duct aerodynamics was investigated only for a mean value of the rotor outlet static to inlet total pressure ($p_{out}/P_{0,in}$) of 0.987 as shown in Fig. 4.4.

As a result, between Plane 1 and Plane 4 (Fig. 4.4(a) – 4.4(d)) the separation developed symmetrically as expected also for an isolated intake (see § 2.2.2). At the Plane 5 (Fig. 4.4(e)), placed downstream of the reattachment point (see Fig. 4.3(c), the streamlines tend to deviate from the center of the plane because of the presence of the spinner placed immediately downstream. Moreover, the two counter-rotating vortices normally occurring in the separation region are no longer symmetric, as expected for an isolated intake (see § 2.2.2). Finally, at the AIP (Fig. 4.4(f)), the flow topology changes up to a configuration where only the counter-rotating vortex exists. A similar trend could be obtained by superimposing a centered uniform bulk swirl to the flow field at the duct outlet expected for an isolated intake. Therefore, it was thought that the rotor introduced a centered bulk swirl in the flow field of the S-duct. Also, at the same plane and at the opposite circumferential direction of the flow separation the direction of the 2D streamlines was irregular. This phenomena was attributed to the transonic disturbances propagating upstream of the rotor face itself.

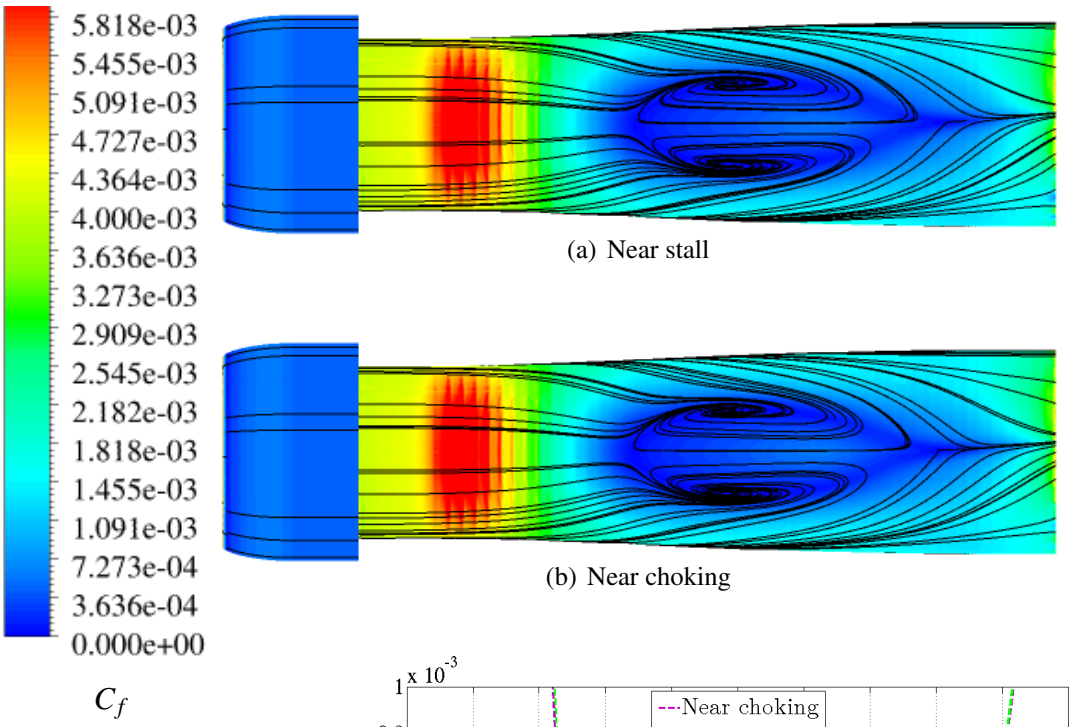

(a) Near stall

(b) Near choking

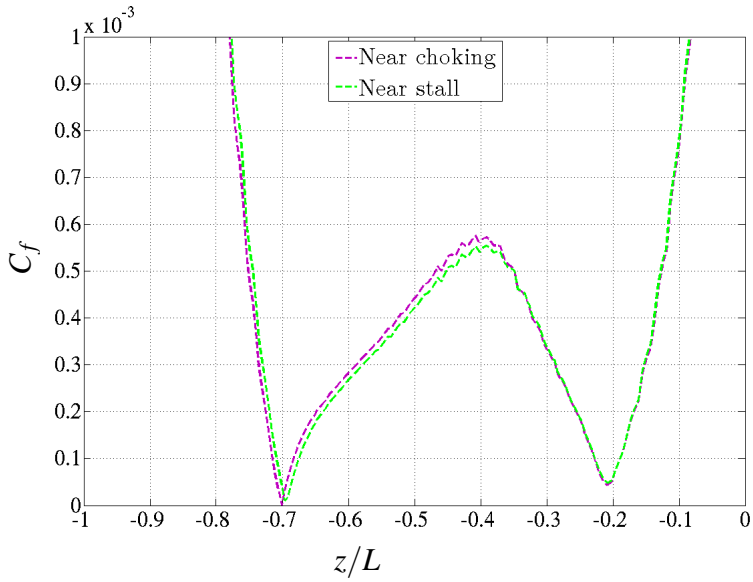

(c) Skin friction coefficient (C_f) versus the axial position (z/L) measured along the starboard edge ($\phi = 0^o$)

Figure 4.3: Contours of skin friction coefficient (C_f) with streaklines (black) at the starboard side of the intake wall with rotor operating at 100% N_d (a) near stall and (b) near choking and (c) the relative distribution along the starboard edge ($\phi = 0^o$)

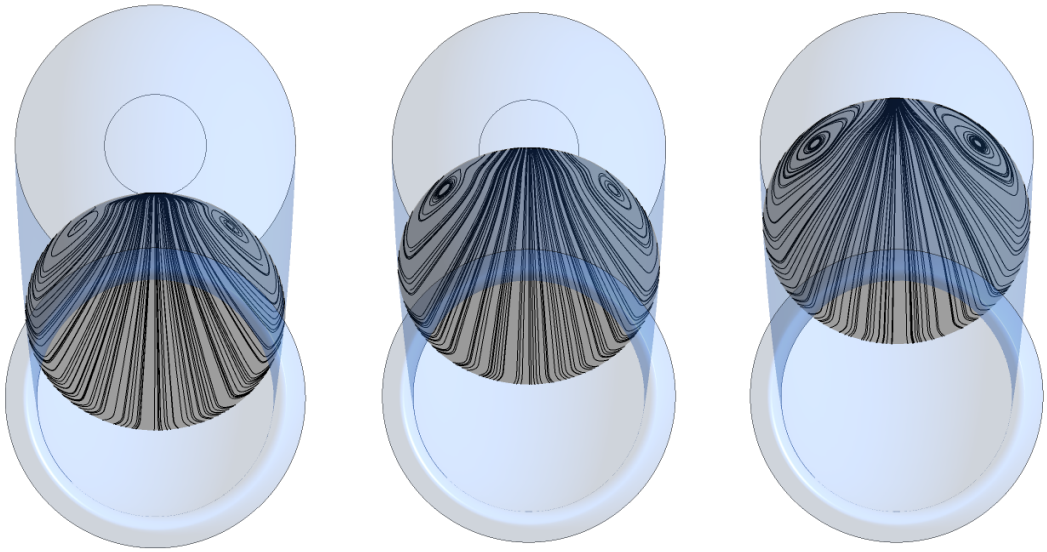

(a) Plane 1 ($z/s = 5.697$ or $z/L =$ 0.611)

(b) Plane 2 ($z/s = 4.583$ or $z/L =$ 0.49)

(c) Plane 3 ($z/s = 3.464$ or $z/L =$ 0.371)

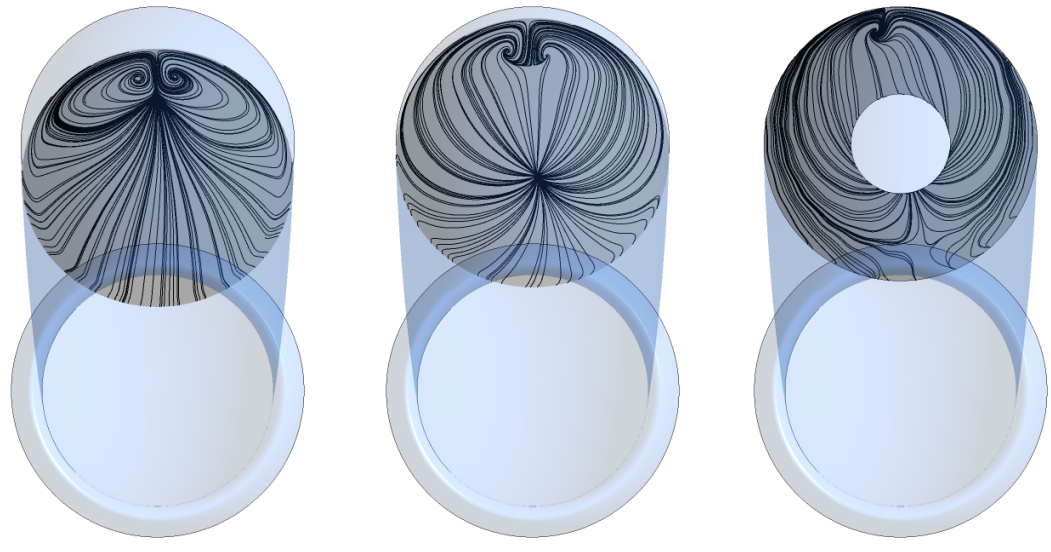

(d) Plane 4 ($z/s = 2.345$ or $z/L =$ 0.251)

(e) Plane 5 ($z/s = 1.226$ or $z/L =$ 0.131)

(f) AIP ($z/s = 0.107$ or $z/L =$ 0.0115)

Figure 4.4: Front view of 2D streamlines on cross flow planes defined in the intake of the coupled system for different axial locations with respect to that of the rotor face and with rotor operating at 100% N_d and $p_{out}/P_{0,in} = 0.987$

4.2.3 Flow field description at the AIP

As already discussed in § 1, the total pressure and swirl distortion attributed to an S-duct such as that of the coupled system proposed in this work (see § 3.2.3) are comparable and, therefore, one could not be neglected with respect to the other. In this section, the description of both total pressure and swirl distortion calculated at the AIP are presented.

4.2.3.1 Total pressure distortion

The total pressure distortion at the AIP of the coupled system was investigated by considering the distribution of non-dimensional total pressure (P_0^*) and the values of total pressure distortion parameter (DC_{60}), defined in § 3.3.7 and 3.3.1, respectively. Figures 4.5(a) and 4.5(b) show the contours at the AIP of non-dimensional total pressure (P_0^*) for near stall and near peak efficiency operating points, respectively.[†] Essentially, the extent of the total pressure distortion remained unchanged within the rotor operability range. Moreover, the total pressure distortion parameter (DC_{60}) between near stall and near choking operating points increased from 0.273 to 0.284. This change was essentially related to that of the mass flow, which will be discussed in § 4.2.4. In these conditions, the total pressure distortion level was above that recommended for engine designs[67]. Therefore, the total pressure distortion could significantly contribute with the swirl distortion to the change of rotor performance.

4.2.3.2 Swirl distortion

As discussed in § 4.2.2.3, the flow topology in the cross flow direction becomes more and more asymmetric as the flow moves towards the AIP. As a result, the vorticity pattern was unbalanced within the rotor operability range as shown Fig. 4.6. This outcome was more notable by considering the trend of the magnitude of positive and negative peaks of non-dimensional streamwise vorticity ($\omega^{\star,+}_{z,peak}$ and $|\omega^{\star,-}_{z,peak}|$), defined in § 3.3.5, within the rotor operability range as shown in Fig. 4.6(c).

Finally, it could have been interesting to compare at a constant intake inlet Mach number the total pressure and swirl distortion of the coupled system with respect to that of the same configuration, but without the presence of rotor blades downstream of the duct itself (pure S-duct configuration). However, for the rotational speed investigated in this section this comparison could not be carried out due to the action of the rotor blades to increase the mass flow of the system. In fact, the minimum intake inlet Mach number reached in the coupled system configuration ($M_{in} = 0.638$) was 4.6% higher than the

[†]Note that all of the contours at the AIP presented in this work are plotted from the point of view of an observer facing downstream of the system

maximum value achieved in the pure S-duct configuration ($M_{in} = 0.610$).

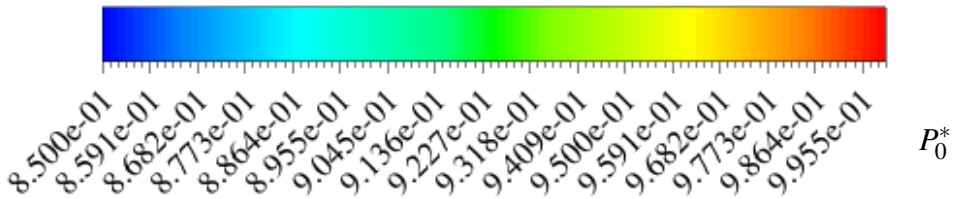

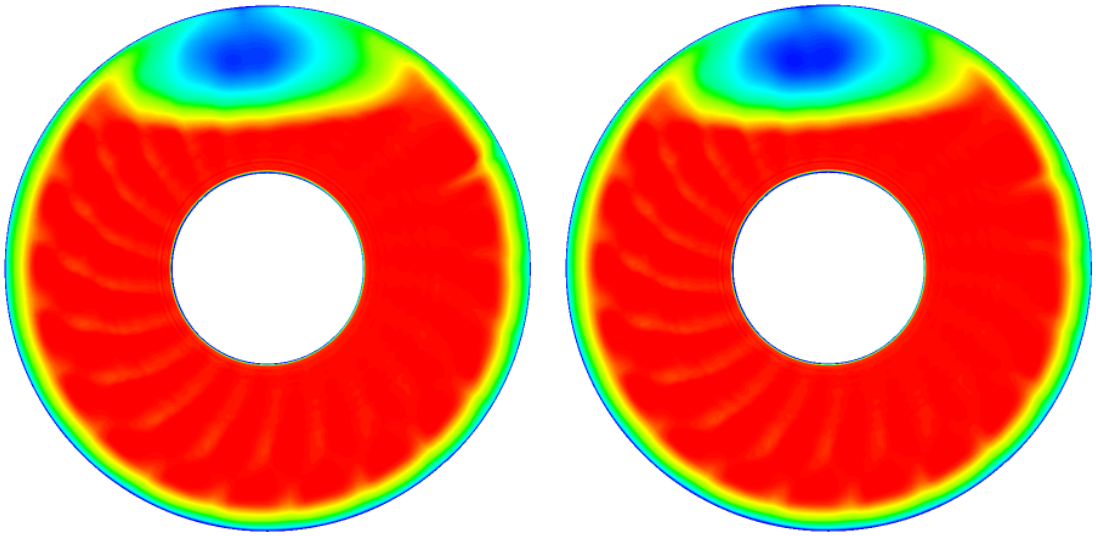

(a) Near stall (b) Near choking

Figure 4.5: Contours of non-dimensional total pressure (P_0^*) at the AIP of the Coupled system with rotor operating at 100% N_d

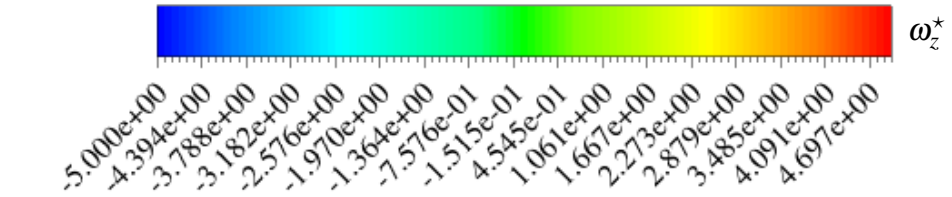

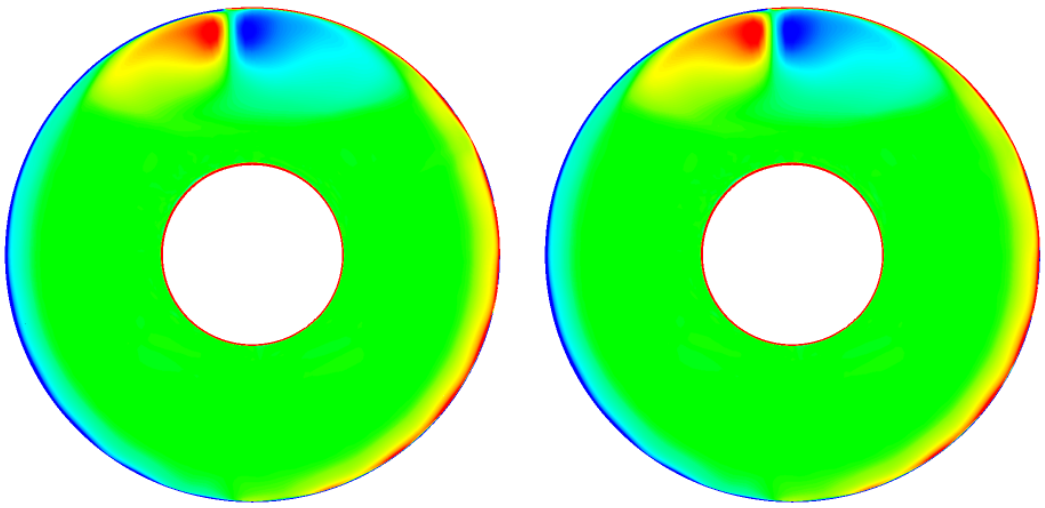

(a) Near stall (b) Near choking

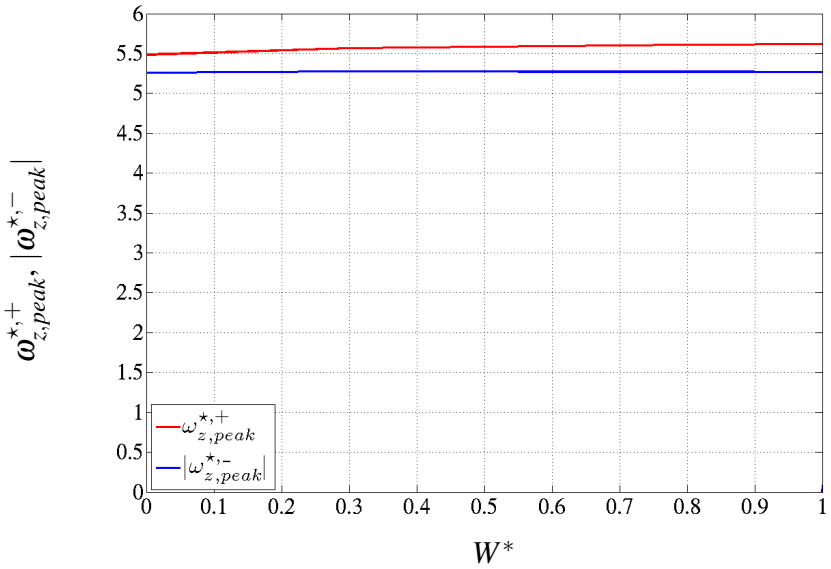

(c) Magnitude of non-dimensional positive and negative peak vorticities ($\omega^{\star,+}_{z,peak}$ and $|\omega^{\star,-}_{z,peak}|$)

Figure 4.6: Visualization of contours of non-dimensional streamwise vorticity ($\omega_z^\star$) at (a) near stall and (b) near peak efficiency and (c) trend of absolute values of non-dimensional positive and negative peak vorticities ($\omega^{\star,+}_{z,peak}$ and $|\omega^{\star,-}_{z,peak}|$) versus rotor normalized mass flow with the rotor operating at 100% N_d

4.2.4 S-duct effect on rotor performance

A comparison of the global performance of the rotor operating with an S- and an annular upstream duct geometry, relative to the CFD domains of the coupled system (§ 3.2.3) and the datum NASA Rotor 67 configuration (§ 3.2.2), respectively, was carried out. Figures 4.7(a) and 4.7(b) show the pressure ratio (PR) and isentropic efficiency (η_{is}), respectively, versus the rotor corrected mass flow (Eq. 4.1) and for both of the aforementioned configurations with the rotor operating at its original design rotational speed (N_d).

$$W_{cor} = W \cdot \sqrt{T_{0,1}/T_{ref}}/(P_{0,1}/P_{ref}) \tag{4.1}$$

Compared to the datum NASA Rotor 67 configuration (see § 3.2.2.3), the near stall operating points of the coupled system was found at higher corrected mass flow (W_{cor}). As a consequence, the rotor operability range reduced significantly. Moreover, the corrected mass flow (W_{cor}), pressure ratio (PR) and isentropic efficiency (η_{is}) along the rotor operability range were significantly reduced. These reductions were quantified by comparing the numerical solutions of the two aforementioned configurations at constant throttle setting condition. This was quantified with the rotor outlet non-dimensional mass flow ($NDMF_2$), calculated relatively to station 2 of the NASA Rotor 67 (see § 3.2.2.2) as given in Eq. 4.2.

$$NDMF_2 = \frac{W \cdot \sqrt{T_{0,2}}}{P_{0,2}} \tag{4.2}$$

Referring to Fig. 4.7, the comparison was carried out between the near stall operating point of the coupled system ($S100$) and the operating point of the datum NASA Rotor 67 configuration $A100$ such that $NDMF_{2,A100} = NDMF_{2,S100}$. As a result, the corrected mass flow (W_{cor}), pressure ratio (PR) and isentropic efficiency (η_{is}) reduced by 1.55, 3.33 and 3.78%, respectively. These reductions were related to that of the total pressure and swirl distortion calculated between the aforementioned configurations at the AIP. Clearly, for the datum NASA Rotor 67 configuration, the total pressure distortion could be neglected with respect to that attributed to the coupled system (see § 4.2.3.1). Therefore, the change of total pressure distortion between the two aforementioned operating points corresponded directly to that calculated for the coupled system (see § 4.2.3.1). On the other hand, the swirl distortion associated to the datum NASA Rotor 67 configuration could not be neglected due to the presence of transonic rotor disturbances[‡].

[‡]The analysis of rotor disturbances is part of the methodology assessed to determine the location of the AIP for swirl distortion (see § 6.2)

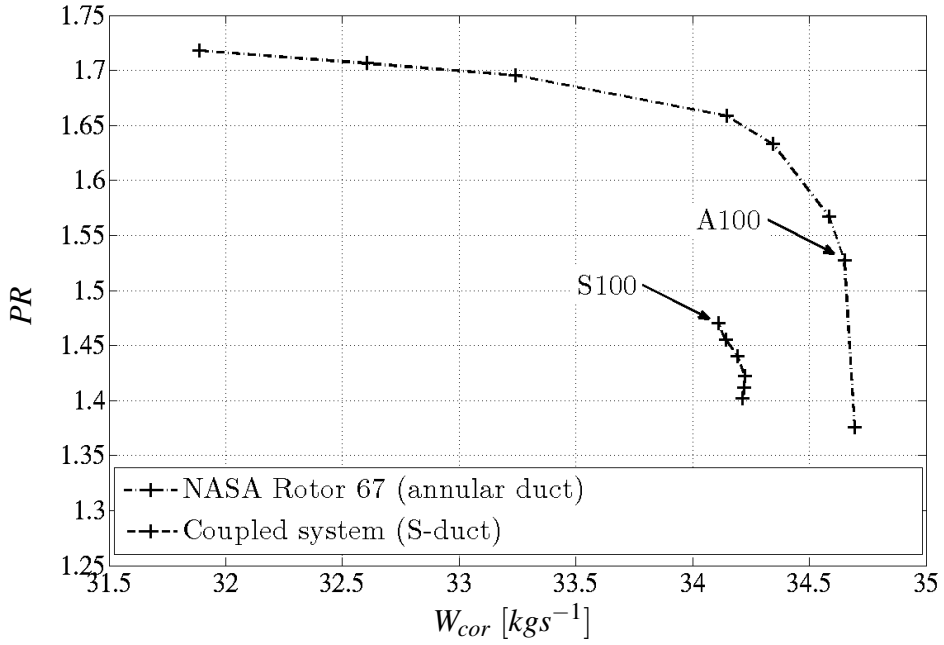

(a) Pressure ratio (PR)

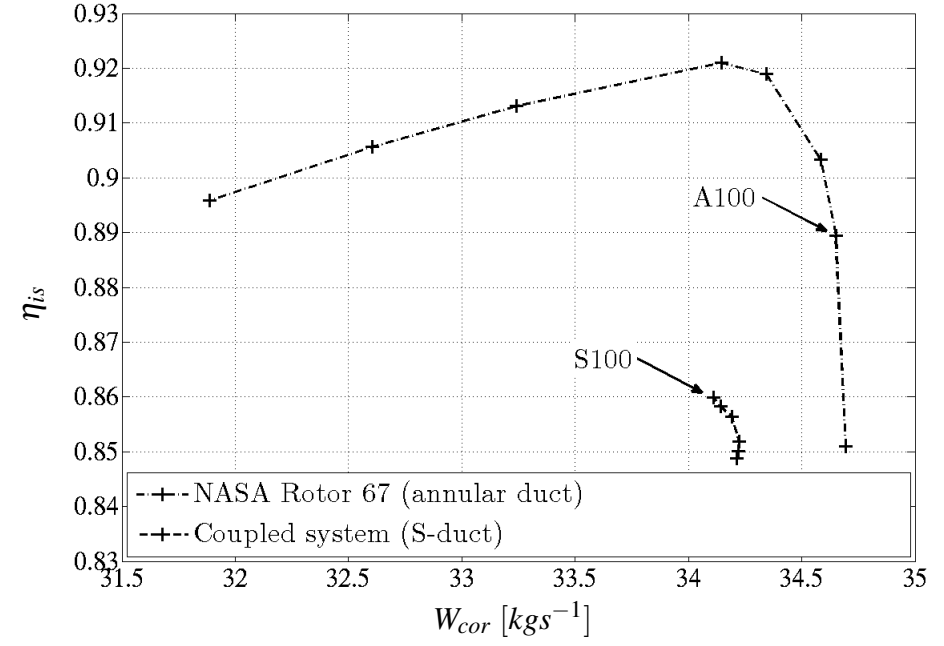

(b) Isentropic efficiency (η_{is})

Figure 4.7: Global performance versus corrected mass flow (W_{cor}) relative to the datum NASA Rotor 67 and coupled system configurations with rotor operating at 100% N_d

Hence, the change in swirl distortion was analyzed in terms of swirl angle and relative axial velocity change ($\Delta\alpha$ and $\Delta V_z\%$), respectively, calculated between the two operating points $S100$ and $A100$ at the AIP[§] as shown in Fig. 4.8(a) and 4.8(b). Note that two representative blades placed where the swirl angle change ($\Delta\alpha$) reaches high magnitude in the counter- and co-rotating direction, blade 5 and blade 8, respectively, are also indicated.

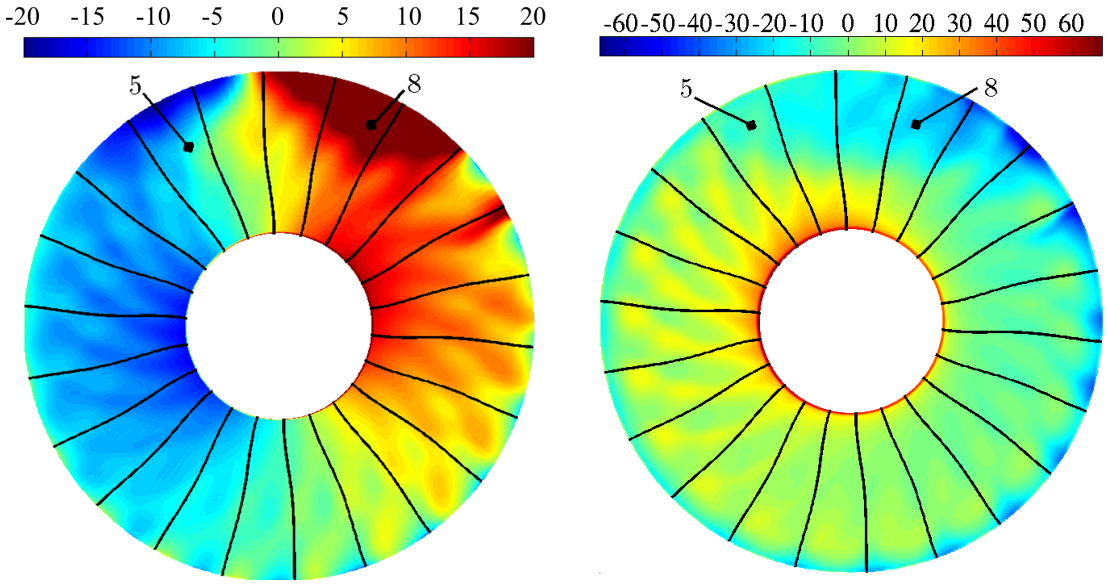

(a) Swirl angle change ($\Delta\alpha$)

(b) Relative axial velocity change ($\Delta V_z\%$)

Figure 4.8: Contours of the (a) swirl angle and (b) relative axial velocity change ($\Delta\alpha$ and $\Delta V_z\%$) at the AIP calculated between the operating points $A100$ and $B100$

Along the spanwise direction, two regions of the swirl angle change ($\Delta\alpha$), one highly positive and one highly negative, were observed at the AIP (Fig. 4.8(a)). These were located near the hub and near the tip. Near the hub, the impact of the flow with the spinner generates of a swirl component of velocity. Meanwhile, near the tip high swirl angle changes are due to the presence of the self-generated distortion. These two phenomena manifest symmetrically and, therefore, a co- and a counter-rotating region of high swirl angle were identified along the circumferential direction.

As a consequence of the swirl angle change combined with that of the total pressure at the AIP, the axial velocity adjusts itself in order to match the outlet conditions as shown

[§]Note, however, that the CFD meshes defined for the two aforementioned configurations were different. Therefore, the calculation of relative changes of flow quantities at the AIP could be accomplished by using a common polar 2D grid defined in Matlab. This presented a resolution of 400 intervals uniformly distributed along both the radial and circumferential direction.

in Fig. 4.8(b). Referring to the swirl angle change ($\Delta\alpha$), the counter- and co-rotating zones are subjected to an increase and decrease of the Mach number relative to the rotor (M_{rel}), respectively. Therefore, the blades within the counter-rotating region are lightly loaded, while those in the co-rotating region are highly loaded. The relative Mach number (M_{rel}) was investigated at 5 and 95% of blade span as shown in Fig. 4.9 and 4.10. Referring to Fig. 4.8, these locations correspond to where the swirl distortion reaches the highest values. Compared to the operating point $A100$, the flow velocity of the rotor at the operating point $S100$ increases in the counter-rotating region located at 5% of blade span. Consequently, a shock wave occurs at the leading edge by causing an increase of rotor loss as shown in Fig. 4.9(b). This is related to the reduction of the rotor isentopic efficiency (η_{is}) shown in Fig. 4.7(b).

Referring to Fig. 4.11, the streaklines on the suction and pressure side of blade 5 and blade 8 relative the coupled system operating at $S100$ were compared with that relative to a generic blade of the datum NASA Rotor 67 configuration operating at $A100$. As compared with the streaklines relative to the pressure side of a generic blade operating at $A100$ (Fig. 4.11(a)), that of the blade 5 operating at $S100$ shows a stronger separation bubble. This takes place throughout the second half of the blade span as shown in Fig. 4.11(b). This is essentially caused by a more intense passage shock wave notable in Fig. 4.10. Therefore, more loss are introduced into the rotor. On the other hand, the hub corner stall normally occurring on the blade suction side disappears due to the large separation induced by the shock wave visible in Fig. 4.9(b).

Regarding the co-rotating distorted region, the comparison of the streaklines relative to the pressure side of a generic blade operating at $A100$ (Fig. 4.11(a)) with that of the blade 8 operating at $S100$ shows that the separation normally occurring near the tip disappears as shown in Fig. 4.11(c). This is due to the reduction in relative Mach number (M_{rel}) occurring in that region (Fig. 4.10(b)). As a consequence, the strength of the shocks upstream of the rotor face are lower. On the other hand, by considering the blade suction side, the comparison of the streaklines on the blade 8 (Fig. 4.11(c)) and a generic blade operating at $A100$ (Fig. 4.11(a)) shows that the line of separation, attributed to the presence of a passage shock normally occurring under clean inlet conditions, disappear on the coupled system configuration while the hub corner stall becomes less extended along the span direction.

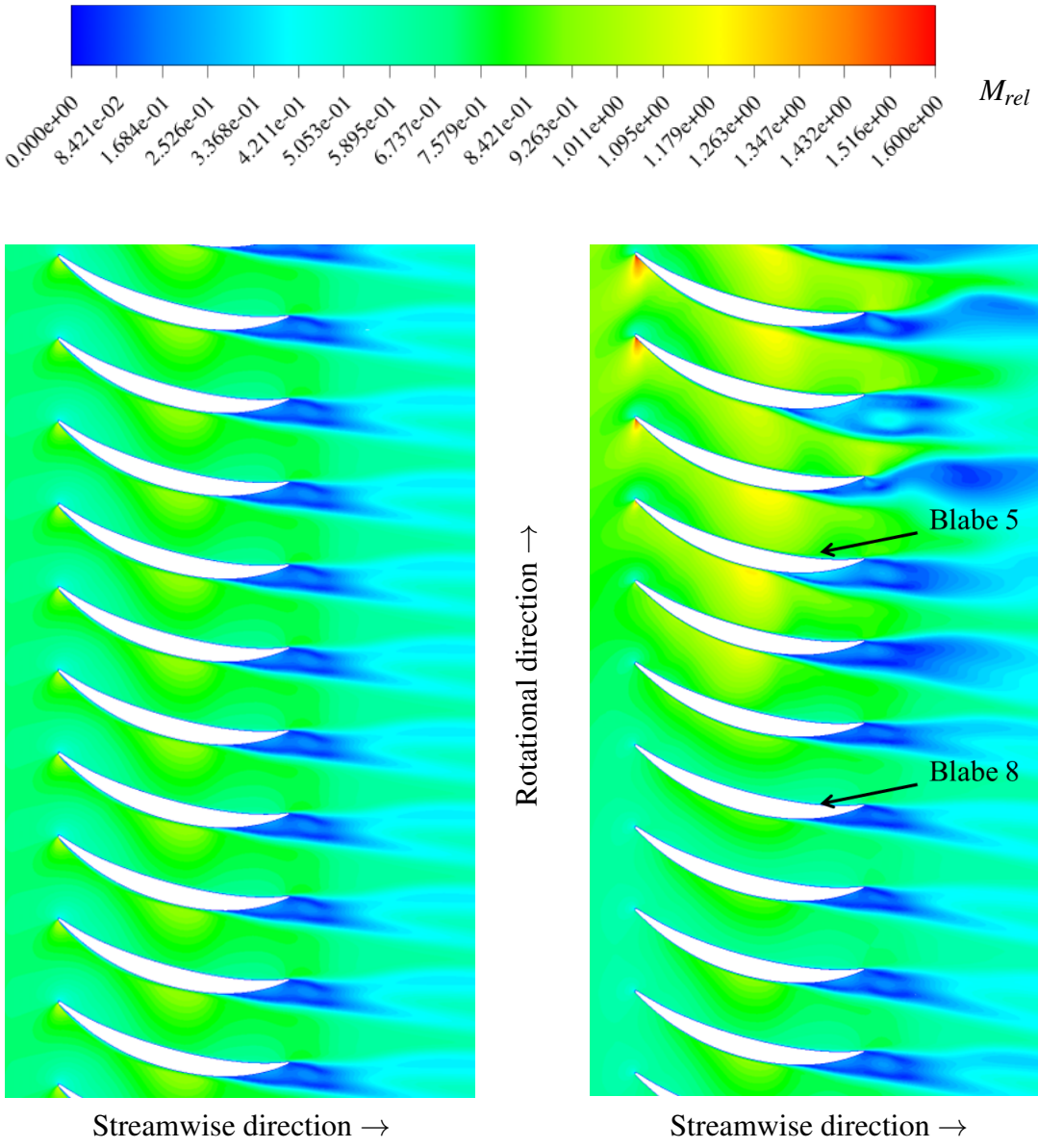

(a) Rotor operating point $A100$

(b) Rotor operating point $S100$

Figure 4.9: Contours of relative Mach Number (M_{rel}) at 5% of blade span compared between the operating point $A100$(annular duct upstream configuration) and the main distorted region at the operating point $S100$ (S-duct upstream configuration)

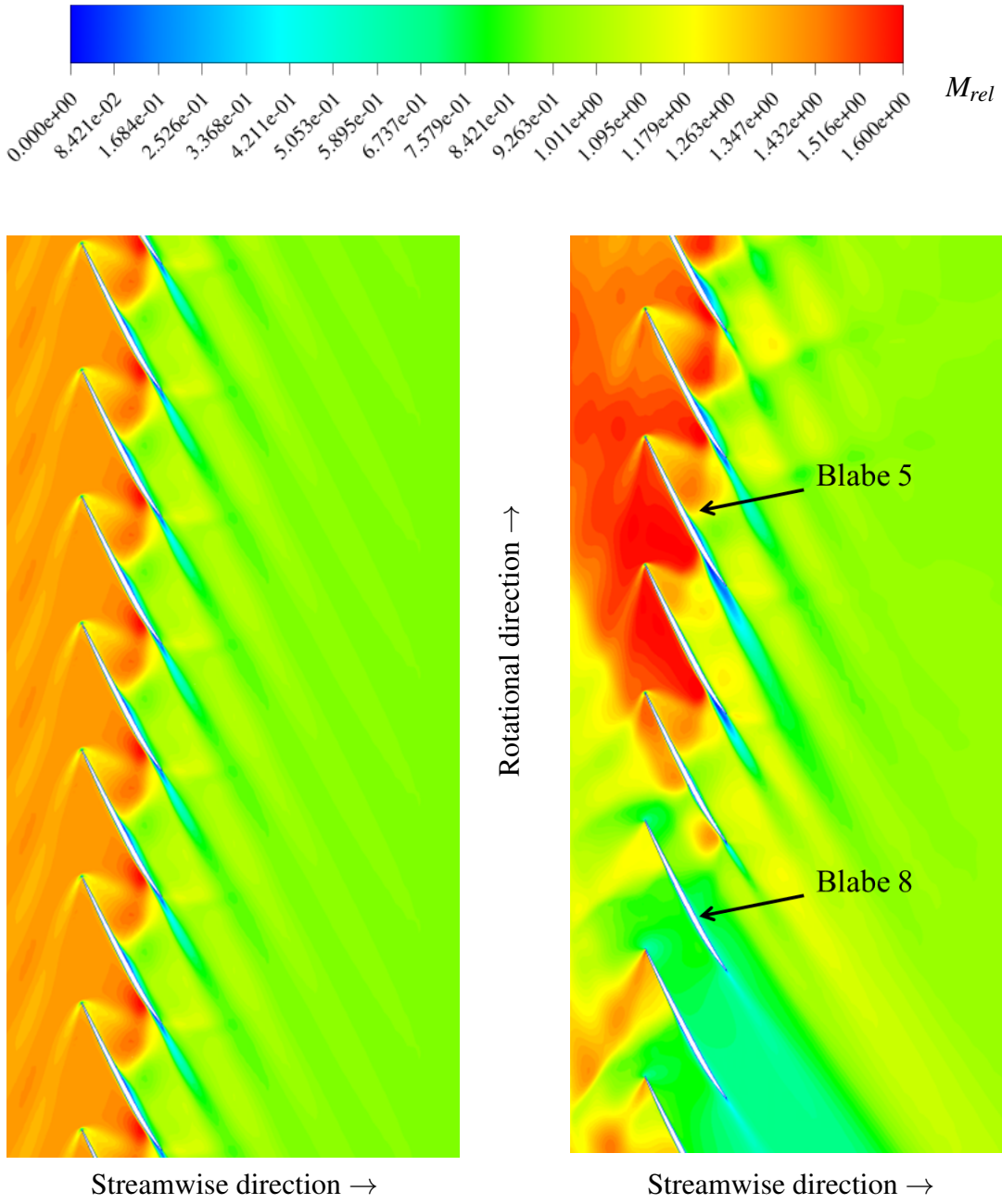

(a) Rotor operating point $A100$

(b) Rotor operating point $S100$

Figure 4.10: Contours of relative Mach Number (M_{rel}) at 95% of blade span compared between the operating point $A100$ and the main distorted region at the operating point $S100$

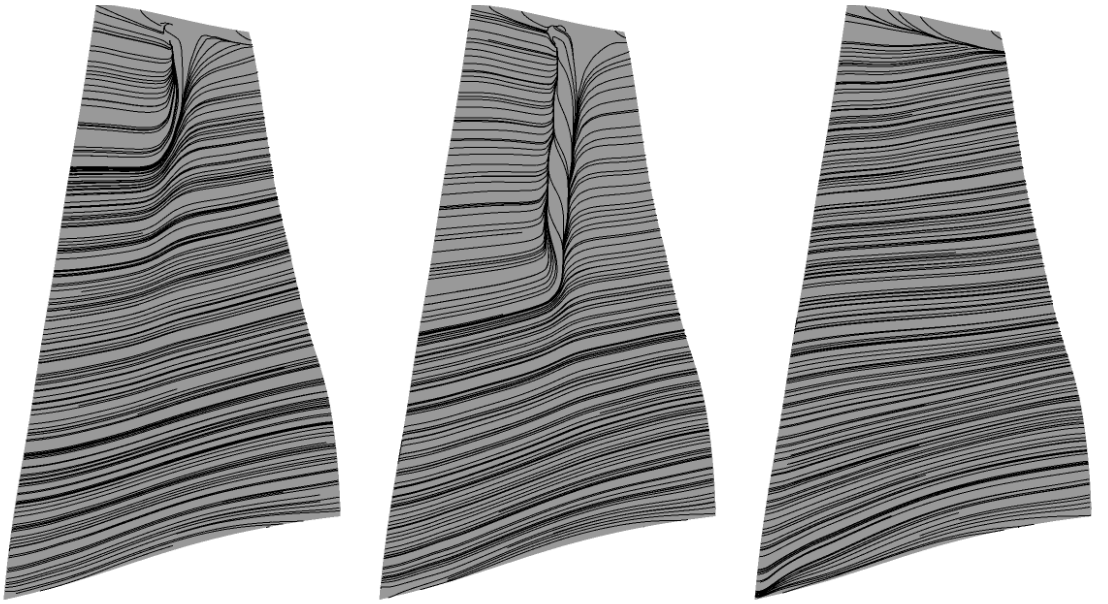

(a) Operating point $A100$, pressure side of generic blade

(b) Operating point $S100$, pressure side of blade 5

(c) Operating point $S100$, pressure side of blade 8

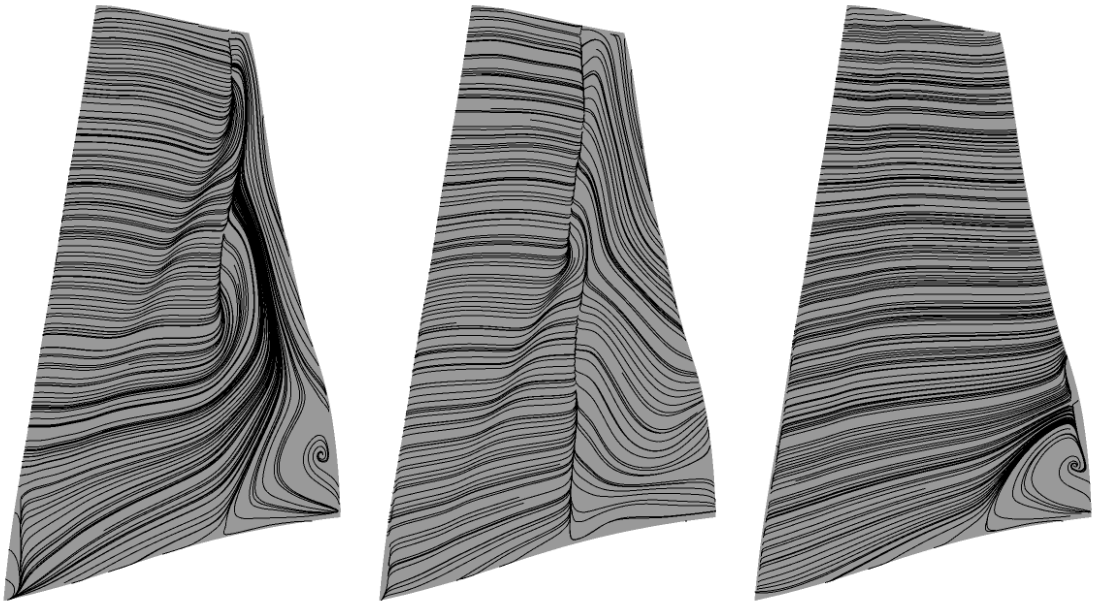

(d) Operating point $A100$, suction side of a generic blade

(e) Operating point $S100$, suction side of blade 5

(f) Operating point $S100$, suction side of blade 8

Figure 4.11: Visualization of blade streaklines on both pressure and suction side for a generic blade of the datum NASA Rotor 67 configuration operating at $A100$ and the 5^{th} and 8^{th} blade of the coupled system operating at $S100$ (streamwise direction from left to right)

4.3 Reduced rotational speed analysis

As discussed in § 4.2.4, the operability range of the rotor running at its design rotational speed (N_d) reduced significantly when mounted on the coupled system. Consequently, the effect of the throttle setting on the flow field of the coupled system could not be observed. For this reason, similar analyses were carried out at a 80% N_d. This value was still sufficiently high to be considered within the typical operability range of the fan rotor. In this section, the aerodynamics of the S-shaped intake, the flow description at the AIP and the effect of the S-duct on the rotor performance are discussed.

4.3.1 Definition of the CFD boundary conditions

The boundary conditions applied for this analysis were similar to that defined in § 4.2.1. Clearly, the only difference was relative to the range of the rotor outlet static to inlet total pressure ($p_{out}/P_{0,in}$). Hence, to obtain the whole rotor speedline between near stall and near choking conditions, this value ranged then between 1.051 and 0.888, respectively.

4.3.2 S-Shaped intake aerodynamics

As will be presented in § 4.2.4, the corrected mass flow of the rotor (W_{cor}) ranged within a 6.315% with respect to its value at the choking conditions ($W_{cor,ch} = 30.501\ kgs^{-1}$). As result, changes in the S-duct aerodynamics were notable within this range and are presented below.

4.3.2.1 Intake performance

As the rotor operability changed from near stall to near choking, the intake performance remained essentially unchanged since the pressure recovery (η) reduced from 0.991 to 0.990. These values were very close to the unit, by indicating already that the intake performance should not affect significantly that of the rotor placed downstream.

4.3.2.2 Description of the S-duct flow separation

Compared to the design rotational speed analysis (see § 4.2.2.2), as the mass flow increases the changes of characteristics of the self-generated distortion occurring within the duct were notable. As compared with the design rotational speed analysis (see § 6.2), the separation pattern remains essentially symmetric within the rotor operability range, although the rotor disturbances were more pronounced. The characteristics of the separation

at near stall and near choking conditions were estimated by considering the distribution of the skin friction coefficient (C_f) along the axial direction at the starboard edge ($\phi = 0^o$) as shown in Fig. 4.12(c). By moving towards the AIP, the skin friction coefficient (C_f) exhibited two minimum values. At the first value corresponded the onset point of separation while at the second value corresponded the point of reattachment. Clearly, their relative distance defined the separation length. The point of separation moved backwards as the operating condition changed from 0.5 to $0.56 \cdot z/L$, between near stall and near choking, respectively. On the other hand, the axial location of the reattachment point ($0.24 \cdot z/L$) was almost independent of the throttle setting. However, a small change of this location occurred. This could be related to the rotor disturbances propagating upstream of the rotor itself. Referring to Fig. 4.12(a) and 4.12(b) these disturbances were more predominant near stall operating conditions.

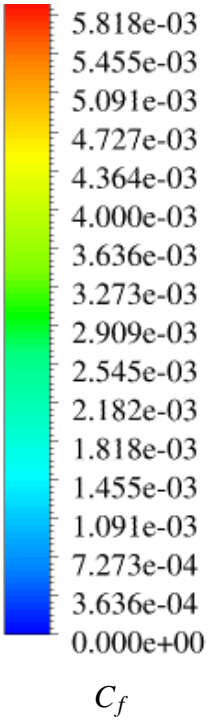

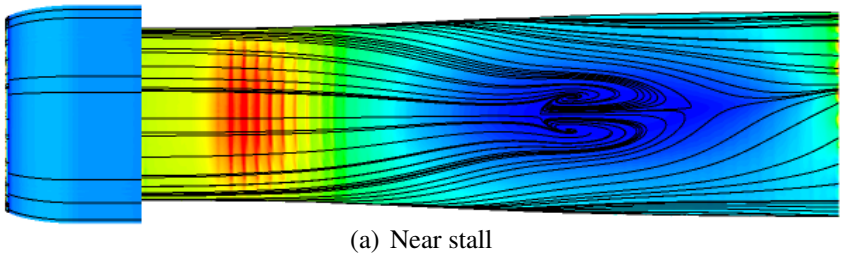

(a) Near stall

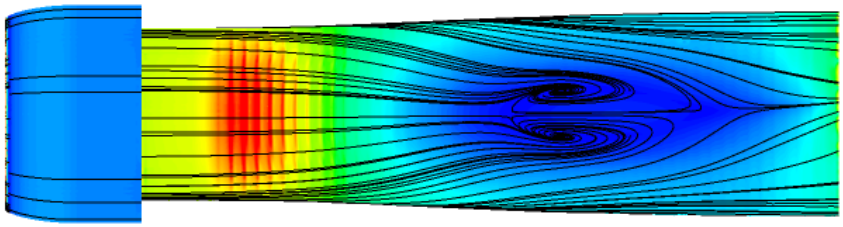

(b) Near choking

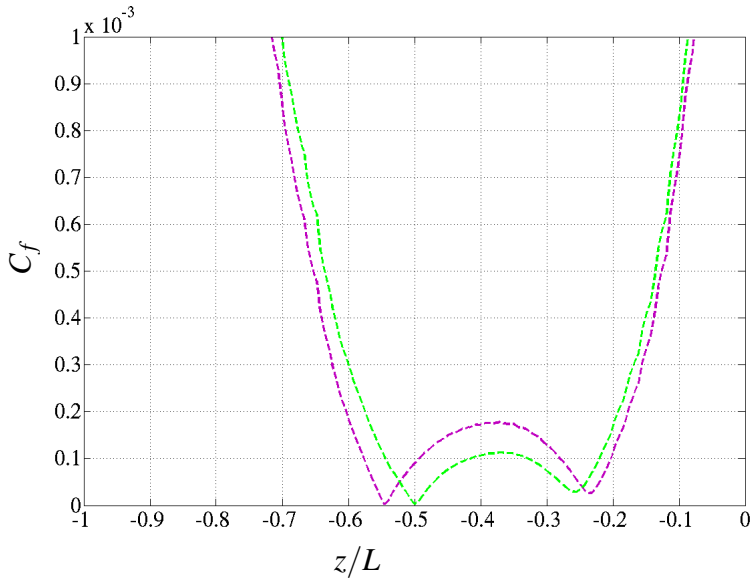

(c) Skin friction coefficient (C_f) versus the axial position (z/L) measured along the starboard edge ($\phi = 0^o$)

Figure 4.12: Contours of skin friction coefficient (C_f) with streaklines (black) at the starboard side of the intake wall with rotor operating at 80% N_d (a) near stall and (b) near choking and (c) the relative distribution along the starboard edge ($\phi = 0^o$)

4.3.2.3 Internal duct aerodynamics

As observed for the design rotational speed analysis (see § 4.2.2.3), the flow topology into the duct was asymmetric due to the presence of the bulk swirl introduced by the rotor in the flow field of the duct itself. This condition was notable from $z/s = 1.226$ upstream of the rotor face. On the other hand, by considering the rotor operating at 80% N_d, the asymmetry of the internal duct aerodynamics was notable only at the AIP. Hence, changes in flow topology were observed at this location at near stall and near choking operating conditions as shown in Fig. 4.13(a) and 4.13(b), respectively. The main differences in flow topology were localised near the intake wall, where the flow relative to the rotor was essentially transonic. Therefore, the change in throttle settings determined that of the shock wave characteristics.

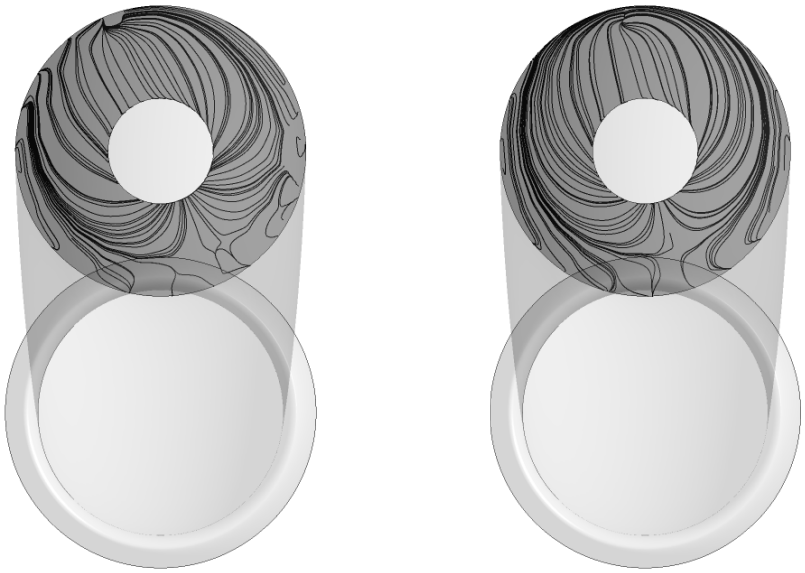

(a) Near stall (b) Near choking

Figure 4.13: Visualization of 2D streamlines at the AIP of the coupled system configuration with rotor operating at 80% N_d

4.3.3 Flow field description at the AIP

In this section, both the total pressure and swirl distortion at the AIP of the coupled system configuration are discussed.

4.3.3.1 Total pressure distortion

Figures 4.14(a) and 4.14(b) show the pattern of non-dimensional total pressure (P_0^*) at the AIP with rotor operating at near stall and near choking respectively. As the rotor operability changed from near stall to near choking conditions, the extent of the total pressure distortion remained essentially unchanged. Meanwhile, the total pressure distortion parameter (DC_{60}) increased from 0.105 to 0.124. Clearly, this change was attributed to the intensification of the self-generated distortion with the mass flow. Also, within this range, the DC_{60} was below the limit value recommended for aircraft design[67]. Nevertheless, the effect of the total pressure distortion on the rotor performance could not be quantified since occurred simultaneously with the swirl distortion.

4.3.3.2 Swirl distortion

To account for the swirl distortion at the AIP the pattern of non-dimensional streamwise vorticity (ω_z^*) was analyzed (Fig. 4.15(a) and 4.15(b)). The self-generated distortion was characterized by two peaks of vorticity, one negative and one positive. As discussed for the design rotational speed analysis (see § 4.2.3.2), these two vorticities are not identical probably due to the influence of bulk flow field introduced by the rotor on the flow field of the S-duct itself. This influence reduces as the throttle settings change from near stall to near choking and, as a result, the flow field tends to become again symmetric as expected for an isolated rotor (see § 2.2.2). This discrepancy was quantified between the stall and choking point with the change of the absolute peak values of positive and negative non-dimensional streamwise vorticities ($\omega^{\star,+}_{z,peak}$ and $|\omega^{\star,-}_{z,peak}|$) as shown in Fig. 4.15(c). This was manifested by an increase of the positive peak vorticity ($\omega^{+}_{z,peak}$), while the negative peak vorticity ($\omega^{\star,-}_{z,peak}$) remained relatively constant. This change, combined with that relative to the total pressure distortion was related to the change in rotor performance with the throttle settings presented in the next section.

For the rotational speed investigated in this section, the level of mass flow was sufficiently low to make possible a comparison at a constant intake inlet Mach number (M_{in}) the flow distortion of the coupled system with respect to that of the same configuration, but without the presence of rotor blades downstream of the duct itself (pure S-duct configuration). Hence, for a mean operating point of the coupled system operating at 80% of the design rotational speed and such that $M_{in} = 0.506$, the total pressure distortion parameter

(DC_{60}) increased significantly from 0.118 to 0.128 as the rotor blades were removed from the system. Meanwhile, the mean value of non-dimensional streamwise peak vorticity (ω_z^*) decreases significantly from 2.75 to 1.99. These results confirm that the presence of the rotor blades downstream of an S-duct change significantly the level of distortion at the AIP and, therefore, have to be accounted onto the CFD model.

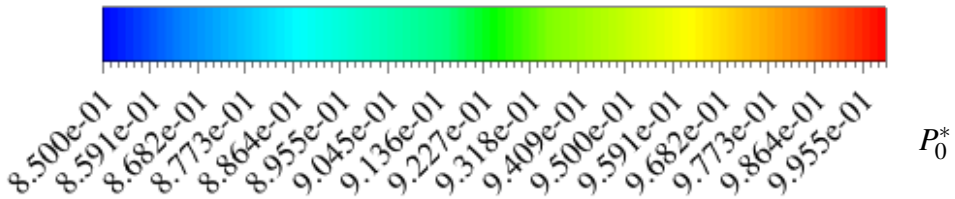

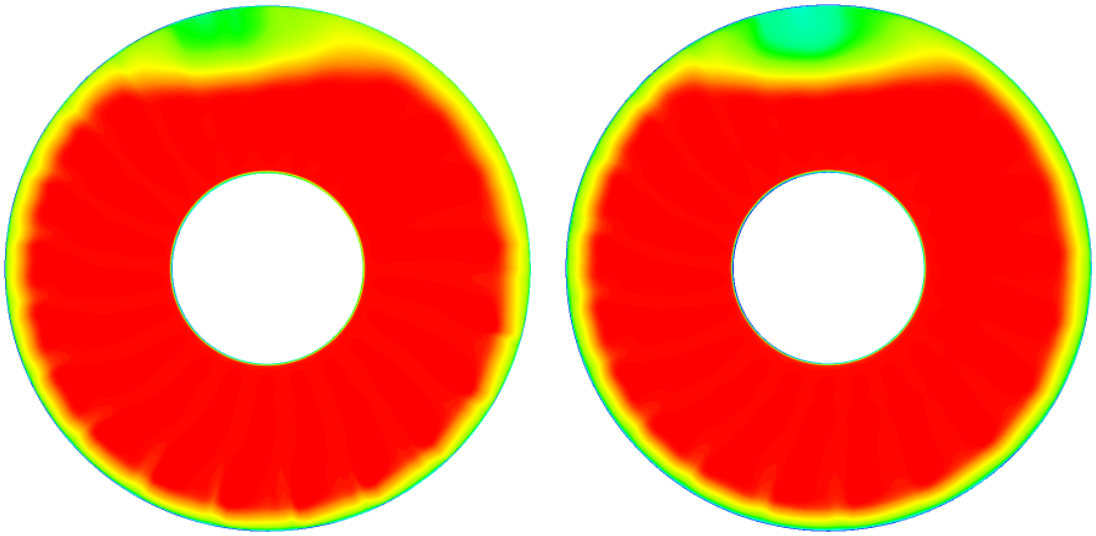

(a) Near stall (b) Near choking

Figure 4.14: Contours of non-dimensional total pressure (P_0^*) at the AIP of the Coupled system with rotor operating at 80% N_d

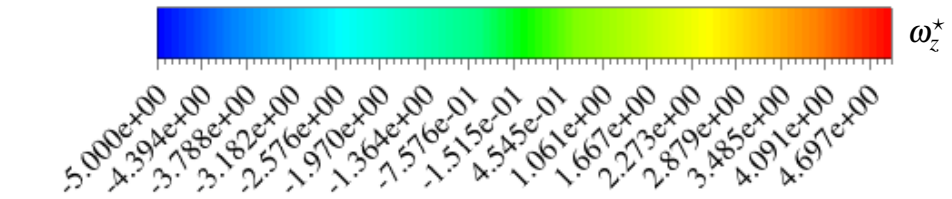

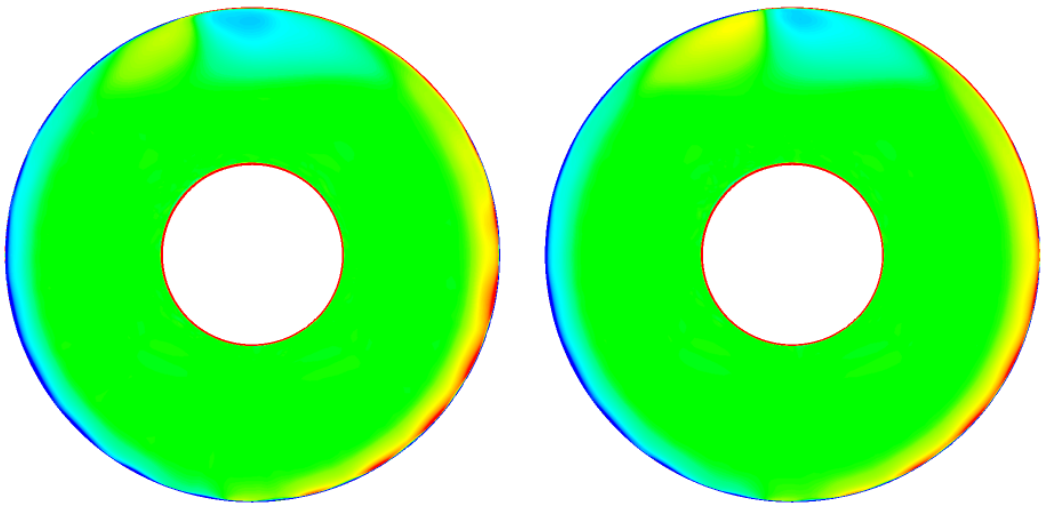

(a) Near stall (b) Near choking

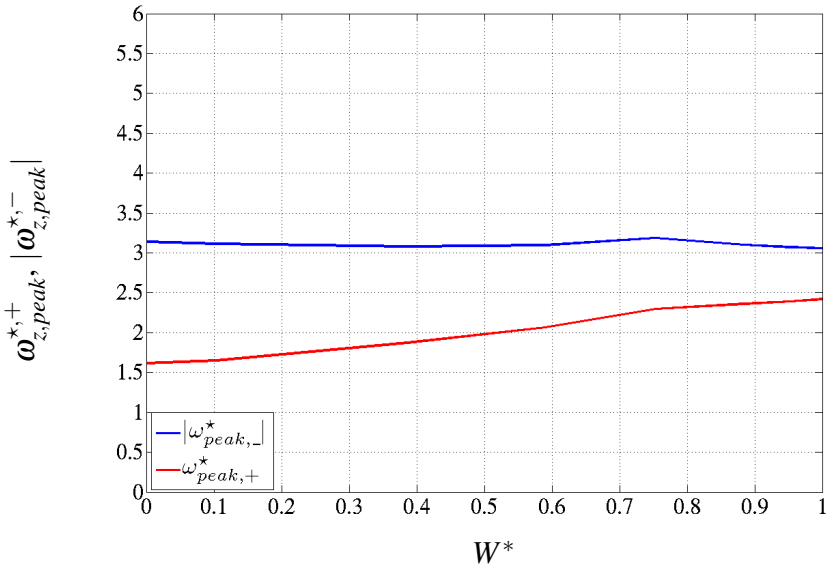

(c) Magnitude of non-dimensional positive and negative peak vorticities ($\omega^{\star,+}_{z,peak}$ and $|\omega^{\star,-}_{z,peak}|$)

Figure 4.15: Visualization of contours of non-dimensional streamwise vorticity ($\omega_z^\star$) at (a) near stall and (b) near peak efficiency and (c) trend of absolute values of non-dimensional positive and negative peak vorticities ($\omega^{\star,+}_{z,peak}$ and $|\omega^{\star,-}_{z,peak}|$) versus rotor normalized mass flow with the rotor operating at 80% N_d

4.3.4 S-duct effect on rotor performance

To quantify the effect of the S-duct on the rotor performance at 80% of the rotor design rotational speed (N_d), CFD simulations were also performed for this rotational speed within the whole operability range on the datum NASA Rotor 67 configuration. For these cases, the boundary conditions imposed around this CFD domain were similar to that presented in § 3.2.2.5. The only difference was relative to the values of rotor outlet static to inlet total pressure ($p_{out}/P_{0,in}$) which varied between 1.125 and 0.437, corresponding to near stall and near choking operating conditions, respectively. Figures 4.16(a) and 4.16(b) show the rotor pressure ratio (PR) and isentropic efficiency (η_{is}) versus corrected mass flow (W_{cor}) for datum NASA Rotor 67 and coupled system configurations and with the rotor operating at 80% N_d. Overall, the operating speedline obtained for the coupled system approaches significantly that of the datum NASA Rotor 67 configuration. This was in agreement to the values of pressure recovery (η) which were very close to unit (see § 4.3.2.1). Also, the mass flow blockage associated with the distortion presented a minor effect on the rotor performance.

A direct comparison of the rotor performance between the two aforementioned configurations was conducted in a similar manner already presented in § 4.2.4, Hence the near stall operating point of the coupled system ($S80$) was compared to the operating point of the datum NASA Rotor 67 configuration ($A80$) such that $NDMF_{2,A80} = NDMF_{2,S80}$ (see Fig. 4.16).

Compared to the rotor speedline of the datum NASA Rotor 67 configuration, the near stall operating point for the coupled system ($A80$) occurred at a higher corrected mass flow (W_{cor}). As discussed in § 4.2.4, this was due to the combination of the total pressure and swirl distortion occurring at the AIP. Regarding the swirl distortion, this outcome was related to the distribution of swirl angle combined with that relative to the axial velocity change ($\Delta\alpha$ and $\Delta V_z\%$) shown in Fig. 4.17(a) and 4.17(b), respectively.

An internal analysis on the turbomachinery was carried out by considering the relative Mach number (M_{rel}) at constant blade span and for the two aforementioned configurations. Compared to the same analysis carried out at the design rotational speed (N_d), the impact of the spinner at low blade span (i.e. 5%) was not such relevant. Meanwhile, the highest change in swirl angle combined with that of the axial velocity was concentrated near the tip of the rotor, where the self-generated distortion occurs. Hence, the flow field into the rotor was observed only at 95% of blade span. The analysis considered the comparison of the relative Mach number (M_{rel}) between the datum NASA Rotor 67 and coupled system configurations as shown in Fig. 4.18(a) and 4.18(b). As discussed in § 4.2.4, a localized overloading of blades placed in the counter-rotating region of the self-generated distortion occurs as shown in Fig. 4.18(b).

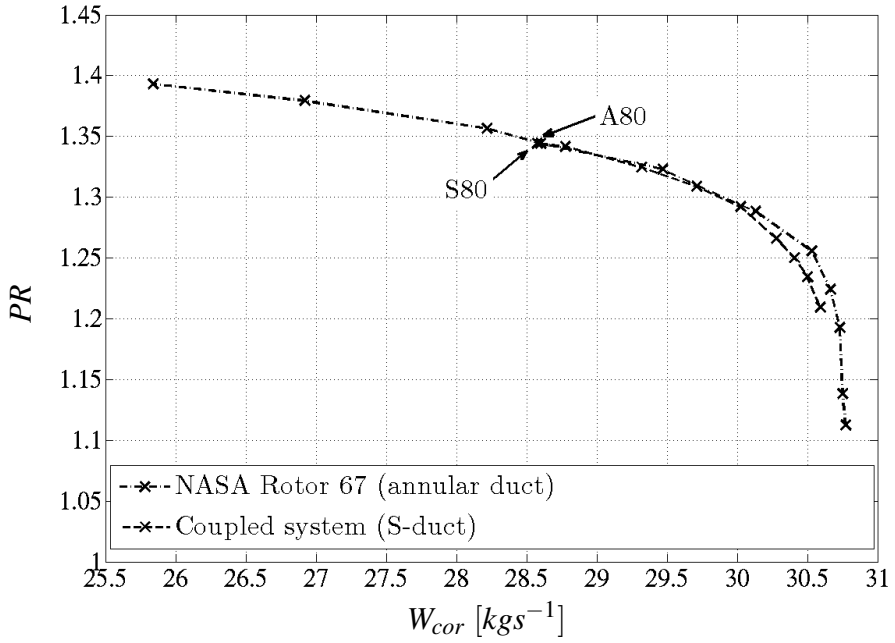

(a) Pressure ratio (PR)

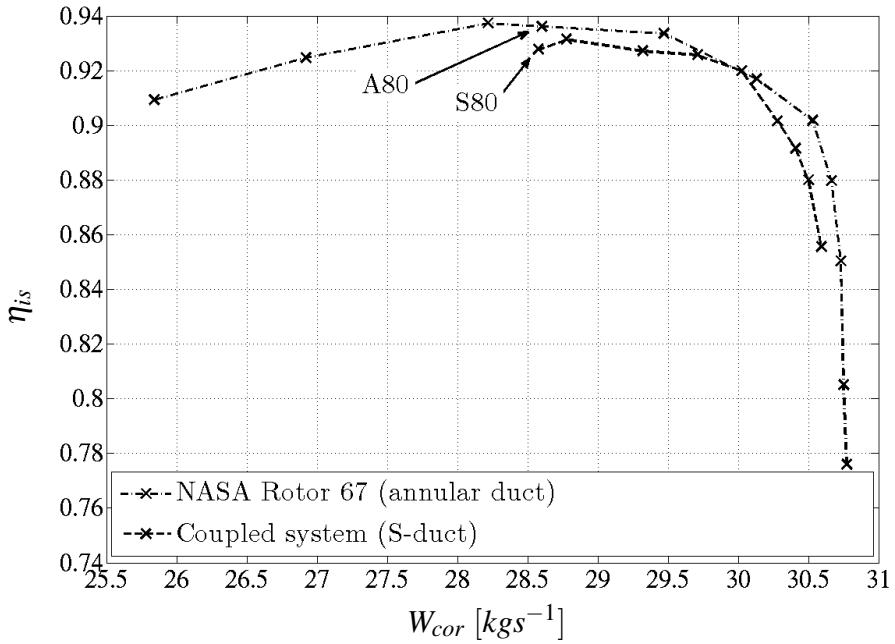

(b) Isentropic efficiency (η_{is})

Figure 4.16: Global performance versus corrected mass flow (W_{cor}) relative to the datum NASA Rotor 67 and coupled system configurations with rotor operating at 80% N_d

Referring to Fig. 4.19, both pressure and suction side of a generic blade of the datum NASA Rotor 67 and the blades 5 and 8 of the coupled system configuration were investigated by considering the surface streaklines. For both blade 5 and 8 of the coupled system (located in the counter- and co-rotating distorted region), the separation region on the pressure side of the blade was as limited as observed for clean inlet conditions (Fig. 4.19(a), 4.19(b) and 4.19(c)). On the other hand, the suction side changed according to the blade considered. In particular, a separation line due to the presence of the the shock wave shown in Fig. 4.18(b) occurred close to the tip region of the blade 5. Consequently, the isentropic efficiency (η_{is}) reduced.

Referring to Fig. 4.16(a), by moving towards near choking conditions, both the pressure ratio (PR) and isentropic efficiency (η_{is}) of the coupled system were lower with respect to that of the datum NASA Rotor 67 configuration. This outcome was attributed to the increase in total pressure and swirl distortion with the throttle setting, presented in § 4.3.3.1 and 4.3.3.2, respectively. However, portions of the change of rotor performance attributed to each types of the aforementioned flow distortion could not be quantified. Meanwhile, the corrected mass flow reduces by indicating that the level of separation increases.

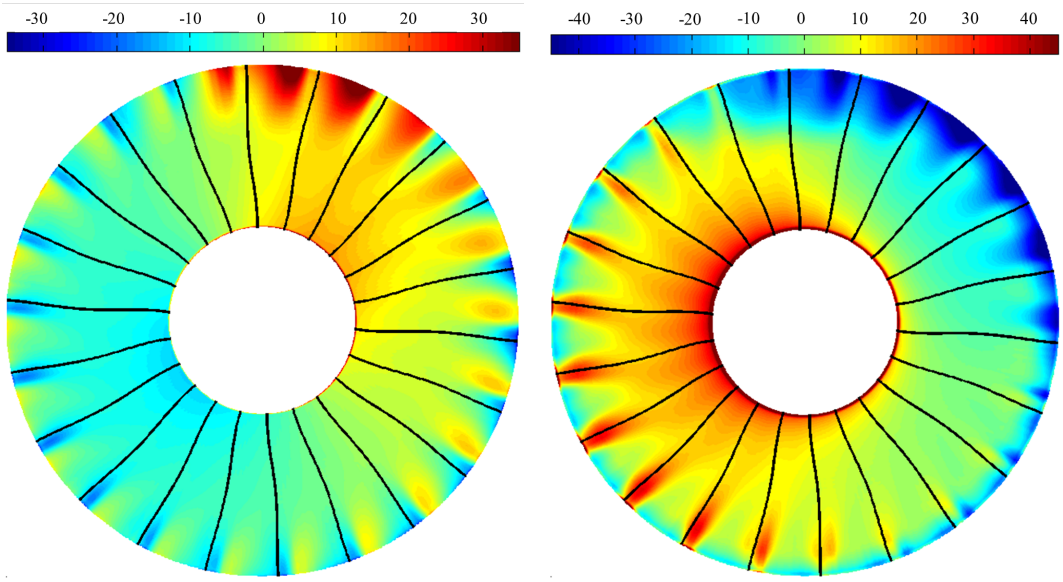

(a) Swirl angle change ($\Delta\alpha$) (b) Relative axial velocity change ($\Delta V_z\%$)

Figure 4.17: Contours of the (a) swirl angle and (b) relative axial velocity change ($\Delta\alpha$ and $\Delta V_z\%$) at the AIP calculated between the operating points $A80$ and $S80$

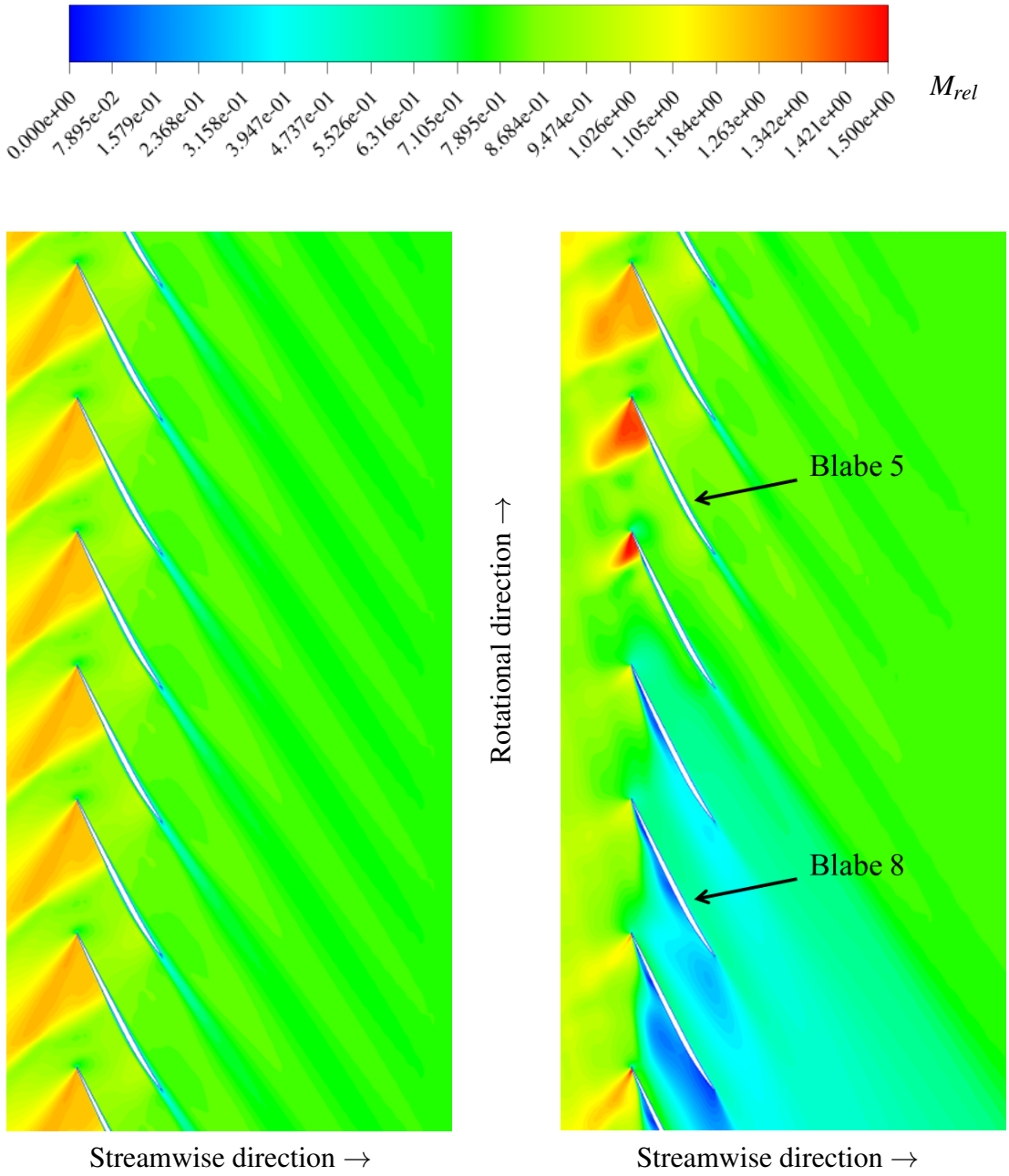

(a) Rotor operating point *A*80

(b) Rotor operating point *S*80

Figure 4.18: Contours of relative Mach Number (M_{rel}) at 95% of blade span compared between the operating point *A*80 and the main distorted region at the operating point *S*80

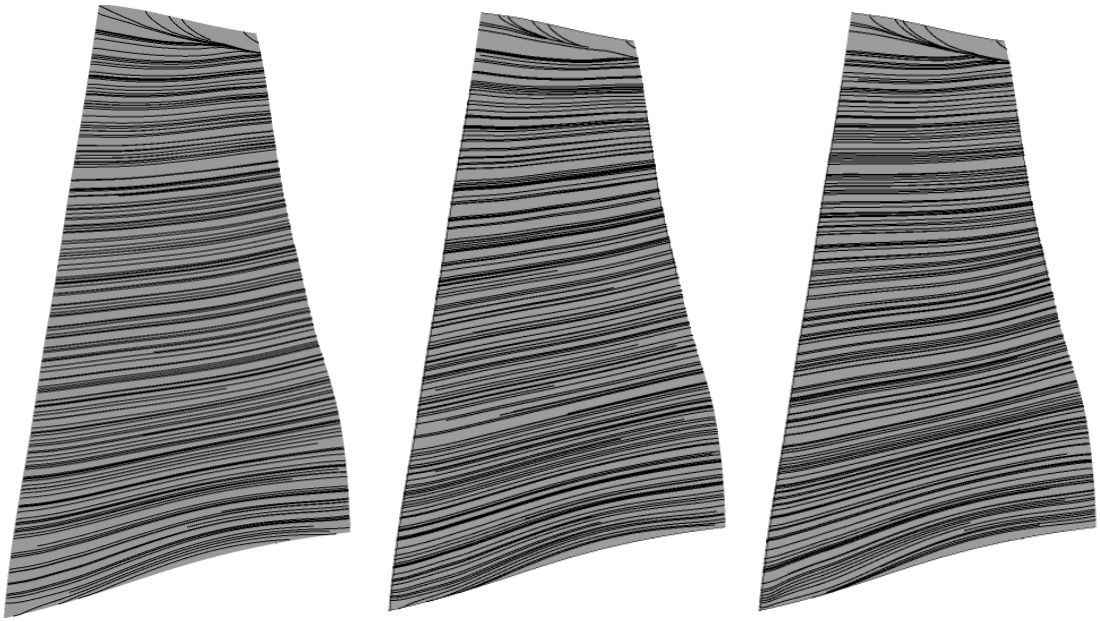

(a) Operating point *A*80, pressure side of generic blade

(b) Operating point *S*80, pressure side of blade 5

(c) Operating point *S*80, pressure side of blade 8

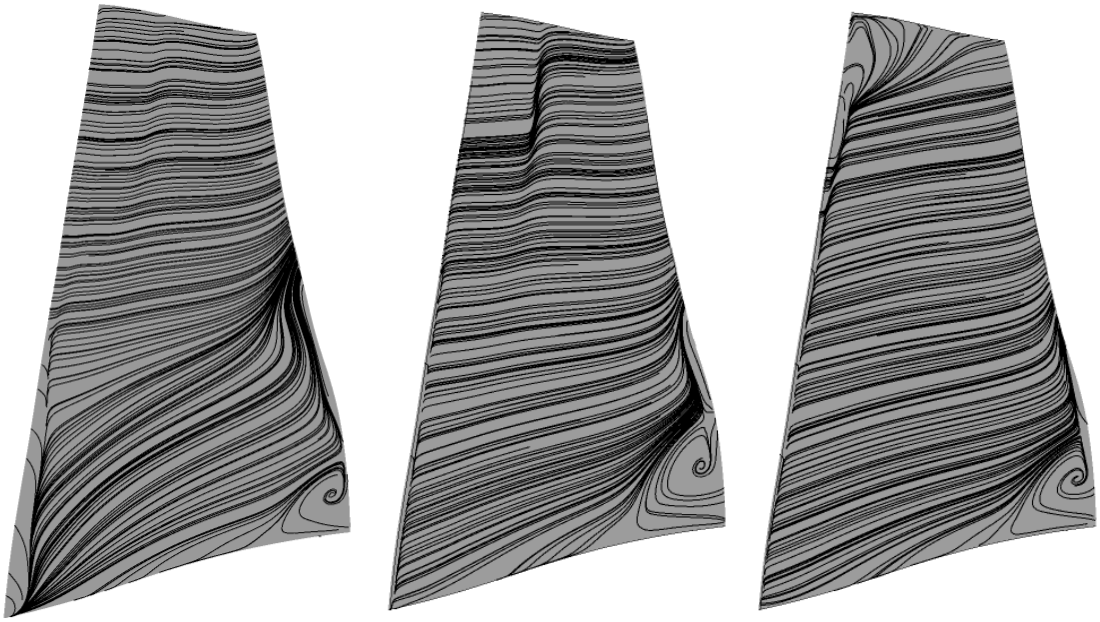

(d) Operating point *A*80, suction side of generic blade

(e) Operating point *S*80, suction side of blade 5

(f) Operating point *S*80, suction side of blade 8

Figure 4.19: Visualization of blade streaklines on both pressure and suction side for a generic blade of the datum NASA Rotor 67 configuration operating at *A*80 and the blade 5 and blade 8 of the Coupled system operating at *S*80 (streamwise direction from left to right)

4.4 Comparison of different rotational speeds solutions

In this section, a comparison of the numerical solutions discussed in § 4.2 and 4.3, i.e. relative to the coupled system configuration with the rotor operating at 100% and 80% of the original rotor design rotational speed (N_d), respectively, is presented. This comparison encompass the analysis of the S-shaped intake aerodynamics, the flow field description at the AIP and the change in rotor performance caused by the presence of the S-duct upstream configuration. This change was quantified with numerical correlations obtained between the loss of stability pressure ratio and the swirl distortion level.

4.4.1 S-shaped intake aerodynamics

As the rotational speed increased, the onset point of separation moved backwards while the point of reattachment moved forwards. By considering the operating points characterized by the lowest and highest rotor corrected mass flow, the pressure recovery reduced from 0.991 to 0.976. Meanwhile, the length of separation increased from 0.25 to $0.5 \cdot z/L$. This change reflected on that relative to the mass flow redistribution observed at the AIP as shown in Fig. 4.20. The increase of both rotational speed and mass flow caused a change of mass flow redistribution. Clearly, this change determined in turn a change in loading relative to each rotor blades.

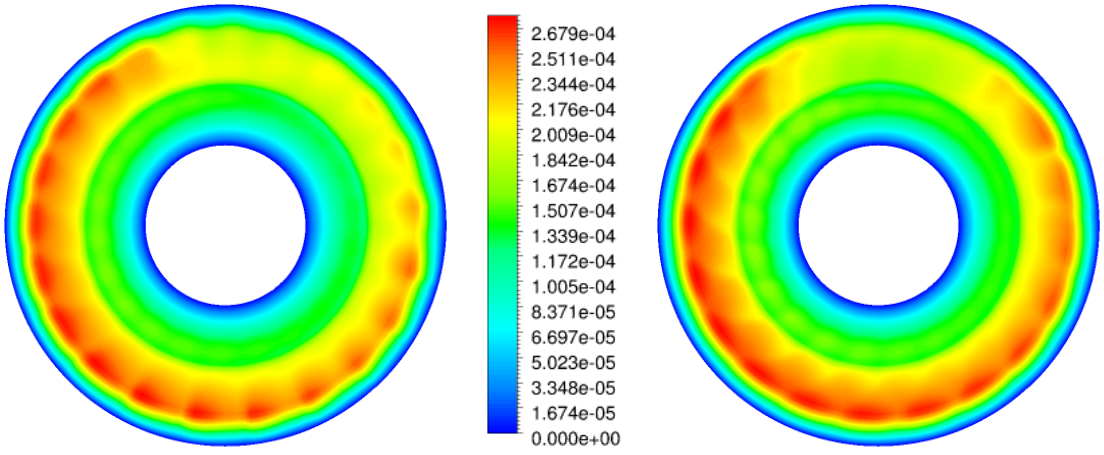

(a) Near stall, 80% N_d (c) Near choking, 100% N_d

Figure 4.20: Contours of local to total mass flow at the AIP of the coupled system configuration

4.4.2 Flow field description at the AIP

In this section, a comparison relative to both the total pressure and swirl distortion between the two rotational speed investigated is discussed.

4.4.2.1 Total pressure distortion

Referring to Fig. 4.21(a), the increase of rotational speed from 80% to 100% N_d was clearly accompained with an increase in corrected mass flow (W_{cor}). Hence, between the near stall operating point at 80% and the near choking operating point at 100% N_d, the total pressure distortion parameter (DC_{60}) increased from 0.105 to 0.284. Within this range, total pressure distortion reached values where its contribution to the change of rotor performance are considered significant[67]. However, the effect of this type of distortion could not be quantified since in the current research occurred simultaneously with the swirl distortion.

4.4.2.2 Swirl distortion

The comparison of the swirl distortion between the two rotational speed investigated was carried out by considering a unique number at the AIP. As discussed in § 4.2.3.2 and 4.3.3.2, the vorticity pattern at the AIP of the coupled system results asymmetric due to the bulk swirl introduced by the rotor placed downstream of the intake itself. Hence, an indication of the swirl distortion was represented by the arithmetic average of peak streamwise vorticity ($\omega^{\star}_{z,mean}$). This parameter was defined as the arithmetical average of the magnitude of the peak positive and negative non-dimensional streamwise vorticities ($\omega^{\star,+}_{z,peak}$ and $|\omega^{\star,-}_{z,peak}|$) as given in Eq. 4.3.

$$\omega^{\star}_{z,mean} = \frac{\omega^{\star,+}_{z,peak} - |\omega^{\star,-}_{z,peak}|}{2} \tag{4.3}$$

Figure 4.21(b) shows the trend of this parameter with the corrected mass flow (W_{cor}) and for the two rotational speed investigated. As observed for the total pressure distortion a large jump of this parameter is observed between the two rotational speed investigated. This confirms that even the swirl distortion does not change linearly. Therefore, for the intake configuration analyzed both total pressure and swirl distortion were related each other.

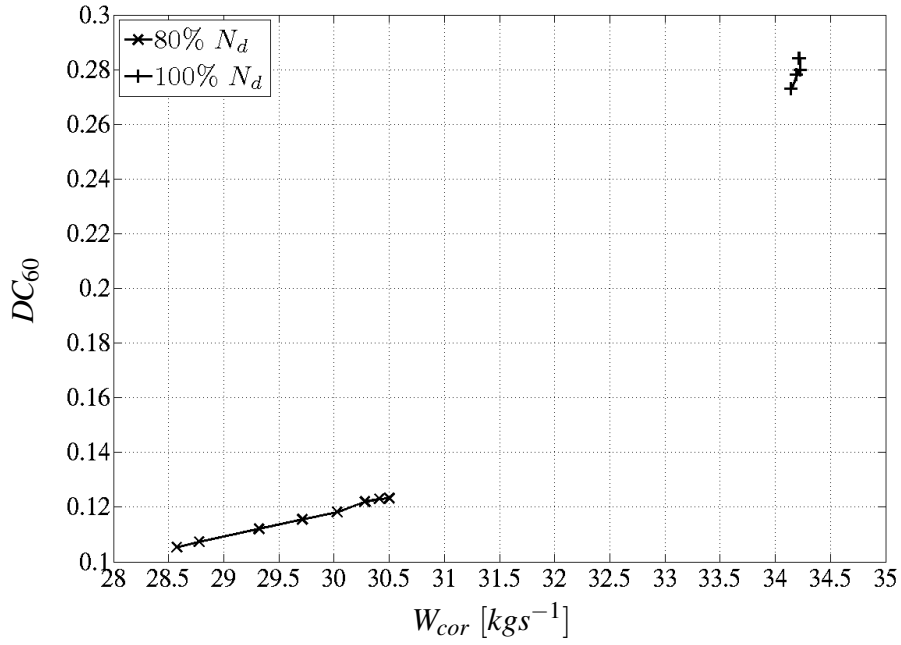

(a) Total pressure distortion parameter (DC_{60})

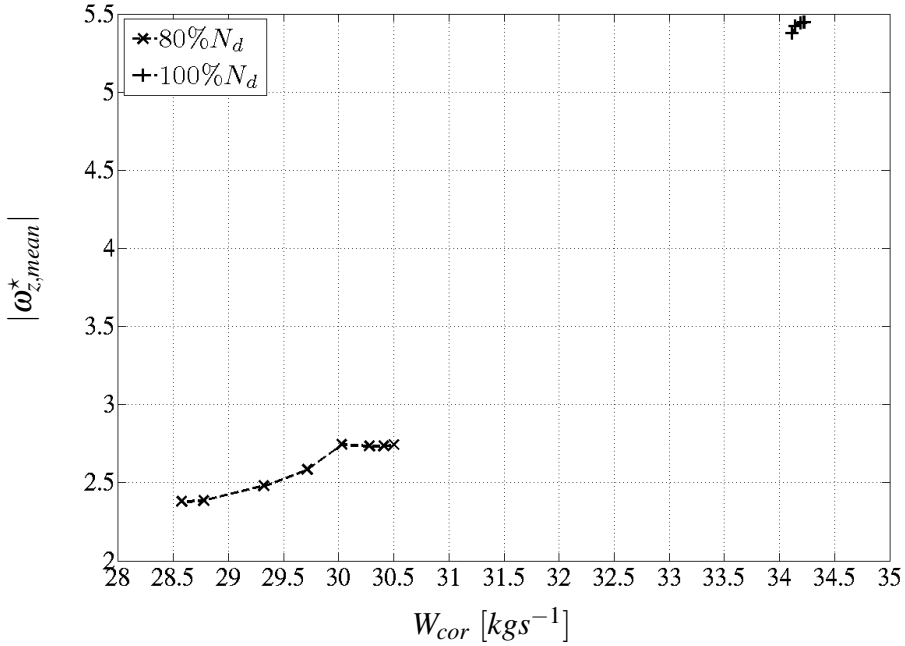

(b) Arithmetic average of non-dimensional peak streamwise vorticity ($|\omega^{\star}_{z,mean}|$)

Figure 4.21: Total pressure and swirl distortion parameters at the AIP versus corrected mass flow (W_{cor}) with the rotor operating at 80% and 100% N_d along the whole operability range

4.4.3 S-duct effect on rotor performance

A comparison of the change of rotor performance for the two rotational speed was carried out by considering the loss of stability pressure ratio (ΔPRS) defined at constant rotational speed (see § 3.3.9). Referring to Table 4.1, this value was calculated for the two rotational speed investigated. Moreover, the swirl distortion was quantified at the AIP with a unique number. For this purpose, two parameters were proposed. They were the mass flow average of the magnitude of the relative flow angle change ($|\overline{\Delta\beta}|$) and the arithmetic average non-dimensional peak streamwise vorticity ($\omega^{\star}_{z,mean}$).

Rotational speed	DC_{60}	$\lvert\overline{\Delta\beta}\rvert$	$\lvert\omega^{\star}_{z,mean}\rvert$	$\Delta PRS\%$
80% N_d	0.11	3.82	2.38	3.52
100% N_d	0.27	3.51	5.38	14.4

Table 4.1: Loss of stability pressure ratio (ΔPRS) and parameters for total pressure and swirl distortion with the rotor operating at 80 and 100% N_d

According to the mass flow average of the magnitude of the relative flow angle change ($|\overline{\Delta\beta}|$), the swirl distortion level remained almost constant while the loss of stability pressure ratio (ΔPRS) increased up to 4.1 times as the rotational speed increased between 80% and 100% N_d. On the other hand, by considering the arithmetic average of non-dimensional streamwise peak vorticity ($\omega^{\star}_{z,mean}$), the swirl distortion increased and in the same manner of the total pressure distortion. This information was more realistic than that provided by $|\overline{\Delta\beta}|$ since an increase of streamwise vorticity implies an increase of the swirl distortion level. Moreover, by following practical recommendations[67], the total pressure distortion reached at 100% N_d could no longer be neglected. Therefore, it was concluded that for the coupled system proposed in this work a possible correlation between the loss of stability pressure ratio and the flow distortion would generally require the knowledge of both total pressure and swirl distortion.

4.5 Summary

In this chapter, an investigation of the Reynolds number effect carried out to ascertain the validity of the CFD solution on a purely numerical coupled system S-shaped intake/fan rotor configuration, defined in this research, have been presented. Then, numerical investigations on the whole coupled system operating under clean inlet conditions and for two rotational speeds defined within the typical range of operability of the fan rotor have been reported. The main findings relative to this chapter are summarized below.

1. Both the total pressure and swirl distortion occur simultaneously at the AIP of the coupled system configuration. Referring to the swirl distortion only, the flow pattern is characterized by the presence of a region where the blades are highly loaded. This causes the rotor to stall at a higher mass flow with respect to that relative to the datum NASA Rotor 67 configuration (annular duct configuration). Consequently, the rotor operability range reduced significantly. Also, the flow separation occurs along the whole speedline by causing a mass flow blockage.

2. As the rotor operability changes from near stall to near choking conditions, the self-generated distortion tends to re-balance towards a symmetric paired swirl configuration such as that relative to an isolated intake, presented in § 2.2.2. As result, the overall swirl distortion level increases. This change was notable at reduced rotational speed analysis where the pressure ratio and corrected mass flow reduced with respect to that of the datum configuration of the original rotor.

3. Loss of stability pressure ratio and inlet swirl distortion at the AIP were calculated for the two rotational speed investigated. In particular, the inlet swirl distortion was quantified by means of the mass flow average of the magnitude of the relative flow angle change ($|\overline{\Delta\beta}|$) and the arithmetic average of non-dimensional streamwise peak vorticity ($\omega^{\star}_{z,mean}$). According to the first parameter, the swirl distortion remained essentially constant as the rotational speed increased between 80% and 100% N_d, while the loss of stability pressure ratio increased significantly. Instead, according to the second parameter, the swirl and total pressure distortion increased simultaneously. Following practical recommendations[67], the total pressure distortion reached at 100% N_d could no longer be neglected. Therefore, it was concluded that for the coupled system proposed in this work a possible correlation between the loss of stability pressure ratio and the flow distortion would generally require the knowledge of both total pressure and swirl distortion.

Chapter 5

Coupled system analysis: vortex ingestion

As discussed in § 2.2.4, previous research was also focused on the investigation of the flow field within an S-duct operating with a prescribed vortex ingested at the inlet. However, no studies have been carried out to analyse the effect on compressor performance caused by the self-generated distortion of an S-duct combined with that attributed to an ingested tightly wound-vortex. Instead, this is one of the aim achieved in this work and discussed in this chapter.

As compared with the numerical investigations of the coupled system already presented in § 4 for clean inlet conditions, this chapter reports the same analyses by considering also the ingestion of a tightly-wound vortex at the CFD inlet plane. In total, one hundred CFD solutions were obtained, each requiring about three days of calculations by using the Cranfield University cluster called ASTRAL[66]. In the first section, an analysis on the effect of vortex characteristics on rotor performance, conducted at the original design rotational speed of the rotor (N_d) is reported. This include the effect of vortex location and polarity as well as that of the vortex maximum swirl velocity and size. On the other hand, the second section reports the analysis relative to the effect of throttle setting. Due to the change of rotor operability when mounted under the coupled system, this analysis was feasible only by considering the rotor operating at 80% N_d investigated in the previous chapter. For these case studies, numerical correlations relating the loss of stability pressure ratio with the swirl distortion are also presented. These correlations were calculated with respect to the datum NASA Rotor 67 configuration and considered also the results obtained under clean inlet conditions presented in § 4.4.3.

5.1 The effect of vortex characteristics

In this section, a sensitivity analysis of the vortex characteristics on the flow field of the coupled system is presented. Firstly, the CFD boundary conditions for all of the combinations of case studies are specified. Then, numerical investigations including the analysis of the S-shaped intake aerodynamics, the flow field description at the AIP and the change of rotor performance are reported. Note that for each type of investigation the results are presented by considering separately the effects of vortex location and polarity with respect to that of the vortex maximum swirl velocity and size. In particular, the effect of vortex location and polarity is presented relatively to the vortex 1 (datum), defined in the next section.

5.1.1 Definition of the CFD boundary conditions

The analysis of the effect of vortex characteristics on rotor performance was investigated with the rotor operating at its original design rotational speed ($N_d = 16043\ RPM$) defined in § 3.2.2. In total, three tightly-wound vortices were defined and their characteristics are listed below.

- Vortex 1. This corresponds to the datum vortex defined for this research and its characteristics are presented in § 3.4.2.
- Vortex 2. Compared to vortex 1, the maximum local circumferential velocity (${}^{L}V_{\theta}$) was doubled while the vortex core radius (r_c) and the axial velocity excess ratio ($\Delta V^{*}_{z,ex}$) remained constant. According to the analytical model used in this research to define the vortex circumferential velocity (see § B.1), this vortex was obtained by doubling the vortex circulation, i.e. the vortex circulation (Γ), with respect to that of vortex 1.
- Vortex 3. Compared to vortex 1, the vortex core radius (r_c) was doubled while the maximum local circumferential velocity (${}^{L}V_{\theta}$) and axial velocity ratio ($\Delta V^{*}_{z,ex}$) remained constant. According to analytical model used in this research to define the vortex circumferential velocity (see § B.1), this vortex was obtained by doubling both the vortex circulation (Γ) and the vortex core radius (r_c).

Referring to the coordinate system localized at the vortex centre introduced in § 3.4.1, the distributions of the circumferential velocity (${}^{L}V_{\theta}$) along the radial location (${}^{L}r$) for the three vortices specified above is shown in Fig. 5.1. On the other hand, the numerical values of characteristics for these vortices are listed in Table 5.1.

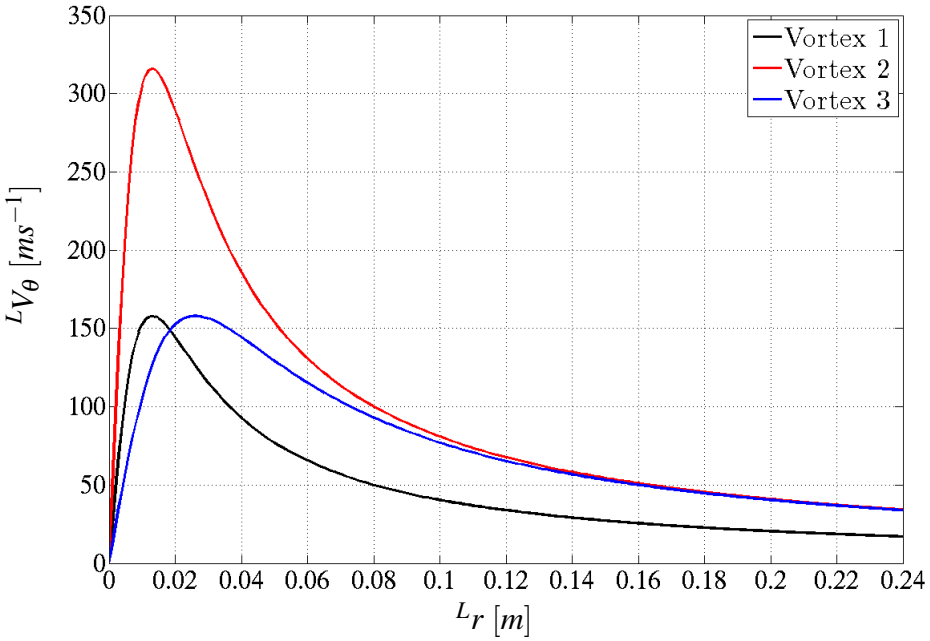

Figure 5.1: Local tangential velocity ($^{L}V_{\theta}$) versus the radial location from the vortex centre (^{L}r)

Vortex characteristic	Vortex 1	Vortex 2	Vortex 3
Γ	25.8	51.6	51.6
r_c	$6\% \cdot D_{in}$	$6\% \cdot D_{in}$	$12\% \cdot D_{in}$
n	1	1	1
ΔV_z^*	0.5	0.5	0.5

Table 5.1: Characteristics of the tightly-wound vortices ingested into the coupled system

Referring to Fig. 3.21, the following boundary conditions were imposed on the CFD domain of the coupled system. The aforementioned vortices were prescribed at the farfield inlet plane, by following the procedure defined in § 3.4.1 and for five different locations. These were aligned with the centre of the intake inlet plane (P_C), and the starboard, bottom, port and top edges (P_S, P_B, P_P and P_T, respectively) as indicated in Fig. 5.2. For each vortex location the two of possible vortex polarities, were investigated. Hence, a total of thirty case studies were investigated.

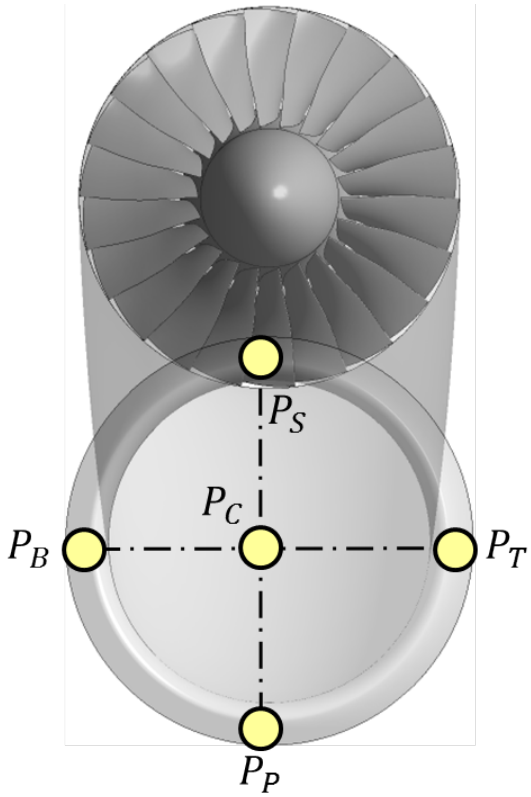

Figure 5.2: Visualization of the vortex locations at the farfield inlet plane of the coupled system CFD domain

As already discussed in § 4.2.4, the S-duct configuration upstream of the rotor operating at its design speed caused a significant reduction of the rotor operability. Therefore, the rotor outlet static to inlet total pressure ($p_{out}/P_{0,in}$) was kept constant to a mean value of 0.987 for all of the case studies. This value corresponded to an operating point found at the middle of the rotor speedline of the coupled system operating under clean inlet conditions (see Fig. 4.7). Consequently, the throttle setting condition was not remaining constant between the ingested cases and therefore a direct comparison of the case studies could not be accomplished. However, the changes relative to the clean inlet conditions were relatively small and are presented in § C.

The 'free-slip wall' boundary condition was imposed at the farfield wall to avoid the generation of a boundary layer and, then, its influence on the flow of the farfield zone. Finally, a uniform static pressure field was imposed at the farfield outlet plane in a similar manner already discussed in § 4.2.1.

5.1.2 S-shaped intake aerodynamics

As a vortex was prescribed at the farfield inlet plane of the CFD domain of the coupled system, it travelled towards the intake and then was ingested into it. According to the combination of intake size and mass flow range of the system, a contracted capture streamtube was defined upstream of the intake inlet plane. Within this zone, a generic vortex was subjected to a stretching due to the streamtube contraction ratio. Meanwhile, vortices prescribed at the locations aligned with the edge of the intake (i.e. at P_S, P_B, P_P and P_T) moved radially towards the centre of the intake inlet plane up to $0.7 \cdot R_i$, independently of the vortex characteristics. On the other hand, the vortex centre location remained unchanged when ingested at the centre of the intake inlet plane (i.e. prescribed at P_C). In general, due to limitations associated with the CFD model, the ingested vortices could be subjected to numerical dissipation before entering within the intake. However, the focus of the current research is to reveal the change of rotor performance associated with a flow distortion pattern measured at the AIP. Therefore, numerical analyses were carried out in the intake and rotor rotor part of the coupled system.

In this section, the intake performance, a qualitative description of the S-duct flow separation and the internal S-duct aerodynamics are discussed.

5.1.2.1 Intake performance

The intake performance was measured with the pressure recovery (η). According to its definition (§ 3.3.8), this parameter requires the specification of the total pressure at infinity upstream ($P_{0,\infty}$). For the coupled system configuration, this quantity corresponds to the mass flow average of the total pressure calculated on the portion of the farfield inlet plane defined within the capture streamtube. Under clean inlet conditions, this value corresponded to that specified as boundary condition at the farfield inlet plane ($P_{0,in}$). On the other hand, as a vortex was ingested into the coupled system, the total pressure field within the capture streamtube was altered. However, according to the total pressure perturbation associated with the vortices defined in this work, it was assumed that $P_{0,\infty} = P_{0,in}$.

Effect of vortex location and polarity Figures 5.3(a) and 5.3(b) show the pressure recovery (η) for co- and counter-rotating vortex 1 (datum), respectively, ingested in the coupled system at different locations. The same parameter calculated under clean inlet conditions (see § 4.2.2) is also indicated. As compared with the pressure recovery (η) calculated under clean inlet conditions, this was generally higher for a co- than for a counter-rotating vortices ingested. Due to the flow distortion associated with an ingested vortex, the mass flow adjusts itself to adapt to the static pressure imposed at the CFD rotor outlet plane. This generally increased or decreased as a counter- or co-rotating vortex was

ingested. In particular, the highest pressure recovery was observed for the co-rotating vortex ingested at the centre of the intake inlet plane (i.e. prescribed at P_C). This result was explained by considering that, as will be discussed in see § 5.1.4, the mass flow reached in these conditions was the lowest.

Effect of vortex maximum swirl velocity and size The increase of either the maximum swirl velocity or size of the co-rotating vortex 1 (datum), i.e. by ingesting vortex 2 or vortex 3, respectively, the pressure recovery (η) was not affected significantly with respect to that calculated under clean inlet conditions (Fig. 5.3(a)). This was valid for any of the vortex locations investigated unless for those ingested at the centre of the intake inlet plane and near the top edge (i.e. prescribed at P_C and P_T, respectively). Regarding the co-rotating vortices ingested at the centre (i.e. prescribed at P_C) a notable increase of η occurred. This outcome was related to the significant reduction of rotor corrected mass flow as vortex 2 or vortex 3 were ingested (see § 5.1.4. On the other hand, for co-rotating vortices ingested at the top edge of the intake (i.e. prescribed at P_T) the pressure recovery reduced significantly as both the maximum swirl velocity or size increased. As will be discussed in § 5.1.2.2, in these conditions a strong interaction was observed between the vortex and the self-generated distortion. This was accompanied with high pressure loss along the intake and notable with the description of the total pressure distortion at the AIP (see 5.1.3.1).

On the other hand, for a counter-rotating vortex ingested, the increase of either the maximum swirl velocity or size of the vortex (obtained with vortex2 and vortex 3, respectively) determined an additional reduction of η as shown in Fig. 5.3(b). This was more pronounced with the ingestion of vortex 2 rather than with that of the vortex 3. This difference could be attributed to a higher dissipation to which the vortex 2 was subjected with respect to the vortex 3. Therefore, lower total pressure values were achieved with the ingestion of the vortex 2 around its perturbation as also shown in § 5.1.3.1.

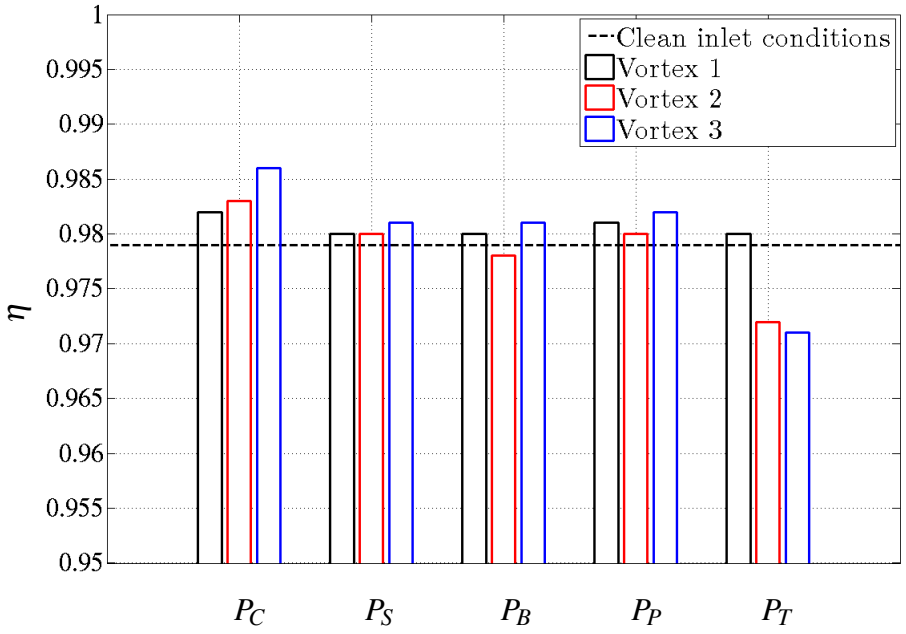

(a) Co-rotating vortices ingested

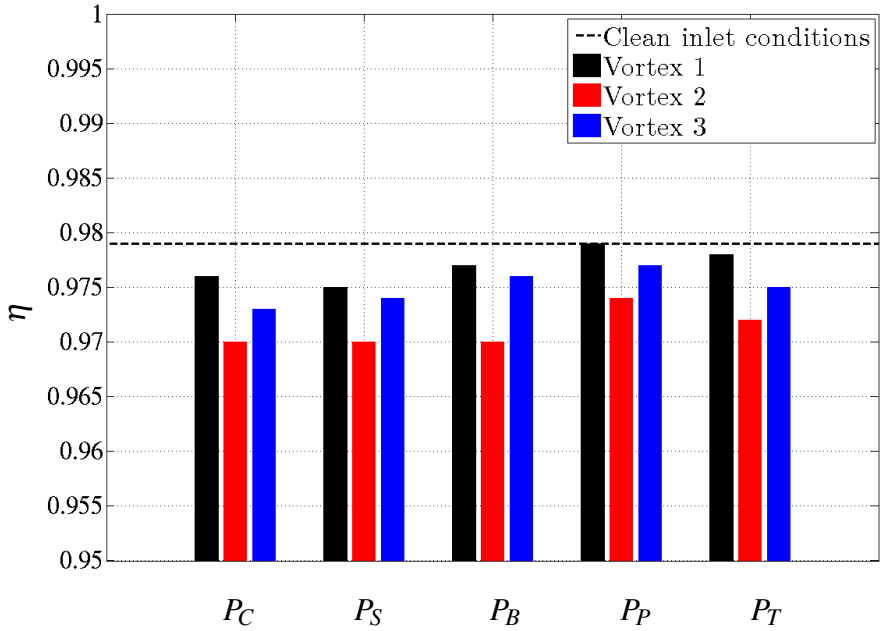

(b) Counter-rotating vortices ingested

Figure 5.3: Pressure recovery (η) for different vortex locations and polarities and with the rotor operating at 100% N_d and $p_{out}/P_{0,in} = 0.987$

5.1.2.2 Description of the S-duct flow separation

In this section, a qualitative description regarding the change of the S-duct flow separation pattern caused by the vortex ingestion is presented. Note that, a quantitative analysis of the flow separation pattern, such as that presented in § 4.2.2.2 and 4.3.2.2, could not accomplished since this was no longer identifiable for part of the ingested vortex cases.

Effect of vortex location and polarity Figures 5.4 and 5.5 show the contours of skin friction coefficient (C_f) with the streaklines on the starboard side of the intake wall relative to the coupled system operating under clean inlet conditions and by ingesting at different locations co- and counter-rotating vortex 1 (datum), respectively. Regardless of the vortex location and polarity, the S-duct flow separation tended to become asymmetric and shifted circumferentially according to the path followed by the vortex within the S-duct. As already observed by Anderson[2], this spiraled out around the intake wall in the rotational direction of the vortex itself. This result was also notable with the description of the flow field at the AIP (see in § 5.1.3). Moreover, as the interaction level between the S-duct self-generated distortion and the ingested vortex increased, the number of wall streaklines reduced and tended to converge towards a circumferential location dictated by the vortex polarity. As already indicated by Wendt et al.[33], this phenomena revealed the vortex surface trajectory and indicated a secondary (transverse) flow separation within the duct itself (see § 2.2.4.1).

Amongst the vortex locations investigated, that ingested near the starboard edge (i.e prescribed at P_S) (Fig. 5.4(c)) caused the largest change in S-duct flow separation pattern with respect to that obtained under clean inlet conditions (Fig. 5.4(a) or 5.5(a)). Then, the S-duct flow separation change was still significant for the co-rotating and counter-rotating vortices ingested near the top and bottom edge (i.e prescribed at P_T and P_B) as shown in Fig. 5.4(f) and 5.5(d), respectively. On the other hand, vortices ingested at the centre of the intake inlet plane (i.e. prescribed at P_C) determined no significant changes in S-duct flow separation as shown in Fig. 5.4(b) and 5.5(b). However, the influence of the vortex was notable downstream of the reattachment point with the coalescence of the wall streaklines towards the rotor face. Finally, the location of vortices ingested near the port (i.e. prescribed at P_P) throughout the duct remained circumferentially opposite to that of the S-duct flow separation. Therefore, this was not significantly affected by the vortex itself (Fig. 5.4(e) and 5.5(e)).

Effect of vortex maximum swirl velocity and size The increase of either maximum swirl velocity or size of the co-rotating vortex 1 (datum) ingested, obtained by ingesting vortex 2 or vortex 3, respectively, determined a similar change of separation pattern. This outcome was consistent with the methods of images[68]. According to this method, the shift along the circumferential direction is proportional to the distance of the vortex centre from

the wall and the vortex strength. As discussed in § 5.1.2 and 5.1.1, these two parameters remained unchanged for vortex 2 and vortex 3.

According to the analysis of vortex location reported in the previous paragraph, the vortex 1 ingested near the starboard edge (i.e. prescribed at P_S) caused the largest influence on the S-duct flow separation (Fig. 5.6(a)). For this location, as either the maximum swirl velocity (Fig. 5.6(b) and 5.6(e)) or the size of the vortex 1 increased (Fig. 5.6(c) and 5.6(f)) the extent of the self-generated distortion reduced. As a result, only the halve of the self-generated distortion opposite to the vortex path remained alive while its intensity increased.

Referring to Fig. 5.7, the counter- and co-rotating vortex 1 ingested near the bottom and the top (i.e. prescribed at P_B and P_T), respectively, impacted directly the S-duct flow separation around the lowest velocity region. As either the vortex maximum swirl velocity or size increased, i.e. with the ingestion of vortex 2 or vortex 3, the interaction between the ingested vortex and the self-generated distortion increased. Therefore, the resulting duct separation region was significantly affected and unsteadiness were obtained in the CFD solution.

Finally, for the remaining combinations of vortex location and polarity defined in § 5.1.1, the effect of vortex characteristics on the separation pattern was minor as shown in Fig. 5.9 and 5.10.

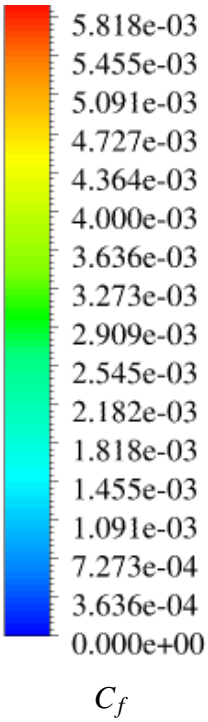

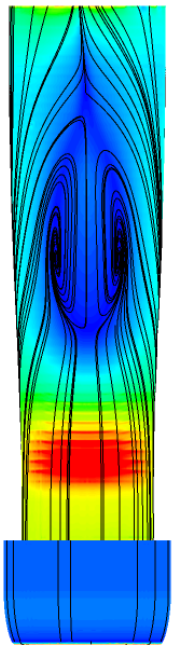

(a) Clean inlet conditions

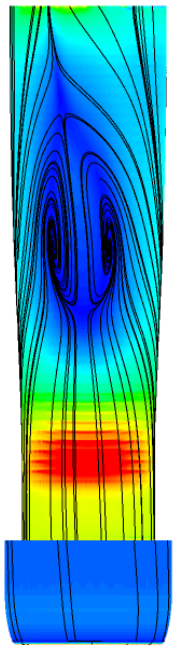

(b) Vortex 1 prescribed at P_C

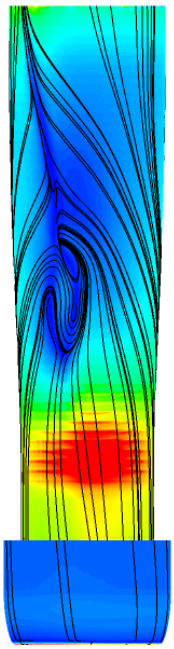

(c) Vortex 1 prescribed at P_S

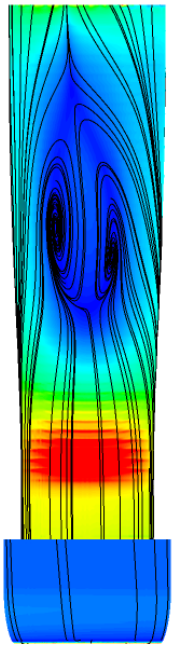

(d) Vortex 1 prescribed at P_B

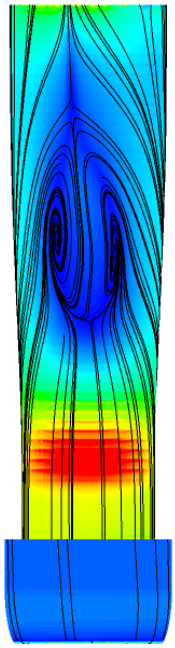

(e) Vortex 1 prescribed at P_P

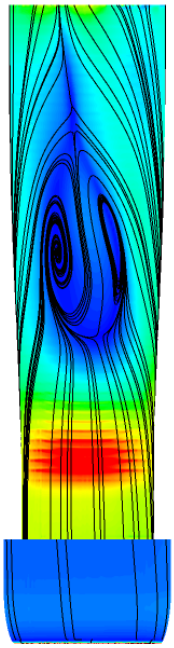

(f) Vortex 1 prescribed at P_T

Figure 5.4: Contours of skin friction coefficient (C_f) with streaklines (black) at the starboard side of the intake wall for co-rotating vortex 1 (datum) prescribed at different locations and with rotor operating at 100% N_d and $p_{out}/P_{0,in} = 0.987$

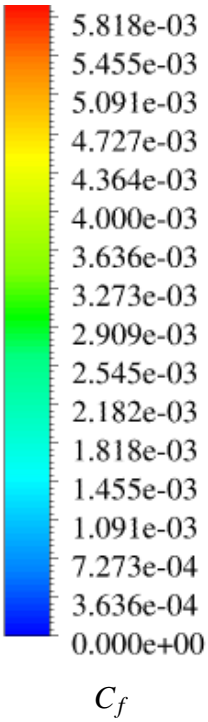

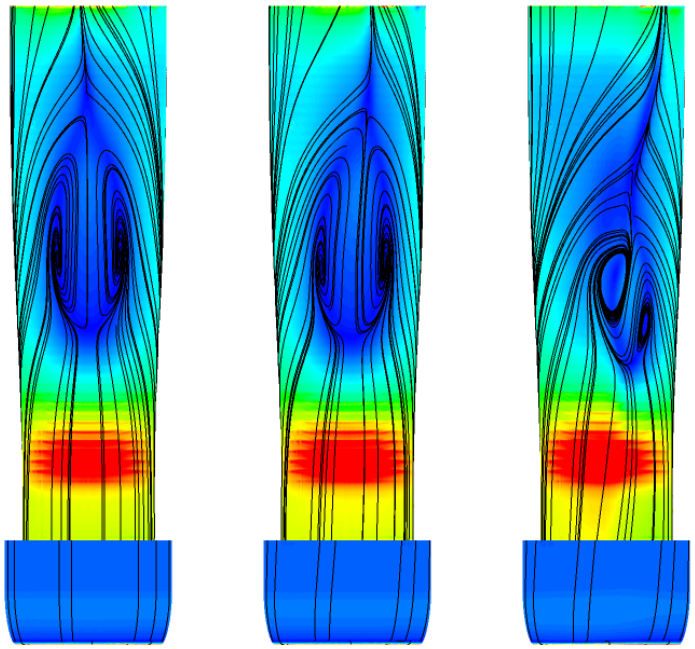

(a) Clean inlet conditions

(b) Vortex 1 prescribed at P_C

(c) Vortex 1 prescribed at P_S

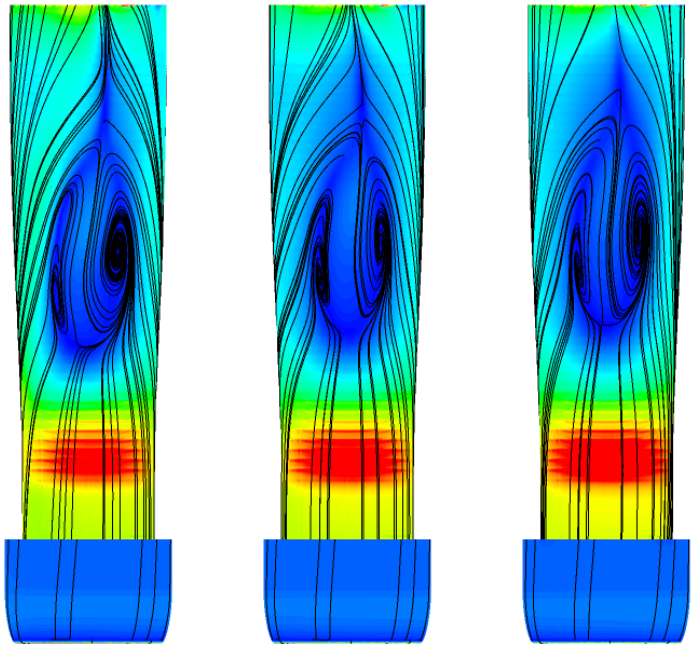

(d) Vortex 1 prescribed at P_B

(e) Vortex 1 prescribed at P_P

(f) Vortex 1 prescribed at P_T

Figure 5.5: Contours of skin friction coefficient (C_f) with streaklines (black) at the starboard side of the intake wall for counter-rotating vortex 1 (datum) prescribed at different locations and with rotor operating at 100% N_d and $p_{out}/P_{0,in} = 0.987$

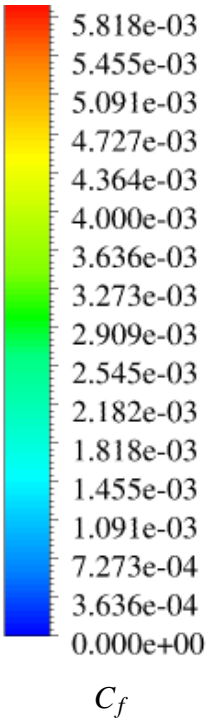

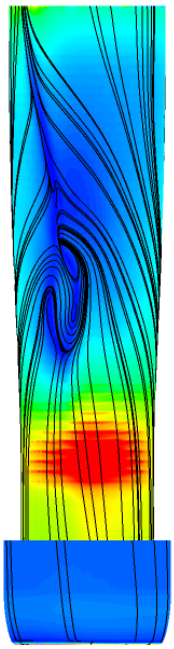

(a) Co-rotating vortex 1

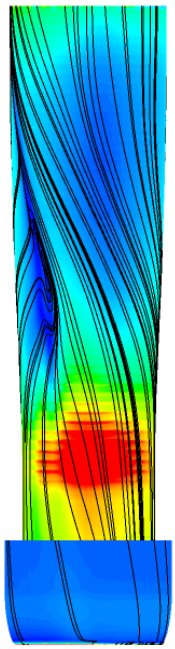

(b) Co-rotating vortex 2

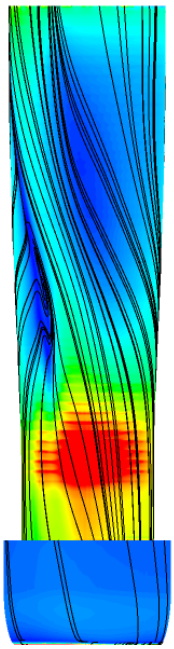

(c) Co-rotating vortex 3

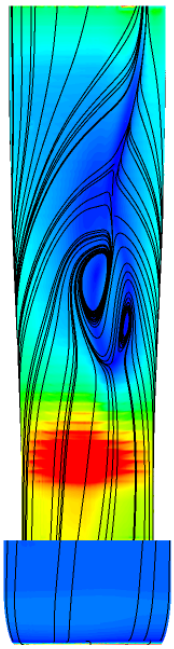

(d) Counter-rotating vortex 1

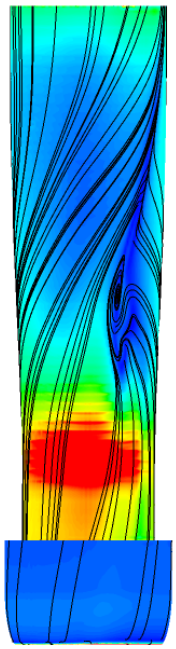

(e) Counter-rotating vortex 2

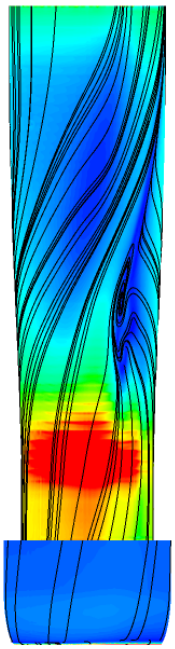

(f) Counter-rotating vortex 3

Figure 5.6: Contours of skin friction coefficient (C_f) with streaklines (black) at the starboard side of the intake wall for vortices ingested near the starboard (i.e. prescribed at P_S) prescribed at different locations and with rotor operating at 100% N_d and $p_{out}/P_{0,in} = 0.987$

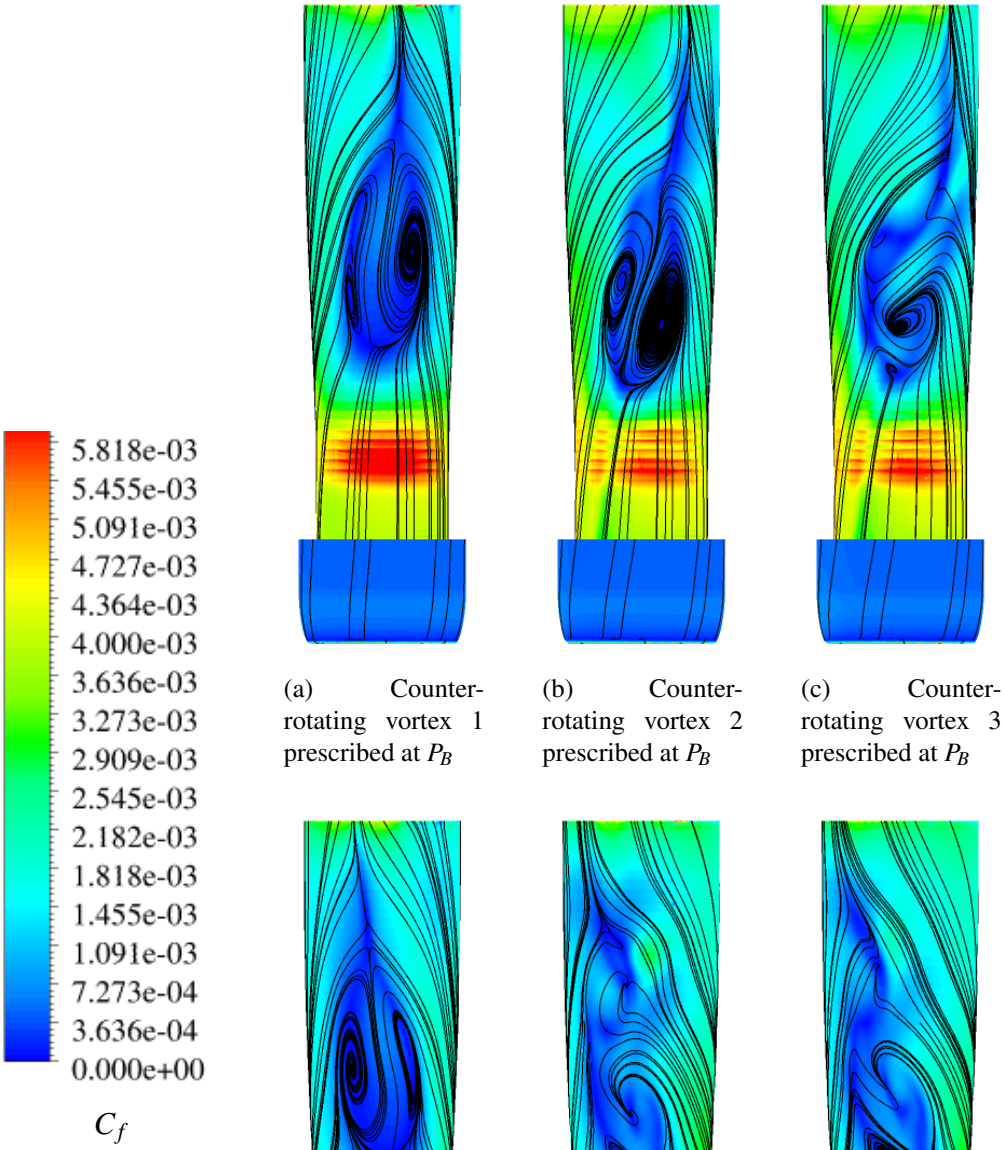

(a) Counter-rotating vortex 1 prescribed at P_B

(b) Counter-rotating vortex 2 prescribed at P_B

(c) Counter-rotating vortex 3 prescribed at P_B

(d) Co-rotating vortex 1 prescribed at P_T

(e) Co-rotating vortex 2 prescribed at P_T

(f) Co-rotating vortex 3 prescribed at P_T

Figure 5.7: Contours of skin friction coefficient (C_f) with streaklines (black) at the starboard side of the intake wall for counter- and co-rotating vortices prescribed at P_S and P_T, respectively, prescribed at different locations and with rotor operating at 100% N_d and $p_{out}/P_{0,in} = 0.987$

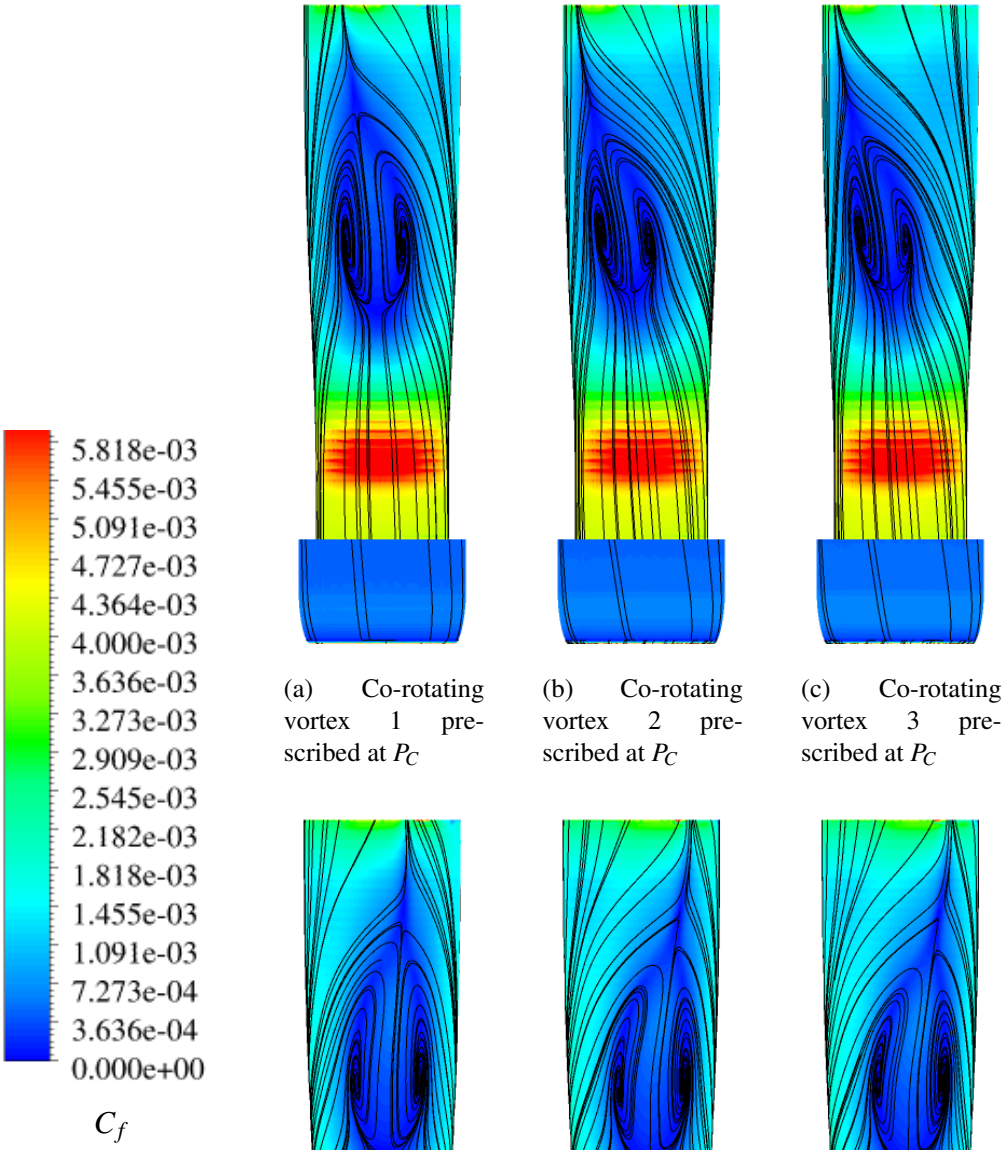

(a) Co-rotating vortex 1 prescribed at P_C

(b) Co-rotating vortex 2 prescribed at P_C

(c) Co-rotating vortex 3 prescribed at P_C

(d) Counter-rotating vortex 1 prescribed at P_C

(e) Counter-rotating vortex 2 prescribed at P_C

(f) Counter-rotating vortex 3 prescribed at P_C

Figure 5.8: Contours of skin friction coefficient (C_f) with streaklines (black) at the starboard side of the intake wall for vortices ingested at centre (i.e. prescribed at P_C) prescribed at different locations and with rotor operating at 100% N_d and $p_{out}/P_{0,in} = 0.987$

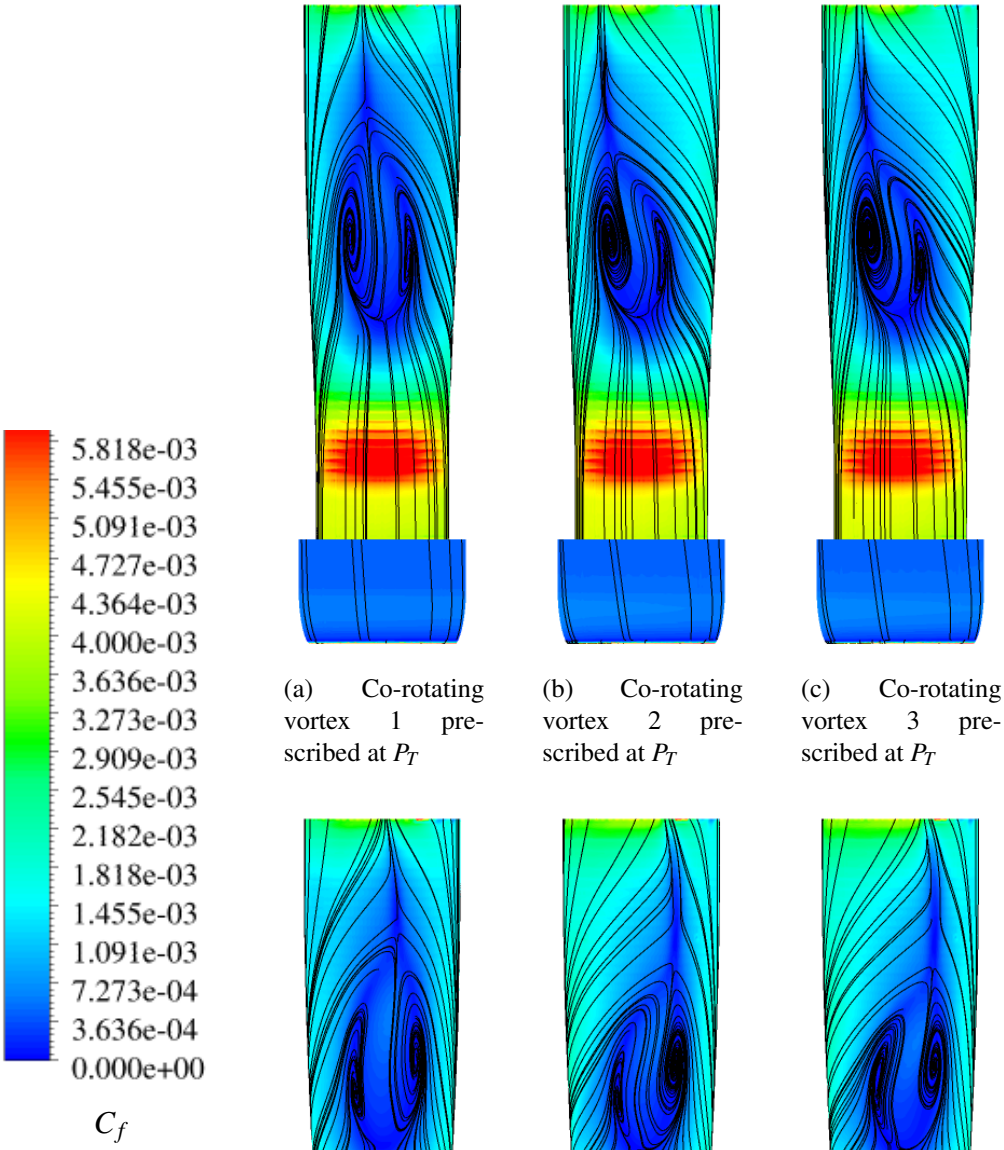

(a) Co-rotating vortex 1 prescribed at P_T

(b) Co-rotating vortex 2 prescribed at P_T

(c) Co-rotating vortex 3 prescribed at P_T

(d) Counter-rotating vortex 1 prescribed at P_T

(e) Counter-rotating vortex 2 prescribed at P_T

(f) Counter-rotating vortex 3 prescribed at P_T

Figure 5.9: Contours of skin friction coefficient (C_f) with streaklines (black) at the starboard side of the intake wall for vortices ingested near the port (i.e. prescribed at P_T) prescribed at different locations and with rotor operating at 100% N_d and $p_{out}/P_{0,in} = 0.987$

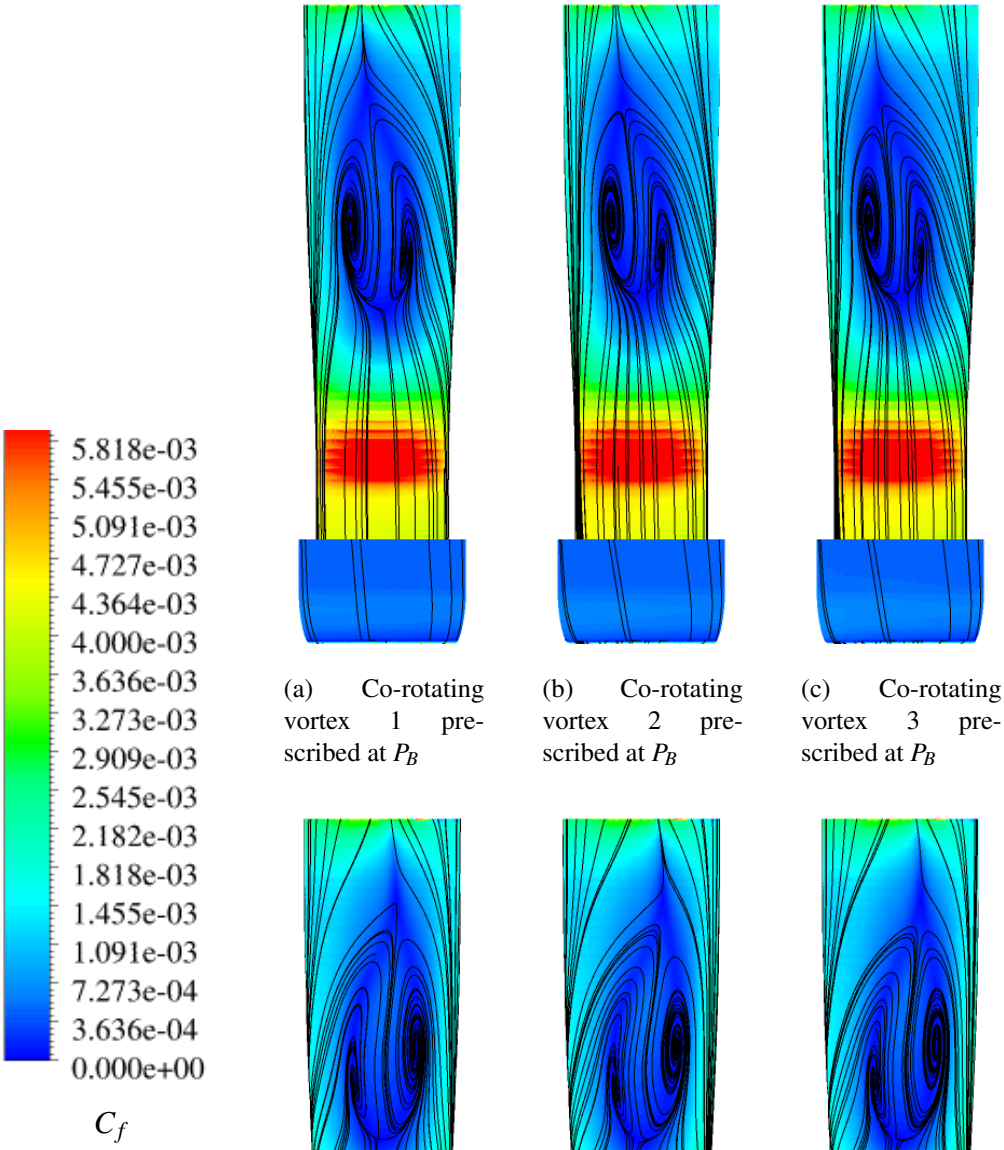

(a) Co-rotating vortex 1 prescribed at P_B

(b) Co-rotating vortex 2 prescribed at P_B

(c) Co-rotating vortex 3 prescribed at P_B

(d) Counter-rotating vortex 1 prescribed at P_T

(e) Counter-rotating vortex 2 prescribed at P_T

(f) Counter-rotating vortex 3 prescribed at P_T

Figure 5.10: Contours of skin friction coefficient (C_f) with streaklines (black) at the starboard side of the intake wall for vortices ingested near the bottom and starboard (i.e. prescribed at P_B and P_T, respectively) prescribed at different locations and with rotor operating at 100% N_d and $p_{out}/P_{0,in} = 0.987$

5.1.2.3 Internal duct aerodynamics

In this section, an investigation of the internal S-duct aerodynamics is presented. This was accomplished by considering the flow field on cross flow planes defined perpendicularly to the centerline.

Effect of vortex location and polarity Figures 5.11 and 5.12 show the 2D streamlines obtained on cross flow planes with co- and counter-rotating vortex 1 (datum), respectively, ingested at the centre of the intake inlet plane (i.e. prescribed at P_C). Regardless of its polarity, this vortex remained essentially aligned with the duct centerline along the whole duct itself. Therefore, the ingested vortex introduced a centered bulk swirl which was superimposed to the baseline flow of the S-duct itself (see § 4.2.2.3). On the other hand, vortices ingested near the intake wall (i.e. prescribed at P_S, P_B, P_P and P_T) followed a spiral around the inside part of the duct wall in a direction corresponding to that of the ingested vortex itself. This outcome was in agreement with the numerical results obtained by Anderson[2] (see § 2.2.4.2) and was notable with the description of the flow field at the AIP presented in § 5.1.3.

Effect of vortex maximum swirl velocity and size The numerical results presented in this paragraph were necessary to confirm the effect of the vortex maximum swirl velocity and size on the S-duct flow separation discussed in § 5.1.2.2. Figures 5.13 – 5.17 show the trends of spatial fluctuations of the static pressure and tangential velocity component ($(p')^*$ and $(V'_\theta)^*$), both defined in § 3.3.2, calculated on planes disposed perpendicularly to the S-duct centerline and for different combinations of vortex location and polarity. For clean inlet conditions and by moving towards the AIP, the spatial fluctuation of static pressure ($(p')^*$) presented a maximum at the first bend where the flow changed the streamwise direction. Then, it reduced until zero at the half of the duct due to the change of the sign of the duct centerline curvature*. Finally, a maximum relative was reached at $z/L = 0.1$ due to the presence of the spinner placed downstream. On the other hand, the standard deviation of tangential velocity component ($(V'_\theta)^*$) reached two minimum at the axial locations which indicated the limits of the S-duct flow separation (see 4.2.2.2). Downstream of the reattachment point a continuous increase of the spatial fluctuations occurred since the rotor disturbances increased up to the AIP.

As a vortex was ingested in the S-duct, this caused a shift of the spatial fluctuations which varied along the S-duct itself. The sign and magnitude of this shift was the result of the interaction between the ingested vortex and the S-duct flow field and the fluctuation introduced by the vortex itself.

Referring to Fig. 5.14(b), the increase of either the maximum swirl velocity or size

*The same phenomena was also observed during experiments by Wellborn[1]

of the vortex 1 (i.e. vortex 2 or vortex 3) ingested near the starboard edge (i.e. prescribed at P_S) caused the disappearance the two minimum of $(V'_\theta)^*$, while this parameter increased towards the AIP due to the presence of rotor disturbances. On the other hand, the influence of vortex characteristics was minor on the spatial fluctuations of static pressure ($(p')^*$) as shown in Fig. 5.14(a).

On the other hand, by considering the ingestion of counter- and co-rotating vortices ingested near the bottom and the top of the intake edge (i.e. prescribed at P_B and P_T), respectively, the trends of the spatial fluctuations was irregular along the S-duct with the ingestion of vortex 2 or vortex 3 as shown in Fig. 5.15 and 5.17. For these cases, the CFD solutions presented oscillations of the RMS of residuals equations with numerical iterations, resulting then unsteady.

Finally, for vortices ingested either at the centre intake inlet and near the port intake edge (i.e. prescribed at P_C and P_P), the interaction between the wall and the self-generated distortion was minor and, consequently, the trends of spatial fluctuations throughout the intake was similar to that obtained under clean inlet conditions as shown in Fig. 5.13 and 5.16.

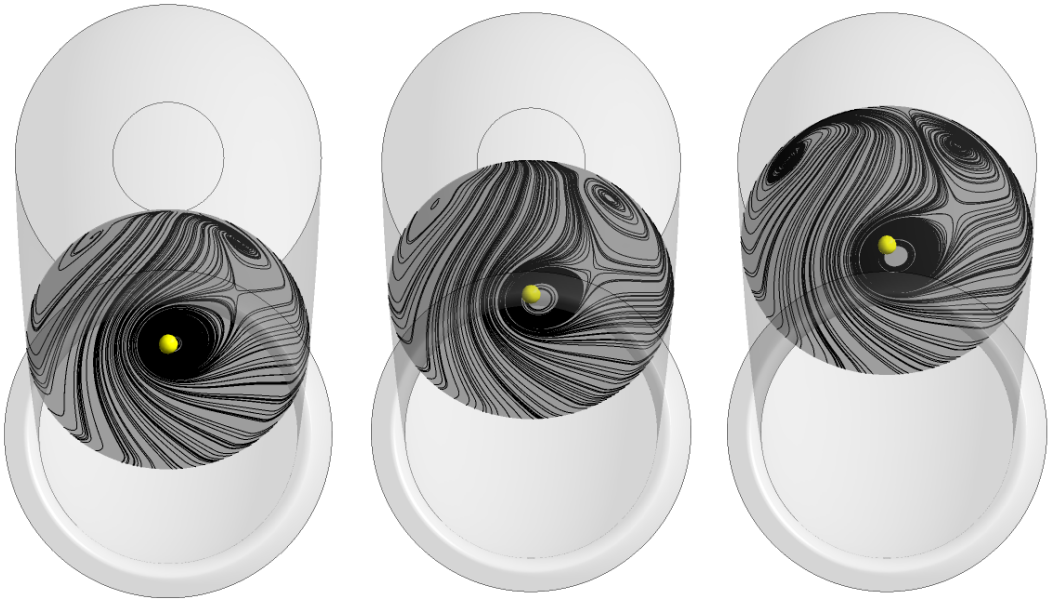

(a) Plane 1 ($z/s = 5.697$) (b) Plane 2 ($z/s = 4.583$) (c) Plane 3 ($z/s = 3.464$)

(d) Plane 4 ($z/s = 2.345$) (e) Plane 5 ($z/s = 1.226$) (f) AIP ($z/s = 0.107$)

Figure 5.11: Front view of 2D streamlines on cross flow planes defined along the S-duct of the coupled system for counter-rotating vortex 1 (datum) ingested at the centre of the intake inlet plane (i.e. prescribed at P_C) and indication of the centerline point (yellow) upstream of the spinner with rotor operating at 100% N_d and $p_{out}/P_{0,in} = 0.987$

(a) Plane 1 ($z/s = 5.697$) (b) Plane 2 ($z/s = 4.583$) (c) Plane 3 ($z/s = 3.464$)

(d) Plane 4 ($z/s = 2.345$) (e) Plane 5 ($z/s = 1.226$) (f) AIP ($z/s = 0.107$)

Figure 5.12: Front view of 2D streamlines on cross flow planes defined along the S-duct of the coupled system for counter-rotating vortex 1 (datum) ingested at the centre of the intake inlet plane (i.e. prescribed at P_C) and indication of the centerline point (yellow) upstream of the spinner with rotor operating at 100% N_d and $p_{out}/P_{0,in} = 0.987$

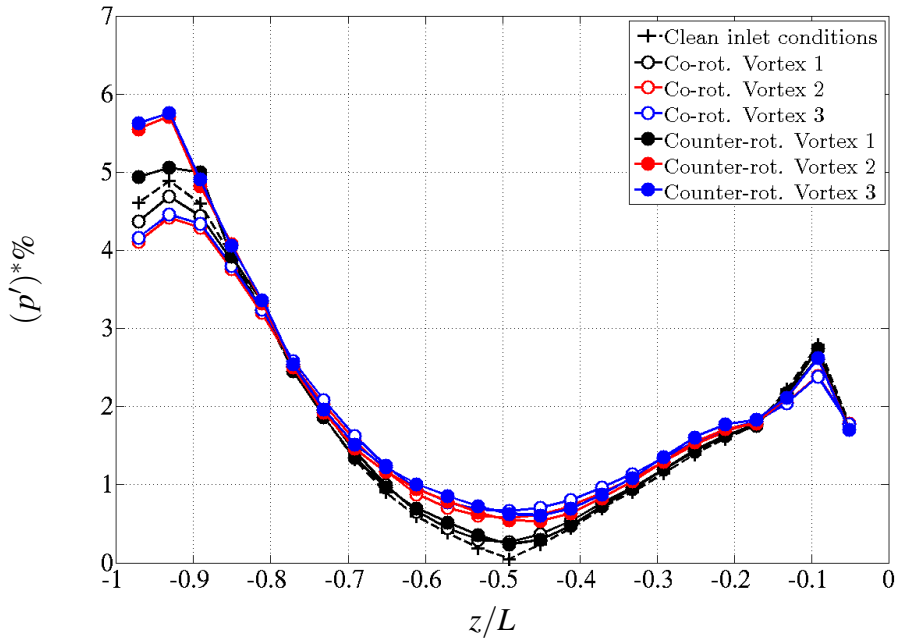

(a) Non-dimensional standard deviation of static pressure ($(p')^*\%$)

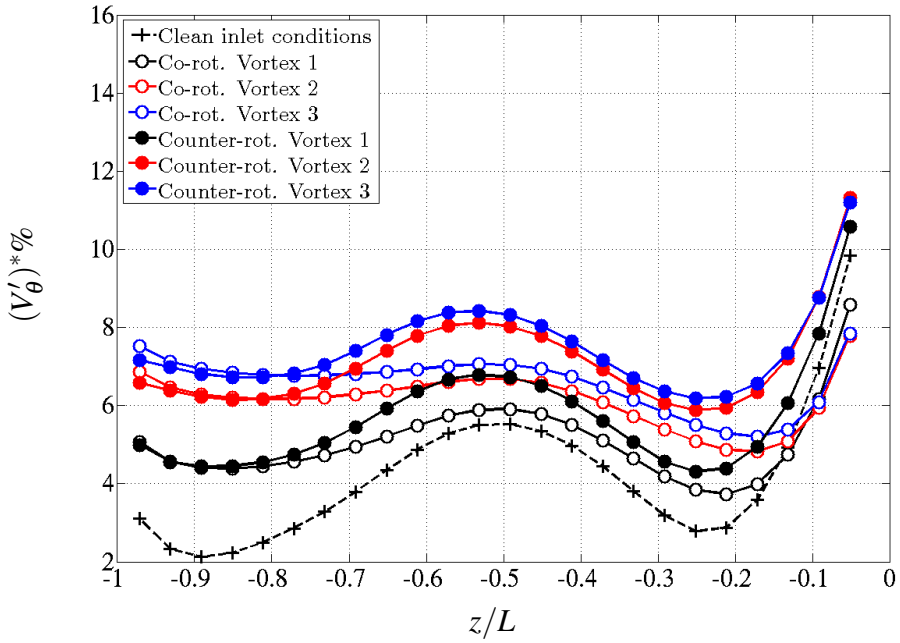

(b) Non-dimensional standard deviation of tangential velocity ($(V'_\theta)^*\%$)

Figure 5.13: Non-dimensional standard deviations calculated along the S-duct for vortices ingested at the centre of the intake inlet plane (i.e. prescribed at P_C) and with rotor operating at 100% N_d and $p_{out}/P_{0,in} = 0.987$

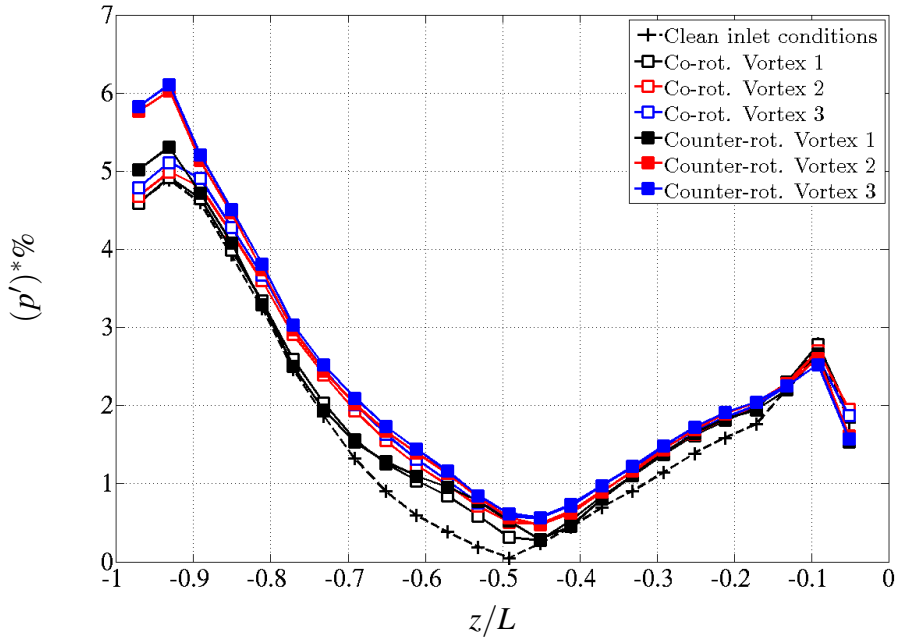

(a) Non-dimensional standard deviation of static pressure ($(p')^*\%$)

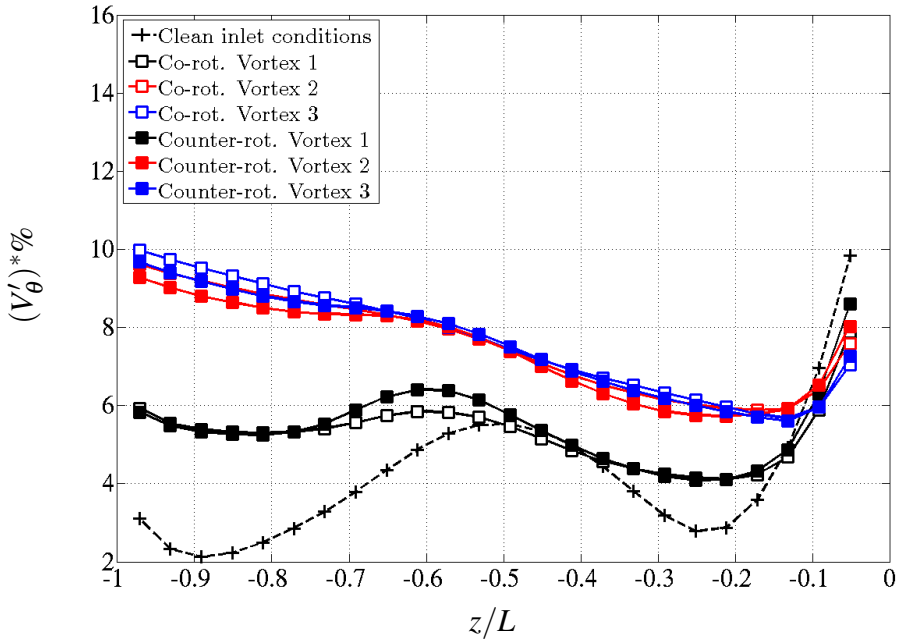

(b) Non-dimensional standard deviation of tangential velocity ($(V'_\theta)^*\%$)

Figure 5.14: Non-dimensional standard deviations calculated along the S-duct for vortices ingested near the starboard edge (i.e. prescribed at P_S) and with rotor operating at 100% N_d and $p_{out}/P_{0,in} = 0.987$

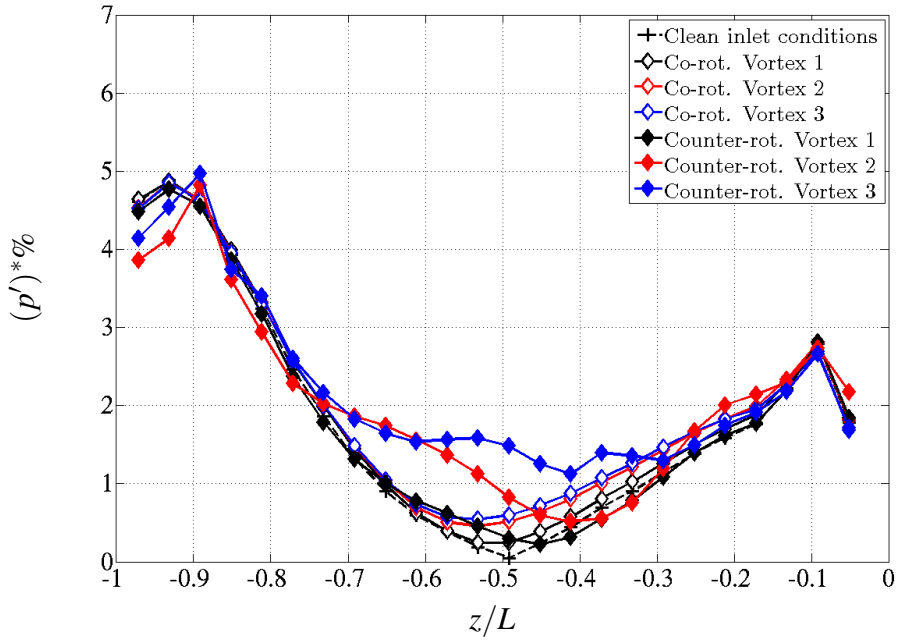

(a) Non-dimensional standard deviation of static pressure ($(p')^*\%$)

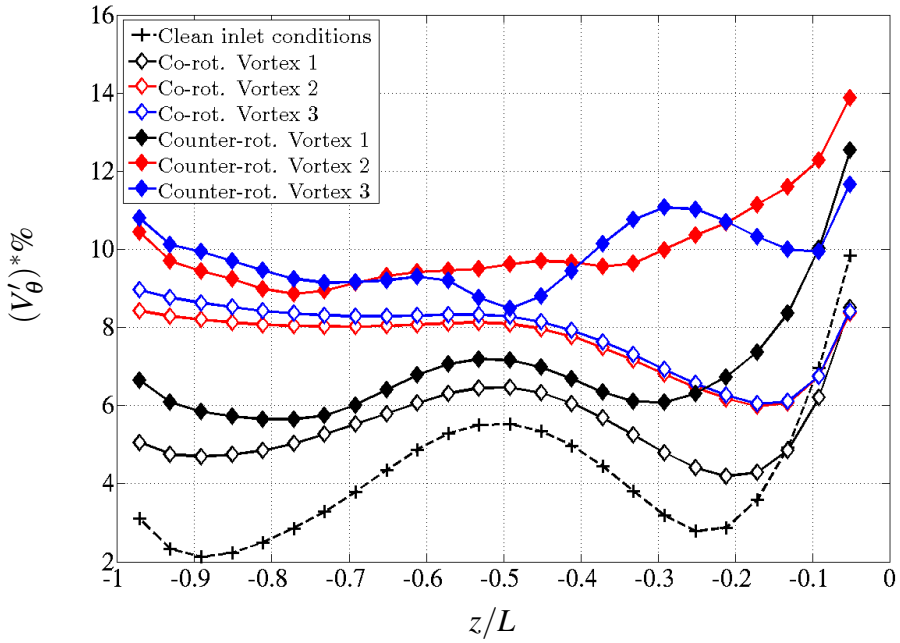

(b) Non-dimensional standard deviation of tangential velocity ($(V'_\theta)^*\%$)

Figure 5.15: Non-dimensional standard deviations calculated along the S-duct for vortices ingested near the bottom edge (i.e. prescribed at P_B) and with rotor operating at 100% N_d and $p_{out}/P_{0,in} = 0.987$

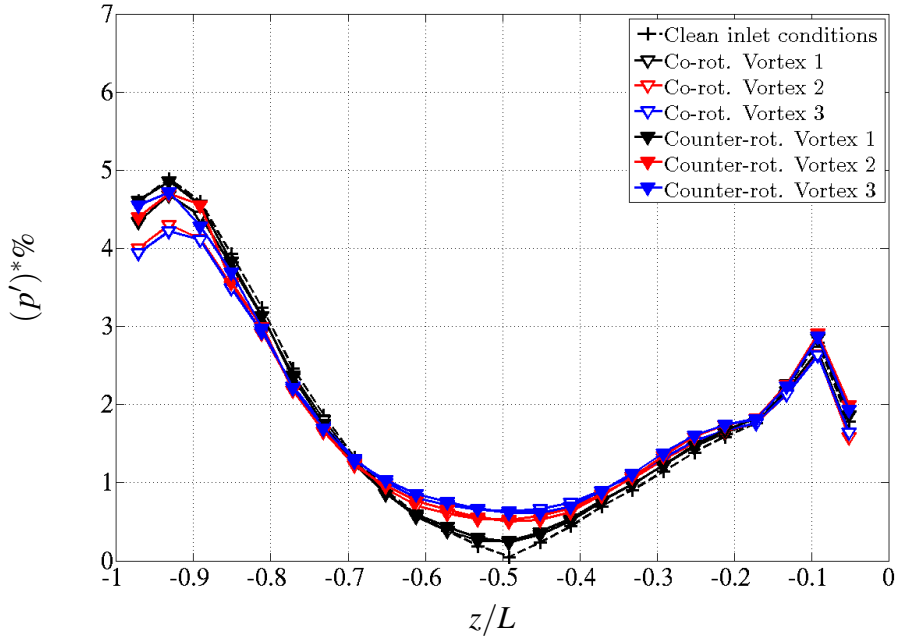

(a) Non-dimensional standard deviation of static pressure ($(p')^*\%$)

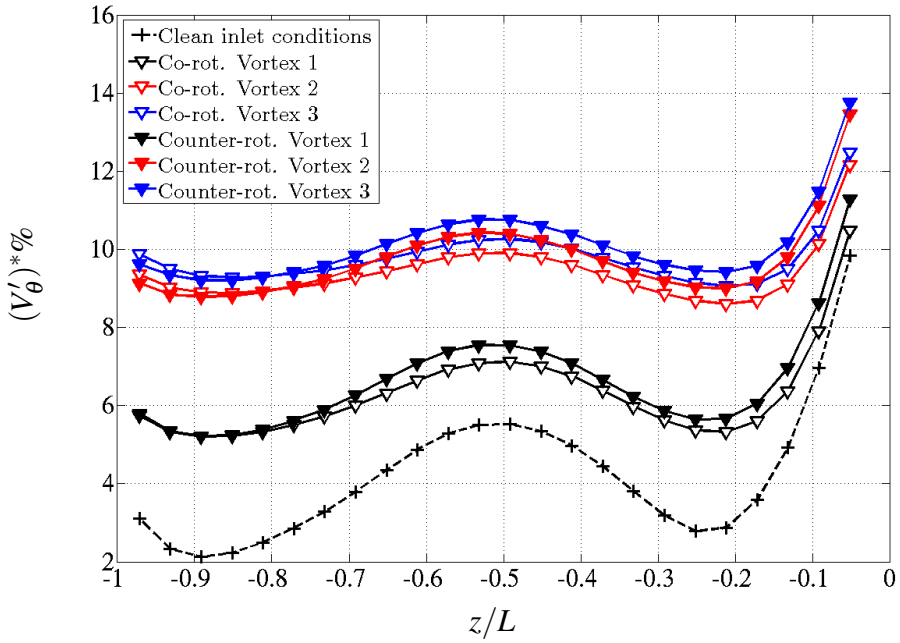

(b) Non-dimensional standard deviation of tangential velocity ($(V'_\theta)^*\%$)

Figure 5.16: Non-dimensional standard deviations calculated along the S-duct for vortices ingested near the port edge (i.e. prescribed at P_P) and with rotor operating at 100% N_d and $p_{out}/P_{0,in} = 0.987$

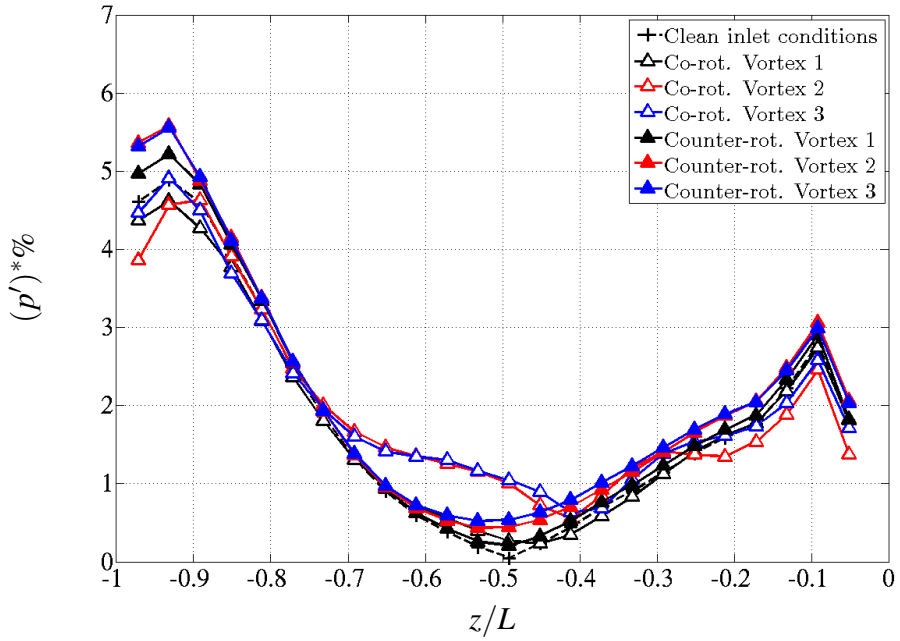

(a) Non-dimensional standard deviation of static pressure ($(p')^*\%$)

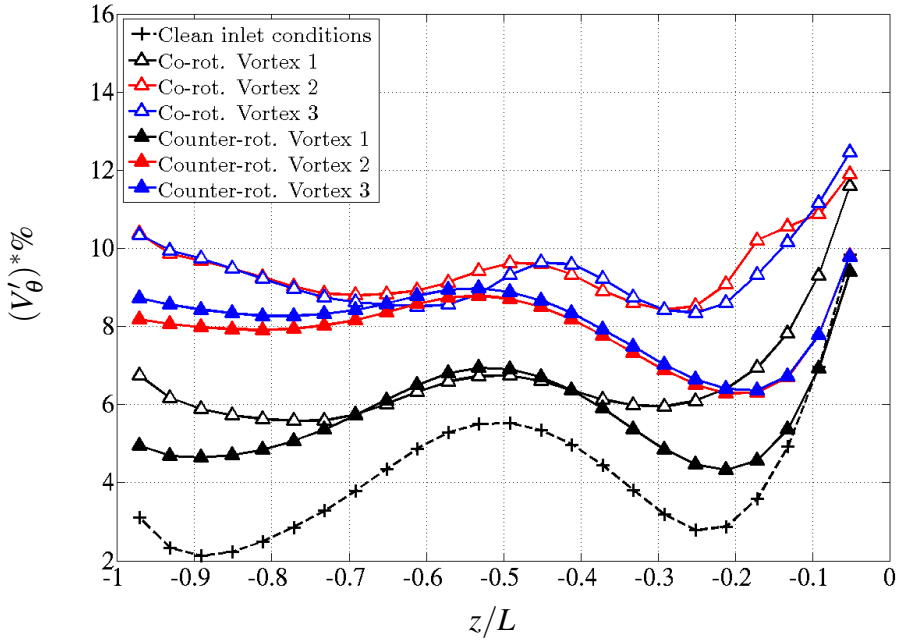

(b) Non-dimensional standard deviation of tangential velocity ($(V'_\theta)^*\%$)

Figure 5.17: Non-dimensional standard deviations calculated along the S-duct for vortices ingested near the top edge (i.e. prescribed at P_T) and with rotor operating at 100% N_d and $p_{out}/P_{0,in} = 0.987$

5.1.3 Flow field description at the AIP

This section reports the description of both total pressure and swirl distortion calculated at the AIP and relative to the coupled system operating according to the boundary conditions defined in § 5.1.1.

5.1.3.1 Total pressure distortion

The total pressure distortion was measured with the total pressure distortion parameter (DC_{60}). Note, however, that this parameter does not provide any information regarding the distortion extent since it is calculated on the worst total pressure sector of 60^o (see § A.1). As discussed in § 1.1.1.1, the rotor stability pressure ratio reduces as the distortion extent increases. This characteristic was investigated by means of contours of non-dimensional total pressure ($P_0^\star$) as shown in Fig. 5.19 and 5.20.

Effect of vortex location and polarity Figure 5.18 shows the total pressure distortion parameter (DC_{60}) for vortex 1 (datum) ingested at different locations and polarities and with the rotor operating at 100% N_d and $p_{out}/P_{0,in} = 0.987$. The value calculated under clean inlet conditions, presented in § 4.2.3.1, is also indicated. Amongst the case studies investigated, the DC_{60} was generally greater than 0.1. According to practical recommendations[67], this value corresponds to the limit below which the total pressure distortion could be neglect. Therefore, the total pressure distortion could contribute significantly with the swirl distortion to the change in rotor performance.

The change of the total pressure parameter (DC_{60}) with the vortex location and polarity was explained by considering that, in general, the total pressure loss at the AIP are the results of two combined mechanisms. The first mechanism is the mass flow and then the flow velocity involved into the system. This aspect was already evident with the validation study of the RAE S-shaped intake 2129 (see § 4.2.3.1 and 4.3.3.1). On the other hand, the second mechanism is attributed to the interaction of an ingested vortex with the existing intake flow field, especially with that of the self-generated distortion.

As discussed in § 5.1.2.3, the vortex ingested at centre of the intake inlet plane (i.e. prescribed at P_C) impacted directly on the spinner by affecting mainly the flow field at the AIP around the hub region of the rotor. This result was evident especially with the description of the swirl distortion at the AIP carried out by considering the relative rotor incidence change ($\Delta\beta$) or non-dimensional streamwise vorticity ($\omega_z^\star$) which will be discussed in § 5.1.3.2. In these conditions, a change of mass flow occurred with a sign depended on the vortex polarity (see § 5.1.4). Most likely, the vortex interacted with the self-generated distortion. Therefore, both of the aforementioned mechanisms occurred simultaneously. However, the change of total pressure distortion with respect to the clean

inlet conditions attributed to these two mechanisms thought acting separately could not be quantified. Similar considerations were also valid for vortex ingested near the starboard edge (i.e. prescribed at P_S). For this location the vortex perturbation merged significantly with that associated with the self-generated distortion as shown in Fig. 5.19(c) and 5.20(c). Note, however, that this condition did not necessarily imply an increase of the total pressure distortion since a reduction of DC_{60} occurred as the co-rotating vortex 1 (datum) was ingested at this location.

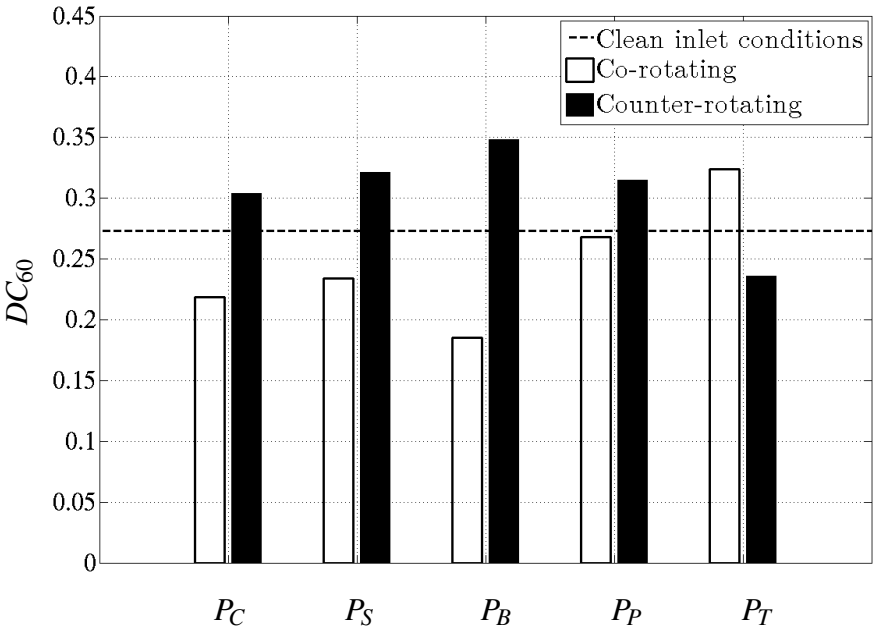

Figure 5.18: Total pressure distortion parameter (DC_{60}) calculated at different locations and polarities of the vortex 1 and with rotor operating at 100% N_d and $p_{out}/P_{0,in} = 0.987$

For the remaining vortex locations investigated, the change of DC_{60} was explained by considering the location of the vortex perturbation reached at the AIP relative to that of the self-generated distortion. As discussed in § 2.2.4.2, the vortex moved circumferentially in agreement with the observations carried out by Anderson[2]. Hence, as the co-rotating vortex 1 (datum) was ingested at different locations along the co-rotating direction and sequentially near the bottom, port and top edge (i.e. prescribed at P_B, P_P and P_T) the vortex perturbation approached more and more that of the self-generated distortion as shown in Fig. 5.19(d), 5.19(e), and 5.19(f). Meanwhile, the DC_{60} increased more and more as shown in Fig. 5.18. As a result, the perturbation of the vortex ingested near the top was almost merged with that of the self-generated distortion and the extent and magnitude of the total pressure distortion reached the highest values. A similar phenomena occurred by ingesting counter-rotating vortices along the counter-rotating direction sequentially near the top, port and bottom edge (i.e. prescribed at P_T, P_P and P_B) (see Fig.

5.20(f), 5.20(e), and 5.20(d)). As a result, the highest change of total pressure distortion with the polarity occured for vortices ingested near the bottom and top edge. Note, however, that a difference in DC_{60} between the mirror vortices existed. In particular, this value was lower for co- than for counter-rotating vortex ingested as shown in Fig. 5.18. As will be discussed in § 5.1.4, this difference was related to the mass flow of the system. Compared to the clean inlet conditions, this increased and decreased due to the swirl distortion effect attributed to counter- and co-rotating vortices ingested, respectively.

Finally, it was observed that the perturbations of the vortices ingested at the port (Fig. 5.19(e) and 5.20(e)) were less significant compared to that attributed to the co- or counter-rotating vortex ingested near the bottom or top edge of the intake wall, respectively, (Fig. 5.19(d) or 5.20(f)). The reason of this outcome could be related to the different local wall curvature encountered by the vortex along the S-duct.

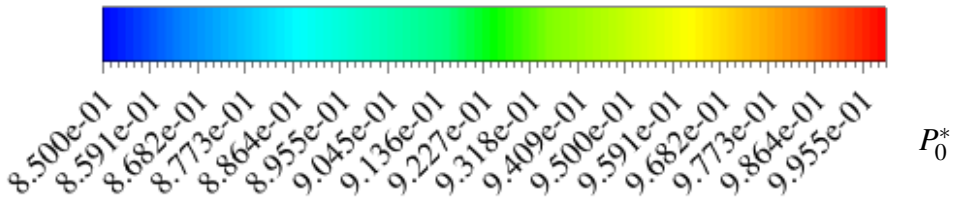

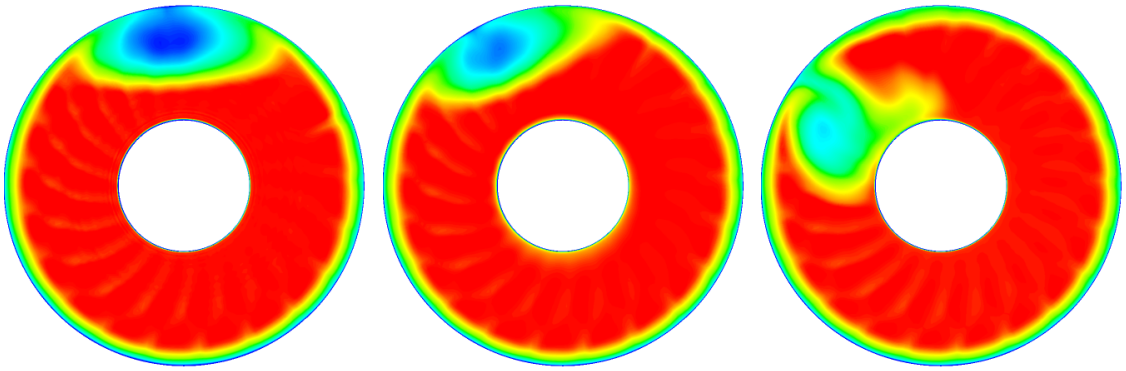

(a) Clean inlet conditions (b) Vortex prescribed at P_C (c) Vortex prescribed at P_S

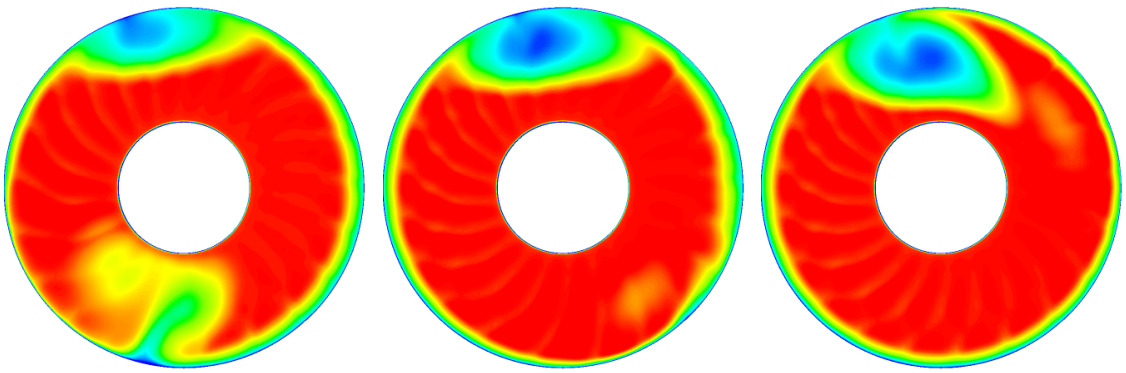

(d) Vortex prescribed at P_B (e) Vortex prescribed at P_P (f) Vortex prescribed at P_T

Figure 5.19: Contours of non-dimensional total pressure distortion (P_0^*) at the AIP for co-rotating vortex 1 ingested at different locations and with rotor operating at 100% N_d and $p_{out}/P_{0,in} = 0.987$

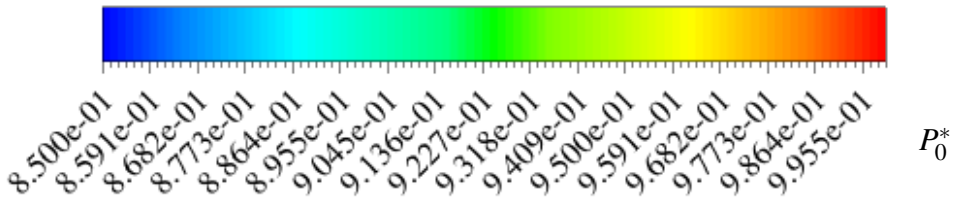

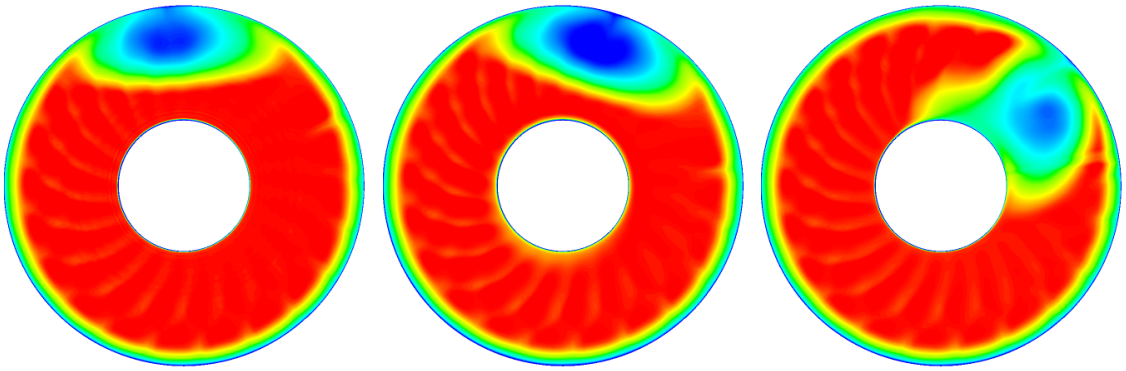

(a) Clean inlet conditions (b) Vortex prescribed at P_C (c) Vortex prescribed at P_S

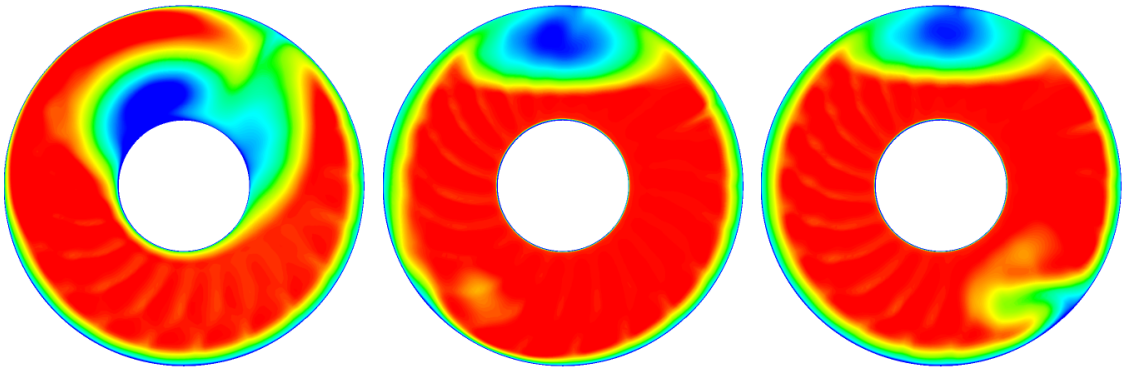

(d) Vortex prescribed at P_B (e) Vortex prescribed at P_P (f) Vortex prescribed at P_T

Figure 5.20: Contours of non-dimensional total pressure distortion (P_0^*) at the AIP for counter-rotating vortex 1 ingested at different locations and with rotor operating at 100% N_d and $p_{out}/P_{0,in} = 0.987$

Effect of vortex maximum swirl velocity and size The increase of the maximum swirl velocity or size of the vortex 1 (datum) (i.e. obtained with vortex 2 or vortex 3, respectively), could cause an increase of the extent relative to the worst total pressure sector at the AIP. The magnitude of this increase was related to the level of interaction between the vortex and the self-generated distortion. In particular, it was significant for vortices ingested near the starboard edge as well as for co- and counter-rotating vortices ingested near the top and the bottom, respectively (see Fig. 5.22 and 5.23). For these cases, the angular extent of the worst total pressure distortion sector became larger than 60^o and, therefore, the DC_{60} was no longer recommended as metric. Therefore, this parameter was improved by considering the angular extent of the worst total pressure sector of 120^o (DC_{120}). Figures 5.21(a) and 5.21(b) show the values of this parameter calculated for co- and counter-rotating vortices ingested, respectively, and at different locations. In general, the minimum total pressure achieved within the vortex perturbation zone was higher with the ingestion of vortex 3 rather than relative to vortex 2 (Fig. 5.22 and 5.23). As discussed in § 5.1.2.1, this outcome could be attributed to a higher dissipation to which the vortex 2 was subjected compared to that relative to vortex 3.

Referring to Fig. 5.21(a), a reduction of DC_{120} occurred for co-rotating vortices ingested that, according to the distributions of non-dimensional total pressure (Fig. 5.22), were not interacting significantly with the self-generated distortion. Therefore, this reduction was essentially attributed to that of the corrected mass flow of the system which will be discussed in § 5.1.4. For the vortex polarity considered, this condition occurred for vortices ingested at the centre of the intake inlet plane and at the bottom (i.e. prescribed at the P_C and P_B, respectively). Meanwhile, for the remaining vortex locations investigated, where the vortex interacted significantly with the self-generated distortion, the DC_{120} increased and decreased with the ingestion of vortex 2 and vortex 3 essentially due to the difference in the lowest total pressure reached around the core of the vortex itself (Fig. 5.22).

Regarding the vortices ingested in the counter-rotating direction (Fig. 5.21(b), the DC_{120} remained the lowest as vortex 2 or vortex 3 were ingested near the top edge of the intake. For the remaining vortex locations the same parameter increased with the ingestion of the vortex 2. Then, by substituting this vortex with vortex 3 a reduction of this parameter occurred essentially due to the higher total pressure reached at the vortex centre as discussed above.

Overall, it could be noticed that the perturbation relative to the Vortex 2 and vortex 3 ingested at the AIP was found at an angular location which was common for the two vortices ingested (Fig. 5.22 and 5.23). This outcome confirmed, then, the validity of the method of images, already discussed in § 5.1.2.2.

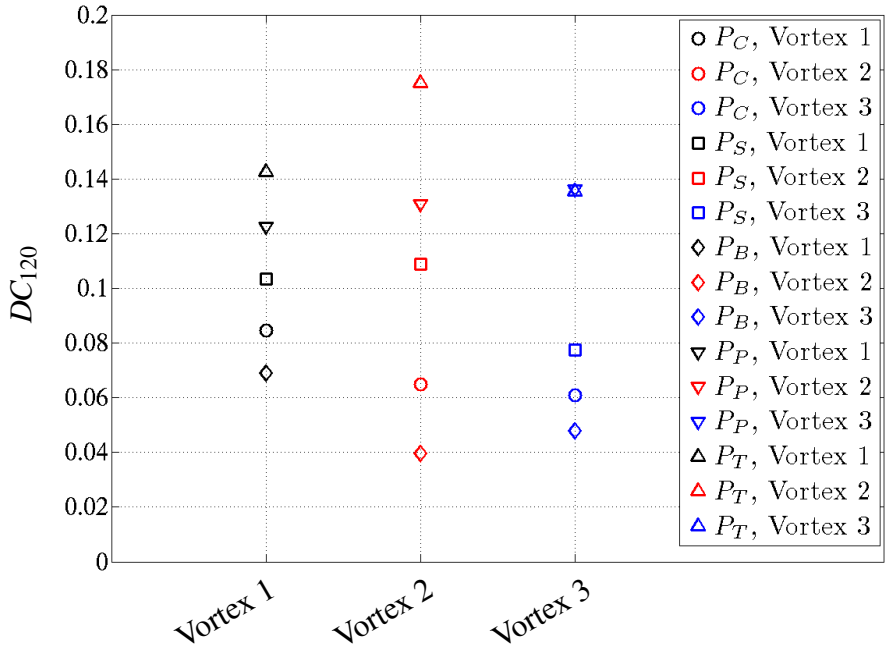

(a) Co-rotating vortices ingested

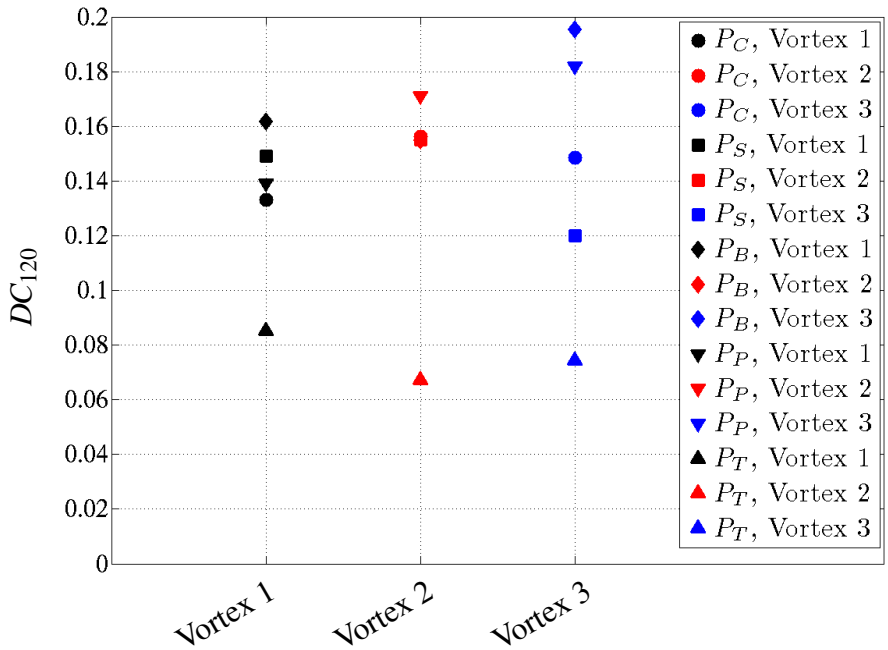

(b) Counter-rotating vortices ingested

Figure 5.21: Total pressure distortion parameter (DC_{120}) for different vortex ingestion and polarities and with rotor operating at 100% N_d and $p_{out}/P_{0,in} = 0.987$

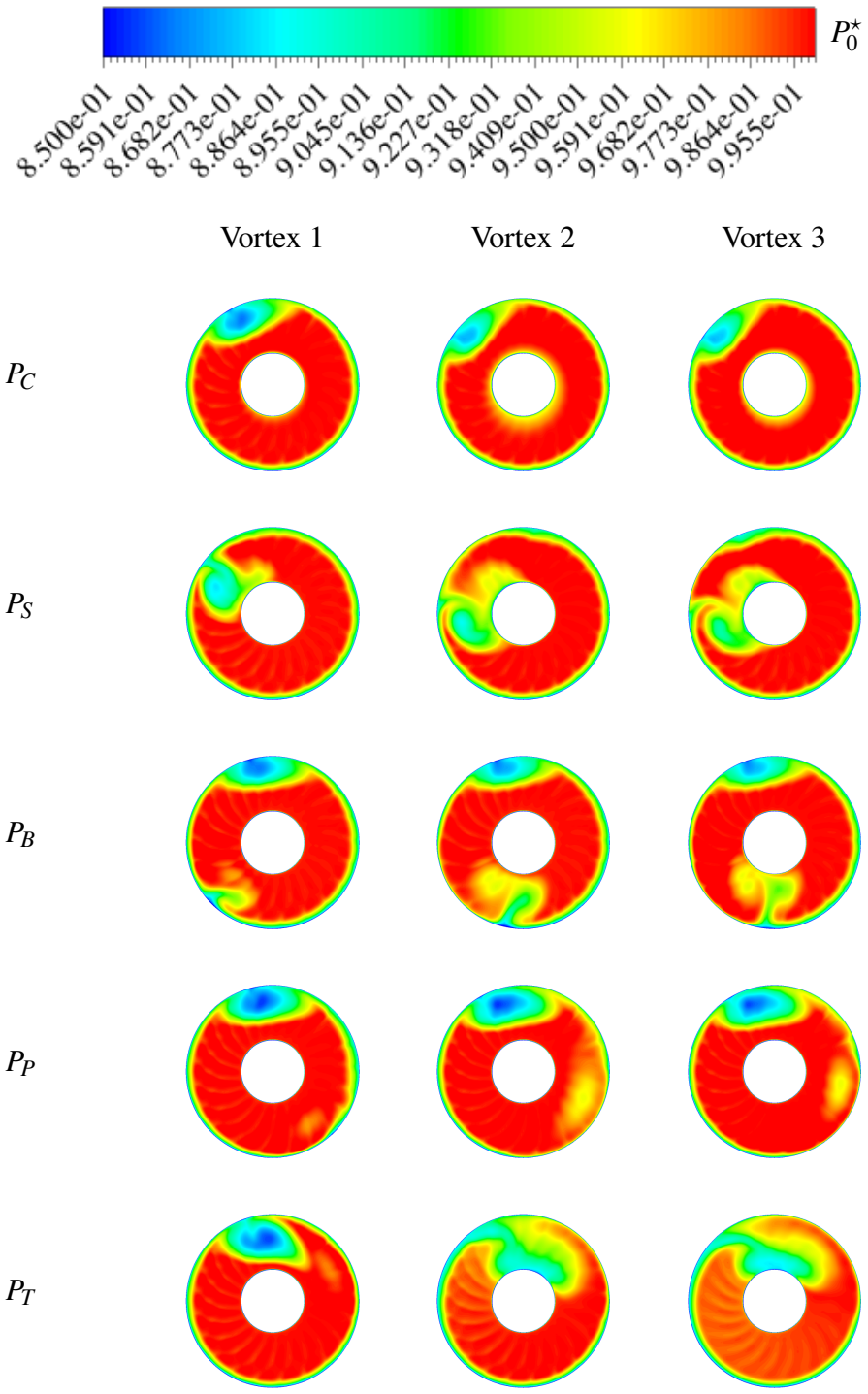

Figure 5.22: Contours of non-dimensional total pressure ($P_0^\star$) for co–rotating vortices ingested and with rotor operating at 100% N_d and $p_{out}/P_{0,in} = 0.987$

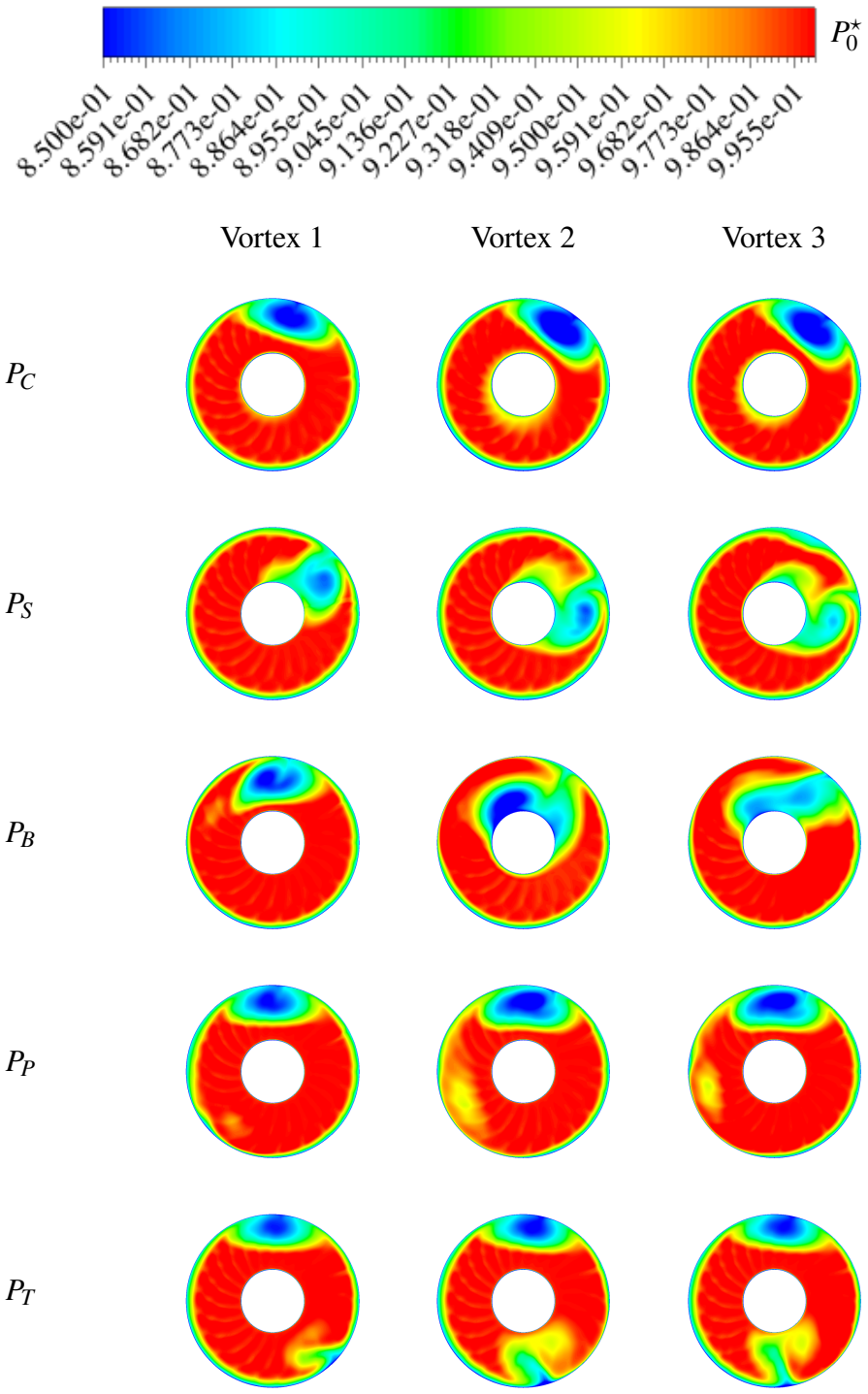

Figure 5.23: Contours of non-dimensional total pressure ($P_0^\star$) for counter–rotating vortices ingested and with rotor operating at 100% N_d and $p_{out}/P_{0,in} = 0.987$

5.1.3.2 Swirl distortion

In this section, a description of the swirl distortion at the AIP of the coupled system is presented. For this purpose, the distribution of the non-dimensional streamwise vorticity (ω_z^*) and the relative flow angle change ($\Delta\beta$) were considered. Moreover, a quantification of the swirl distortion was carried out by calculating the mass flow average of the magnitude of the relative flow angle change ($\overline{|\Delta\beta|}$). Note that the aforementioned parameters were defined in § 3.3.

Effect of vortex location and polarity Referring to Fig. 5.25 and 5.26, as the vortex 1 (datum) was ingested in the coupled system for different combinations of location and polarity, the distribution of ω_z^* at the AIP was significantly altered compared to that obtained under clean inlet conditions. Consequently, a characterization of the swirl distortion at the AIP similar to that applied for clean inlet conditions (see § 4.2.3.2 and 4.3.3.2) could no longer be carried out. For this reason, the distribution of ω_z^* at the AIP was described only qualitatively. This is presented below for each combination of vortex location and polarity.

As discussed in § 5.1.2.3, the vortices ingested at the centre of the intake inlet plane (i.e. prescribed at P_C) remained located along the S-duct centreline. Therefore, it impacted directly the spinner and the hub region of the rotor at the AIP. As a result, higher values of vorticity occurred almost uniformly around the whole rotor hub as shown in Fig. 5.25(b) and 5.26(b). Meanwhile, a reduction or increase of the self-generated distortion imbalance occurred as the counter- or co-rotating vortex direction was considered, respectively. Referring to Fig. 5.27(a) and 5.28(a), the relative flow angle change ($\Delta\beta$) close to the vortex perturbation affected mainly the hub region along the whole annulus. Also, the co- and counter-rotating regions of the self-generated distortion were subjected to a change of this parameter in opposite manner, due to the centered bulk swirl associated with the vortex itself.

The vortices ingested near the starboard edge (i.e. prescribed at P_S) merged with the part of the self-generated distortion zone having the same vorticity sign as shown in Fig. 5.25(c) and 5.26(c)). This resulting vorticity zone extended and propagated towards the hub region. In turn, the self-generated distorted zone originally with the opposite vorticity extended and propagated towards the hub region. In terms of $\Delta\beta$, the presence of the vortex was recognized by two spots of this parameter having opposite sign and located around the location of the vortex reached at the AIP (see Fig. 5.27(b) and 5.28(b)). A similar observation could be carried out for any other vortex ingested near the wall which are presented below.

For co-rotating vortex ingested near the bottom edge (i.e. prescribed at P_B) the self-generated distortion remained essentially separated by the vortex perturbation. Instead,

the vortex interacted with the duct wall by arising two spots of induced vorticity as shown in Fig. 5.25(d). On the other hand, by inverting the vortex polarity the vortex perturbation moved in the circumferential direction towards the self-generated distorted zone as shown in Fig. 5.26(d). Therefore, a large positive vorticity zone arose along the whole span as result of the interaction between the vortex and the self-generated distortion. This condition induced an enlargement of the negative vorticity zone relative to the self-generated distortion.

Regardless of the polarity, the perturbation of the vortex ingested near the port (i.e. prescribed at P_P) remained in a circumferential location essentially opposite to that of the self-generated distortion which was, therefore, not directly affected by the ingested vortex itself. On the other hand, the vortex interacted with the wall and two induced vorticity zones arose between the vortex and the wall (Fig. 5.25(e) and 5.26(e)). Moreover the change of swirl distortion in terms of $\Delta\beta$ was relatively low around the self-generated distortion.

Finally, the numerical solutions obtained for vortices ingested near the top edge of the intake (i.e. prescribed at P_T), were qualitatively mirrored compared to that relative to vortices ingested at the bottom and by inverting the vortex polarity (see Fig. 5.25(f) and 5.26(f)). As will be discussed in § 5.1.4, the corrected mass flow for a co- and a counter-rotating vortex ingested was lower and higher with respect to the clean inlet conditions. Differences between the mirror vortices were attributed to that of rotor operability.

Overall, the aforementioned description confirmed that the swirl distortion was not only attributed to that of self-generated distortion and the vortex ingested, thought acting separately. Instead, additional swirl distortion arose from the interaction occurring between the self-generated distortion or the duct wall and the ingested vortex itself.

Moreover, the inlet swirl distortion was measured by means of the mass flow average of the magnitude of the relative flow angle change ($\overline{|\Delta\beta|}$) calculated at the AIP as shown in Figure 5.24. The results confirmed that by considering the swirl distortion magnitude the flow patterns were essentially mirrored between vortices of opposite polarity ingested at the centre of the intake inlet plane and near the port and starboard edge of the intake wall. On the other hand, for vortices ingested near the bottom or top edge the level of swirl distortion depended on their polarity. This outcome was related to the possibility of these vortices to mainly interact either with the self-generated distortion or the intake wall. According to the rotor operability investigated and for both of the aforementioned locations, the interaction of the vortex with the self-generated distortion caused higher swirl distortion than that relative to interaction of the vortex with the intake wall. Finally, by considering the total pressure and swirl distortion quantified by means of DC_{60} and $\overline{|\Delta\beta|}$, respectively, (Fig. 5.18 and 5.24) the two types of distortion were inter-correlated for vortices ingested near the bottom and the top edge.

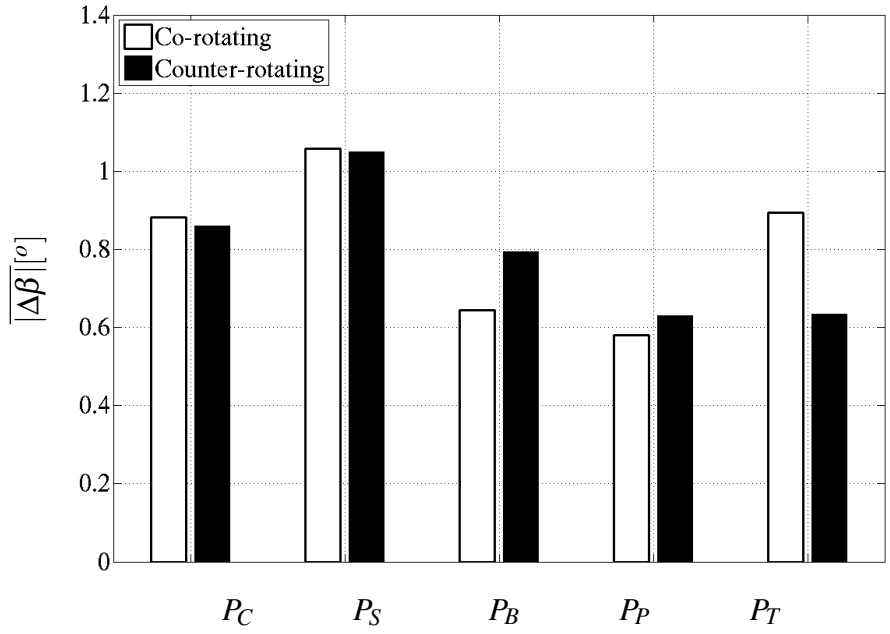

Figure 5.24: Mass flow average of the magnitude of the relative flow angle change ($\overline{|\Delta\beta|}$) calculated at different locations and polarities of the vortex 1 and with rotor operating at 100% N_d and $p_{out}/P_{0,in} = 0.987$

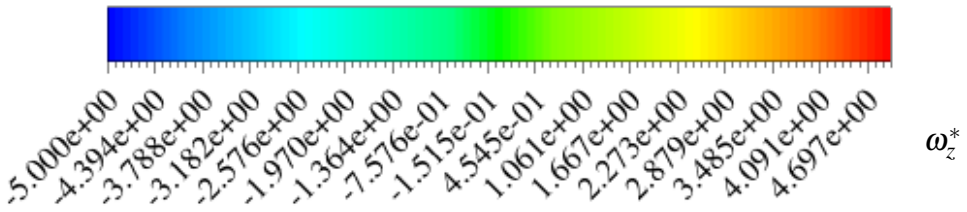

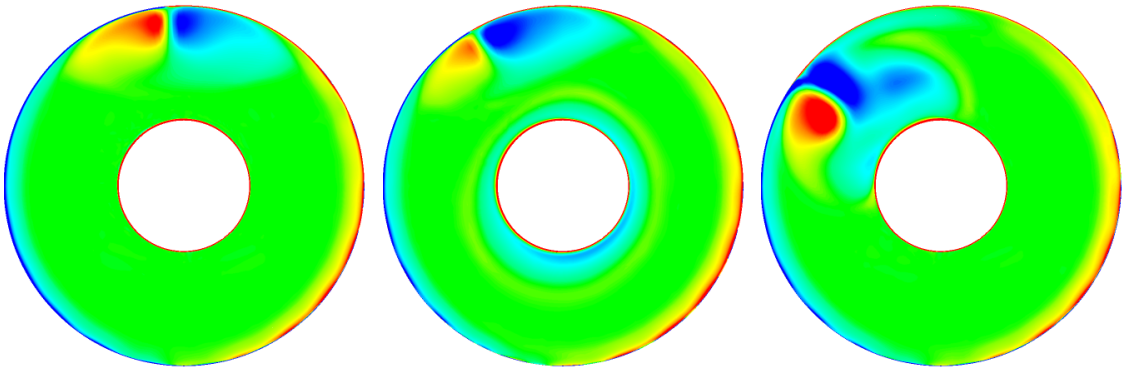

(a) Clean inlet conditions (b) Vortex prescribed at P_C (c) Vortex prescribed at P_S

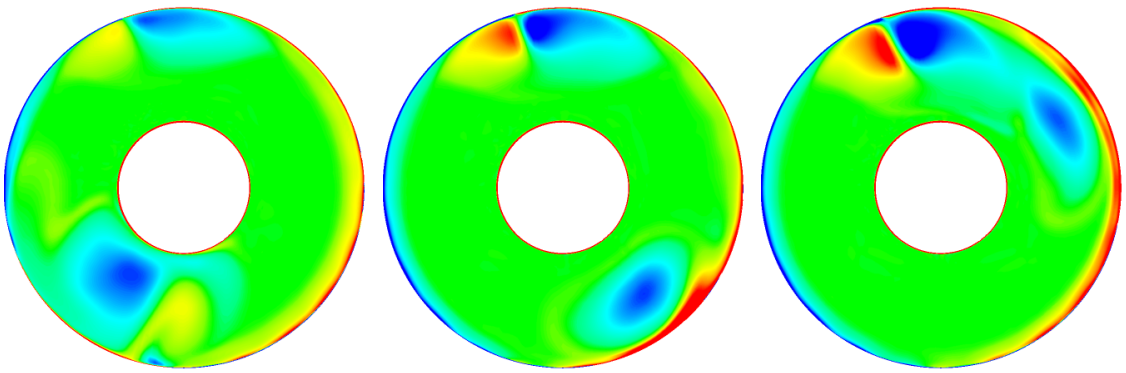

(d) Vortex prescribed at P_B (e) Vortex prescribed at P_P (f) Vortex prescribed at P_T

Figure 5.25: Contours of non-dimensional streamwise vorticity (ω_z^*) at the AIP for co-rotating vortex 1 ingested at different locations and with rotor operating at 100% N_d and $p_{out}/P_{0,in} = 0.987$

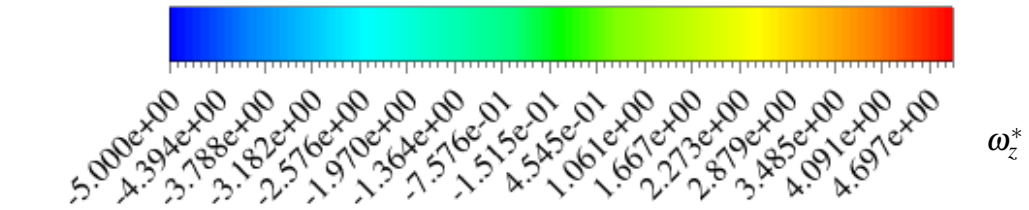

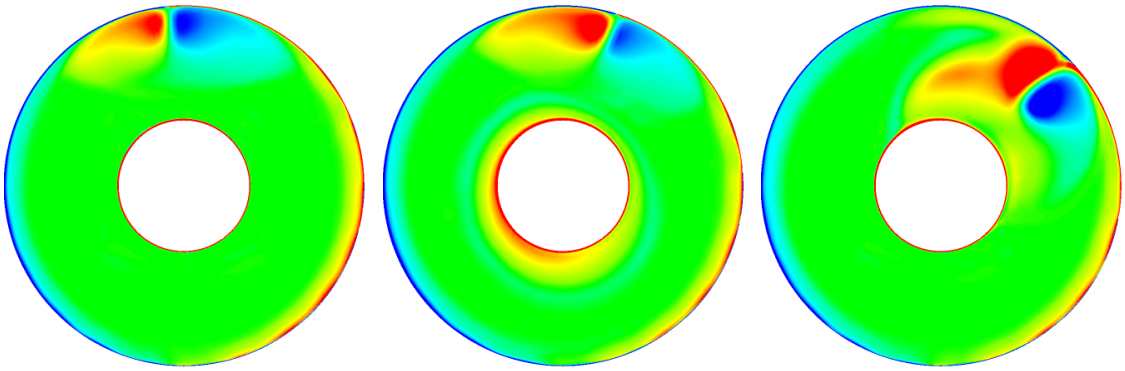

(a) Clean inlet conditions (b) Vortex prescribed at P_C (c) Vortex prescribed at P_S

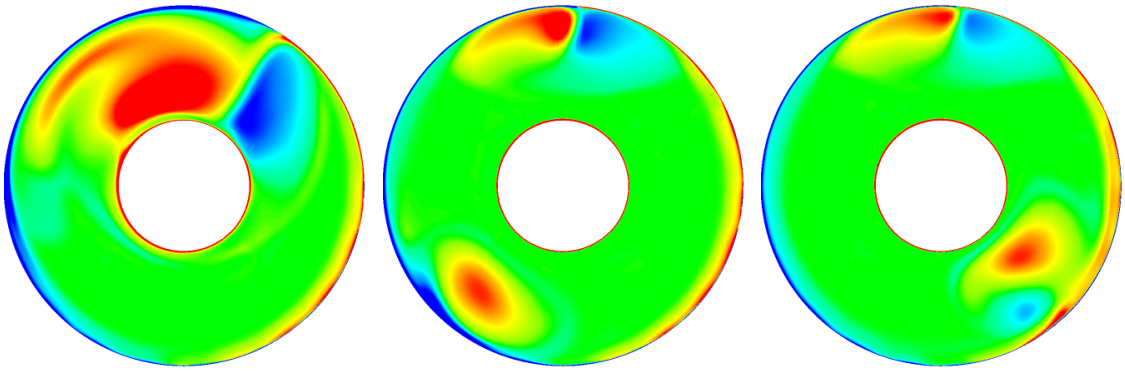

(d) Vortex prescribed at P_B (e) Vortex prescribed at P_P (f) Vortex prescribed at P_T

Figure 5.26: Contours of non-dimensional streamwise vorticity (ω_z^*) at the AIP for counter-rotating vortex 1 ingested at different locations and with rotor operating at 100% N_d and $p_{out}/P_{0,in} = 0.987$

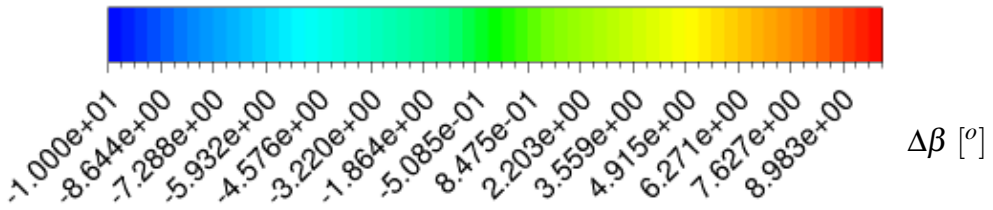

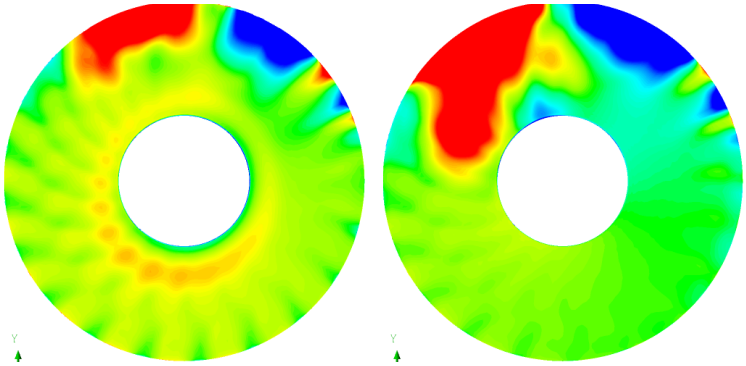

(a) Vortex prescribed at P_C (b) Vortex prescribed at P_S

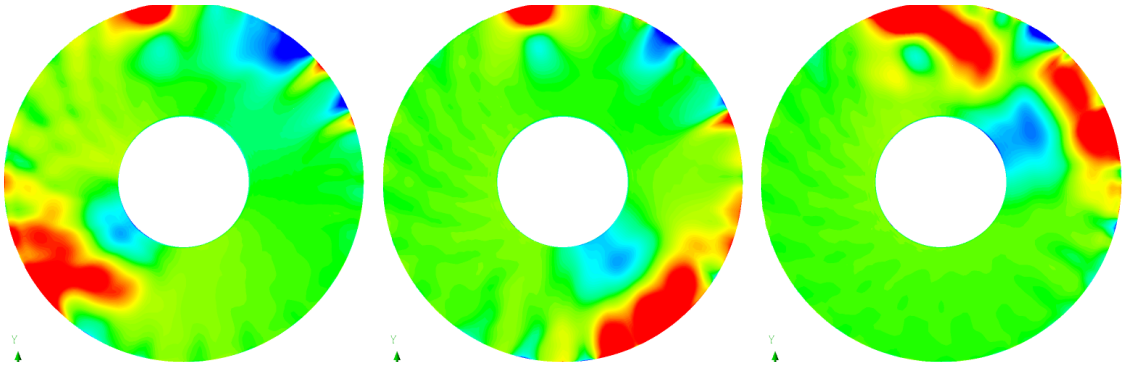

(c) Vortex prescribed at P_B (d) Vortex prescribed at P_P (e) Vortex prescribed at P_T

Figure 5.27: Contours of relative flow angle change ($\Delta\beta$) at the AIP for co-rotating vortex 1 ingested at different locations and with rotor operating at 100% N_d and $p_{out}/P_{0,in} = 0.987$

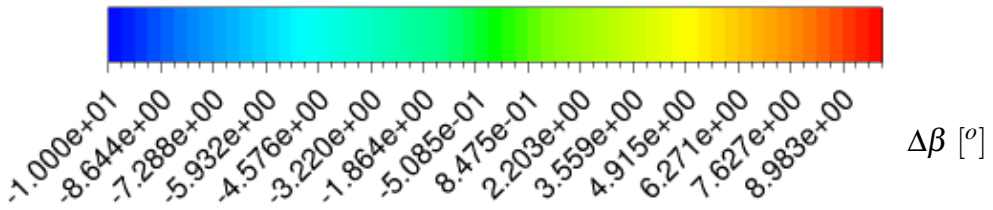

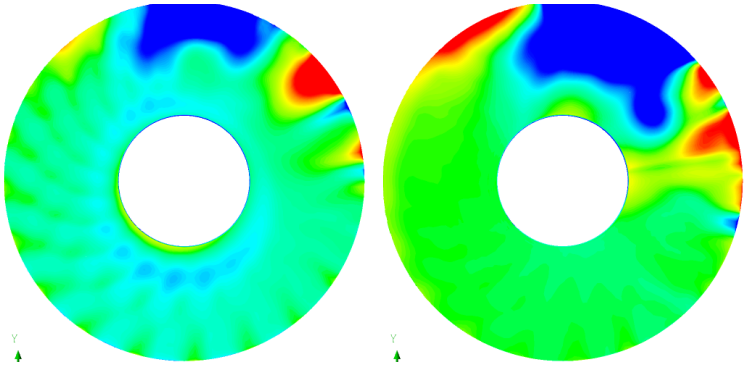

(a) Vortex prescribed at P_C (b) Vortex prescribed at P_S

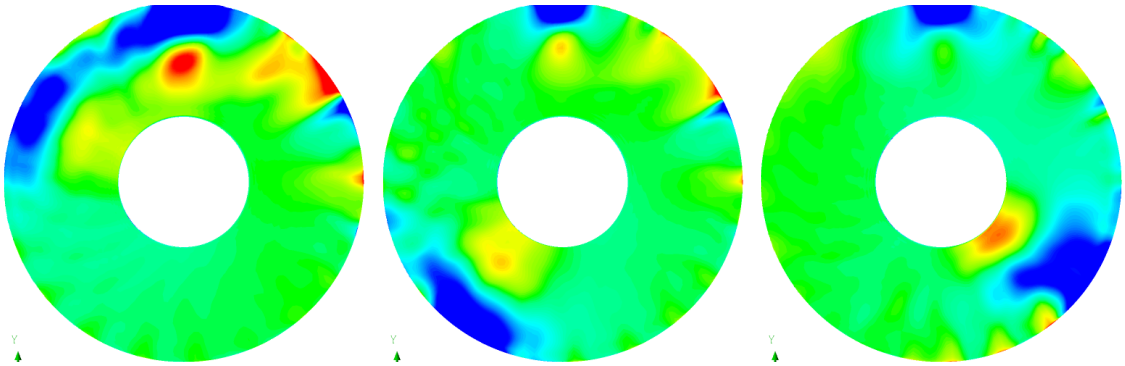

(c) Vortex prescribed at P_B (d) Vortex prescribed at P_P (e) Vortex prescribed at P_T

Figure 5.28: Contours of relative flow angle change ($\Delta\beta$) at the AIP for counter-rotating vortex 1 ingested at different locations and with rotor operating at 100% N_d and $p_{out}/P_{0,in} = 0.987$

Effect of maximum swirl velocity and size Figure 5.29 and 5.30 show the non-dimensional streamwise vorticity ($\omega_z^\star$) for co- and counter-rotating vortices, respectively, ingested at different locations. The extent as well as the location of the perturbation were in agreement with that relative to the total pressure distortion (see Fig. 5.22 and 5.22). Also, according to the inlet boundary conditions relative to vortex 2 and vortex 3 (obtained by doubling the maximum swirl velocity and size of the vortex 1) it was expected that the vorticity attributed to the vortex 2 was higher compared to that relative to vortex 3. However, the numerical results obtained in this work showed an opposite outcome (Fig. 5.29 and 5.30). This could be due to a higher dissipation at which the vortex 2 was subjected with respect to the vortex 3.

The swirl distortion was quantified by means of the mass flow average of the magnitude of the relative flow angle change ($\overline{|\Delta\beta|}$), for co- and counter-rotating vortices ingested as shown in Fig. 5.31(a) and 5.31(b), respectively. In general, as the vortex 2 or vortex 3 were ingested in the coupled system, the swirl distortion increased, due to higher swirl velocities introduced by vortex itself. In particular, amongst the co-rotating vortices ingested the highest swirl distortion was reached for that ingested near the top due to the strong interaction of the vortex with the self-generated distortion notable in Fig. 5.29. On the other hand, the lowest swirl distortion was relative to the vortex ingested near the bottom where the vortex perturbation moved towards the opposite location with respect to that of the self-generated distortion and interacted with the intake wall (Fig. 5.29). Referring to counter-rotating vortices (see Fig. 5.31(b)), the lowest swirl distortion was relative to that ingested near the top. On the other hand, the highest swirl distortion was observed for vortex ingested near the bottom and near the starboard as either the maximum swirl velocity and the size of the vortex 1 (datum) were doubled, respectively. Overall, these results were in agreement with that relative to the total pressure distortion measured by means of DC_{120} indicated in Fig. 5.21(a) and 5.21(b) for co- and counter-rotating vortices ingested, respectively.

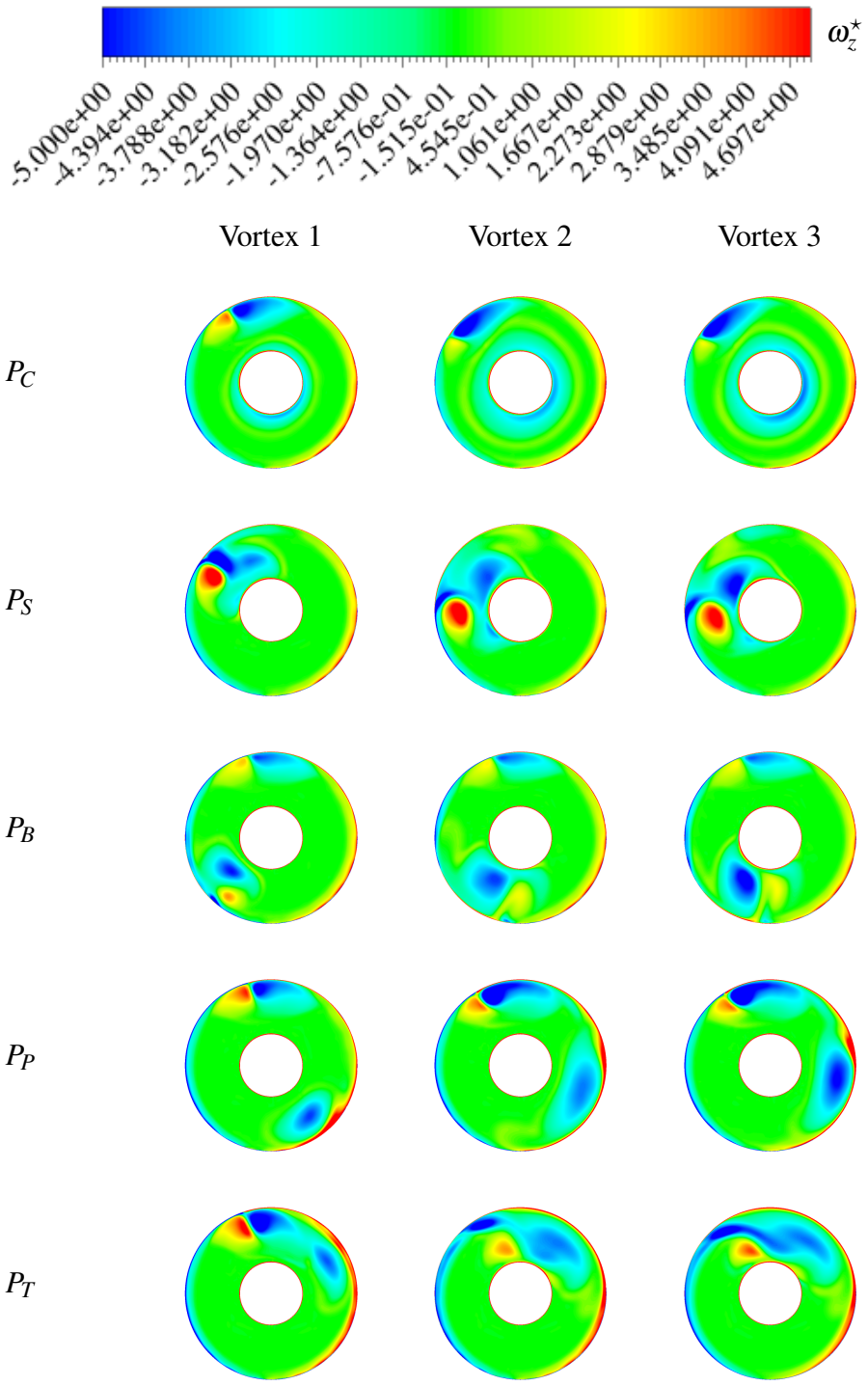

Figure 5.29: Contours of non-dimensional streamwise vorticity ($\omega_z^\star$) for co–rotating vortices ingested and with rotor operating at 100% N_d and $p_{out}/P_{0,in} = 0.987$

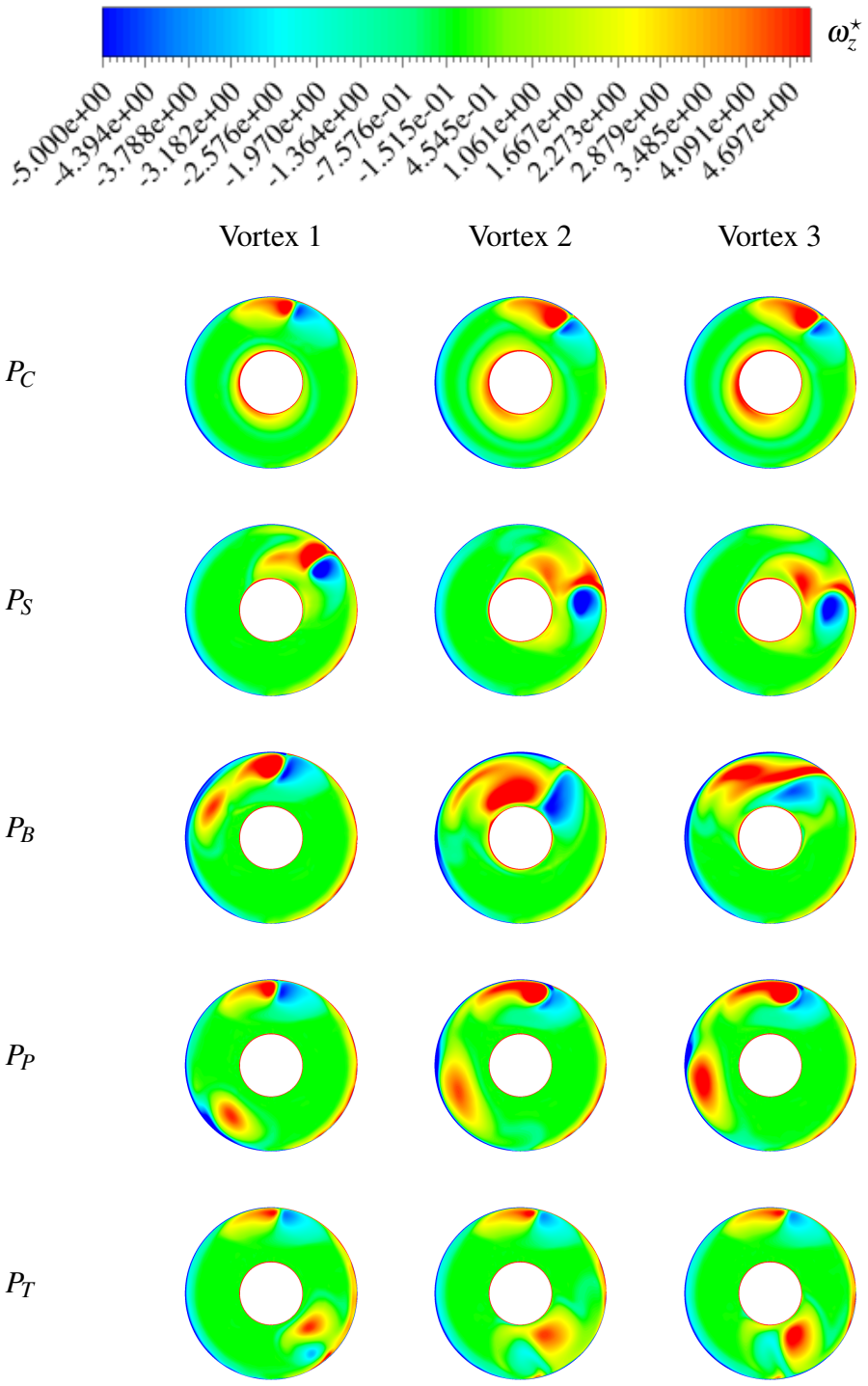

Figure 5.30: Contours of non-dimensional streamwise vorticity ($\omega_z^\star$) for counter–rotating vortices ingested and with rotor operating at 100% N_d and $p_{out}/P_{0,in} = 0.987$

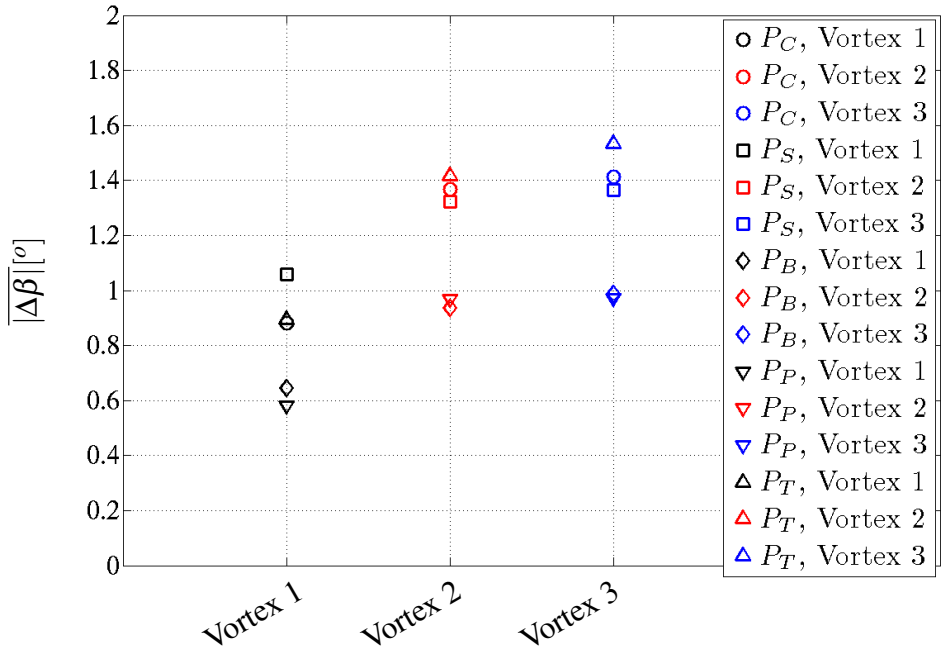

(a) Co-rotating vortices ingested

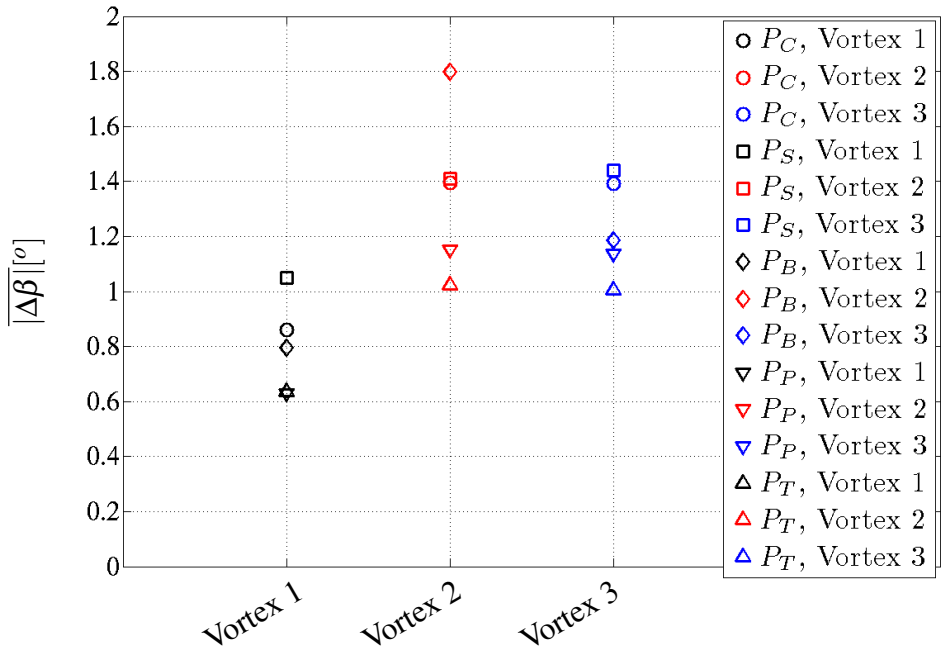

(b) Counter-rotating vortices ingested

Figure 5.31: Mass flow average of the magnitude of the relative flow angle change ($\overline{|\Delta\beta|}$) calculated at different locations and polarities of the vortex 1 and with rotor operating at 100% N_d and $p_{out}/P_{0,in} = 0.987$

5.1.4 Change of rotor performance

In this section, the rotor pressure ratio (PR) versus the corrected mass flow (W_{cor}) relative to the coupled system operating under clean inlet conditions and by considering the boundary conditions defined in § 5.1.1 are presented. As discussed in § 5.1.1, for these cases the rotor static to inlet total pressure ($p_{out}/P_{0,in}$) remained constant, instead of being varied in order to reach the near stall operating point. For this reason, similar numerical correlations to that presented for clean inlet conditions (see § 4.4.3) could not obtained.

Effect of vortex location and polarity Generally, the sign as well as the magnitude of the change of rotor corrected mass flow is the result of the combination of total pressure and swirl distortion effect. As discussed in 1.1.1, the increase of total pressure distortion causes a shift of the operating point towards lower corrected mass flow. Meanwhile, the swirl distortion causes a shift of the operating point depending on the predominant swirl direction at the AIP. In particular, for a co- and a counter-rotating pure bulk swirl the rotor corrected mass flow reduces and increases, respectively (see § 1.1.1.2). Figures 5.34(a) and 5.34(b) show the pressure ratio (PR) versus corrected mass flow (W_{cor}) relative to the rotor of the coupled system when the vortex 1 (datum) was ingested in co- and counter-rotating direction, respectively. The results showed that a reduction and an increase of corrected mass flow was observed for co- and counter-rotating vortices ingested. Following the aforementioned considerations and by assuming that the interaction effects between different types of flow distortion were negligible, the effect of total pressure was minor compared to that of the swirl distortion. Hence, the changes in rotor performance explained below considered the effects of these two types of flow distortion in a separated manner.

As discussed in § 5.1.3.2, the ingestion of vortex 1 (datum) at locations near the wall (i.e. prescribed at P_S, P_B, P_P and P_T) arose two zones of opposite relative rotor incidence change ($\Delta\beta$) close to the vortex perturbation at the AIP (Fig. 5.27 and 5.28). Clearly, their effects on the global rotor corrected mass flow were opposite. Meanwhile, the relative rotor incidence was also affected near the self-generated distorted region in a direction corresponding to that of the vortex polarity. According to the results shown in Fig. 5.34, the effect on rotor corrected mass flow was similar to that of a bulk swirl imposed in the same rotational direction of the vortex ingested. On the other hand, when the vortex was ingested at the centre of the intake inlet plane (i.e. prescribed at P_C) this impacted mainly the hub region at the AIP where a zone of $\Delta\beta$ arose in one direction corresponding to that of the vortex polarity (Fig. 5.27(a) and 5.28(a)). Meanwhile, the relative rotor incidence near the self-generated distorted region was affected almost equally in both directions. Hence, compared to vortices ingested near the wall, the increase of change in rotor corrected mass flow was not contrasted by an opposite zone of $\Delta\beta$ arising close to the vortex. As a result, the change of rotor corrected mass flow

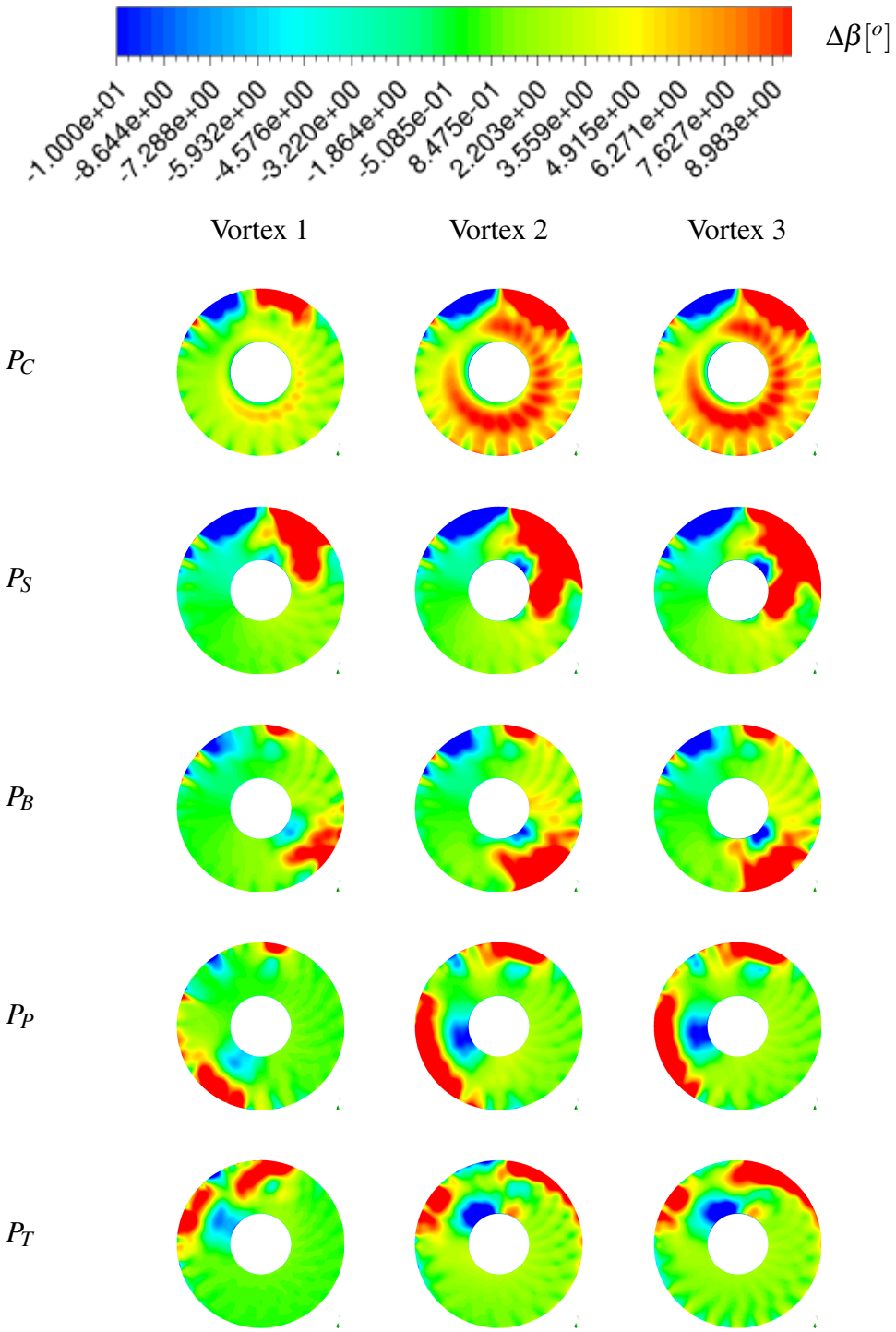

Figure 5.32: Contours of relative flow angle change ($\Delta\beta$) for co–rotating vortices ingested and with rotor operating at 100% N_d and $p_{out}/P_{0,in} = 0.987$

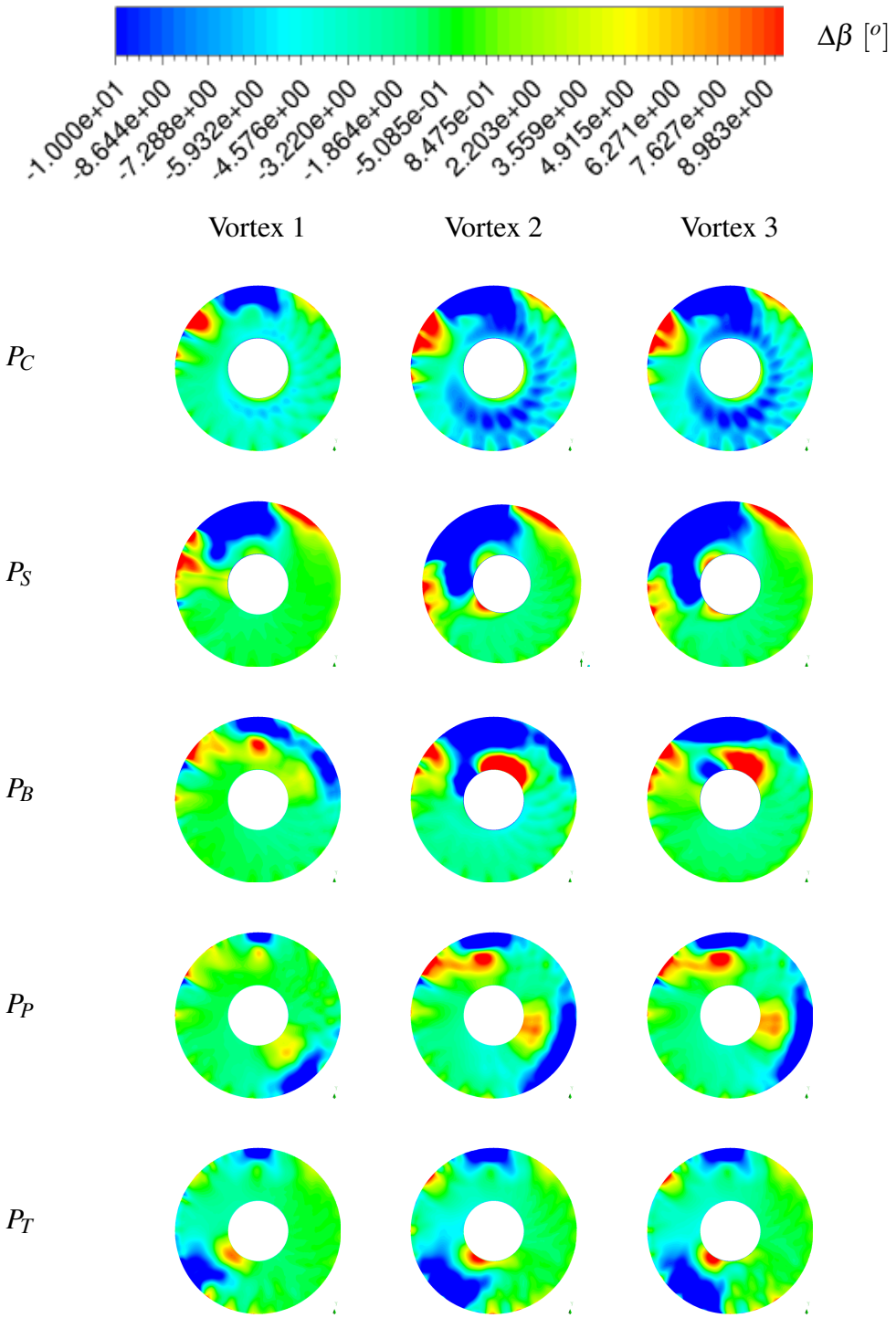

Figure 5.33: Contours of relative flow angle change ($\Delta\beta$) for counter–rotating vortices ingested and with rotor operating at 100% N_d and $p_{out}/P_{0,in} = 0.987$

was relatively high. The aforementioned explanation considered only the existence of the swirl distortion. The inclusion of the total pressure distortion effect is presented below.

Regarding the vortex ingested at the centre of the intake inlet plane (i.e. prescribed at P_C), the DC_{60} was lower for co- than for counter-rotating vortex direction (see § 5.1.3.1). Meanwhile, as discussed in § 5.1.3.2, the swirl distortion measured with the mass flow average of the magnitude of the relative flow angle change ($\overline{|\Delta\beta|}$) remained unchanged. Also, the relative value was not the largest amongst the cases investigated. Referring to Fig. 5.34, the change of the operability points with respect to the clean inlet conditions was of about 1.3% excess or deficit of corrected mass flow, as the co- and counter-rotating vortex, respectively, was ingestedat the centre. As compared with any other vortex locations, this change was relatively high. By supposing the total pressure distortion acting alone, this would move both of the operating points towards lower corrected mass flow. However, according to the aforementioned results, the contribution of the swirl distortion on the rotor performance was more significant than that of total pressure distortion. Therefore, it was concluded that the sign as well as the location of the swirl distortion along the span could be significant to identify the change of rotor performance (see Fig. 5.27 and 5.27).

Referring to Fig. 5.18 and 5.24, for the co-rotating vortex 1 (datum) ingested near the bottom (i.e. prescribed at P_B) both swirl and total pressure distortion were relatively low. For this reason, the rotor operating point moved towards corrected mass flow slightly lower than that relative to the clean inlet conditions (Fig. 5.34(a)). On the other hand, for counter-rotating vortex ingested near the bottom, both the total pressure and swirl distortion increased significantly due to the interaction of the vortex with the self-generated distortion. Normally, the effect of the total pressure distortion tended to move the rotor operating point towards lower mass flow. Instead, the swirl distortion, occurring mainly in the counter-rotating direction (Fig. 5.28(c)) tended to increase the corrected mass flow. Overall, the operating point moved towards corrected mass flow slightly higher than that relative to the clean inlet conditions due to the predominant effect of swirl distortion (Fig. 5.34(b)).

Referring to Fig. 5.18 and 5.24, for the co-rotating vortex 1 (datum) ingested near the top (i.e. prescribed at P_T) both swirl and total pressure distortion were relatively high. Referring to Fig. 5.27(e), the change in swirl distortion at the AIP occurred mainly in the co-rotating direction. Therefore, both total pressure and swirl distortion contributed to move the operating point towards lower corrected mass flow. On the other hand, by inverting the polarity for the same vortex location, both the total pressure and swirl distortion reduced significantly. The outcome relative to this vortex case indicated that the effect of total pressure distortion was minor as compared to that of the swirl distortion.

Finally, the vortices ingested near the port were characterized by intermediate levels of total pressure and swirl distortion compared to that relative, for the same polarity, to

vortices ingested near the bottom and top (see Fig. 5.18 and 5.24). Therefore, their operating points were found between that relative to the vortices ingested near the bottom and top (Fig. 5.34(a) and 5.34(a)).

Effect of maximum swirl velocity and size Generally, the ingestion of vortices with increased maximum swirl velocity or size with respect to that of vortex 1 (i.e. vortex 2 or vortex 3, respectively), caused an increase of the magnitude of the corrected mass flow change as shown in Fig. 5.34. Equivalently, this corresponded to the ingestion of a stronger bulk swirl applied in the same direction of the ingested vortex itself. Regarding the vortices ingested near the wall (i.e. prescribed at P_S, P_B, P_P and P_T), they arose a zone of $\Delta\beta$ close to the vortex perturbation as shown in Fig. 5.32 and 5.33. Although this was contrasting the change in corrected mass flow obtained, its influence was therefore minor compared to that acting in opposite direction. On the other hand, the ingestion of vortices at the centre of the intake inlet plane (i.e. prescribed at P_C) arose one zone of relative rotor incidence close to the vortex itself having a sign dependent of the vortex polarity as shown in Fig. 5.32 and 5.33. Meanwhile, a change in relative rotor incidence around the self-generated distorted zone occurred equally in both of directions. Therefore, the increase of the rotor corrected mass flow change was not contrasted by an opposite relative rotor incidence close to the vortex as observed for vortices ingested near the wall. As a result, for this vortex location the highest change in corrected mass flow occurred as the vortex 2 or vortex 3 were ingested as shown in Fig. 5.34.

However, this outcome was not valid for co- and counter-rotating vortices ingested near the top and bottom edge of the intake (i.e. prescribed at P_T and P_B, respectively). For these cases, the S-duct aerodynamics as well as the flow distortion at the AIP were highly affected compared to other vortices ingested and the RMS of the residuals oscillated with the numerical iterations (see § 5.1.2 and 5.1.3). As a result, the change of corrected mass flow was opposite to that expected for a generic vortex with the same polarity (Fig. 5.34).

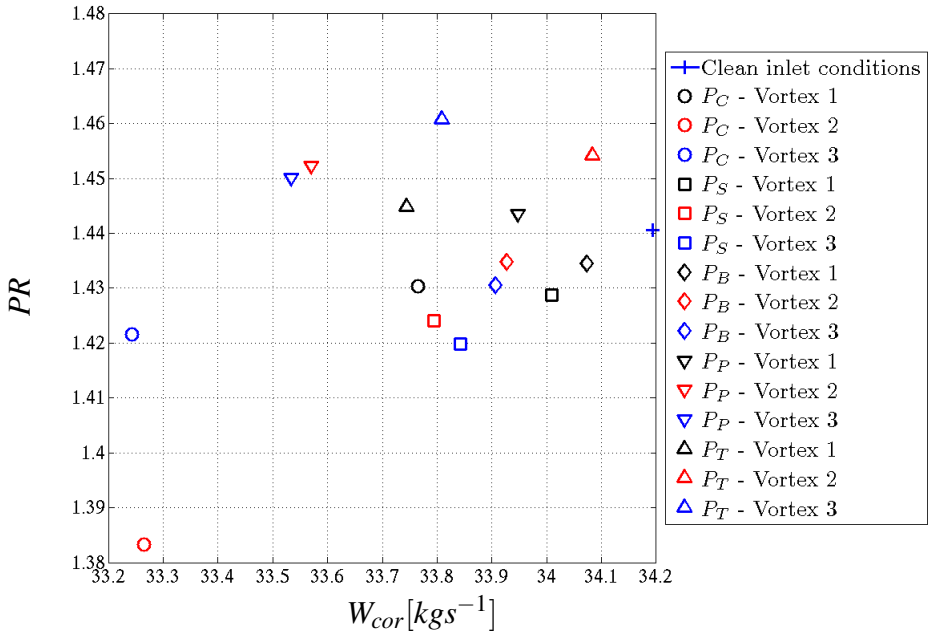

(a) Co-rotating ingested vortices

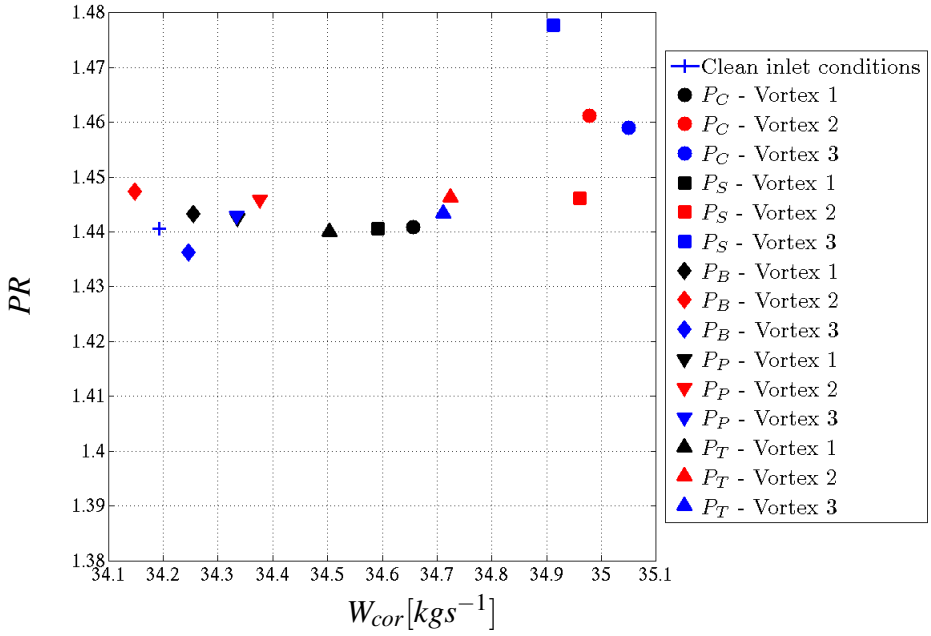

(b) Counter-rotating ingested vortices

Figure 5.34: Rotor pressure ratio (PR) versus corrected mass flow (W_{cor}) with rotor operating at 100% N_d and $p_{out}/P_{0,in} = 0.987$

5.2 The effect of throttle setting

In this section, a sensitivity analysis of the throttle setting on the flow field of the coupled system operating with the vortex 1 (datum) ingested at the intake inlet plane is presented. Firstly, the boundary conditions specified around the computational domain are defined. Then, similar analysis already considered for the vortex characteristics effect analysis (see § 5.1) are reported. In addition, the change of rotor performance were also evaluated in terms of numerical correlations established between the loss of stability pressure ratio and the swirl distortion calculated at near stall operating point.

Compared to the analyses presented in § 5.1, the effect of vortex location and polarity was accomplished. The numerical results were similar to that relative to the vortex characteristics analysis (see § 5.1.2.2) and, therefore, are presented in § D.

5.2.1 Definition of the CFD boundary conditions

The effect of the rotor throttle setting on the coupled system was investigated with the rotor operating at 80% of its original design rotational speed (N_d). As discussed in § 4.3.4, the operability range of the NASA Rotor 67 mounted on the coupled system was width enough to allow the investigation of the throttle setting effect. Referring to Fig. 3.28, the boundary conditions imposed around the CFD domain of the coupled system were similar to that presented in § 4.2.1. The only differences were relative to the boundary conditions imposed at the farfield inlet and CFD rotor outlet plane. At the farfield inlet plane, the vortex 1 (datum), defined in § 3.4.2, was prescribed at the locations defined in § 5.1.1 and for the two polarities. Hence, ten different vortices were ingested. On the other hand, CFD rotor outlet plane the static pressure was varied to obtain for each vortex ingested the whole rotor speedline between near choking and near stall operating conditions. This parameter ranged between values depending on the location and polarity of the ingested vortex itself.

5.2.2 S-Shaped intake aerodynamics

In this section, the intake performance as well as a qualitative description of the S-duct flow separation with the throttle setting are provided.

5.2.2.1 Intake performance

As the rotor operability changed from near stall to near choking conditions, the pressure recovery (η) slightly reduced as indicated in Table 5.2. This change was essentially due

to the increase of the flow velocity in the duct. Note that, regardless of the vortex ingested, the values of η were very close to the unit, indicating that the intake performance should not affect significantly that of the rotor placed downstream (see § 3.3.8).

Vortex location	Polarity	Near stall	Near choking
P_C	Co	0.992	0.991
	Counter	0.989	0.991
P_S	Co	0.990	0.992
	Counter	0.990	0.991
P_B	Co	0.990	0.993
	Counter	0.990	0.991
P_P	Co	0.991	0.992
	Counter	0.990	0.992
P_T	Co	0.990	0.991
	Counter	0.990	0.992

Table 5.2: Pressure recovery (η) for vortex 1 ingested at different locations and polarities and with rotor operating at 80% N_d and at near stall and near choking conditions

5.2.2.2 Description of the S-duct flow separation

As the rotor operability changed from near stall to near choking, the mass flow of the system increased and, therefore, the intensity of the S-duct flow separation increased as shown in Fig. 5.35 and 5.36. Moreover, by following the method of images, mentioned in § 5.1.2.2, the angular shift of the ingested vortex within the duct would be affected by the mass flow change. By assuming that the speed of the vortex in the circumferential direction within the S-duct was constant, the higher the mass flow the lower the angular shift of the vortex in the S-duct. Clearly, this change could affect directly the S-duct flow separation.

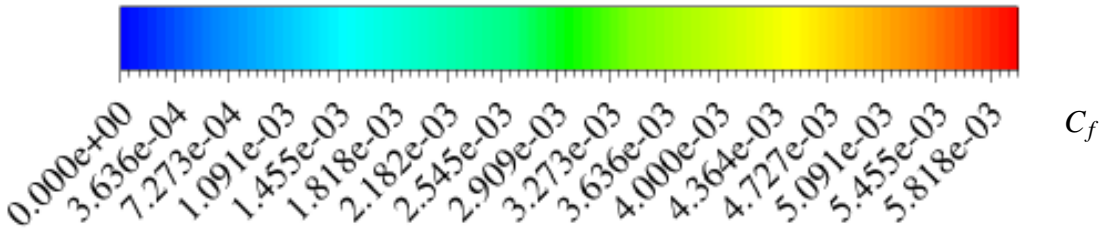

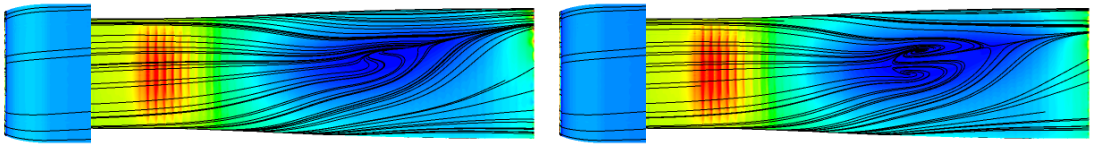

(a) Vortex prescribed at P_C, near stall

(b) Vortex prescribed at P_C, near choking

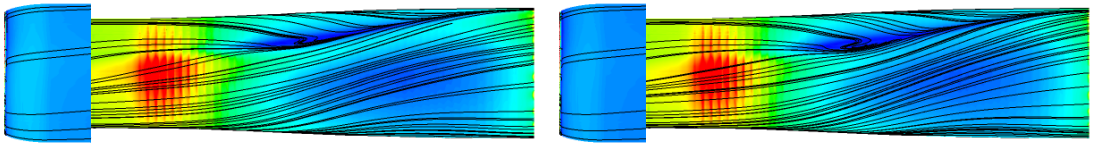

(c) Vortex prescribed at P_S, near stall

(d) Vortex prescribed at P_S, near choking

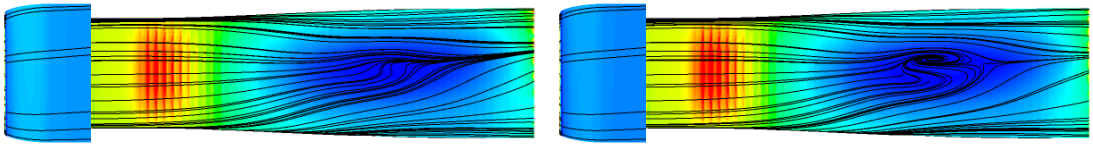

(e) Vortex prescribed at P_B, near stall

(f) Vortex prescribed at P_B, near choking

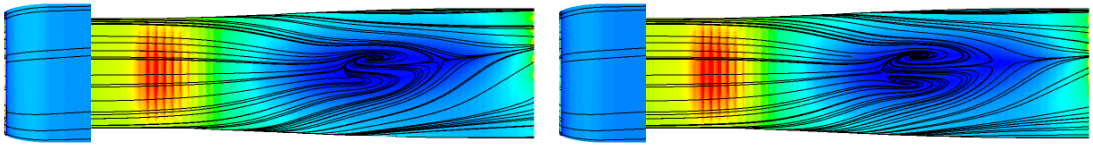

(g) Vortex prescribed at P_P, near stall

(h) Vortex prescribed at P_P, near choking

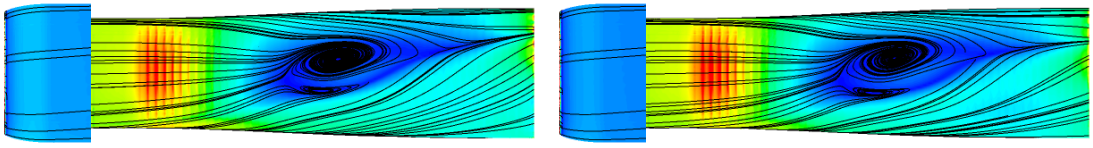

(i) Vortex prescribed at P_T, near stall

(j) Vortex prescribed at P_T, near choking

Figure 5.35: Contours of skin friction coefficient (C_f) with streaklines (black) at the starboard side of the intake wall for co-rotating vortex 1 (datum) ingested at different locations with rotor operating at 80% N_d and at near stall and near choking conditions

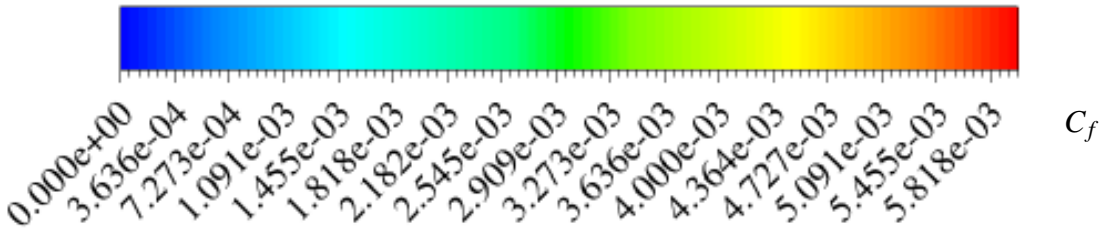

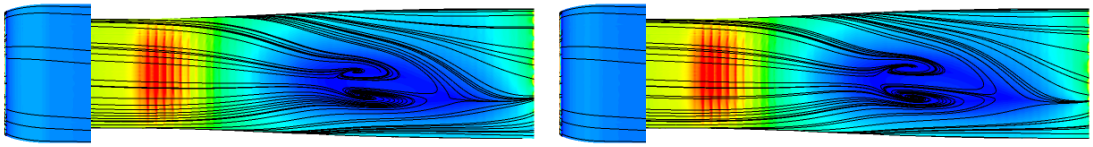

(a) Vortex prescribed at P_C, near stall

(b) Vortex prescribed at P_C, near choking

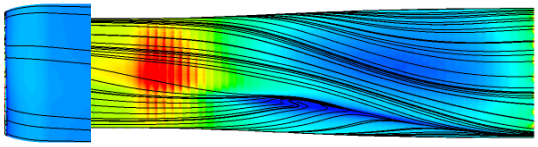

(c) Vortex prescribed at P_S, near stall

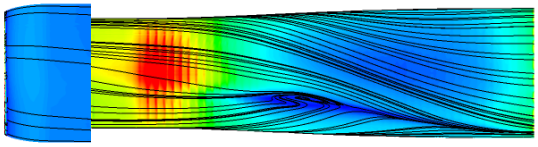

(d) Vortex prescribed at P_S, near choking

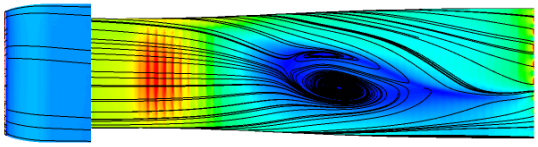

(e) Vortex prescribed at P_B, near stall

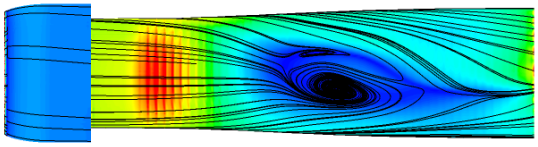

(f) Vortex prescribed at P_B, near choking

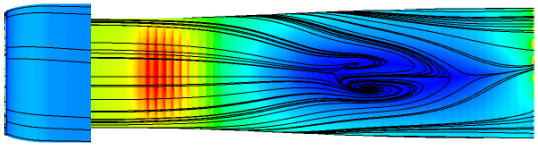

(g) Vortex prescribed at P_P, near stall

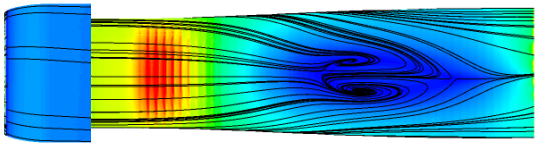

(h) Vortex prescribed at P_P, near choking

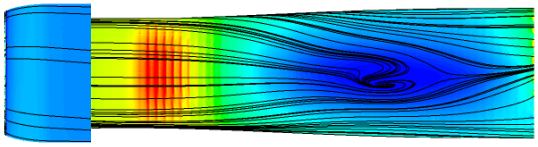

(i) Vortex prescribed at P_T, near stall

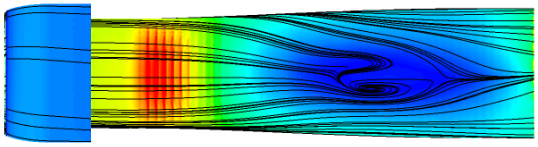

(j) Vortex prescribed at P_T, near choking

Figure 5.36: Contours of skin friction coefficient (C_f) with streaklines (black) at the starboard side of the intake wall for counter-rotating vortex 1 (datum) ingested at different locations with rotor operating at 80% N_d and at near stall and near choking conditions

5.2.3 Flow field description at the AIP

In this section, a description of the flow field, in terms of both total pressure and swirl distortion, at the AIP of the coupled system operating according to the boundary conditions defined in § 5.2.1 is presented.

5.2.3.1 Total pressure distortion

Regardless of the vortex location and polarity investigated, the extent of the total pressure distortion at the AIP remained essentially unchanged and within a 60^o sector as the rotor operability changed from near stall to near choking (Fig. 5.38). Therefore, the DC_{60} could be used as a metric to quantify the total pressure distortion. This parameter increased linearly with the mass flow and with a rate which was independent of the vortex location and polarity (Fig. 5.37). According to practical recommendations[67], the values of DC_{60} obtained were negligible for the rotor performance unless that relative to co- and counter-rotating vortices ingested near the top and bottom edge (i.e. prescribed at P_T and P_B), respectively. As discussed in § 5.1.3.1, for these combinations of vortex location and polarity a strong interaction occurred between the self-generated distortion and the vortex itself.

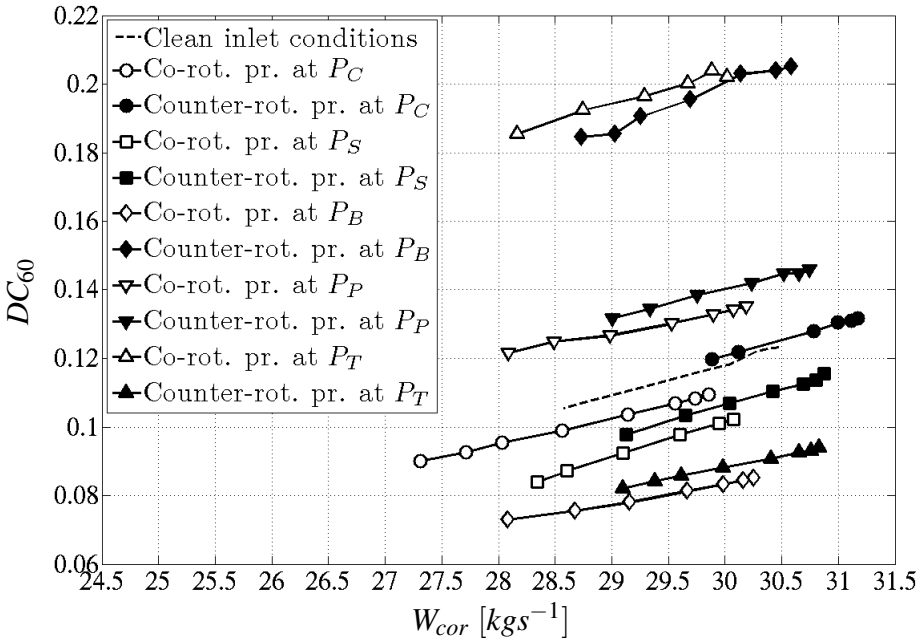

Figure 5.37: Total pressure distortion parameter (DC_{60}) versus corrected mass flow (W_{cor}) for vortex 1 ingested at different locations and polarities and with rotor operating at 80% N_d

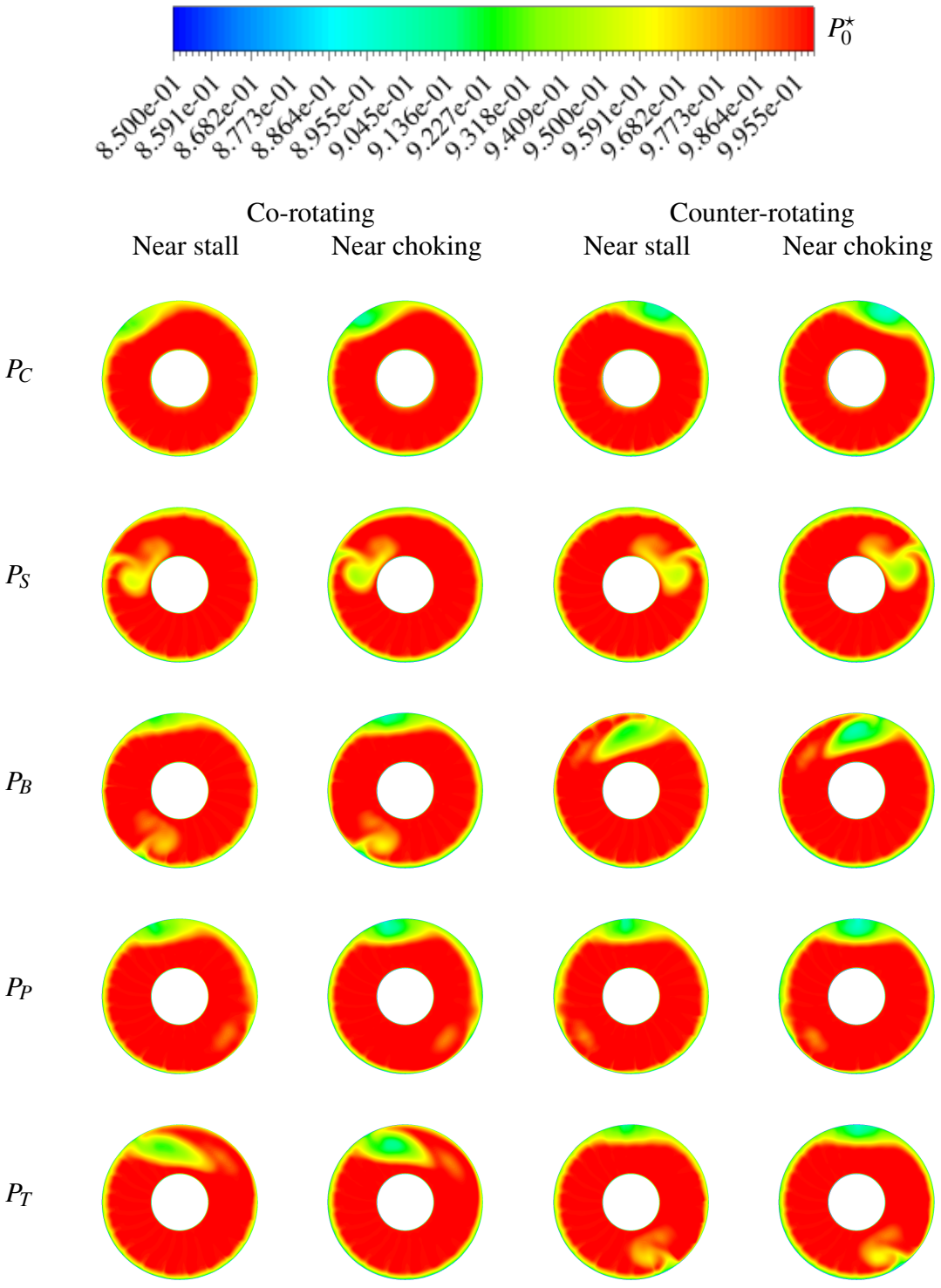

Figure 5.38: Contours of non-dimensional total pressure $P_0^\star$ for co- and counter-rotating vortex 1 (datum) ingested and with rotor operating at 80% N_d and at near stall and near choking conditions

5.2.3.2 Swirl distortion

Figures 5.39(a) and 5.39(b) show the values of the mass flow average of the magnitude of the relative flow angle change ($\overline{|\Delta\beta|}$), defined in § 3.3.1, with the rotor operating at 80% N_d and for a rotor outlet non-dimensional mass flow ($NDMF_2$) equal to 3.87 and $4.22 \cdot 10^{-3}\ kgs^{-1}K^{0.5}Pa^{-1}$. These values corresponded to operating conditions towards near stall and near choking operating conditions, respectively. In general, as the rotor operability changes from near choking to near stall a reduction in axial velocity occurs. Therefore, the influence of the swirl distortion related to the vortex ingested increased. This condition manifested with a general increase of $\overline{|\Delta\beta|}$ observed from near stall to near choking conditions.

Referring to Fig. 5.39(a), the swirl distortion level for vortices ingested near stall depended on the vortex polarity. In particular, the swirl distortion was higher for co- than for counter-rotating vortices ingested. This outcome confirmed that the co-rotating vortices contributed with the bulk swirl introduced by the rotor to increase the swirl distortion level. Meanwhile, counter-rotating vortices ingested contrasted the swirl introduced by the rotor and, therefore, the overall swirl distortion reduced. Note also that, for vortices ingested near the bottom the swirl distortion was higher when ingested in co- rather than in counter-rotating direction. This result confirmed that the swirl distortion was higher when the vortex was mainly interacting with the wall rather than with the self-generated distortion.

On the other hand, as the rotor operability changed to near choking conditions, the mass flow was sufficiently high that the change in swirl distortion attributed to the vortex was essentially independent of its polarity for vortices ingested at the centre of the intake inlet plane and near the starboard and port edge of the intake wall (see Fig. 5.39(b)). Meanwhile, a significant change of $\overline{|\Delta\beta|}$ with the polarity was observed for vortices ingested near the bottom and top edge of the wall, due to the possibility of these vortices to interact either with the self-generated distortion or simply with the wall. For these vortex locations, the relative values of swirl distortion calculated for the two polarities were consistent with that presented in § 5.1.3.2.

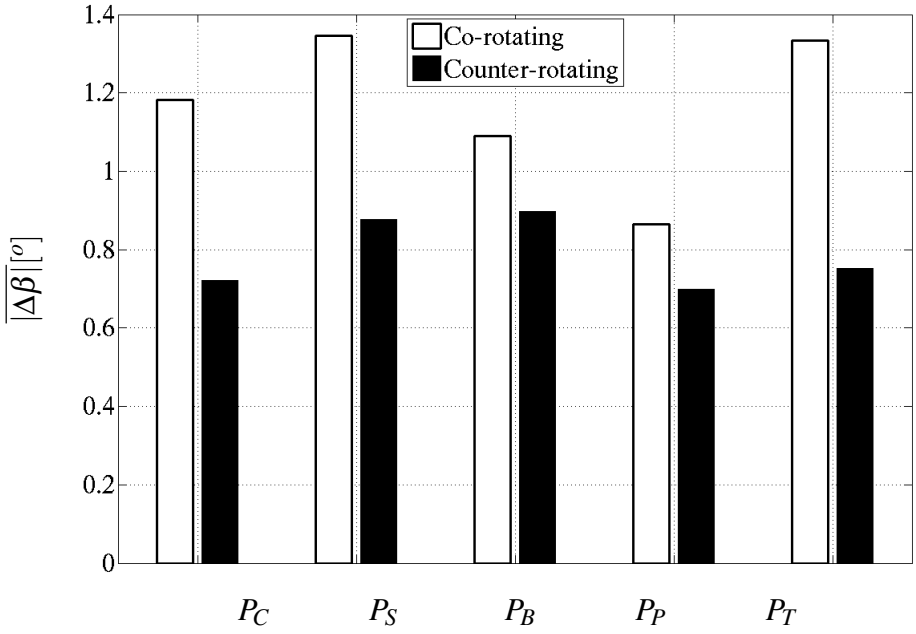

(a) $NDMF_2 = 3.87 \cdot 10^{-3}\ kgs^{-1}K^{0.5}Pa^{-1}$ (near stall)

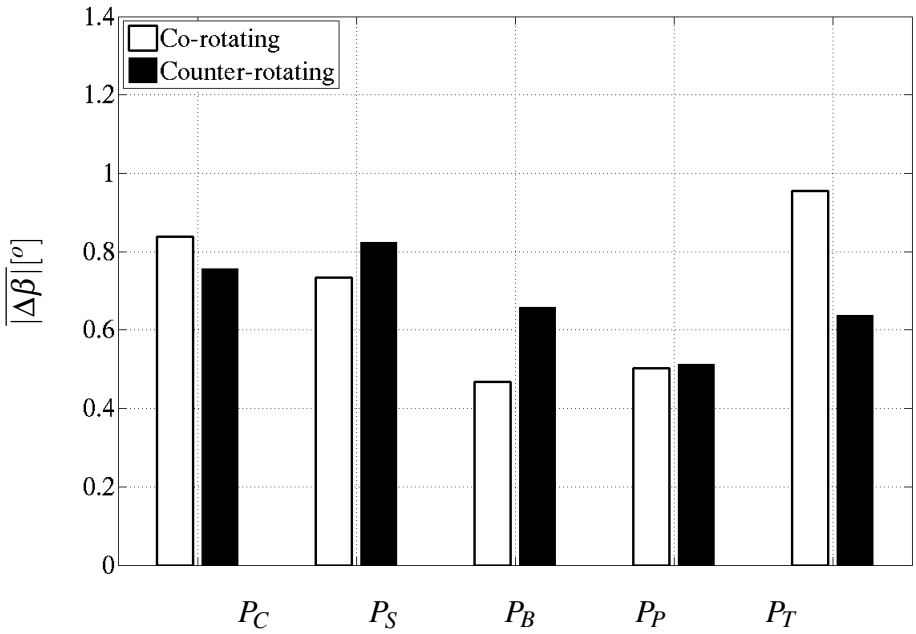

(b) $NDMF_2 = 4.22 \cdot 10^{-3}\ kgs^{-1}K^{0.5}Pa^{-1}$ (near choking)

Figure 5.39: Mass flow average of the magnitude of the relative flow angle change ($\overline{|\Delta\beta|}$) calculated at different locations and polarities of the vortex 1 and with rotor operating at 80% N_d and near stall and near choking operating conditions

5.2.4 Change of rotor performance

In this section, the changes of rotor performance relative to the coupled system operating by considering the boundary conditions defined in § 5.2.1 with respect to the clean inlet conditions are presented. They were quantified in terms of pressure ratio (PR) versus corrected mass flow (W_{cor}) as well as loss of stability pressure ratio (ΔPRS) related with the inlet swirl distortion expressed with the mass flow average of the magnitude of the relative flow angle change ($\overline{|\Delta\beta|}$). Note that, as compared with the analyses discussed in § 5.2.2 and 5.2.3, the effect of throttle setting is presented together with that of the vortex location and polarity.

5.2.4.1 Global performance

Figures 5.40(a) and 5.40(b) show the rotor speedlines of pressure ratio (PR) versus corrected mass flow (W_{cor}) for co- and counter-rotating vortex 1 (datum), respectively, ingested at different locations and with the rotor operating at 80% of the rotor design rotational speed (N_d). As discussed in § 5.1.4, the ingestion of a co- and a counter-rotating vortex in the coupled system caused a reduction and an increase of corrected mass flow with respect to the that calculated under clean inlet conditions, respectively. The effect of swirl distortion was generally predominant with respect to that associated to the total pressure distortion when the vortex 1 (datum) was ingested at different locations, as already observed at 100% N_d (see § 5.1.4).

As discussed in § 5.2.3.1, the highest total pressure distortion was observed for co- and counter-rotating vortices ingested near the top and bottom edges of the duct, respectively. For these cases, the rotor speedlines were shifted towards lower corrected mass flow compared to that attributed to any other vortex ingested near the wall as shown in Fig. 5.40(a) and 5.40(b).

Regardless of the vortex location and by observing the numerical results at constant pressure ratio (PR), the change of corrected mass flow with respect to the clean inlet conditions increased as the rotor operability changed from near choking to near stall conditions (Fig. 5.40). By considering the swirl distortion only, this difference was attributed to the increase of the level of impact determined by the vortex ingested which increased moving towards near stall.

Moreover, a comparison of the stability pressure ratio (near stall) was carried out between a generic ingested vortex case and that relative to the clean inlet conditions. Regardless of the vortex location, the ingestion of a co-rotating vortex was characterized by lower stability pressure ratio than that relative to a counter-rotating vortex. This outcome was essentially due to the increase and decrease of blade loading associated with the reduction and increase of mass flow as a co- and a counter-rotating vortex was ingested,

respectively. In particular, for co-rotating vortices ingested near the top (i.e. prescribed at P_T), the stability pressure ratio was relatively low compared to other co-rotating vortices ingested (see Fig. 5.40(a)). This outcome was related to the high total pressure distortion occurring for this vortex (see § 5.2.3.1). A similar result was expected for the counter-rotating vortex ingested near the bottom (see Fig. 5.40(b)). For this case, however, the stability pressure ratio was as high as that calculated for other counter-rotating vortices ingested. Therefore, although the total pressure distortion was relatively high, the effect of swirl distortion was more predominant.

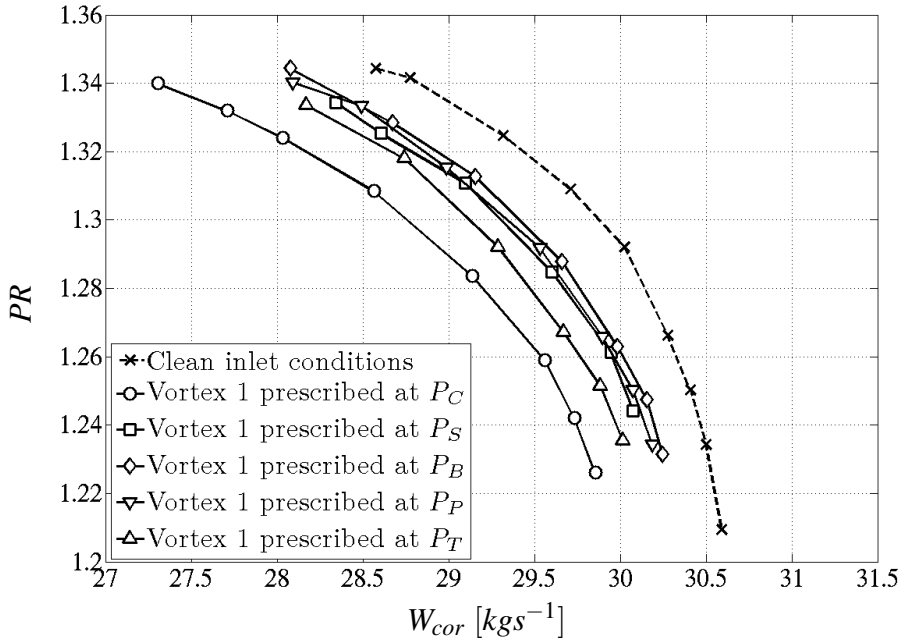

(a) Co-rotating ingested vortices

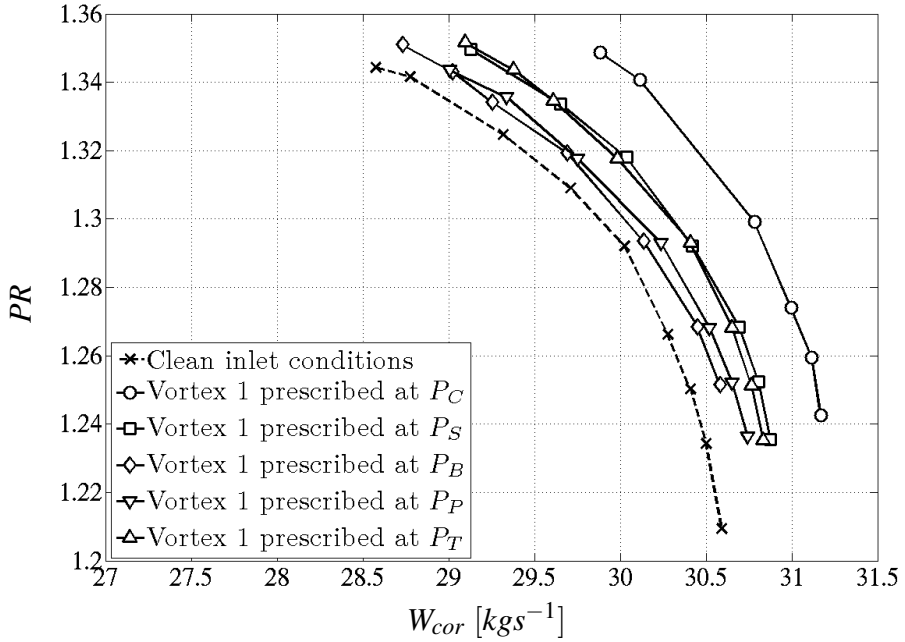

(b) Counter-rotating ingested vortices

Figure 5.40: Rotor pressure ratio (PR) versus corrected mass flow (W_{cor}) with vortex 1 (datum) ingested at different locations and polarities and rotor operating at 80% N_d

5.2.4.2 Swirl distortion correlations

Figure 5.41 shows the loss of stability pressure ratio (ΔPRS) versus the swirl distortion quantified with $\overline{|\Delta\beta|}$ and relative to the distorted cases presented in this section as well as to the clean cases presented in § 4.4.3. A correlation line was calculated by considering only the CFD solutions obtained on the coupled system configuration with the rotor operating at 80% N_d. Note that, the cases investigated at this rotational speed were characterized by low values of total pressure distortion parameter (DC_{60}) as discussed in § 5.2.3.1. On the other hand, the ΔPRS calculated at 100% N_d was significantly affected by the total pressure distortion as discussed in § 5.1.3.1. Therefore, the correlation line obtained was based assumed that only the swirl distortion was affecting the rotor performance. Additionally, the correlation was obtained by assuming that ΔPRS was zero as no change of relative rotor incidence occurred ($\overline{|\Delta\beta|} = 0^o$). The results showed that a slight scatter between the correlation points with respect to the correlation line occurred for the cases relative to the ingestion of the vortex 1 (datum) in the coupled system at different locations and polarities. Clearly, this was attributed to the change of total pressure distortion amongst these cases, discussed in § 5.2.3.1. Note, however, that according to the amount of information provided in this work, additional CFD simulations would be necessary to validate the correlation line obtained.

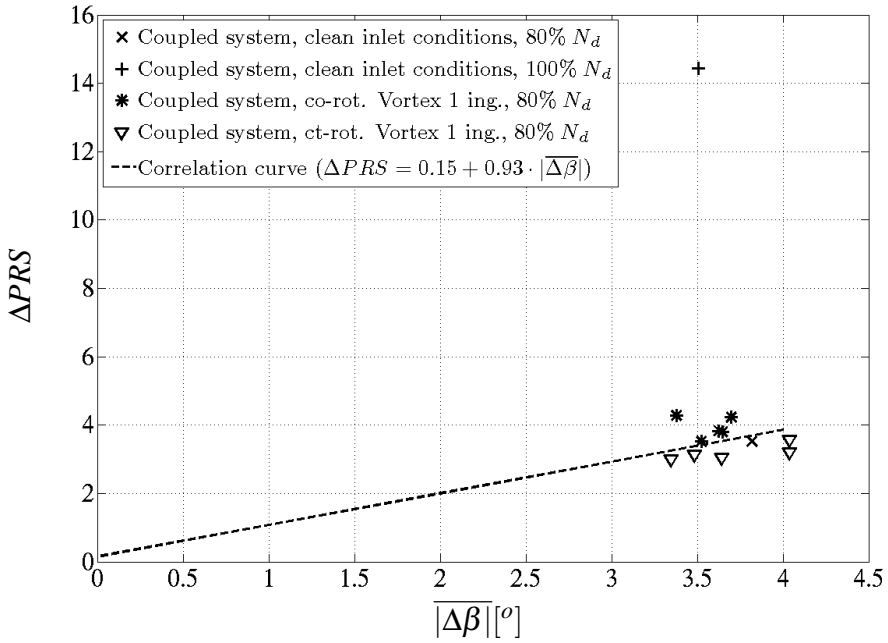

Figure 5.41: Loss of stability pressure ratio (ΔPRS) versus the mass flow average of the magnitude of the relative flow angle change ($\overline{|\Delta\beta|}$)

5.3 Summary

In this chapter, numerical investigations relative to the coupled system operating with vortex ingestion have been presented. They were based on the analyses carried out on the same system operating under clean inlet conditions (see § 4). In particular, two types of parametric studies were considered. They included the effect of the vortex characteristics and throttle setting on the rotor performance with the rotor operating at 100% and 80% of its original design rotational speed (N_d), respectively. For each of these analyses, the vortex was ingested at five locations aligned with the centre of the intake inlet plane and near the starboard, bottom, port and top edge of the intake wall. Also, both of the vortex polarities were considered. The key messages for this chapter are summarised below.

1. The vortices ingested at the centre of the intake inlet plane remained aligned with the intake centerline up to the AIP and introduced a centered bulk swirl which superimposed to the intake flow field relative to the clean inlet conditions. On the other hand, the vortices ingested near the intake wall spiraled out around the wall itself in the same direction of the vortex as already observed by Anderson[2].

2. As a vortex was ingested in the coupled system, this could interact with the existing intake flow field and, in particular, with that attributed to the self-generated distortion. This interaction was significant for counter- and co-rotating vortices ingested near the bottom and top edge of the intake wall, respectively. In these conditions, the S-duct flow separation pattern was significantly altered. Meanwhile, the level and extent of the flow distortion reached at the AIP were relatively high. Therefore, compared to other vortices of the same polarities ingested at other locations, the rotor corrected mass flow relative to these cases was lower. Moreover, for these critical combinations of vortex location and polarity, the doubling of maximum swirl velocity or size of the vortex caused an increase of the aforementioned interaction. As a result, the CFD solutions became unsteady while the operating points of the rotor obtained presented opposite trend compared to that normally expected for other vortex locations.

3. Vortices ingested near the wall were characterized by two zones of opposite relative rotor incidence ($\Delta\beta$) around the vortex. Clearly, their effects on the global rotor corrected mass flow were opposite. Meanwhile, the rotor incidence was also altered around the self-generated distortion mainly in a direction corresponding to that of the vortex polarity. On the other hand, vortices ingested at the centre of the intake inlet plane arose only a single zone of change of relative rotor incidence close to the vortex and distributed around the whole hub annulus. As a consequence, the change of rotor corrected mass flow was relatively high compared to that calculated for other vortices ingested near the wall. This result could also be related to the location of the swirl distortion along the span.

4. For a constant rotor pressure ratio (*PR*), the change of corrected mass flow mainly related to the swirl distortion caused an increase and reduction of blade loading as co- and counter-rotating vortices were ingested in the system. As a result, the stability pressure ratio for co- was lower than for counter-rotating vortices ingested. Also, the stability pressure ratio depended on the magnitude of total pressure occurring at the AIP. In particular, a significant reduction of *PR* was observed for co-rotating vortex ingested near the top where the total pressure distortion was relatively high.

5. A swirl distortion-based correlation was defined between the loss of stability pressure ratio and the swirl distortion measured by means of the mass flow average of the magnitude of the relative flow angle change ($\overline{|\Delta\beta|}$). This correlation considered all of the case studies obtained on the coupled system configuration unless for that obtained under clean inlet conditions and with the rotor operating at its original design rotational speed (N_d). In this condition, the DC_{60} reached a value which, according to practical recommendations[67], could no longer be neglected. Compared to the values expected on the correlation line, a scatter relative to the CFD solutions obtained in this work was observed. This outcome was related either to the change of total pressure distortion. A complete validation of the proposed correlation could be obtained in further research for case studies characterized by different values of $\overline{|\Delta\beta|}$.

Chapter 6

AIP analysis for swirl distortion

This chapter discussed the assessment of a methodology to determine the AIP for swirl distortion on the datum NASA Rotor 67 configuration, defined in § 3.2.2. Two preliminary numerical analyses under clean inlet conditions, to ascertain the validity of the CFD results upstream of the rotor face, are discussed. They include the validation of the shock wave system as well as the analysis of rotor disturbances. Finally, examples of determination of the AIP for swirl distortion are reported. They were considering the ingestion of the datum vortex, defined in § 3.4.2, at the CFD inlet domain.

6.1 Shock wave propagation analysis

In this section, the shock wave analysis is discussed. Firstly, an overview regarding the mechanisms governing the shock wave system occurring upstream of the transonic compressor rotors as well as the analytical models proposed in previous research are presented. Then, the methodology applied to extract the information of the shock waves from the CFD results and the prediction of the shock wave system are reported.

6.1.1 Shock wave systems on transonic compressors

The requirements imposed by airlines for reducing the Specific Fuel Consumption (SFC) and increasing the specific power of the gas turbines, have led design engineers to high pressure ratio compressors and, then, rotational speed. For this reason, the 1^{st} or 2^{nd} stage of aero-engine gas turbines operate usually in transonic flow regimes[40,69]. The flow field upstream of the rotor face of a transonic compressor is characterized by a shock wave system. Previous research was addressed to this aspect due to its effect on compressor efficiency. Prasad[40] and Chauvin et al.[70] confirmed that about $15-20\%$ of the total loss

attributed to the rotor is due to the shock waves. Hence, it is important to accurately capture these shock waves in CFD analysis. A lack of sufficient grid resolution in the region upstream of the rotor leading edge would artificially dissipate the shock system and, therefore, influence the total loss associate to the rotor[40].

The axial Mach number of the flow approaching the rotor leading edge is usually higher than that required to obtain the relative Mach number (M_{rel}) parallel to the stagger angle of the blade. This is because an oblique shock wave generated from the leading edge decreases the axial Mach number component accompanied with an increase of static pressure[71]. This oblique shock wave is the suction side part of a bow shock wave, which propagates upstream and is also responsible of the flow distortion. Prasad et al.[40] indicates that the shock waves propagate upstream unless supersonic axial velocities occur (Fig. 6.1)

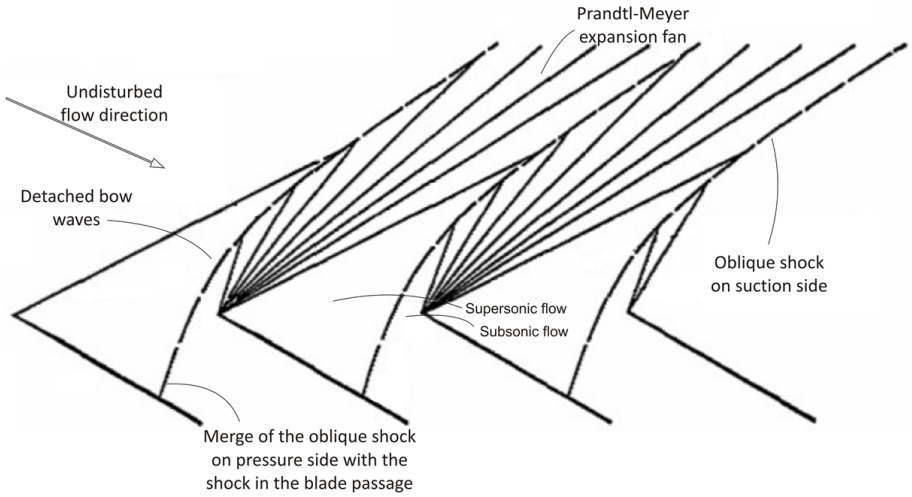

Figure 6.1: Shock wave system upstream of a transonic compressor rotor[71]

According to Kantrowitz[71], these oblique shock waves are usually detached from the blade because of the finite thickness of the leading edge. When the shock wave is detached enough, both pressure and suction side parts of the bow shock wave are aligned and form a unique straight shock wave, which is the case of CFD simulations carried out by Prasad[40] on the NASA Rotor 35. Once the flow passes through the bow shock wave and then becomes parallel to the rotor stagger angle, it must follow the curvature of the blade suction side. The mechanism through which the flow is deflected is a Prandtl-Meyer expansion fan, generated at the leading edge just downstream of the oblique shock wave[71]. This expansion fan is characterized by a reduction of the static pressure[71]. The analysis of Prasad[40] shows that a necessary condition for periodicity in circumferential direction is that the change in flow angle across a shock wave is exactly compensated by a commensurate negative change in angle across its companion expansion wave. Prasad[40]

also indicate the presence of another normal shock wave spanning the width of the passage, which is one of the main mechanisms through which the compression manifests. This normal shock wave usually merges with the part of the bow shock wave located at the blade pressure side[69] as shown in Fig. 6.1.

6.1.2 Analytical models for shock waves propagation

The intensity of shock waves is quantified by the shock wave strength (Π). This is defined as the ratio between the static pressure jump ($p^+ - p^-$) and the arithmetic static pressure average (p_{mean}) manifested across the shock (Eq. 6.1).

$$\Pi = \frac{p^+ - p^-}{p_{mean}} \tag{6.1}$$

where

$$p_{mean} = \frac{p^+ + p^-}{2}$$

The shock wave strength (Π) varies along its main propagation direction and its distribution can be described by means of an analytical model. Referring to transonic compressor rotors, the propagation of the shock waves occurring upstream was investigated by Mendousse[72] and Morfey et al.[73].

Mendousse[72] developed a model to estimate the shock wave decay, using the weak shock waves theory. This model assumed a sawtooth shock wave propagating in a 1D quiescent flow. For this model, the distribution of the shock wave strength (Π) as function of time (or space) requires also the specification of the speed of sound (c_0), the shock wave length (λ), the specific heat ratio (γ) and the initial shock strength (Π_0) as given in Eq. 6.2.

$$\frac{c_0 \cdot t}{\lambda} = \frac{2\gamma}{\gamma+1}\left(\frac{1}{\Pi} - \frac{1}{\Pi_0}\right) \tag{6.2}$$

On the other hand, Morfey et al.[73] extended the Mendousse model (Eq. 6.2) eliminating the restriction of weak shock by using a non-linear acoustics analysis on a 2D axial-tangential plane upstream of the rotor. Referring to Fig. 6.2, the application of this model for a ducted rotor requires the specification of the quantities listed below.

- Shock wave angle with respect to the axial direction (ϕ). This is obtained from trigonometric considerations as function of the axial, circumferential and relative

Mach number (M_z, M_θ and M_{rel}) as given in Eq. 6.3.

$$\tan(\phi) = \frac{M_z + M_\theta \sqrt{M_{rel}^2 - 1}}{M_\theta - M_z \sqrt{M_{rel}^2 - 1}} \tag{6.3}$$

In turn, the tangential Mach number (M_θ) is derived from trigonometric considerations as given in Eq. 6.4.

$$M_\theta = \sqrt{M_{rel}^2 - M_z^2} \tag{6.4}$$

- Blade pitch (τ).
- Axial Mach number (M_z).
- Initial shock wave strength (Π_0), measured at the rotor leading edge.
- Axial location upstream of the rotor leading edge (z).

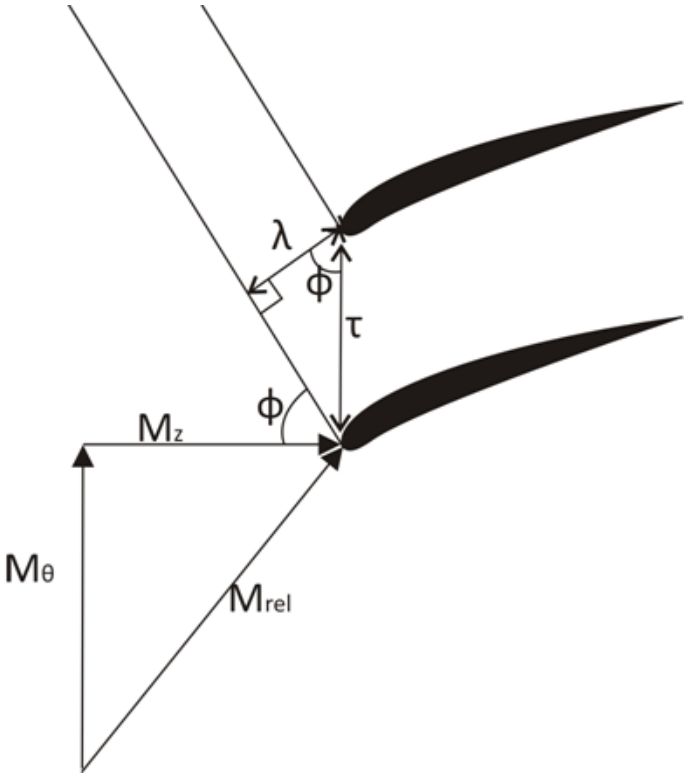

Figure 6.2: Visualization of shock waves upstream of a transonic rotor at constant span location

Hence, the Morfey model is analytically expressed as given in Eq. 6.5.

$$\frac{z}{\tau} = \frac{2\gamma}{\gamma+1}\cos(\phi)(\sin(\phi)-M_z)\left(\frac{1}{\Pi}-\frac{1}{\Pi_0}\right)\left[1+\left(\frac{\gamma+1}{4\gamma}\frac{\sin(\phi)}{\sin(\phi)-M_z}\right)^2\frac{\Pi^3}{\Pi_0}\right]^2 \quad (6.5)$$

This model was initially validated using experimental data from three supersonic fan rotors of Rolls-Royce plc and General Electric Co[73]. However, inaccuracies were observed in predicting the shock wave strength. Hence, it was suggested that they were attributed to the assumption in the model of exact uniformity of the shock wave pattern and absence of three dimensional effects.

The same model was also validated by Prasad[40] with CFD results carried out on a 2D midspan of the NASA Rotor 35. As a result, the shock wave propagation model was accurately predicted. Referring to the shock wave propagation model, Prasad et al.[40] concluded that the shock wave strength decays as the inverse of the axial distance upstream of the rotor (z^{-1}) for supersonic flow regimes. On the other hand, the disturbances in a subsonic flow decay exponentially. For a transonic rotor, the flow regime changes from subsonic to supersonic along the span location. Therefore, the rotor disturbances produced near the tip propagate further upstream than those produced near the hub. The Morfey model was considered for this research.

In the next section the methodology applied to analyse the shock wave propagation system as well as the validation of the shock wave system are reported. The former corresponded to that proposed by Prasad[40]. The latter was carried out on the datum NASA Rotor 67 configuration operating at near peak efficiency operating point (see § 3.2.2.2).

6.1.3 Methodology for shock wave propagation analysis

The shock wave propagation system upstream of the datum NASA Rotor 67 configuration was extracted from CFD solutions of the fan rotor operating under clean conditions and validated against the Morfey analytical model presented in § 6.1.2. Although this was defined for a 2D and inviscid flow, Prasad[40] showed that the model was still valid at a span location where the endwall effects and the influence of the tip clearance flow can be neglected. In the model proposed of NASA Rotor 67, no tip clearance was modelled. Also, he confirmed that although the flow is modelled as viscous, there were no large discrepancies on the prediction of the shock waves. This confirmed that the shock wave is basically an inviscid phenomena.

Data extraction from CFD results Figure 6.3 shows a sketch of the shock wave system at constant blade span propagating upstream of a transonic compressor rotor operat-

ing under clean inlet conditions. Also, the typical trend of the static pressure along the centerline is also indicated. Hence, the static pressure was extracted from the CFD results along a curve, called passage centerline, defined at constant span within the blade passage as shown in Fig. 6.3. This curve lies circumferentially midway between the suction and pressure side of the two consecutive rotor blades. Also, it extends upstream of the rotor leading edge by keeping the slope reached at this location (α). Therefore, it draws a helix into the space. By moving along the centreline, a steep rise in static pressure occurs each time that a shock wave is crossed. The magnitude of this rise at a specific axial location defines the shock wave strength ($\Pi(z)$).

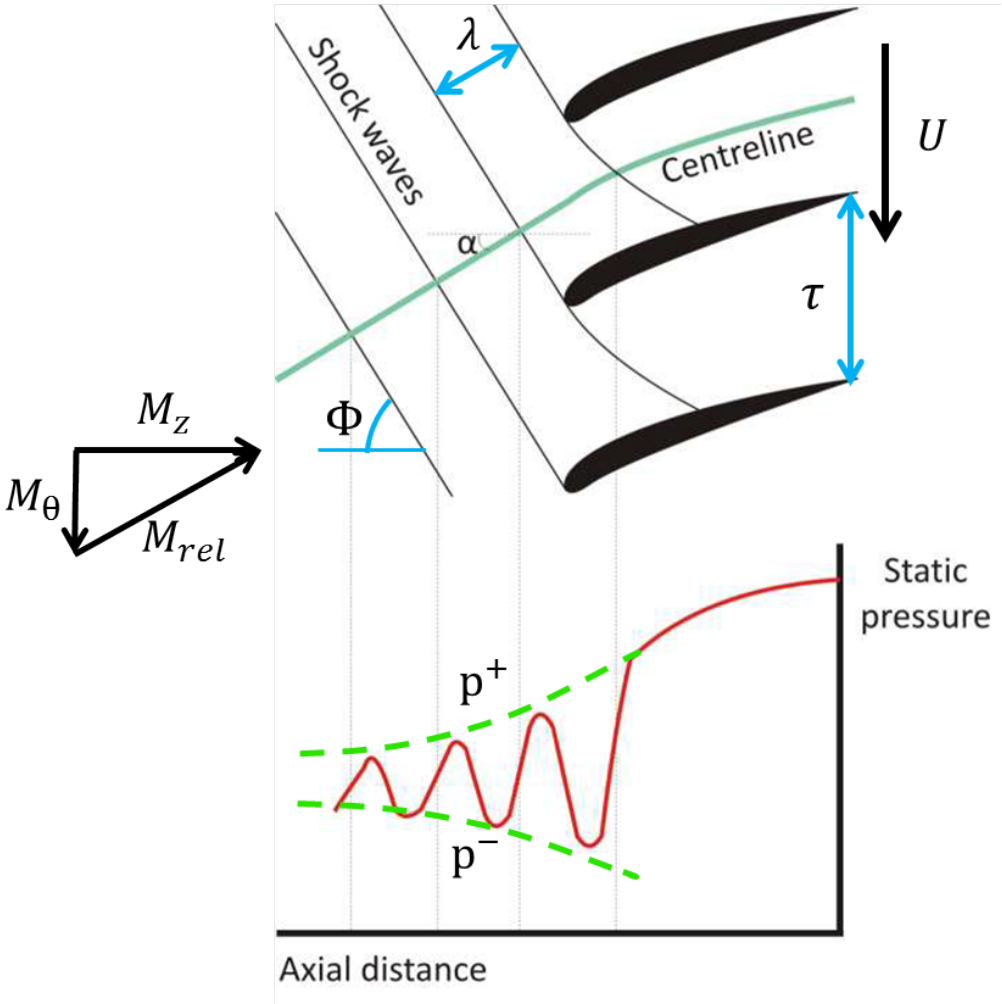

Figure 6.3: Visualization of the shock waves system upstream of the rotor blade at constant span (top) and static pressure distribution along the axial location measured on the centreline (bottom)[74]

Inputs for the Morfey model As discussed in § 6.1.2, the shock wave propagation model of Morfey (Eq. 6.5) requires the following input data: the blade pitch (τ), the relative and axial Mach numbers far upstream of the rotor leading edge, (M_{rel} and M_z) and the initial shock wave strength (Π_0). The Mach numbers were calculated as the mass flow circumferential average at the inlet of the domain for a specific value of span.

Regarding the initial shock wave strength (Π_0), this was extracted at the point of formation of the shock wave identifiable within the CFD solution. As a result of the CFD validation relative to the datum NASA Rotor 67 configuration, the shock wave at near peak efficiency operating conditions was relatively attached to the rotor leading edge as presented in § 3.2.2.5. Therefore, two oblique shocks coming from the rotor leading edge, behaving in different manners, were identified. However, the Morfey model (Eq. 6.5) is applicable only on the shock wave coming from the suction side and propagating upstream of the rotor. Therefore, it was assumed that the location relative to the initial shock wave strength (Π_0) was found just upstream of the rotor leading edge as shown in Fig. 6.4.

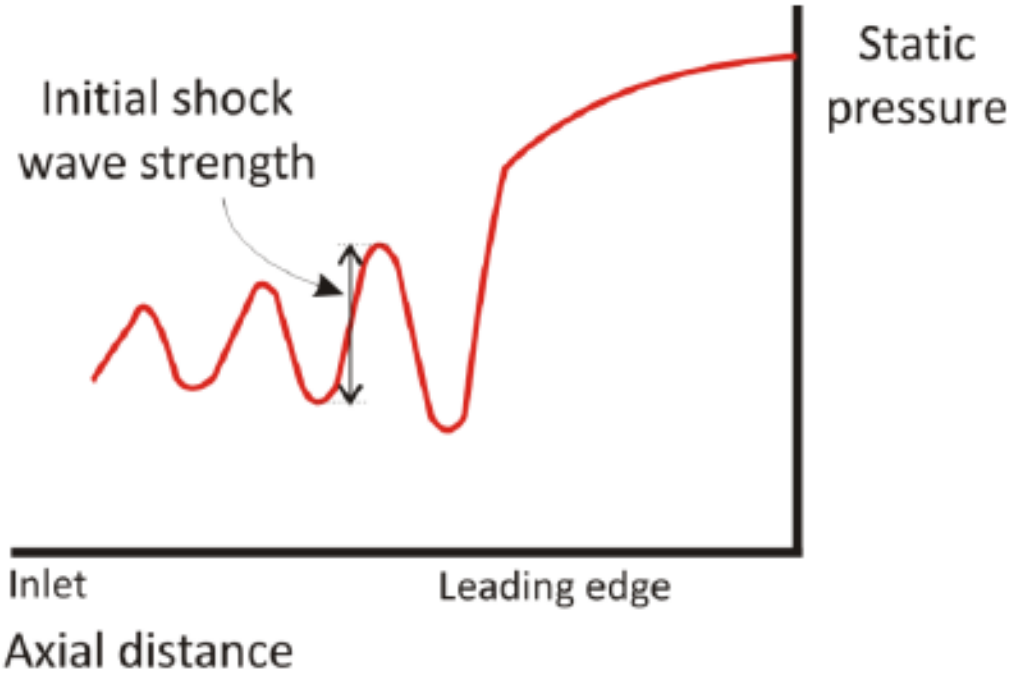

Figure 6.4: Visualization of the location relative to the initial shock wave strength (Π_0) assumed upstream of the NASA Rotor 67[74]

Implementation of the Morfey model into the CFD code The model of Morfey defines implicitly the axial distribution of the shock wave strength (Π) upstream of the leading edge (Eq. 6.5). Since this model is non-linear, it was solved by applying a numeri-

cal method such as that of Newton-Raphson. Once the shock wave strength distribution ($\Pi(z)$) was calculated, the axial distribution of static pressure upstream and downstream of the shock wave ($p^-(z)$ and $p^+(z)$) were derived from the shock wave strength definition (Eq. 6.1) as given in Eq. 6.6 and 6.7, respectively.

$$p^-(z) = p_{mean} \cdot (1 - \Pi(z)/2) \tag{6.6}$$

$$p^+(z) = p_{mean} \cdot (1 + \Pi(z)/2) \tag{6.7}$$

These two static pressure distributions represent the final output of the Morfey model indicated in Fig. 6.3. Note that, according to Morfey model, the mean pressure (p_{mean}) is assumed constant along the direction of propagation. However, slight variations of this quantity were observed into the CFD solution. Therefore, the mean pressure (p_{mean}) is measured at different axial positions and then obtained along the inlet domain by polynomial interpolation.

Estimation of the shock wave angle Referring to Fig. 6.5, the following relationship obtained by trigonometric considerations as given in Eq. 6.8.

$$\frac{\lambda}{\sin(\pi - \phi - \alpha)} = \frac{a}{\cos\alpha} \tag{6.8}$$

Referring to Fig. 6.2, the shock wave length (λ) can be expressed in function of the blade pitch (τ) and the shock wave angle (ϕ) from trigonometric considerations as given in Eq. 6.9. This expression is valid when the rotational periodicity of the flow exists.

$$\lambda = \tau \cdot \cos(\phi) \tag{6.9}$$

According to the definition of the shock wave length (λ) (Eq. 6.9) and considering Eq. 6.8 the shock wave angle (ϕ) is expressed as given in Eq. 6.10.

$$\phi = \arctan(\frac{\tau}{a} - \tan\alpha) \tag{6.10}$$

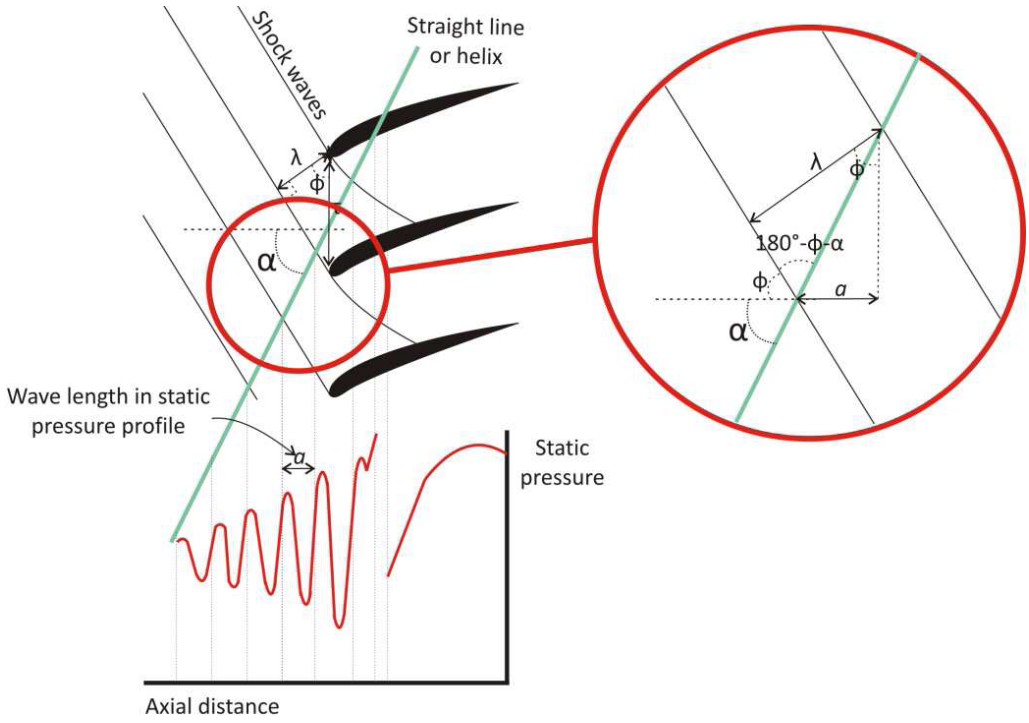

Figure 6.5: Visualization of the shock waves length along the axial direction (a) and perpendicular to shock wave direction (λ)

6.1.4 Validation of the shock wave system

The shock wave propagation upstream of the NASA Rotor 67 was initially validated by Fernandez[74] on a 2D midspan CFD domain of the NASA Rotor 67 operating at near peak efficiency (see § 3.2.2.5). He conducted a grid dependency study and observed that six mesh elements per cm were sufficient to capture accurately the shock wave system.

Nevertheless, it was necessary to carry out the same analysis on the 3D CFD domain of NASA Rotor 67 defined in § 3.2.2.3 to account for the curvature and endwall effects occurring into the rotor. At near peak efficiency condition, the relative flow upstream of the rotor evolves from subsonic to transonic regime, by moving from hub to shroud. Therefore, according to the design rotational speed, the shock wave pattern is only noticeable above 40% of blade span. Figures 6.6(a) and 6.6(b) show the static pressure distribution normalised against the mass flow circumferential average value at the inlet ($p/\overline{p}_{0,in}$) measured on the centreline and plotted versus the axial position (z/s) for 50 and 75% of blade span, respectively. At these blade span locations the flow is already in transonic regime. As a result, the Morfey shock wave propagation model predicted accurately the shock wave system relative to the NASA Rotor 67 operating at near peak efficiency.

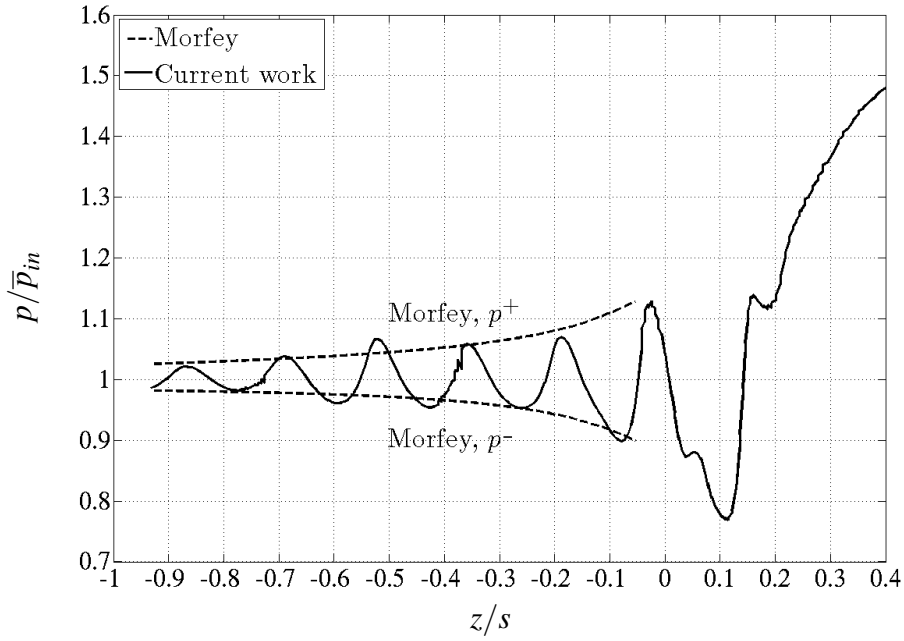

(a) 50% of blade span

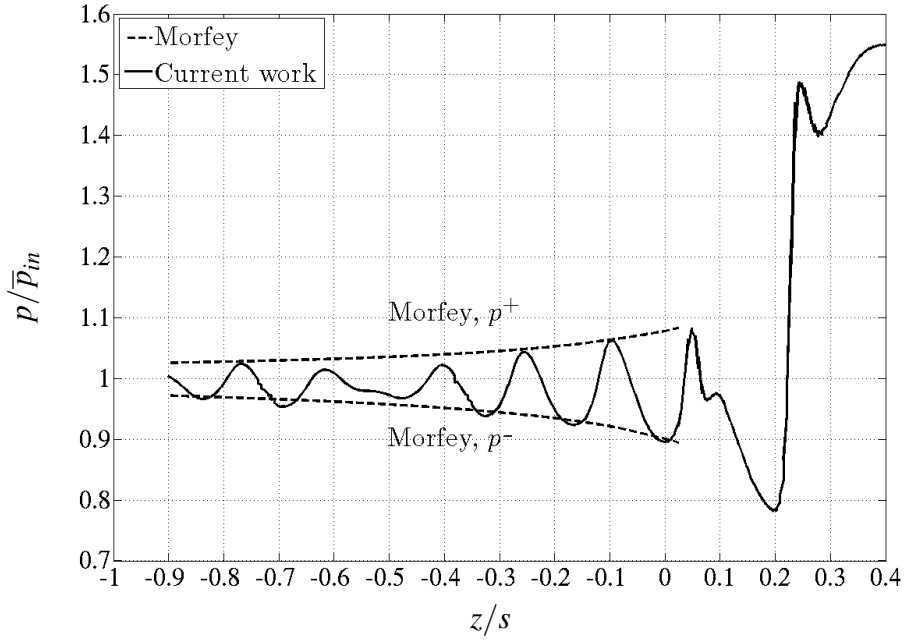

(b) 75% of blade span

Figure 6.6: Normalised static pressure ($p/\overline{p}_{in}$) versus the axial position (z/s) measured on the centerline at near peak efficiency operating point of NASA Rotor 67

6.2 Rotor disturbances analysis

Non-uniform flow field was observed upstream of the rotor face, even by considering clean inlet conditions. Therefore, the rotor disturbances were also analyzed. These were quantified by means of the non-dimensional standard deviations of static pressure and tangential velocity component ($(p')^*$ and $(V'_\theta)^*$), defined in § 3.3.2. This analysis considered the effects of both the throttle setting and rotational speed, presented below.

The throttle settings effect Figures 6.7(a) and 6.7(b) show the distributions of standard deviations of static pressure ($(p')^*$) and tangential velocity components ($(V'_\theta)^*$), respectively. These were calculated at several cross flow planes defined upstream of the rotor face. Also, the rotor operates at its original design rotational speed and at near stall and near choking conditions. As a result, the rotor disturbances persist up to the CFD inlet plane in a similar manner, by indicating that they were intercorrelated. Note that the spatial fluctuations of tangential velocity ($(V'_\theta)^*$) reach zero at the CFD inlet plane due to the nature of the boundary conditions imposed at this plane (see § 3.2.2.5). As the rotor operating conditions change from near choking to near stall, the axial Mach number (M_z) reduces. Therefore, the shock waves propagate further downstream of the rotor face, by becoming predominant with respect the subsonic disturbances. As consequence, the spatial fluctuations assume a 'wave-like' form along the axial direction. This result agrees with the result of Prasad, who indicated that subsonic disturbances decay exponentially, hence faster than the shock wave system which decays as function of z^{-1}.

The rotational speed effect Following the outcomes of the throttle settings analysis presented above additional numerical investigations of the rotor disturbances were conducted considering only the stall points for different rotational speeds: 60%, 70%, 80% and 90% N_d. Figures 6.8(a) and 6.8(b) show the distribution of static pressure ($(p')^*$) and tangential velocity components ($(V'_\theta)^*$), respectively, along the axial position (z/s) and relative to the aforementioned rotational speeds. As a result, it was observed that up to 70% N_d the rotor disturbances were not significant and propagate slightly upstream, up to $z/s = 0.3$. A further increase of rotational speed up to 80% N_d induced an increase of the rotor disturbances. Meanwhile, the inception of transonic regime occurs near the tip, since the sonic relative Mach number is reached at 97.6% of the blade span. For this reason, the spatial fluctuations start also to oscillatedue to the presence of shock waves which suddenly changed the static pressure (see § 6.1.4). A further increase of the rotational speed up to N_d caused the transonic disturbances to become more predominant and, therefore, the spatial fluctuations oscillate strongly along the axial location.

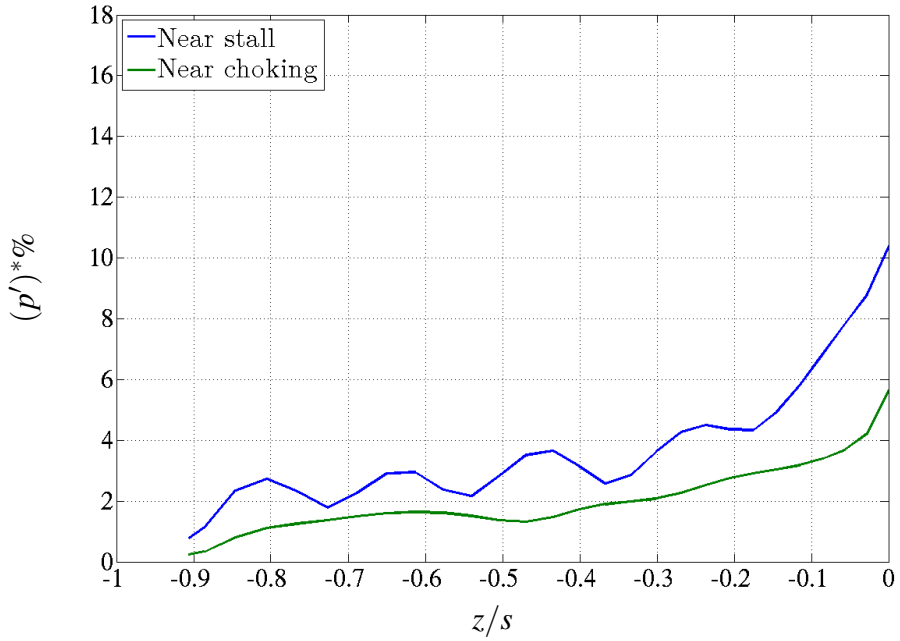

(a) Non-dimensional standard deviation of static pressure ($(p')^*$)

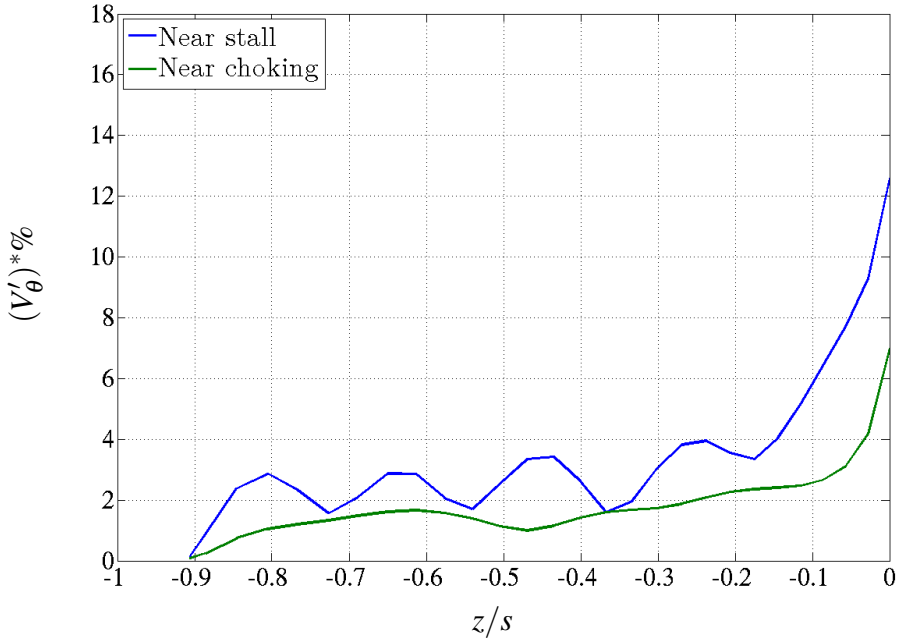

(b) Non-dimensional standard deviation of tangential velocity component ($(V'_\theta)^*$)

Figure 6.7: Non-dimensional standard deviations versus axial position (z/s) with rotor operating at 100% N_d near stall and near choking conditions

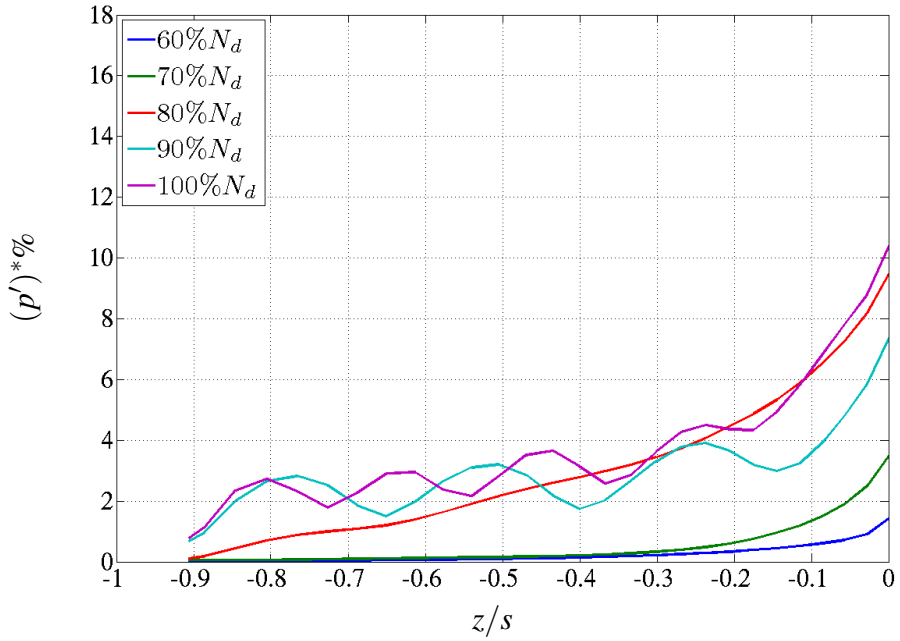

(a) Non-dimensional standard deviation of static pressure ($(p')^*$)

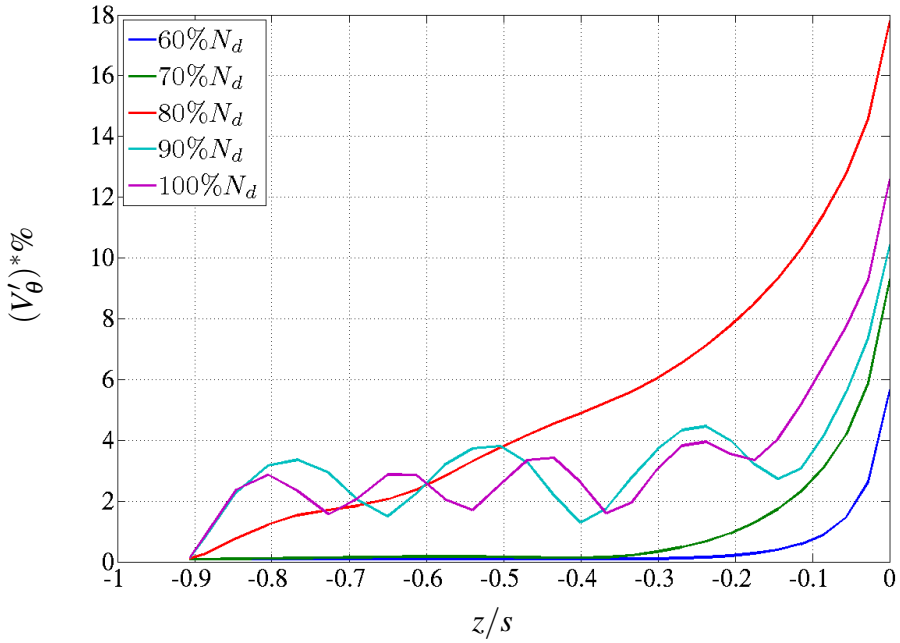

(b) Non-dimensional standard deviation of tangential velocity component ($(V'_\theta)^*$)

Figure 6.8: Distribution of non-dimensional standard deviations versus axial position (z/s) with rotor operating at different rotational speeds and near stall

6.3 Examples of determination of the AIP location

The determination of the AIP location for swirl distortion was accomplished with CFD simulations carried out on the NASA Rotor 67, defined in § 3.2.2.3. The relative results were directly compared to that provided by the SAE5686[16] for a similar upstream configuration. Referring to this configuration, the shock wave propagation analysis at near peak efficiency and the rotor disturbances were carried out and are presented in the previous sections.

The AIP location was determined for two rotor operating conditions: 100% N_d near peak efficiency and 80% N_d near stall, where the rotor outlet static to inlet total pressure ratio was equal to $p_{out}/P_{0,in} = 1.244$ and 1.125, respectively. At the inlet of the CFD domain the datum vortex, defined in § 3.4.2, was prescribed at 25, 50, and 75% of the blade span and by following the methodology described in § 3.4.1.

According to the inlet boundary conditions specified above, a flow field particularly distorted is also expected downstream of the trailing edge. Longley et al.[61] indicated that the length scale of the inlet flow distortion is as large as the mean radius of the compressor system. Therefore, the rotor outlet was extended up to three times the hub rotor trailing edge in order to redistribute the flow up to the rotor outlet as much uniformly as possible.

Hence, CFD calculations were conducted with distorted inlet boundary conditions where the whole CFD domain was modelled in a rotating frame of reference. The execution of steady-state calculations implied that the inlet boundary conditions rotate at the same angular velocity of the rotor without remaining in a fixed position with respect to an absolute observer. Instead, by performing the CFD simulations using an unsteady-state approach, it was possible to impose the inlet boundary conditions counter-rotating against the sense of rotation of the rotor and the same angular velocity of the rotor itself. In this manner, the inlet boundary condition was fixed with respect to an absolute observer. Compared to steady-state (RANS), the assessment of the unsteady-state (URANS) simulations required also the specification of the time resolution. From practical experience matured during the doctoral research it was confirmed that CFD results sufficiently accurate were achieved with a time resolution of two timesteps per degree of rotor revolution.

6.3.1 Time dependency analysis

The application URANS CFD solutions for the determination of the AIP location involved the rotor to cut through the vortex once this was convected to the rotor face. Clearly, at different time-steps the blade passage will be at a different azimuthal position relative to the vortex centre. Therefore, the approaching distortion may be affected by the rotor disturbances analyzed in § 6.2 this relative phase of the blade passage and vortex. As a first step, the sensitivity of the non-uniform flow field, including the vortex upstream of

the rotor, was assessed at different time-steps where the rotor leading edge is at different positions across the vortex diameter. The relative phase position of the vortex to the rotor passage was measured with the non-dimensional vortex angular location relative to that of the blade passage ($(\Delta\gamma)^*$), expressed in Eq. 6.11.

$$\Delta\gamma^* = \frac{\gamma - \gamma_0}{\Delta\gamma_p} \tag{6.11}$$

where γ and γ_0 are the angular vortex locations at a generic time-step and that of reference, respectively. Whereas $\Delta\gamma_p$ is the angle extent relative to the single blade passage. For NASA Rotor 67, having 22 blades, $\Delta\gamma_p = 16.36^o$.

Thus, the flow field distortion was quantified in terms of non-dimensional standard deviation of the static pressure ($(p')^*$) upstream of the rotor face. As a result, the CFD solution upstream of the rotor face was not time dependent (Fig. 6.9) and, therefore, for the unsteady calculations it was sufficient and appropriate to evaluate the AIP metrics at just a single time-step.

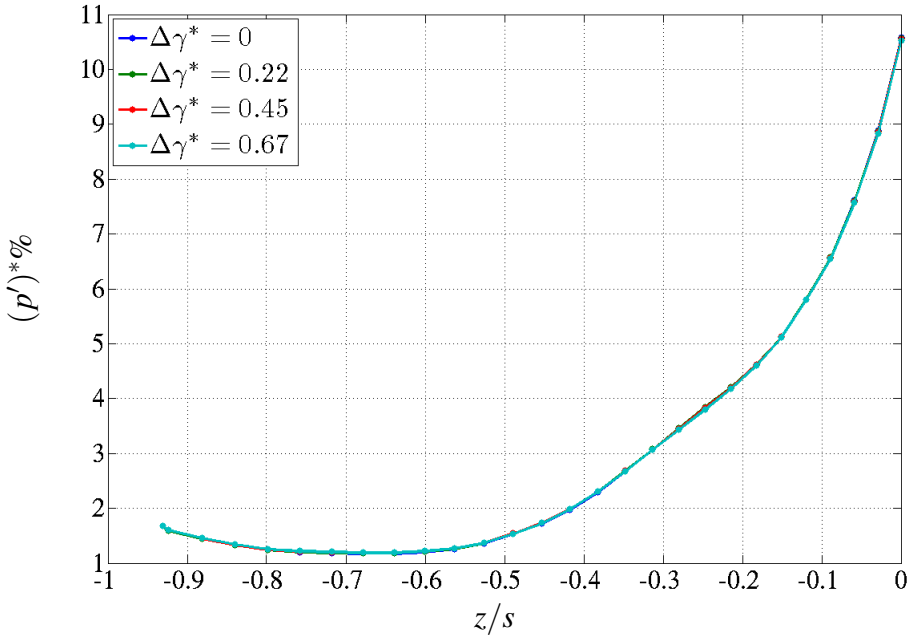

Figure 6.9: Non-dimensional standard deviation of static pressure ($(p')^*$) versus the axial position (z/s) for different non-dimensional vortex angular location relative to that of the blade passage ($\Delta\gamma^*$) with the datum vortex prescribed at 50% of blade span and rotor operating at 80% N_d and $p_{out}/P_{0,in} = 1.125$ (near stall)

Determination of the AIP location The establishment of the AIP for swirl distortion considered the evaluation of the non-dimensional standard deviation of tangential velocity component ($\left(V'_\theta\right)^*$) upstream of the rotor face as shown in Fig. 6.10. The details relative to the boundary conditions are defined in § 6.3. As the vortex moves towards the rotor face, the rotor disturbances analyzed in the previous section should affect the aerodynamics of the vortex being ingested. However, the vortex defined in this research was sufficiently strong to remain unaffected by the rotor disturbances themself. This assumption was considered valid since the level of standard deviations calculated in distorted conditions were an order of magnitude higher than that associated with the rotor disturbances calculated under clean inlet conditions (see § 6.2).

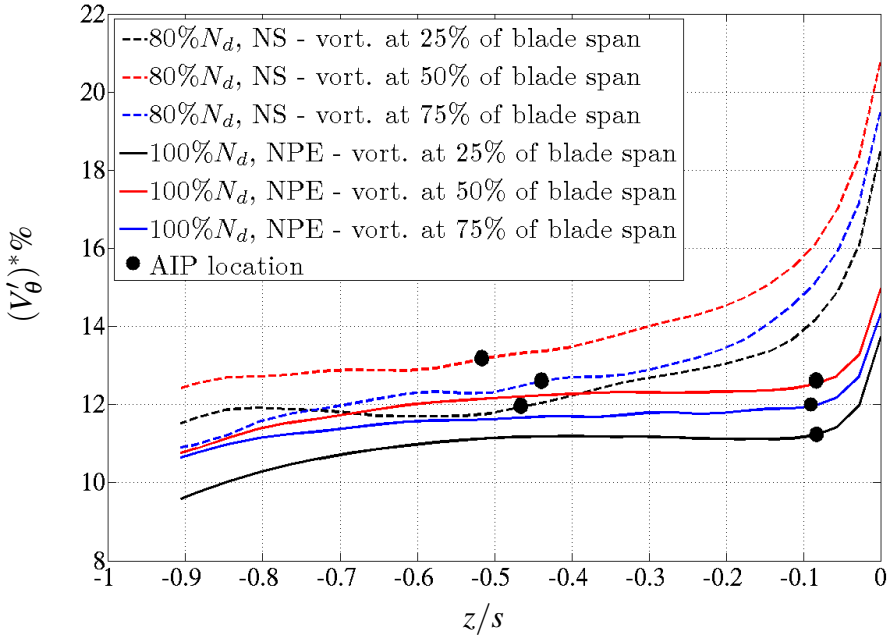

Figure 6.10: Non-dimensional standard deviation of tangential velocity component ($\left(V'_\theta\right)^*$) versus the axial position (z/s) with indication of the AIP location

As a result, the vortex flow field evolves from the CFD inlet domain up to the rotor face and, consequently, by moving forwards three zones were identified (Fig. 6.11). As the vortex, modelled as incompressible, starts to travel downstream it adapts itself to the flow modelled as compressible. This manifests with a stabilization of the distortion level towards a constant value (zone 1). Then, the amount of distortion level remain constant within a specified margin (zone 2). Finally, the distortion level increases since the rotor disturbances become predominant (zone 3). Conventionally, the location of the AIP was that where the distortion level relative to the zone 2 was higher than a percentage of its value (δ) by moving towards the rotor face. For the current work, it was imposed $\delta = 5\%$.

As a result, the AIP location, indicated in Fig. 6.10 was essentially independent of the vortex location along the blade span.

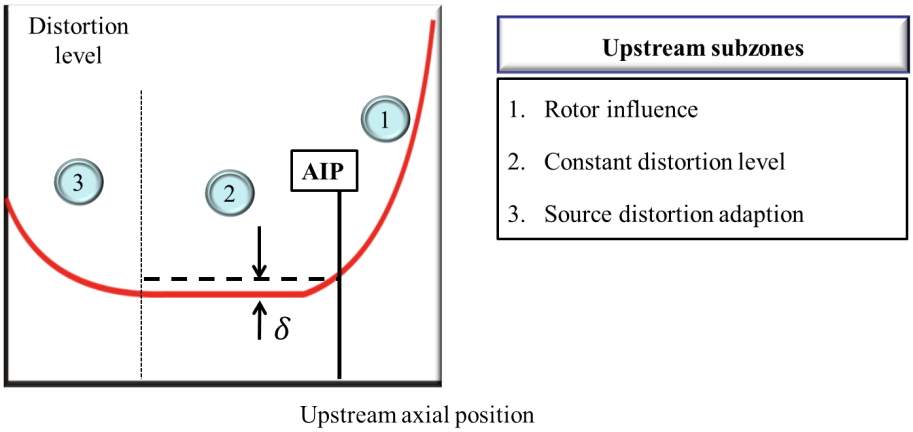

Figure 6.11: Schematization of the distortion level upstream of the rotor face

As discussed in § 2.1, the SAE S-16 Committee [16] declared that for engines without IGVs the AIP for the total pressure distortion should be located at 1.5 fan diameters upstream of the rotor face. On the other hand, the numerical investigations conducted in the current research confirmed that for the worst scenario, the AIP for swirl distortion was located at 0.18 fan diameters upstream of the rotor face. Therefore, the recommended AIP declared for total pressure distortion resulted to be much more conservative than that found in this research for swirl distortion. The author concluded that a much shorted inlet duct could be used in experiments to measure effectively both total pressure and swirl distortion. However, this would require the determination of the AIP for the total pressure distortion by adopting a CFD approach for the specific case investigated.

6.4 Summary

In this chapter, the validation of the shock wave propagation system upstream of the rotor face against the Morfey analytical model has been presented. This was carried out on the datum NASA Rotor 67 configuration operating at near peak efficiency operating point. Moreover, the rotor disturbances upstream of the rotor face were analyzed under clean inlet conditions and for different throttle settings and rotational speeds. They were evaluated in terms of spatial fluctuations of static pressure and tangential velocity component. As a result, the rotor disturbances propagated further downstream by moving towards near stall operating conditions. Meanwhile, as the rotational speed increased, the transonic disturbances became predominant and decaied less. Based on the results relative to

rotor disturbances, the AIP was determined on the datum NASA rotor 67 configuration operating at 80% N_d near stall and 100% N_d near peak efficiency. The datum vortex, defined in § 3.4.2, was prescribed at the CFD inlet plane and for three span locations. The AIP location was determined by considering the trend of spatial fluctuations of tangential velocity components. According to the characteristics of the vortex ingested, the rotor disturbances could be neglected. As a result, the AIP identified for the swirl distortion was less conservative with respect to that relative to the total pressure distortion suggested by the SAE S-16 Committee[16]. Therefore, it was concluded that a much shorted inlet duct could be used in experiments to measure both total pressure and swirl distortion. However, this would require the determination of the AIP for total pressure distortion by assessing a CFD-based methodology similar to that considered in this research for the swirl distortion.

Chapter 7

Conclusions

In this research, a comprehensive analysis of the effect on a fan rotor performance of inlet flow distortion attributed to an S-shaped intake and combined with that of an ingested vortex has been accomplished. For this purpose, a purely numerical coupled system S-shaped intake/fan rotor configuration was defined in this research (see § 3.2.3). This was obtained as a combination of the CFD domains defined for RAE S-shaped intake 2129 scaled up to the size of NASA Rotor 67 and the NASA Rotor 67 itself. In addition, a methodology to determine the AIP location for swirl distortion has been assessed. This was applied on the datum NASA Rotor 67 configuration operating with a vortex prescribed at the CFD inlet plane. The key findings of the overall research are summarised in the following sections.

7.1 Coupled system analysis: clean inlet conditions

Numerical analyses were carried out on the flow field calculated across the coupled system operating under clean inlet conditions and with the rotor running at 80% and 100% of its original design rotational speed (N_d). The main findings relative to this part of the research are listed below.

- The replacement of an annular with an S-duct configuration upstream of the rotor face caused a reduction of the rotor pressure ratio, isentropic efficiency and corrected mass flow. Meanwhile, the near stall operating point was reached for higher values of mass flow with respect to that relative associated with an annular upstream configuration. These changes were related to the combination of both total pressure and swirl distortion occurring at the AIP within the self-generated separated zone. Referring to the swirl distortion, this caused a redistribution of the rotor relative Mach number and, therefore, a localised blade overloading occurring in the co-rotating region of the self-generated distortion. On the other hand, the reduction of

isentropic efficiency was mainly caused by the presence of more pronounced shock waves occurring in the counter-rotating region of the self-generated distortion. Finally, the reduction in terms of corrected mass flow was attributed to a mass flow blockage caused by a large separations. These were induced by the shock waves occurring along the whole span in the counter-rotating region of the self-generated distortion.

- Loss of stability pressure ratio and inlet swirl distortion at the AIP were calculated for the two rotational speed investigated. The loss of stability pressure ratio was quantified according to the methodology proposed by ARP 1420[11]. Meanwhile, the inlet swirl distortion was quantified by means of the mass flow average of the magnitude of the relative flow angle change ($|\overline{\Delta\beta}|$) and the arithmetic average of non-dimensional streamwise peak vorticity ($\omega^{\star}_{z,mean}$). According to the first parameter, the swirl distortion remained essentially constant as the rotational speed increased between 80% and 100% N_d, while the loss of stability pressure ratio increased significantly. Instead, according to the second parameter, the swirl distortion increased with the rotational speed and in the same manner relative to the total pressure distortion. Following practical recommendations[67], the total pressure distortion reached at high rotational speed could no longer be neglected. Therefore, it was concluded that for a coupled system similar to that proposed in this work a possible correlation between the loss of stability pressure ratio and the flow distortion would generally require the specification of both total pressure and swirl distortion.

7.2 Coupled system analysis: vortex ingestion

For the first time, the analysis of the effect on a fan rotor performance related to the flow distortion attributed to an S-shaped intake combined with that of a tightly-wound vortex at the AIP has been accomplished. For this purpose, CFD calculations were carried out on the coupled system operating with a vortex ingested at five different locations of the intake inlet plane and for the two polarities. In these conditions, the effects of both vortex characteristics and throttle setting on rotor performance were investigated at 80% and 100% N_d, respectively. In this section, the effects relative to vortex location and polarity, vortex characteristics and throttle setting are discussed separately.

7.2.1 The effect of vortex location and polarity

The effect of vortex location and polarity were analyzed by considering the ingestion of vortex 1 (see § 5.1.1) at constant throttle setting conditions and for both of the aforementioned rotational speeds. In particular, the vortex was ingested at the centre of the

intake inlet plane, and near the starboard, bottom, port and top edge of the intake wall. The results obtained at each rotational speed were qualitatively similar, although a direct comparison of the relative results could not be accomplished due to the different throttle setting conditions. The key findings relative to this part of the research are summarized below.

- The interaction between the ingested vortex and the self-generated distortion was significant to establish the level of both total pressure and swirl distortion. This depended on vortex location and polarity. In particular, for co- and counter-rotating vortices ingested near the top and the bottom, respectively, the DC_{60} reached the highest values. Compared to other vortex locations, this condition caused an significant shifting of the compressor performance curves towards lower mass flows as expected when total pressure distortion occurs alone.

- As a co- and a counter-rotating vortex was ingested in the system, the rotor corrected mass flow decreased and increased, respectively. Therefore, the effect relative to the change in swirl distortion was predominant with respect to that attributed to the change in total pressure distortion attributed to the vortex ingestion.

- The vortices ingested near the intake wall, arose at the AIP two opposite zones of change in relative rotor incidence ($\Delta\beta$) close to the perturbation of the vortex itself and their effects on the rotor global performance were contrasting. Meanwhile, values of $\Delta\beta$ in the same direction of the vortex ingested occurred around the self-generated distortion. Overall, the predominant effect was coincident to that relative to a bulk swirl imposed in the same direction of the vortex ingested. On the other hand, the vortices ingested at the centre of the intake inlet plane arose at the AIP a zone of unique sign of $\Delta\beta$ close to the vortex perturbation i.e around the whole hub region of the rotor. Meanwhile, values of $\Delta\beta$ were observed in both direction around the self-generated distorted zone. As a result, the change in corrected mass flow was relatively high.

7.2.2 The effect of vortex maximum swirl velocity and size

Three different vortices were ingested in the coupled system configuration with the rotor operating at 100% N_d. They were a datum vortex and other two obtained by doubling either the maximum swirl velocity and size of the datum vortex itself. The main findings relative to their effects on the flow distortion and fan rotor performance are listed below.

- The increase of either the maximum swirl velocity or size of the vortices ingested near the wall caused an increase of the angular shift of its perturbation at the AIP. The magnitude of this shift was the same for the two aforementioned vortices. Hence, it was considered valid the method of images since for both of the vortices ingested the distance from the wall as well as the vortex circulation remained unchanged.
- The increase of either the maximum swirl velocity or size of the vortex caused an increase of the flow distortion extent at the AIP. The total pressure distortion, measured by means of DC_{120} reduced or increased according to the interaction level with the self-generated distortion as well as the possibility for the vortex to affect the pressure recovery (η). Regarding the swirl distortion, a general increase of the mass flow average of the relative rotor incidence ($|\overline{\Delta\beta}|$) was observed as the aforementioned vortex characteristics increased. The magnitude of this increase was attributed to the interaction of the vortex with the self-generated distortion or with the intake wall. Overall, it was found that the strongest interaction occurred as either counter- and co-rotating vortices were ingested near the bottom and top edge of the intake wall. Therefore, the increase of the aforementioned vortex characteristics caused unsteadiness on the CFD solutions.

7.2.3 The effect of throttle setting

The analysis of the throttle setting was conducted on the coupled system proposed in this research with the rotor part operating at 80% N_d. The main findings relative to this part of the research are listed below.

- At constant pressure ratio, as the rotor operability changed from near stall to near choking, the change of rotor corrected mass flow caused by the vortex ingestion reduced. By assuming negligible the change of total pressure distortion, this reduction confirmed that the effect of the swirl attributed to the vortex reduced due to the increase in axial velocity.
- For a constant pressure ratio, an increase and reduction of blade loading was induced by a reduction and increase of the corrected mass flow associated with the

ingestion of a co- and a counter-vortex, respectively. Consequently, the stability pressure ratio with respect to that relative to the clean inlet condition decreased and increased, respectively. A more pronounced reduction of the stability pressure ratio was relative to the co-rotating vortex ingested near the top edge of the intake wall, where the DC_{60} reached the highest value between the co-rotating vortices.

- The Loss of stability pressure ratio and the swirl distortion at the AIP were calculated for the cases relative to this analysis. Referring to the swirl distortion, this was measured with the mass flow average of the magnitude of the relative flow angle change ($|\overline{\Delta\beta}|$). Then, a swirl distortion-based correlation line was obtained and a scatter relative to the CFD data obtained in this work was attributed to the change in total pressure distortion.

7.3 AIP analysis for swirl distortion

A methodology to determine the location of the AIP for swirl distortion was assessed. This consisted of three different analyses which were sequentially applied as presented below.

- Validation of the shock wave system propagating upstream of the rotor face against an analytical model proposed by Morfey. This step was carried out at near peak efficiency operating point of the datum NASA Rotor 67 configuration. The analysis was successfull after the accomplishment of a grid dependency study relative to the part of the CFD domain upstream of the rotor itself.

- Rotor disturbances propagating upstream of the rotor itself were investigated by means of spatial fluctuations of static pressure and tangential velocity component. For this purpose, CFD simulations were performed within the rotor operability at different rotational speeds. The results showed that the disturbances propagate further upstream as the rotor operability moved towards near stall operating conditions. Moreover, as the rotational speed increased, the transonic disturbances became more predominant by decaying slower than subsonic disturbances.

- Finally, examples of determination of the AIP for swirl distortion were carried out. They were relative to the datum NASA Rotor 67 configuration, defined in § 3.2.2.3, with the rotor operating at near peak efficiency and near stall conditions for 100% and 80% of the rotor design rotational speed (N_d), respectively. Meanwhile, a datum vortex was prescribed at the CFD inlet plane and for 25, 50 and 75% of the blade span. The trend of spatial fluctuations of the tangential velocity component (V'_θ) was used as criteria to establish the location of the AIP. According to the characteristics of the vortex ingested, the rotor disturbances could be neglected with

respect to that attributed to the vortex itself. The results showed that the AIP for swirl distortion was essentially independent of the vortex location along the span. Moreover, compared to the AIP location provided by the S-16 Committee [16] for total pressure distortion, that indicated in this work for swirl distortion resulted much less conservative. Hence, it was concluded that shorter upstream ducts than that required for total pressure distortion could be applied. This, however, would require the assessment of a methodology to determine accurately the location of the AIP for total pressure distortion.

7.4 Recommendations for future work

This research provides a qualitative and quantitative study on the effect of the flow distortion attributed to an S-shaped intake, tightly-wound vortex and their combination. Although several aspects have been numerically analyzed, there are a number of relevant issues which are outlined below.

1. Improvement of the CFD domain defined for the coupled system configuration (see § 3.2.3) with the implementation of a conv.-div. nozzle placed downstream of the rotor trailing edge and operating in supersonic outlet conditions. In this manner, the rotor operating point would correspond to the intersection between its speedline and the curve characteristics of the nozzle. Therefore, the change of the rotor operability would be obtained by varying the minimum cross-section of the nozzle. Previous numerical research [19] confirmed that this modification would allow a better prediction of the rotor stall onset.

2. Improvement of the swirl descriptor proposed in this work ($\overline{|\Delta\beta|}$) in order to take into account the sign and the location of the change in incidence relatively to the span location.

3. Improvement of the definition of the stability pressure ratio. As defined in § 3.3.9, this parameter was based on flow quantities averaged on the whole annulus. On the other hand, the self-generated distortion of the duct, eventually combined with that of the vortex ingested, are local phenomena. Therefore, a local compressor stall onset may occur before the prediction of that considered in this work.

4. Implementation of the tip clearance on the rotor relative to the CFD configuration of the coupled system. This would imply a reduced and more realistic operability range of the fan rotor due to the presence to the leakage vortex which creates a source of blockage [56]. However, this feature will require more computational power since an additional numerical interface will be placed in the tip region of each rotor blade.

5. Assessment of URANS calculations to investigate the time dependency of the inlet flow distortion and the relative effect on the turbomachinery.

6. Numerical investigation of coupled systems made up by adopting more realistic intake geometries where the cross section shape changes along the axial direction. The inlet S-duct of the F/A-18 aircraft is an example.

7. Assessment of a methodology to identify the location of the AIP for total pressure distortion by using CFD. This analysis may indicate a location of the AIP for total pressure distortion less conservative with respect to that provided by the SAE S-16 Committee [16] for conventional aircraft inlets. Hence, by considering the analysis of the AIP for swirl distortion conducted in this work, a common AIP valid for both total pressure and swirl distortion will be defined more accurately.

8. Realization of experiments finalised to validate the CFD solutions conducted on the coupled system configuration. As discussed in § 4.1, the increase of the Reynolds number due to an increase of the model scale causes a decrease of the flow distortion parameters up to 4% only. Therefore, these experiments could be conducted on a original scale model and, consequently, costs could be reduced drastically.

References

1. Wellborn, S. R., Reichert, B. A. and Okiishi, T. H. *An experimental investigation of the flow in a diffusing S-duct*. Technical Memorandum NASA TM-105809, National Aeronautics and Space Administration, Lewis Research Centre, Cleveland, Ohio, August 1992.

2. Anderson, B. H. *The aerodynamic characteristics of vortex ingestion for the F/A-18 inlet duct*. Technical Memorandum NASA TM-103703, National Aeronautics and Space Administration, Lewis Research Centre, Cleveland, Ohio, January 1991.

3. Wellborn, S. R. and Okiishi, T. H. *A study of the compressible flow through a diffusing S-duct*. Technical Memorandum NASA TM-106411, National Aeronautics and Space Administration, Lewis Research Centre, Cleveland, Ohio, December 1993.

4. Reichert, B. A. and Wendt, B. J. *Improving diffusing S-duct performance by secondary flow control*. Technical Memorandum NASA TM-106492, National Aeronautics and Space Administration, Lewis Research Centre, Cleveland, Ohio, February 1994.

5. AIRBUS. *New aircraft research in NACRE. A five-year syntesis (2005-2010)*. available at: `http://www.cdti.es/recursos/doc/eventosCDTI/Aerodays2011/7G1.pdf`, 2011. Accessed 04 May 2013.

6. Glenny, D. *Ingestion of debris into intakes by vortex action*. Technical Report C.P. 1114, Ministry of Technology, Aeronautical Research Council, London, 1970.

7. Rodert, L. and Garrett, B. *Ingestion of foreign objects into turbine engines by vortices*. Technical Note NACA-TN-3330, National Advisory Committee for Aeronautics, 1958.

8. Gorrell, S. E., Yao, J. and Wadia, A. R. "High fidelity URANS analysis of swirl generation and fan response to inlet distortion". In *44th AIAA/ASME/SAE/ASEE Joint Propulsion Conference and Exhibit*, number AIAA 2008-4985, Hartford, CT, 21 - 23 July 2008. American Institute of Aeronautics and Astronautics.

9. Bissinger, N. C. and Breuer, T. "Basic principles-gas turbine compatibility-intake aerodynamics aspects". *Encyclopedia of Aerospace Engineering*, 8(Chapter EAE487), 2010.

10. SAE. *Current assessment of the inlet/engine temperature distortion problem*. Technical Report SAE ARD 50015-1991, Society of Automotive Engineers, January 1991.

11. SAE. *Gas turbine engine inlet flow distortion guidelines*. Aerospace Recommended Practice SAE ARP1420, Society of Automotive Engineers, 400 Commonwealth Drive, Warrendale, PA, February 2002.

12. SAE. *Inlet total-pressure-distortion considerations for gas-turbine engines*. Aerospace Information Report AIR1419, Society of Automotive Engineers, 400 Commonwealth Drive, Warrendale, PA, March 1999.

13. Seddon, J. "Understanding and countering the swirl in S-ducts: Tests on the sensitivity of swirl to fences". *Aeronautical Journal*, 88(874):117–127, 1984.

14. Govardhan, M. and Viswanath, K. "Effect of circumferential inlet flow distortion and swirl on the flow field of an axial flow fan stages". *ASME*, (96-GT-263), 1996.

15. Stocks, C. P. and Bissinger, N. C. "The design and development of the tornado engine air intake". In *Aerodynamics of Power Plant Installation*, number AGARD-CP-2808, Toulouse, France, 11–14 May 1981. Advisory Group for Aerospace Research and Development.

16. SAE S-16 Turbine Engine Inlet Distortion Committee. *A metodology for assessing inlet swirl distortion*. Aerospace Information Report SAE AIR5686, Society of Automotive Engineers, 400 Commonwealth Drive, Warrendale, PA, August 2007.

17. Hah, C. C., Rabe, D. C., Sullivan, T. J. and Wadia, A. R. "Effect of inlet distortion on the flow field in a transonic compressor rotor". *Journal of Turbomachinery*, 120(2):233–246, 1998.

18. Kurzke, J. "Effect of inlet flow distortion on the performance of aicraft gas turbines". *Journal of Engineering for Gas Turbines and Power*, 130(4):041201–1–041201–7, April 2008.

19. Jerez Fidalgo, V., Hall, C. A. and Colin, Y. "A study of fan-distortion interaction within the NASA rotor 67 transonic stage". In *Proceedings of ASME Turbo Expo 2010: Power for Land, Sea and Air*, number GT2010-22914, Glasgow, UK, 14 – 18 June 2010. American Society of Mechanical Engineers.

20. Longley, J. P. and Greitzer, E. M. "Inlet distortion effects in aicraft propulsion system integration". *AGARD, Steady and Transient Performance Prediction of Gas Turbine Engines*, (92-28458), 1992.

21. Castaneda, J. *Modelling inlet swirl distortion using CFD*. MSc Thesis, Cranfield University, August 2010.

22. Sheoran, Y., Bouldin, B. and Krishnan, P. M. "Compressor performance and operability in swirl distortion". *Journal of Turbomachinery*, 134(041008):1–13, July 2012.

23. Murphy, J. *Intake ground vortex aerodynamics*. PhD Thesis, Cranfield University, December 2008.

24. Anand, R. B., Singh, S. N. and Rai, L. "Effect of swirl on the flow characteristics of s-shaped diffusing duct". *Indian Journal of Engineering and Materials Sciences*, 15(4):317–325, August 2008.

25. Britchford, K. M., Manners, A. P., McGuirk, J. J. and Stevens, S. J. "Measurement and prediction of flow in annular S-shaped ducts". *Experimental Thermal and Fluid Science*, 9(2):197–205, August 1994.

26. Kim, J., Choi, C. H., Noh, J. and Lee, D. "Numerical flow investigation of an annular S-shaped duct". In *24th Congress of the International Council of the Aeronautical Sciences*, Yokohama, Japan, 29 August – 3 September 2004.

27. Ibrahim, I. H., Ng, E. Y. K., Wong, K. and Gunasekaran, R. "Effects of centerline curvature and cross-sectional shape transitioning in the subsonic diffuser of the F-5 fighter jet". *Journal of Mechanical Science and Technology*, 22(10):1993–1997, July 2008.

28. Miller, D. S. *Internal Flow Systems*, 2nd edition. Miller Innovations, 2009.

29. Lighthill, M. J. *Attachment and Separation in Three-Dimensional Flow. Laminar boundary layers*. Oxford University Press, Oxford, UK, 1963.

30. Hornung, H. and Perry, A. E. "Some aspects of three-dimensional separation. Part I: Streamsurface bifurcations". *Zeitschrift fur Flugwissenschaften und Weltraumforschung*, 8(2):77–87, 1984.

31. Porro, A. R., Keith, T. G. and Hingst, W. R. *A laser-induced heat flux technique for convective heat transfer measurements in high speed flows*. Technical Memorandum NASA TM-105177, National Aeronautics and Space Administration, Lewis Research Centre, Cleveland, Ohio, October 1991.

32. Fluid Dynamics Panel Working Group 13. *Air intakes for high speed vehicles*. Advisory Report AGARD-AR-270, Advisory Group for Aerospace Research and Development, September 1991.

33. Wendt, B. J. and Reichert, B. A. *The effects of vortex ingestion on the flow in a diffusing S-duct*. Technical Memorandum NASA TM-106652, National Aeronautics and Space Administration, Lewis Research Centre, Cleveland, Ohio, June 1994.

34. ANSYS-CFX. *Ansys CFX-Solver modelling guide*, 2012.

35. Spalart, P. R. and Allmaras, S. R. "A one-equation turbulence model for aerodynamic flows". *AIAA Journal*, (92-0439), 1992.

36. Wilcox, D. C. *Turbulence modeling for CFD*, 2nd edition. DCW Industries, Inc., 1998.

37. Menter, F. R. "Two-equation eddy-viscosity turbulence models for engineering applications". *AIAA Journal*, 32(8):1598–1605, August 1994.

38. Johnson, D.A. and King, L.S. "A mathematically simple turbulence closure model for attached and separated turbulent boundary layers". *AIAA Journal*, 23(11):1684–1692, February 1985.

39. Benini, E., Biollo, R. and Ponza, R. "Efficiency enhancement in transonic compressor rotor blades using synthetic jets: A numerical investigation". *Applied Energy*, 88(3):953–962, September 2011.

40. Prasad, A. "Evolution of upstream propagating shock waves from a transonic compressor rotor". *Journal of Turbomachinery*, 125(1):133–140, January 2003.

41. Jones, W. T. *Viscous grid spacing calculator*. available at: `http://geolab.larc.nasa.gov/APPS/YPlus/`, July 1997. Accessed 12 October 2011.

42. Lee, B. J. and Kim, C. "Automated design methodology of turbulent internal flow using discrete adjoint formulation". *Aerospace Science and Technology*, 11(2–3):163–173, January 2007.

43. Menzies, R. D. D. *Investigation of S-shaped intake aerodynamics using computational fluid dynamics*. PhD Thesis, University of Glasgow, October 2002.

44. Whitelaw, J. H. and Yu, S. C. M. "Turbulent flow characteristics in an S-shaped diffusing duct". *Flow Measurement and Instrumentation*, 4(3):171–179, 1993.

45. Chevalier, M. and Peng, S.-H. "Detached eddy simulation of turbulent flow in a highly offset intake diffuser". In *Notes on Numerical Fluid Mechanics and Multidisciplinary Design. Progress in Hybrid RANS-LES Modelling*, volume 111, pages 111–121. Springer, 2010.

46. Menzies, R. D. D., Badcock, K. J., Barakos, G. N. and Richards, B. E. "Validation of the simulation of flow in an S-duct". In *20th Applied Aerodynamics Conference*, number AIAA 2002-2808, Louis, Missouri, 24–27 June 2002. American Institute of Aeronautics and Astronautics.

47. Baals, D. D., Smith, N. F. and Wright, J. B. *The development and application of high-critical-speed nose inlets*. Technical Report 920, National Advisory Committee for Aeronautics, 1945.

48. May, N. E. *The prediction of intake/S-bend diffuser flow using various two-equations turbulence model variants, including non-linear eddy viscosity formulations*. Contactor Report ARA M316/1, Aicraft Research Association, Manton Lane, Bedford, UK, April 1997.

49. Mohler Jr., S. R. "Wind-US flow calculations for the M2129 S-duct using structured and unstructured grids". In *42nd AIAA Aerospace Sciences Meeting and Exhibit*, number AIAA-2004-0525, Reno, Nevada, 5 – 8 January 2004. American Institute of Aeronautics and Astronautics.

50. Tramontin, T. *Numerical analysis of swirl distortion in a subsonic S-duct intake and rotor coupled system*. MSc Thesis, Cranfield University, February 2012.

51. Williams, D. *Propulsion Systems Performance and Integration lecture notes*. Cranfield University, 2010.

52. Strazisar, A. J., Wood, J. R., Hathaway, M. D. and Suder, K. L. *Laser anemometer measurements in a transonic axial-flow fan rotor*. Technical Paper NASA TP-2879, National Aeronautics and Space Administration, Lewis Research Centre, Cleveland, Ohio, November 1989.

53. eCFD. *Explore generic models. NASA Rotor 67*. available at: `http://ecfd.nlr.nl/customhtml/images/NASA-rotor67.jpg`, March 2011. Accessed 05 December 2012.

54. Saravanamuttoo, H. I. H., Rogers, G. F. C., Cohen, H. and Straznicky, P. V. *Gas Turbine Theory*, 6th edition. Pearson Education Limited, 2009.

55. Pierzga, M. and Wood, J. R. *Investigation of the three-dimensional flow field within a transonic fan rotor: Experiment and analysis*. Technical Memorandum NASA

TM-83739, National Aeronautics and Space Administration, Lewis Research Centre, Cleveland, Ohio, June 1984.

56. Adamczyk, J. J., Celestina, M. L. and Greitzer, E. M. "The role of tip clearance in high-speed fan stall". *Journal of Turbomachinery*, 115(1):28–39, January 1993.

57. Chima, R. V. *Viscous three-dimensional calculations of transonic fan performance*. Technical Memorandum NASA TM-103800, National Aeronautics and Space Administration, Lewis Research Centre, Cleveland, Ohio, 1991.

58. Jiyuan T., Guan H. Y., Chaoqun L. *Computational fluid dynamics: a practical approach*, chapter 6, pages 244–276. Butterworth-Heinemann, 2008.

59. Arima, T., Sonoda, T., Shirotori, M., Tamura, A. and Kikuchi, K. "A numerical investigation of transonic axial compressor rotor flow using a low-Reynolds-number k-ε turbulence model". *Journal of Turbomachinery*, 121(1):44–58, 1999.

60. Niazi, S. *Numerical simulation of rotating stall and surge alleviation in axial compressors*. PhD Thesis, Georgia Institute of Technology, July 2000.

61. Longley, J. P. and Greitzer, E. M. *Inlet distorion effects in aircraft propulsion system integration*. Technical report, National Aeronautics and Space Administration, May 1992.

62. Thust Power System Inc. *Air intake design for thrust architecture*. available at: `http://www.allaboutthrust.com/Air_Intake_Design_(3).pdf`. Accessed 06 October 2011.

63. Bhagwat, M. J. and Leishman, J. G. "Generalized viscous vortex model for application to free-vortex wake and aeroacoustic calculations". In *58th Annual Forum and Technology Display of the American Helicopter Society International*, volume 58, Montréal, Canada, 11–13 June 2002. AHS International.

64. Zantopp, S. *Jet engine ground vortex studies*. MSc Thesis, Cranfield University, August 2008.

65. McLelland, G., di Cugno, D., MacManus, D. G. and Pachidis, V. "Boundary conditions for vortex cfd simulations". In *Proceedings of ASME Turbo Expo 2012: Power for Land, Sea and Air*, number GT2012-68718, Copenhagen, Denmark, 11 – 15 June 2012. American Society of Mechanical Engineers.

66. Gittings, A. *Cranfield University Astral HPC Cluster. User guide*. Cranfield University, March 2013.

67. Allan, B. G., Owens, L. R. and Lin, J. C. "Optimal design of passive flow control for a boundary-layer-ingesting offset inlet using design-of-experiments". In *44nd AIAA Aerospace Sciences Meeting and Exhibit*, number AIAA-2006-1049, Reno, Nevada, 9 – 12 January 2006. American Institute of Aeronautics and Astronautics.

68. Kuethe, A.M. and Chow, C.-Y. *Foundations of Aerodynamics*, 4th edition. John Wiley & Sons, 1986.

69. Prasad, D. and Feng, J. "Propagation and decay of shock waves in turbofan engine inlets". *Journal of turbomachinery*, 127(1):118–127, 2005.

70. Chauvin, J., Sieverding, C. and Griepentrog, H. "Flow in cascade with a transonic regime". In *Proc. of the Symposium on Flow Research on Blading*, Amsterdam, 1970.

71. Kantrowitz, A. *The supersonic axial flow compressor*. Report 974, National Advisory Committee for Aeronautics, April 1946.

72. Mendousse, J. S. "Nonlinear dissipative distortion of progressive sound waves at moderate amplitudes". *Journal of the Acoustical Society of America*, 25(1):51–54, 1953.

73. Morfey, C. L. and Fisher, M. J. "Shock-wave radiation from a supersonic ducted rotor". *Aeronautical Journal of the Royal Aeronautical Society*, 74:579–585, 1970.

74. Fernández, F. *Effect of inlet flow distortion on turbomachinery - AIP analysis*. MSc Thesis, Cranfield University, August 2012.

75. Seddon J., Goldsmith E. L. *Intake Aerodynamics*, 2nd edition. AIAA Education Series, 1999.

76. Bouldin, B. and Sheoran, Y. "Inlet flow angularity descriptors proposed for use with gas turbine engines". *SAE Technical Papers*, 2002.

77. Leishman, J. G. *Principles of Helicopter Aerodynamics*. Cambridge University Press, Cambridge, UK, 2006.

78. Devenport, W. J., Rife, M. C., Liapis, S. I. and Follin, G. J. "The structure and development of a wing-tip vortex". *Journal of Fluid Mechanics*, 312:67–106, April 1996.

79. Chow, J. S., Zilliac, G. G. and Bradshaw, P. "Mean and turbulence measurements in the near field of a wingtip vortex". *AIAA Journal*, 35(10):1561–1567, October 1997.

80. Ragab, S. and Sreedhar, M. "Numerical simulation of vortices with axial velocity deficits". *Physics of Fluids*, 7(3):549–558, March 1995.

81. Cotel, A. J. "Turbulence inside a vortex: Take two". *Physics of Fluids*, 14(8):2933–2934, August 2002.

82. Vatistas, G. H., Kozel, V. and Mih, W. C. "A simpler model for concentrated vortices". *Experiments in Fluids*, 11(1):73–76, 1991.

83. Dockrill, S. *Assessment of particle image velocimetry for wing tip flows*. MSc Thesis, Cranfield University, September 2007.

84. Newman, B. G. "Flow in a viscous trailing vortex". *The Aeronautical Quarterly*, 10(2):149–162, 1959.

85. Brix, S., Neuwerth, G. and Jacob, D. "The inlet-vortex system of jet engines operating near the ground". In *18th Applied Aerodynamics Conference*, number AIAA 2000-3998, Denver, CO, 14–17 August 2000. American Institute of Aeronautics and Astronautics.

Appendix A

Flow descriptors

In this appendix, the flow descriptors already defined in the literature which are relevant for the current research are presented. They are the total pressure distortion parameter (DC_{60}) and the swirl descriptors proposed by the SAE S-16 Committee[16]: swirl intensity, swirl directivity and swirl pairs.

A.1 Total pressure distortion parameter

The total pressure distortion parameter (DC_{60}) is defined as the difference between the area weighted averaged total pressure at the AIP ($\overline{P}_{0,AIP}$) and the minimum 60^o sector pressure normalised by the averaged dynamic head in the intake duct (Eq. A.1)[75].

$$DC_{60} = \frac{\overline{P}_{0,AIP} - \overline{P}_{0,60}}{\frac{1}{2}\rho\overline{V}^2} \tag{A.1}$$

This parameter was introduced by Rolls-Royce and used extensively in the European figher programs Tornado and Eurofighter. However, this parameter is limited to one-per-revolution circumferential total pressure distortion[9].

A.2 Swirl descriptors

The swirl descriptors allow the comparison of swirl distortion pattern between different inlet systems during the design and development phase, by establishing limits of acceptability. They are the tools to transfer information taken from test bed and numerical simulations to introduce changes to improve the design. Additionally, these parameters

allow the correlation of the inlet swirl distortion occurring at the AIP with the change in performace relative to the compressor.

The SAE S-16 Committee[16] proposed swirl descriptors, based on the swirl angle (α) which is defined in § 2.1. The swirl descriptors are defined relatively to a coordinate system having the centre defined at the centre of the AIP with positive rotational direction coincident to that of the rotor. Referring to Fig. A.1, two flow quantities can be defined: swirl extents and sector swirl.

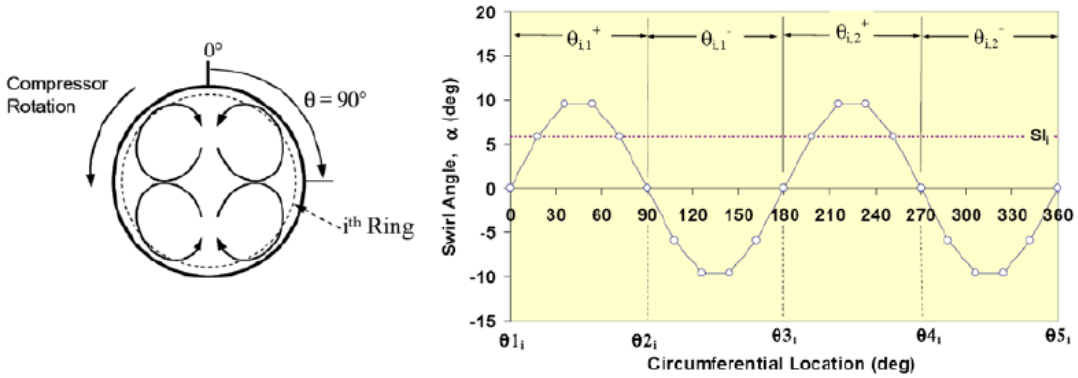

Figure A.1: Visualization of an idealized two-per-rev swirl pattern (left) and swirl angle (α) along the circumferential location relative to the i^{th} ring (right)[16]

Swirl extents The positive and negative swirl extent ($\theta^+_{i,k}$ and $\theta^-_{i,k}$) are defined as the total circumferential extent of the positive and negative swirl region calculated at the i^{th} ring and relative to the k^{th} swirl pair. These parameter account for the portion of positive and negative swirl.

Sector swirl The positive and negative sector swirl ($SS^+_{i,k}$ and $SS^-_{i,k}$) are defined as the integral average of the absolute swirl angle (α) of the positive and negative swirl regions ($\theta^+_{i,k}$ and $\theta^-_{i,k}$) at the i^{th} ring and relative to the k^{th} swirl pair, as given in Eqns. A.2 and A.3.

$$SS^+_{i,k} = \frac{1}{\theta^+_{i,k}} \int_{\theta^+_{i,k}} \alpha(\theta)_{i,k}\, d\theta \tag{A.2}$$

$$SS^-_{i,k} = \frac{1}{\theta^-_{i,k}} \int_{\theta^-_{i,k}} \alpha(\theta)_{i,k}\, d\theta \tag{A.3}$$

The definitions of the aforementioned parameters enable in turn that of three swirl descriptors, where their combination identify univocally the swirl distortion pattern[76].

These are the swirl intensity (*SI*), swirl directivity (*SD*), and swirl pairs (*SP*), presented below.

A.2.1 Swirl intensity

The swirl intensity (*SI*) is defined for a i^{th} ring as the integral average of the swirl angle magnitude which extends uniformly throughout the circumferential domain.

$$SI_i = \frac{\sum_{k=1}^{m} SS_{i,k}^{+} \cdot \theta_{i,k}^{+} + |SS_{i,k}^{-}| \cdot \theta_{i,k}^{-}}{360} \tag{A.4}$$

A.2.2 Swirl directivity

The swirl directivity (*SD*) is a numerical indicator of the predominant swirl direction with respect to that of the compressor at the i^{th} ring, as given in Eq. A.5.

$$SD_i = \frac{\sum_{k=1}^{m} SS_{i,k}^{+} \cdot \theta_{i,k}^{+} + SS_{i,k}^{-} \cdot \theta_{i,k}^{-}}{\sum_{k=1}^{m} SS_{i,k}^{+} \cdot \theta_{i,k}^{+} + |SS_{i,k}^{-}| \cdot \theta_{i,k}^{-}} \tag{A.5}$$

This parameter is comprised between $-1 < SD < 1$. At the values 1 and -1 correspond the pure co- and counter-rotating bulk swirl, respectively. Meanwhile, the value 0 corresponds to a symmetric swirl distortion pattern (Fig. A.2).

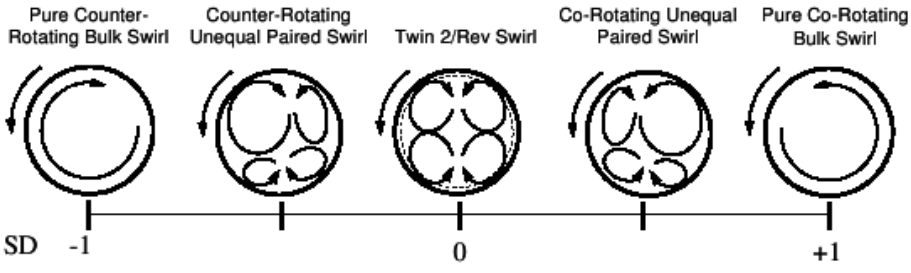

Figure A.2: Swirl directivity spectrum for two-per-rev swirl distortion[16]

A.2.3 Swirl pairs

The swirl pairs (*SP*) is a numerical indicator of equivalent number of swirl pairs at the i^{th} ring (Eq. A.6).

$$SP_i = \frac{\sum_{k=1}^{m} SS_{i,k}^{+} \cdot \theta_{i,k}^{+} + SS_{i,k}^{-} \cdot \theta_{i,k}^{-}}{2 \cdot Max\left[\left(SS_{i,k}^{+} \cdot \theta_{i,k}^{+}\right), \left(|SS_{i,k}^{-}| \cdot \theta_{i,k}^{-}\right)\right]} \tag{A.6}$$

For two-per-rev swirl pattern, the swirl pairs is comprised between 0.5 and 2 to which correspond the pure bulk swirl and two paired twin swirl, respectively (Fig. A.3).

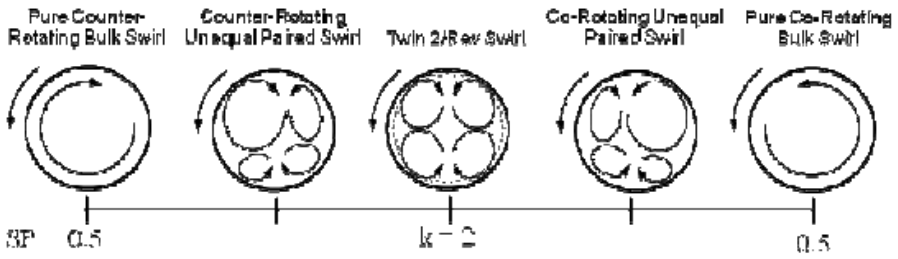

Figure A.3: Swirl pairs spectrum for two-per-rev swirl distortion[16]

Appendix B

Ground vortex

In this appendix, the analytical models proposed in this research to define a vortical flow representative of the ground vortex are presented. Then, the key non-dimensional parameters defined to identify the formation mechanisms and calculate the strength of the vortex are presented. Finally, the procedure assessed by Murphy[23] to calculate the strength of the vortex is described in detail.

B.1 Vortex model theory

In theory, a vortex is defined as a rotating flow with a central viscous vortical region, surrounded by a potential flow[77]. The flow field attributed to the vortex is characterized by tangential, axial and radial velocity distributions, defined in a polar coordinate system with the origin located at the vortex centre, $\mathbf{V}=(V_r, V_\theta, V_z)$. Consequently, a static pressure perturbation due to the high tangential velocities occurs. Then, a total pressure loss occurs due to the increase of entropy associated with the generation and convection of the vortex. Figure B.1 shows a typical distribution of tangential velocity defined with respect to the vortex centre. Within the vortex core, the tangential velocity increases up to a maximum at a distance from the vortex centre called as vortex core radius (r_c). The velocity distribution in the core region is directly proportional to r, that is, of a solid body rotation. Beyond the core, the velocity merges into a potential vortex-type flow, with the tangential velocity inversely proportional to r. On the other hand, the axial velocity perturbation can range from negative to positive values. For instance, wing-tip vortices are characterized by deficits up to 15%[78] and excesses up to 77%[79] of this perturbation. Finally, a radial velocity perturbation exists, which is normally an order of magnitude smaller than tangential and axial velocity perturbations. For the case of an axial velocity deficit and excess, the radial velocity is negative and positive, respectively.

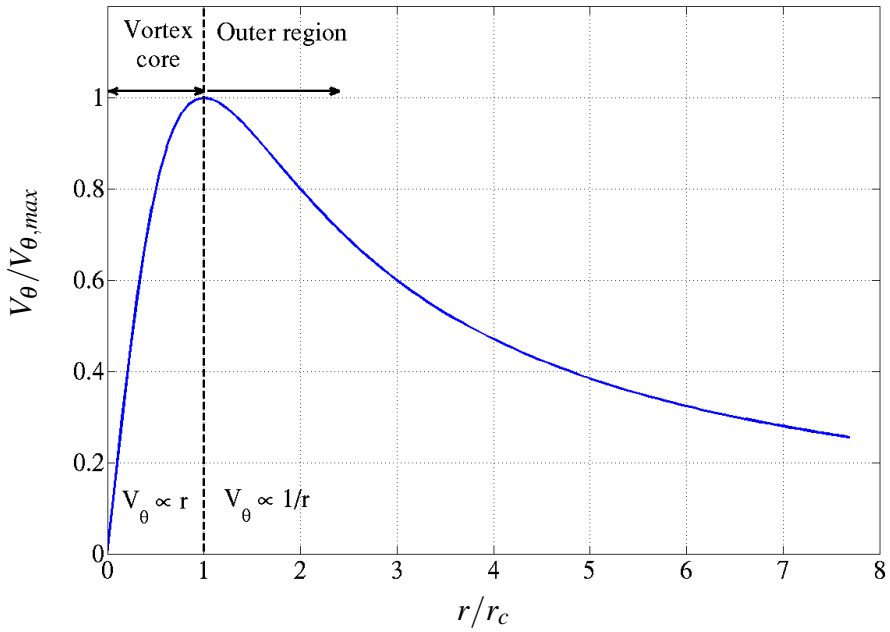

Figure B.1: Tangential velocity distribution attributed to a vortex[77]

CFD simulations[80] confirmed that the magnitude of the axial velocity perturbation has a significant effect on the vortex growth and decay. In particular, a large axial velocity perturbation generates turbulence inside the vortex core, and leads to redistribution of angular and axial momentum from the core to the surrounding flow. For high rotational velocities, the vortex core flow re-laminarizes, and reverts to a more stable condition. Therefore, the axial velocity perturbation reduces in magnitude, while the tangential velocity increases. The Rossby number, which is the ratio of the axial velocity perturbation to the peak tangential velocity, can be used to provide an indication of this stability. In particular, a Rossby number below 1 results in a laminar core[78]. As the vortex convects downstream, only laminar diffusion occurs. This helps explaining the slow decay of tip vortices[78,81]. Based on that, the axial velocity perturbation should be considered in CFD.

In this work, the vortex was assumed axisymmetric and incompressible, while the total temperature was assumed constant. Following these assumptions, a number of vortex models exist, such as the Rankine and Lamb-Oseen models, which generate the tangential velocity profile of a laminar vortex. However, a more recent vortex model which is also in agreement with the nature of the ground vortex[23] is that proposed by Vatistas[82] where the tangential velocity distribution is given in Eq. (B.1). This distribution is generated as a function of radius from the vortex centre (r) by using the vortex circulation (Γ), core radius (r_c) and the Vatistas model constant (n). The value of n is an integer which depends on the application. Experimental observations confirmed that $n = 1$ and 2 are suitable for

ground vortices[23] and wing-tip vortices[83,63], respectively.

$$V_\theta(r) = \frac{\Gamma}{2\pi}\left[\frac{r}{(r_c^{2n}+r^{2n})^{\frac{1}{n}}}\right] \tag{B.1}$$

This model, however, assumes the absence of axial or radial velocities perturbations as also expected for that of Rankine and Lamb-Oseen. On the other hand, these velocity perturbations were assumed following analytical expressions proposed by Bhagwat et al.[63], relative to wing-tip vortices. They were derived using small-perturbation analysis to linearize the Navier-Stokes equations. Hence, by assuming the Vatistas tangential velocity distribution Eq. (B.1) as a solution to the linearized equations, the radial and axial velocity distributions are expressed as given Eqs. (B.2) and (B.3). Note that the constant A is related to the axial momentum across the wake[63,84], while z is the distance downstream of the wing-tip trailing edge. In particular, the sign of A dictates whether the distribution is for an excess or a deficit. A positive or negative value of A generates a deficit or an excess, respectively. Hence, the ratio A/z is the axial velocity perturbation magnitude relative to the vortex centre.

$$V_r(r,z) = -\frac{Ar}{2z^2}\left[1-\frac{r^2}{(r_c^{2n}+r^{2n})^{\frac{1}{n}}}\right] \tag{B.2}$$

$$V_z(r,z) = V_\infty - \frac{A}{z}\left[1-\frac{r^2}{(r_c^{2n}+r^{2n})^{\frac{1}{n}}}\right] \tag{B.3}$$

The static pressure distribution is derived from the radial momentum equation, simplified with respect to the assumptions introduced by Vatistas et al.[82] (Eq. B.4)

$$\frac{V_\theta^2}{r} = \frac{1}{\rho}\frac{\partial p}{\partial r} \tag{B.4}$$

Then, the integration of Eq. B.4 obtained by considering the expression of the Vatistas tangential velocity (Eq. (B.1) provides the static pressure distribution relative to the ground vortex case ($n = 1$) as given in Eq. (B.5).

$$p = p_\infty - \frac{\rho}{2}\left[\frac{\Gamma}{2\pi r_c}\right]^2\left[\frac{r_c^2}{r_c^2+r^2}\right] \tag{B.5}$$

Since the vortex is assumed to be within an incompressible flow, the total pressure is calculated according to Bernoulli as given in Eq. (B.6).

$$P_0 = p + \frac{1}{2}\rho \left(V_\theta^2 + V_r^2 + V_z^2\right) \tag{B.6}$$

B.2 Vortex strength and formation mechanisms

The characteristics defining a ground vortex depend mainly on three non-dimensional parameters: velocity ratio (U^*), ground clearance (h/D_l) and the yaw angle (ψ). The velocity ratio (U^*) is the ratio between the massflow averaged velocity measured at the at the intake highlight plane($\overline{V}_{z,l}$), and the wind velocity (U_∞). The ground clearance (h/D_l) is the ratio between the minimal distance of the engine from the ground (h) and the intake highlight diameter (D_l). This parameter represents the non-dimensional height of the inlet above the ground and is also mostly considered in industry. Finally, The yaw angle (ψ) is that defined between the direction of the engine axis and that of the wind. The combination of these non-dimensional parameters defines the formation mechanism and the strength of a ground vortex. Both of these aspects are presented in the next sections.

B.2.1 Vortex formation mechanisms

According to the dominant vorticity of the vortex, two mechanisms of ground vortex formation have been identified till date. They are applicable under quiescent or headwind conditions and crosswind conditions, respectively.

Quiescent and Headwind Mechanisms Under quiescent (no-wind) conditions the swirl pattern at the intake inlet is unsteady due to the complexity of the flow field. In fact, the flow coming from far downstream interact with that far upstream of the engine. Initially, two counter-rotating vortices appear. However, only one of these vortices become dominant with the time. After this change, the flow no longer changes its configuration. Studies on vortex formation under quiescent conditions have been reported so far by Brix et al.[85] conducted only a qualitative study about the vortex formation. Afterwards, Murphy[23] predicted experimentally the formation of this vortex. Referring to Fig. B.2, the quiescent mechanism (no-wind) occurs for velocity ratios $U^* > 20$, where the flow pattern is characterized by two counter-rotating vortices with a circulation that remains almost constant. As the velocity ratio (U^*) goes below 19, the formation mechanism is in headwind. Hence, the swirl configuration goes from two counter-rotating vortices, relative to quiescent condition, to still to counter-rotating vortices with higher strength that the previous case. The vortex pattern associated with the velocity ratio is shown in Fig. B.2.

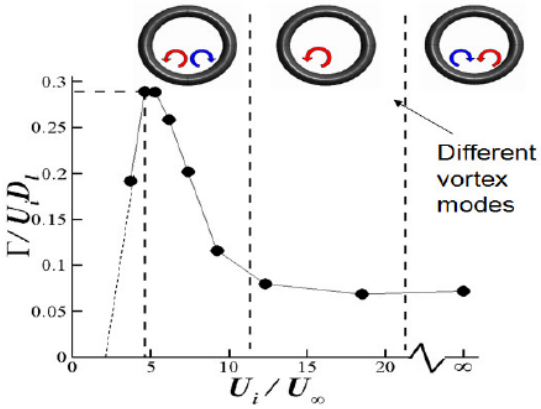

Figure B.2: Transition from quiescent to headwind conditions showing the vortex pattern[21]

Crosswind Mechanism This is a mechanism characterized by the presence of a single vortex. Its intensity increases with the yaw angle (ψ) up to three times that of the headwind condition[23] when $\psi = 90^o$. For this reason, the presented research is based on this mechanism of formation.

B.2.2 Prediction of the vortex circulation

Fig. B.3 shows the flow chart regarding the methodology introduced by Murphy [23] to calculate the vortex strength in terms of non-dimensional circulation (Γ^*). This is defined as the vortex circulation (Γ) non-dimensionalized by the mass flow averaged axial velocity measured at the intake inlet ($\overline{V}_{z,in}$) and the intake highlight diameter (D_l) as given in Eq. B.7.

$$\Gamma^* = \frac{\Gamma}{D_l \cdot \overline{V}_{z,in}} \tag{B.7}$$

In headwind conditions, trend of non-dimensional circulation (Γ^*) versus the velocity ratio (U^*) is characterized by the critical velocity ratio ($U^\star_{crit}$) and that corresponding to its maximum value (U^*_{max}) as shown in Fig. B.4.

The critical velocity ratio (U^*_{crit}) is a function of the ground clearance (h/D_l) and represents the velocity ratio at which the sucked streamtube lifts off the ground plane. This value is calculated from the mass flow conservation, as given in Eq. B.8.

$$U^\star_{crit} = \left(\frac{U_{in}}{U_\infty}\right)_{crit} = 4 \cdot \rho^\star \left(\frac{D_l}{D_{in}} \cdot \frac{h}{D_l} + \frac{D_l}{2D_{in}}\right)^2 \tag{B.8}$$

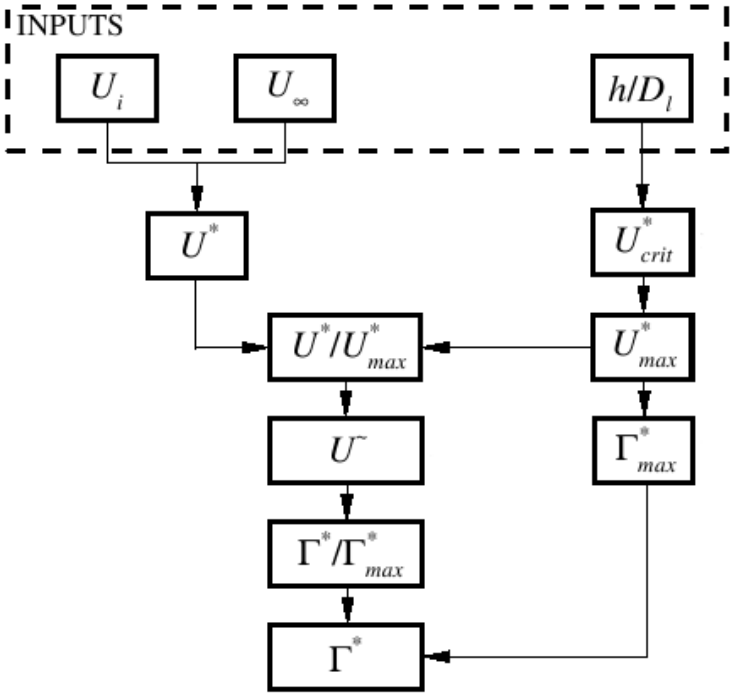

Figure B.3: Procedure for the determination of the non-dimensional vortex circulation (Γ^*) in headwind conditions[23]

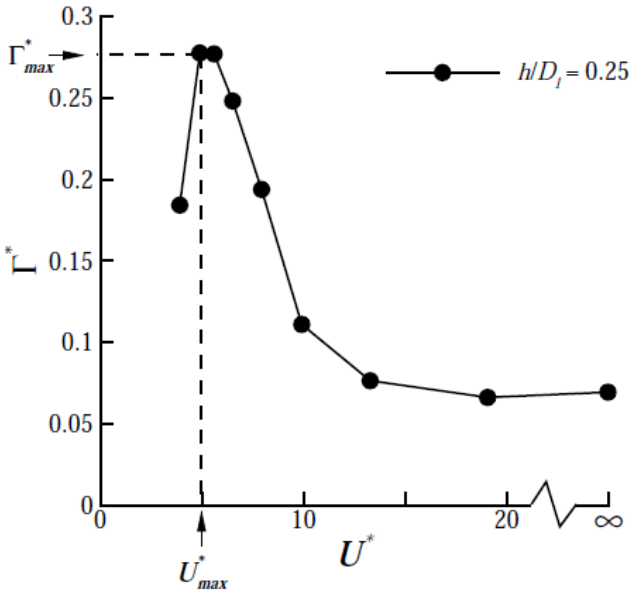

Figure B.4: Non-dimensional circulation (Γ^*) versus velocity ratio (U^*) for $h/D_l = 0.25$ in headwind conditions[23]

Murphy[23] confirmed that the critical velocity ratio (U^{*}_{crit}) is such that $U^{\star}_{R} = U^{\star}_{crit}/U^{\star}_{max} = 0.65$. Also, he related the maximum non-dimensional circulation ($\Gamma^{\star}_{max}$) with $U^{\star}_{max}$ with an empirical expression given in Eq. B.9.

$$\Gamma^{\star}_{max} = 0.83\,(U^{\star}_{max})^{0.7} \tag{B.9}$$

Hence, a new parameter called modified velocity ratio ($U^{\sim}$) as given in Eq. B.10.

$$U^{\sim} = \frac{\frac{U^{\star}}{U^{\star}_{max}} - U^{\star}_{R}}{1 - U^{\star}_{R}} \tag{B.10}$$

Then, the non-dimensional vortex circulation relative to the maximum value ($\Gamma^{\star}/\Gamma^{\star}_{max}$) calculated using Eq. B.11, where the value of k was found to be 1.1[23].

$$\frac{\Gamma^{\star}}{\Gamma^{\star}_{max}} = \frac{2^{1/k}U^{\sim}}{[1 + U^{\sim 2k}]^{1/k}} \tag{B.11}$$

The aforementioned procedure followed to determine the vortex strength in headwind is no longer valid for crosswind conditions, which were considered for the current research. However, corrections factors were applied to the vortex strength calculated for headwind conditions to obtain that valid for crosswind conditions. According to Murphy, the total pressure distortion parameter (DC_{60}) in headwind and pure crosswind conditions is given in Eq. B.12 and B.13, respectively.

$$DC_{60}^{\psi=0} = 0.0567 \cdot \Gamma^{\star} + 0.0141 \tag{B.12}$$

$$DC_{60}^{\psi=90} = (-25.3(h/D_l) + 15.3) \cdot DC_{60}^{\psi=0} \tag{B.13}$$

Then, the non-dimensional circulation for pure crosswind condition ($\Gamma^{\star}_{\psi=90}$) is given in Eq. B.14.

$$\Gamma^{\star}_{\psi=90} = 11.1 DC_{60}^{\psi=90} + 0.0075 \tag{B.14}$$

Once obtained the aforementioned parameters, the normalised non-dimensional circulation (η) was introduced to define the change of non-dimensional circulation ($\Gamma^{\star}$) as function of the yaw angle (ψ) as given in Eq. B.15. Note that for the current research the pure crosswind conditions ($\psi = 90^{o}$) were considered.

$$\eta = \frac{\Gamma^{\star}_{\psi} - \Gamma^{\star}_{\psi=0}}{\Gamma^{\star}_{\psi=90} - \Gamma^{\star}_{\psi=0}} = \sin^{3}(\psi) \tag{B.15}$$

Appendix C

Thermodynamic rotor outlet condition for the Coupled system

The analysis of the vortex characteristics conducted on the coupled system configuration, presented in § 5.1.1, assumed that the rotor outlet static to inlet total pressure ($p_{out}/P_{0,in}$) was kept constant at 0.987. This condition, unfortunately, did not guarantee a constant throttle setting condition between all of the case studies. Nevertheless, according to the results obtained the changes in throttle settings were relatively small. In this appendix, the numerical values of the changes in throttle setting are reported for all of the aforementioned cases. They were quantified by means of the relative change of the rotor outlet non-dimensional mass ($\Delta NDMF_2\%$) defined as given in Eq. C.1.

$$\Delta NDMF_2\% = \frac{NDMF_{2,cl} - NDMF_{2,dist}}{NDMF_{2,cl}} \cdot 100 \tag{C.1}$$

Hence, the numerical values of the relative change of rotor outlet non-dimensional mass flow ($\Delta NDMF_2\%$) relative to the case studies of the vortex characteristics analysis are listed in Table C.1.

		$\Delta NDMF_2\%$		
Vortex location	**Vortex polarity**	**Vortex 1**	**Vortex 2**	**Vortex 3**
P_C	Co-rotating	0.722	−0.608	1.805
	Counter-rotating	−1.450	−1.268	−1.619
P_S	Co-rotating	−0.109	0.278	−0.135
	Counter-rotating	−1.249	−2.027	−0.017
P_B	Co-rotating	0.026	0.506	0.297
	Counter-rotating	−0.077	0.375	−0.453
P_P	Co-rotating	0.930	2.596	2.568
	Counter-rotating	−0.350	−0.319	−0.373
P_T	Co-rotating	1.599	1.162	2.308
	Counter-rotating	−1.005	−1.301	−1.438

Table C.1: Values of relative change of rotor outlet non-dimensional mass flow ($\Delta NDMF_2\%$) for the coupled system operating with vortex prescribed at different location and rotor operating at 100% N_d and $p_{out}/P_{0,in} = 0.987$

Appendix D

The effect of vortex location and polarity at reduced rotational speed

This appendix reports analyses relative to the effects of vortex location and polarity on the coupled system configuration with the rotor part operating at 80% of its original design rotational speed (N_d). In particular, they include the investigations of the S-shaped intake aerodynamics as well as the description of the flow field at the AIP. On the other hand, the change of rotor performance relative to these cases are directly presented § 5.2.4.

Note that similar analyses were carried out by considering the rotor operating at 100% N_d (see § 5.1). However, a direct comparison of the results obtained between two aforementioned rotational speeds could not be accomplished since no common throttle setting could be obtained. However, these results could be considered in the future research if other rotational speeds relative to the same system will be investigated.

D.1 Definition of the CFD boundary conditions

The analyses presented in this rotational speed of the rotor was kept constant at 80% N_d Referring to Fig. 3.28, the vortex 1 (datum) defined in § 3.4.2 was prescribed at the farfield inlet plane at the locations introduced in § 5.1.1. Both of the vortex polarity were considered. The value of static pressure imposed at the CFD rotor outlet plane was such that the rotor outlet non-dimensional mass flow ($NDMF_2$) remained constant at $3.872 \cdot 10^{-3}\ kgs^{-1}K^{0.5}Pa^{-1}$. This value corresponded to a condition near stall. Finally, the boundary conditions imposed at the farfield outlet plane and at the farfield wall were similar to that defined in § 4.2.1.

D.2 Numerical investigations

The numerical analyses presented in this section include the analysis of the S-shaped intake aerodynamics and the description of the flow field at the AIP. Note that the relative results were similar to that already presented in § 5.1.

D.2.1 S-shaped intake aerodynamics

The intake performance was evaluated by means of the pressure recovery (η), defined in § 3.3.8. The change in pressure recovery was generally very close to unit and presented a low sensitivity to the ingestion of vortices as shown in Fig. D.1.

A qualitative description of the flow separation occurring into the S-duct when vortex 1 (datum) was ingested at different locations and for the two of possible polarities was accomplished. The results were similar to that relative to the analysis carried out at 100% N_d, where the S-duct flow separation was mostly affected for vortices ingested near the starboard and co- and counter-rotating vortices ingested near the top and bottom edge of the intake (see Fig. D.2 and D.3).

D.2.2 Flow field description at the AIP

The flow field at the AIP was described in terms of both total pressure and swirl distortion in a similar manner presented in § 5.1.3, relatively to the ingestion of vortex 1.

The magnitude and the extent of the total pressure distortion calculated at the AIP was related to the mass flow as well as to the interaction existing between the ingested vortex and the self-generated distortion occurring into the S-duct. Referring to Fig. D.6, the total pressure distortion parameter (DC_{60}) calculated for different combinations of vortex location and polarity were similar to that presented in § 5.1.3.1.

In terms of swirl distortion, the distribution of non-dimensional streamwise vorticity (ω_z^*) (Fig. D.7 and D.8) as well as that of the relative rotor incidence change ($\Delta\beta$) (Fig. D.9 and D.10) were analyzed. Both of these distributions were used to identify the location of the vortex at the AIP and its interaction either with the self-generated distortion or the wall. The results were qualitatively similar to that discussed in § 5.1.3.2.

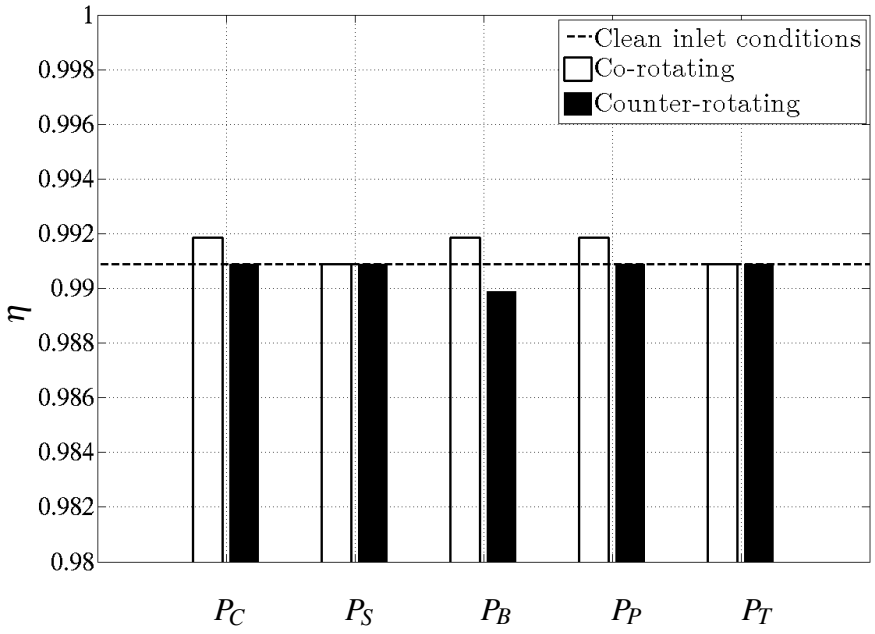

Figure D.1: Pressure recovery (η) for vortex 1 ingested at different locations and polarities and with rotor operating at 80% N_d and $NDMF_2 = 3.872 \cdot 10^{-3}\ kgs^{-1}K^{0.5}Pa^{-1}$

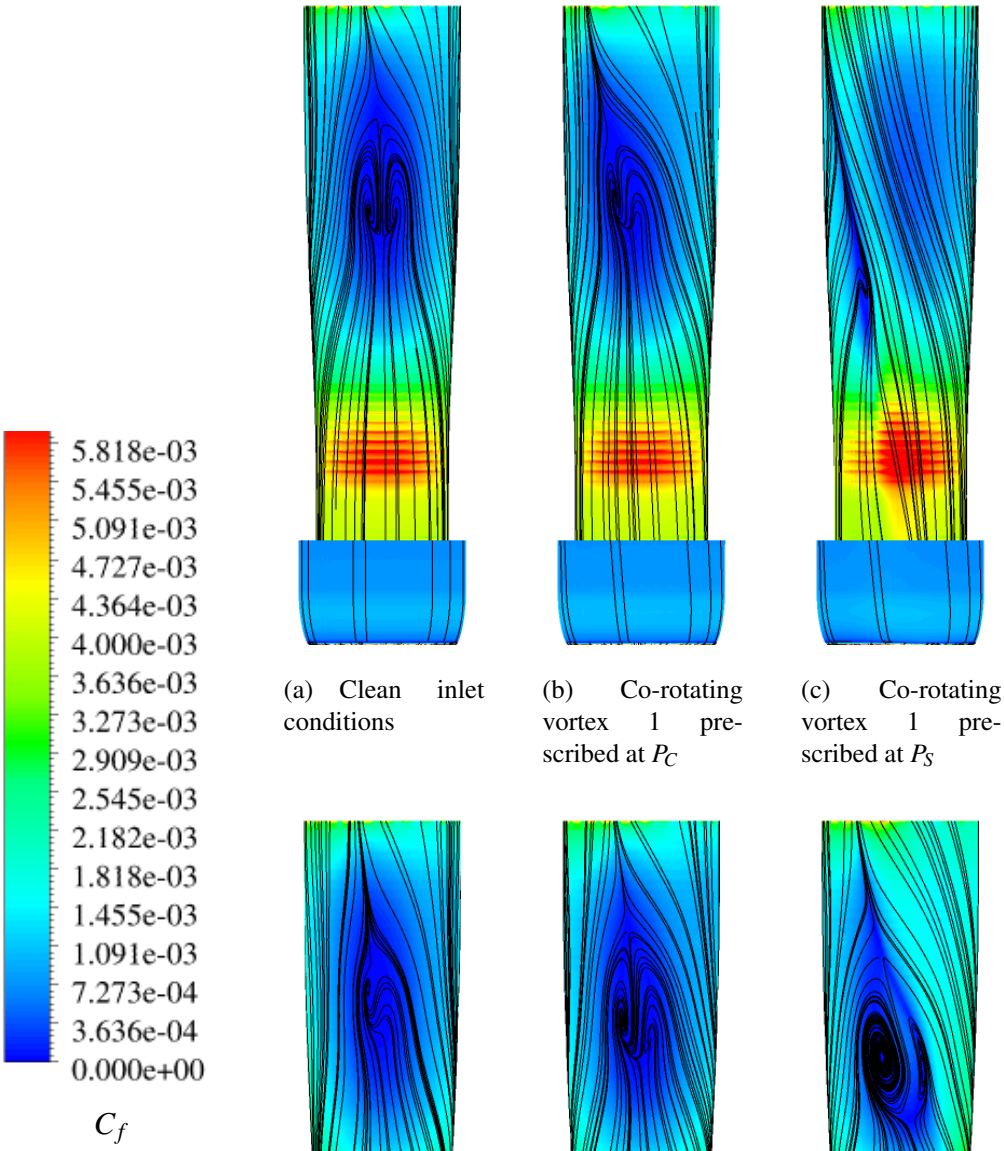

(a) Clean inlet conditions

(b) Co-rotating vortex 1 prescribed at P_C

(c) Co-rotating vortex 1 prescribed at P_S

(d) Co-rotating vortex 1 prescribed at P_B

(e) Co-rotating vortex 1 prescribed at P_P

(f) Co-rotating vortex 1 prescribed at P_T

Figure D.2: Contours of skin friction coefficient (C_f) with streaklines (black) at the starboard side of the intake wall for co-rotating vortex 1 (datum) ingested at different locations) prescribed at different locations and with rotor operating at 80% N_d and $NDMF_2 = 3.872 \cdot 10^{-3}\ kgs^{-1}K^{0.5}Pa^{-1}$

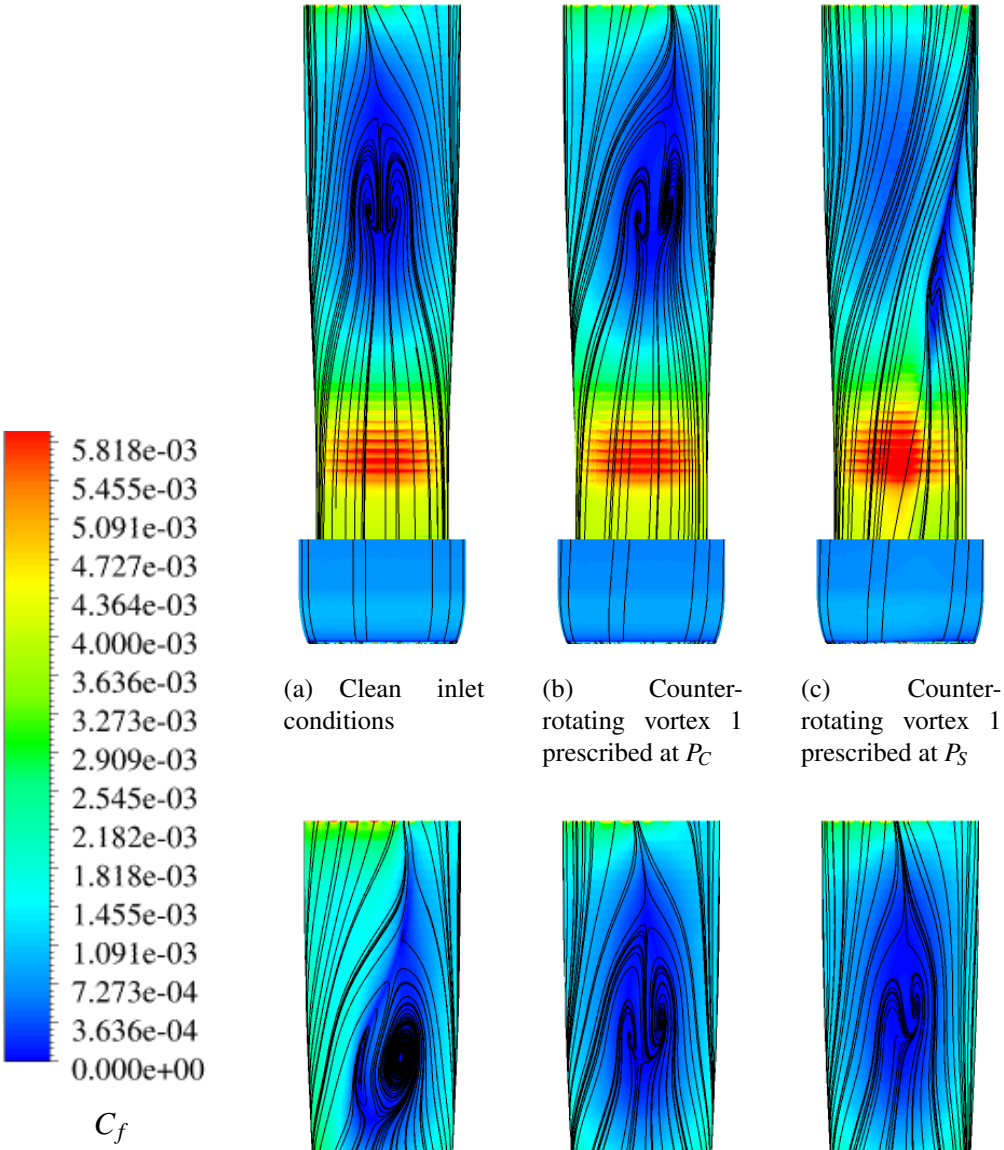

(a) Clean inlet conditions

(b) Counter-rotating vortex 1 prescribed at P_C

(c) Counter-rotating vortex 1 prescribed at P_S

(d) Counter-rotating vortex 1 prescribed at P_B

(e) Counter-rotating vortex 1 prescribed at P_P

(f) Counter-rotating vortex 1 prescribed at P_T

Figure D.3: Contours of skin friction coefficient (C_f) with streaklines (black) at the starboard side of the intake wall for counter-rotating vortex 1 (datum) ingested at different locations) prescribed at different locations and with rotor operating at 80% N_d and $NDMF_2 = 3.872 \cdot 10^{-3}\ kgs^{-1}K^{0.5}Pa^{-1}$

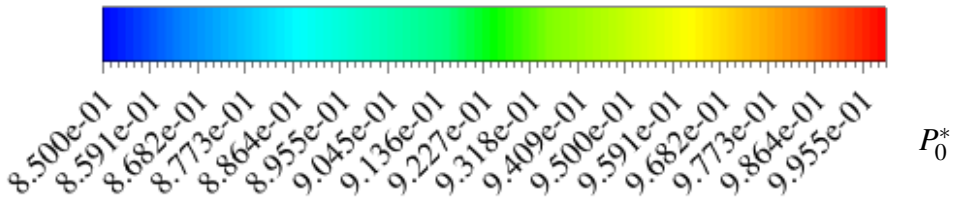

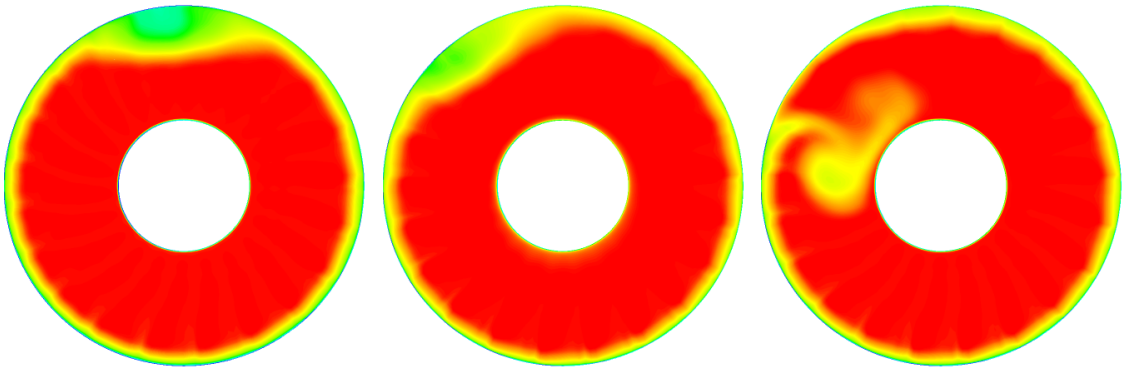

(a) Clean inlet conditions (b) Vortex prescribed at P_C (c) Vortex prescribed at P_S

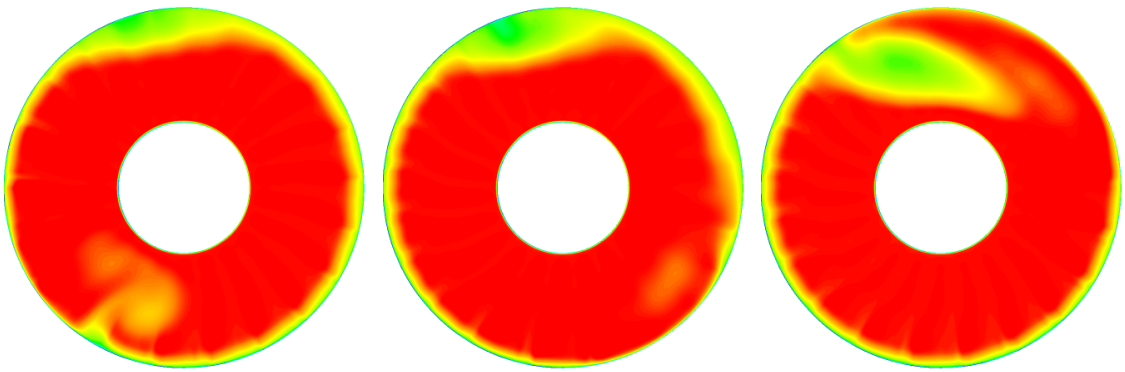

(d) Vortex prescribed at P_B (e) Vortex prescribed at P_P (f) Vortex prescribed at P_T

Figure D.4: Contours of non-dimensional total pressure distortion (P_0^*) at the AIP for co-rotating vortex 1 ingested at different locations and with rotor operating at 80% N_d and $NDMF_2 = 3.872 \cdot 10^{-3}\ kgs^{-1}K^{0.5}Pa^{-1}$

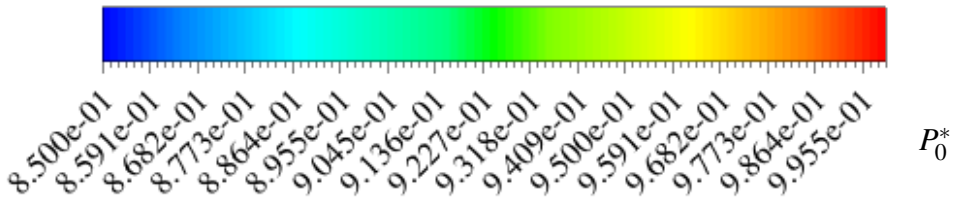

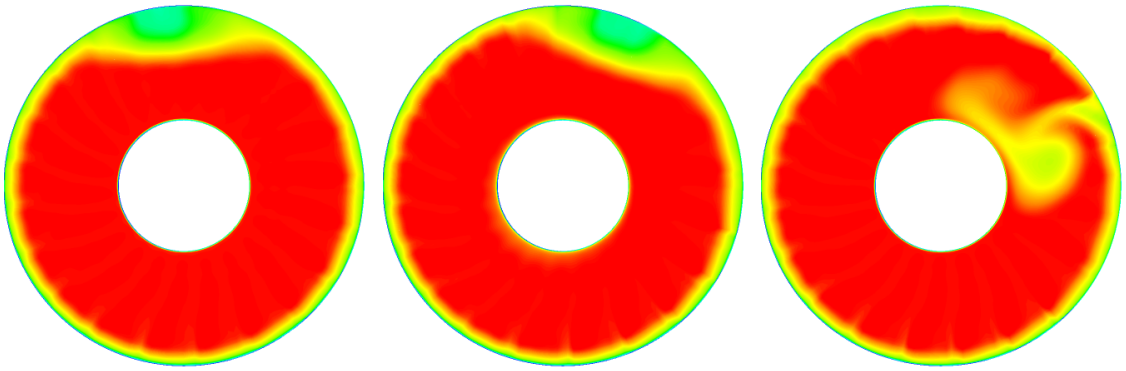

(a) Clean inlet conditions (b) Vortex prescribed at P_C (c) Vortex prescribed at P_S

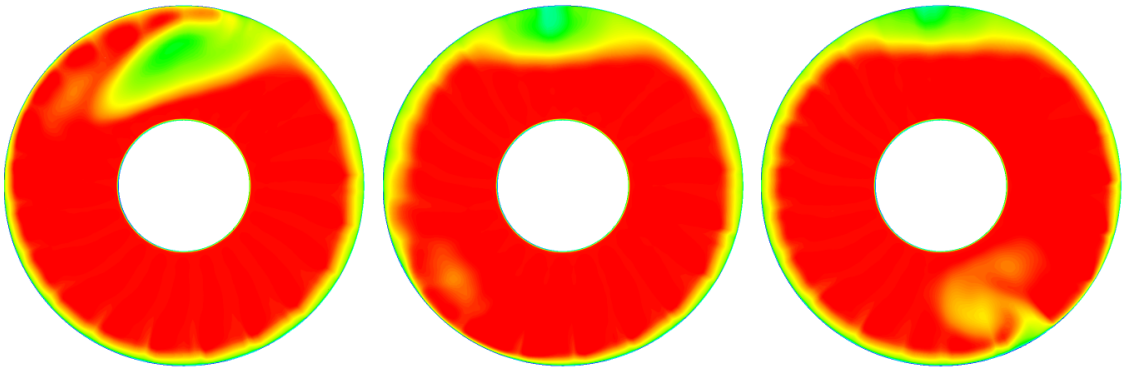

(d) Vortex prescribed at P_B (e) Vortex prescribed at P_P (f) Vortex prescribed at P_T

Figure D.5: Contours of non-dimensional total pressure distortion (P_0^*) at the AIP for counter-rotating vortex 1 ingested at different locations and with rotor operating at 80% N_d and $NDMF_2 = 3.872 \cdot 10^{-3}\ kgs^{-1}K^{0.5}Pa^{-1}$

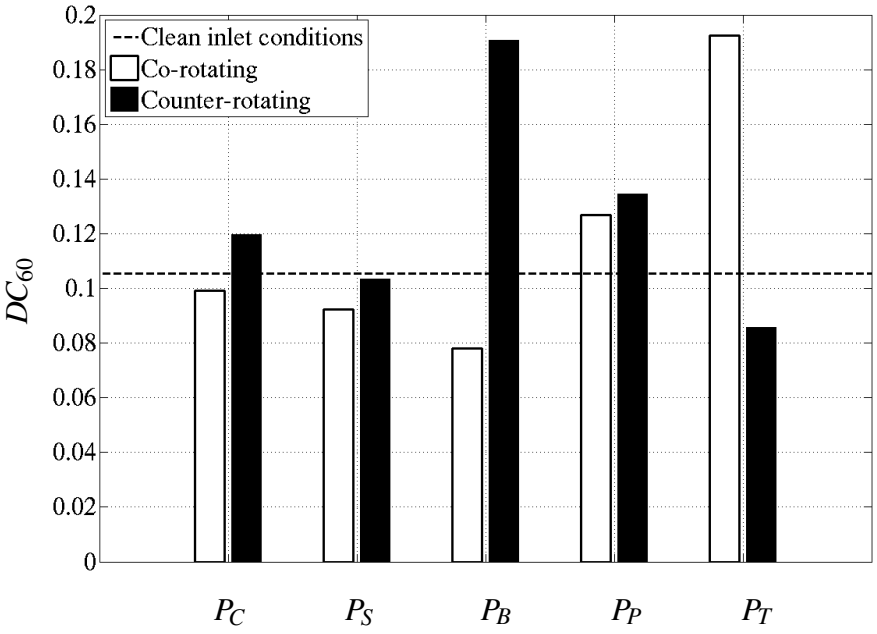

Figure D.6: Total pressure distortion parameter (DC_{60}) for different ingested vortex locations and polarities andwith rotor operating at 80% N_d and $NDMF_2 = 3.872 \cdot 10^{-3}$ $kgs^{-1}K^{0.5}Pa^{-1}$

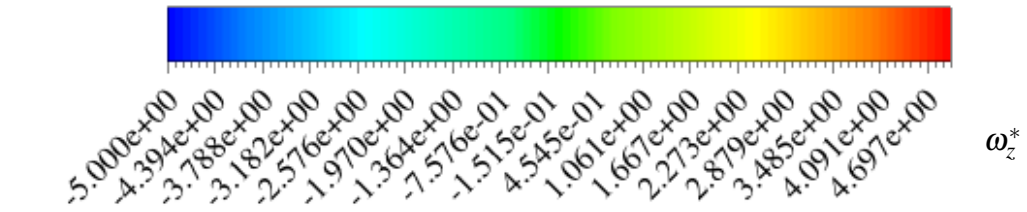

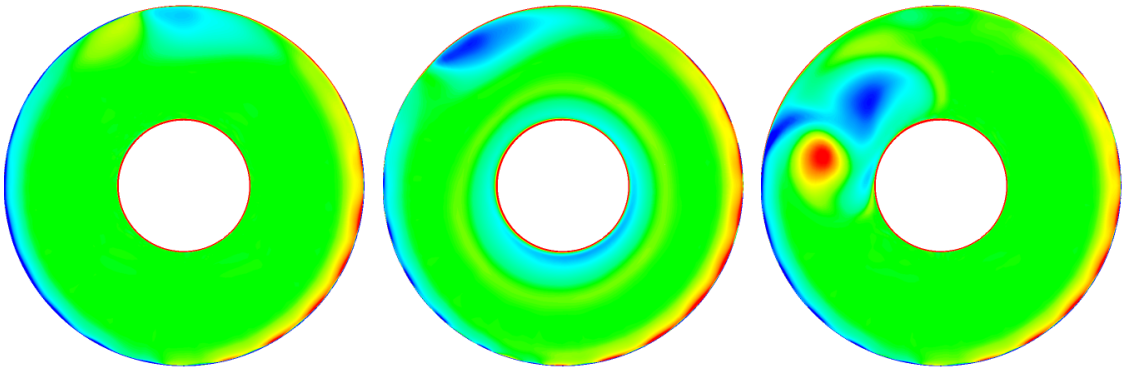

(a) Clean inlet conditions (b) Vortex prescribed at P_C (c) Vortex prescribed at P_S

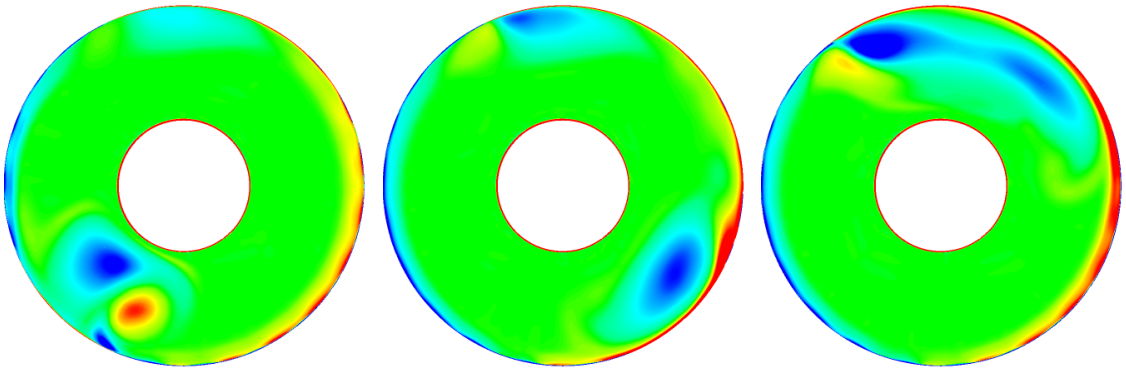

(d) Vortex prescribed at P_B (e) Vortex prescribed at P_P (f) Vortex prescribed at P_T

Figure D.7: Contours of non-dimensional streamwise vorticity at the AIP for co-rotating vortex 1 ingested at different locations and with rotor operating at 100% N_d and $NDMF_2 = 3.872 \cdot 10^{-3}\ kgs^{-1}K^{0.5}Pa^{-1}$

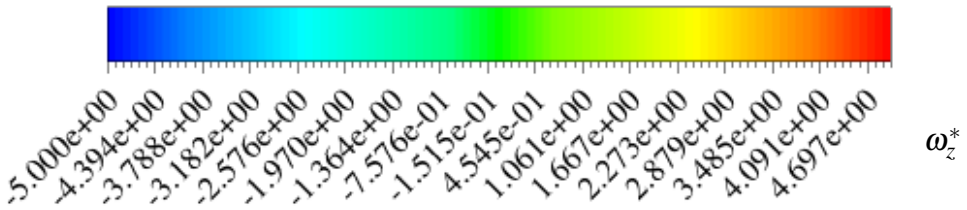

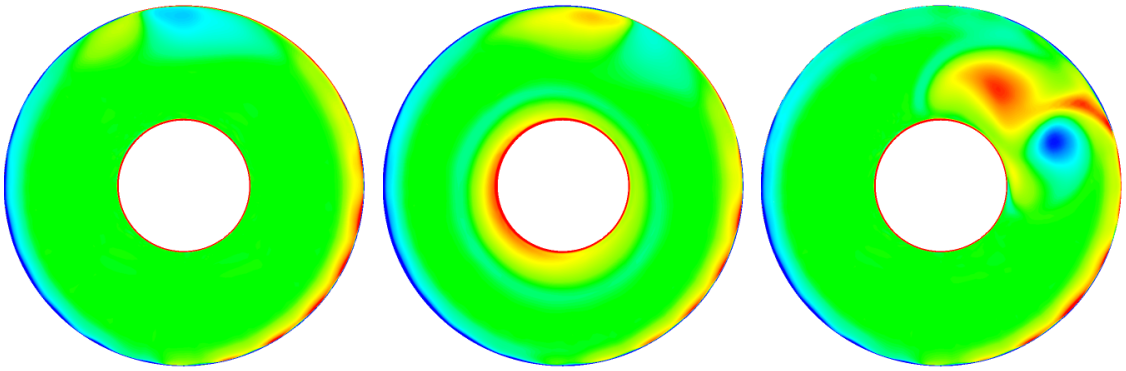

(a) Clean inlet conditions (b) Vortex prescribed at P_C (c) Vortex prescribed at P_S

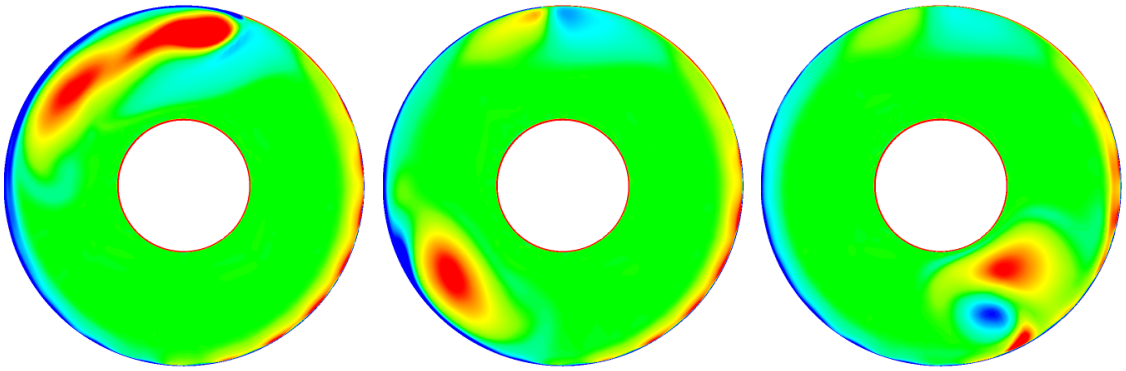

(d) Vortex prescribed at P_B (e) Vortex prescribed at P_P (f) Vortex prescribed at P_T

Figure D.8: Contours of non-dimensional streamwise vorticity (ω_z^*) at the AIP for counter-rotating vortex 1 ingested at different locations and with rotor operating at 100% N_d and $NDMF_2 = 3.872 \cdot 10^{-3}\ kgs^{-1}K^{0.5}Pa^{-1}$

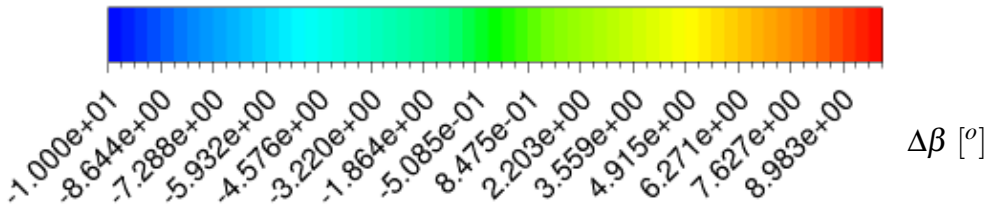

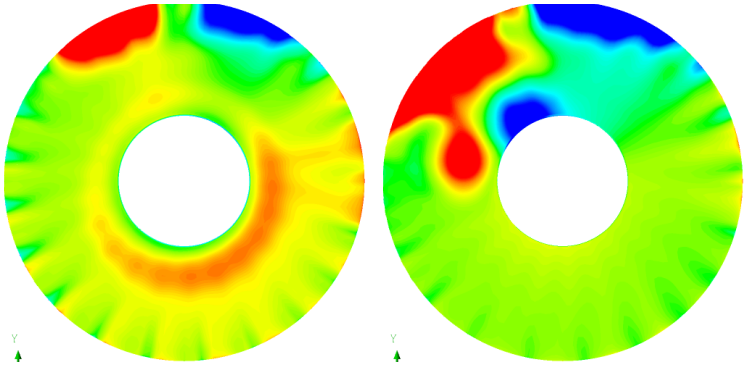

(a) Vortex prescribed at P_C (b) Vortex prescribed at P_S

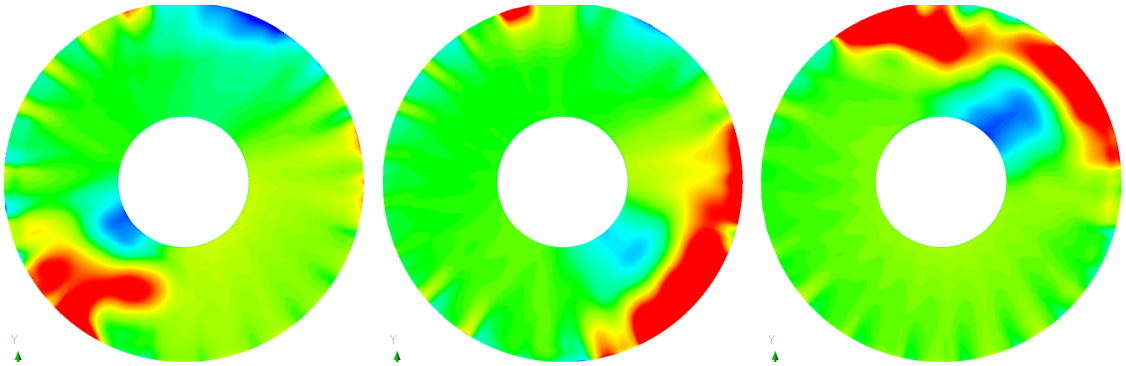

(c) Vortex prescribed at P_B (d) Vortex prescribed at P_P (e) Vortex prescribed at P_T

Figure D.9: Contours of relative flow angle change ($\Delta\beta$) at the AIP for co-rotating vortex 1 ingested at different locations and with rotor operating at 80% N_d and $NDMF_2 = 3.872 \cdot 10^{-3}\ kgs^{-1}K^{0.5}Pa^{-1}$

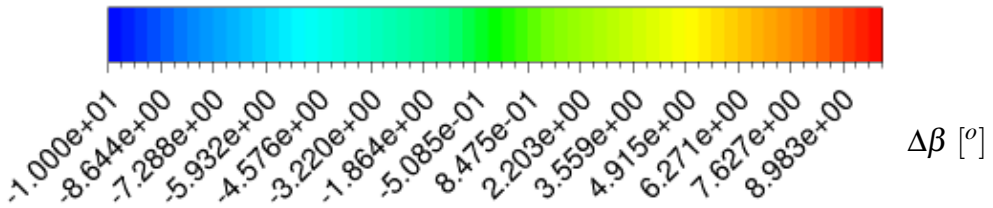

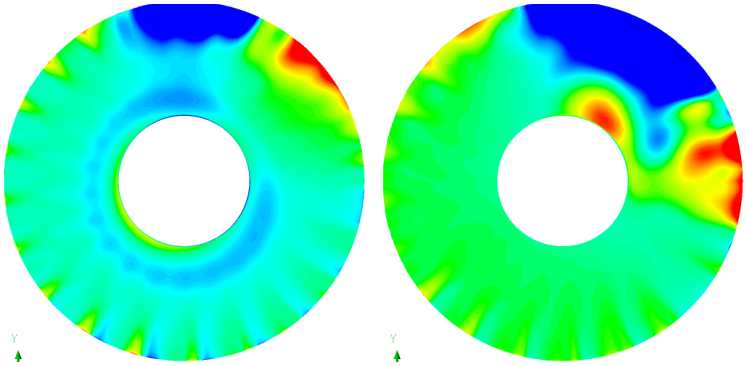

(a) Vortex prescribed at P_C (b) Vortex prescribed at P_S

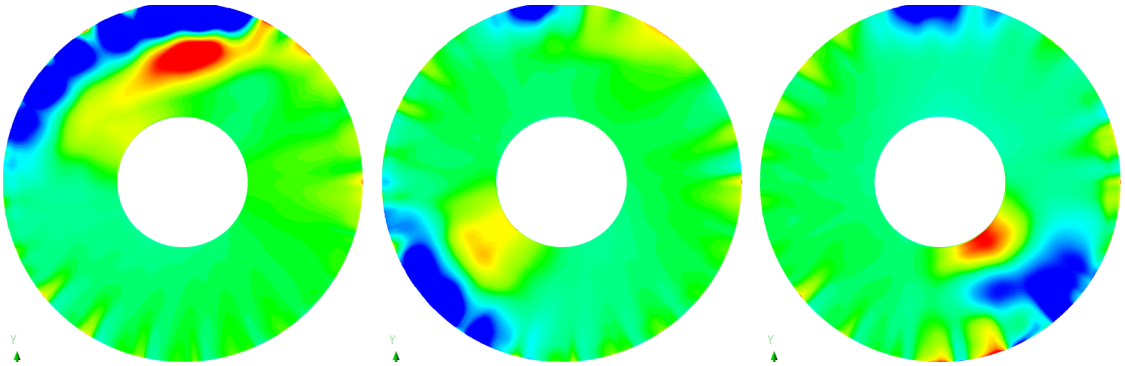

(c) Vortex prescribed at P_B (d) Vortex prescribed at P_P (e) Vortex prescribed at P_T

Figure D.10: Contours of relative flow angle change ($\Delta\beta$) at the AIP for counter-rotating vortex 1 ingested at different locations and with rotor operating at 80% N_d and $NDMF_2 = 3.872 \cdot 10^{-3}\ kgs^{-1}K^{0.5}Pa^{-1}$